INFORMATION TO USERS

This manuscript has been reproduced from the microfilm master. UMI films the text directly from the original or copy submitted. Thus, some thesis and dissertation copies are in typewriter face, while others may be from any type of computer printer.

The quality of this reproduction is dependent upon the quality of the copy submitted. Broken or indistinct print, colored or poor quality illustrations and photographs, print bleedthrough, substandard margins, and improper alignment can adversely affect reproduction.

In the unlikely event that the author did not send UMI a complete manuscript and there are missing pages, these will be noted. Also, if unauthorized copyright material had to be removed, a note will indicate the deletion.

Oversize materials (e.g., maps, drawings, charts) are reproduced by sectioning the original, beginning at the upper left-hand corner and continuing from left to right in equal sections with small overlaps. Each original is also photographed in one exposure and is included in reduced form at the back of the book.

Photographs included in the original manuscript have been reproduced xerographically in this copy. Higher quality 6" x 9" black and white photographic prints are available for any photographs or illustrations appearing in this copy for an additional charge. Contact UMI directly to order.

U·M·I
University Microfilms International
A Bell & Howell Information Company
300 North Zeeb Road. Ann Arbor, MI 48106-1346 USA
313/761-4700 800/521-0600

Order Number 9409329

Evaluation of a planar optic waveguide as a platform for evanescent field chemical sensor development

Kuhn, Kevin John, Ph.D.

University of Washington, 1993

U·M·I
300 N. Zeeb Rd.
Ann Arbor, MI 48106

Evaluation of a Planar Optic Waveguide as a Platform for Evanescent Field Chemical Sensor Development

by

Kevin John Kuhn

A dissertation submitted in partial fulfillment
of the requirements for the degree of

Doctor of Philosophy

University of Washington

1993

Approved by ______________________________
(Chairman of Supervisory Committee)

____

Program Authorized
to Offer Degree Chemistry

Date August 11, 1993

Doctoral Dissertation

In presenting this dissertation in partial fulfillment of the requirements for the Doctoral degree at the University of Washington, I agree that the Library shall make its copies freely available for inspections. I further agree that extensive copying of this dissertation is allowable only for scholarly purposes, consistent with "fair use" as prescribed in the U.S. Copyright Law. Requests for copying or reproduction of this dissertation may be referred to University Microfilms, 1490 Eisenhower Place, P.O. Box 975, Ann Arbor, MI 48106, to whom the author has granted "the right to reproduce and sell (a) copies of the manuscript in microform and/or (b) printed copies of the manuscript made from microform."

Signature Kevin J. Kuhn

Date August 11, 1993

University of Washington

Abstract

Evaluation of a Planar Optic Waveguide as a Platform for Evanescent Field Chemical Sensor Development

by Kevin John Kuhn

Chairman of the Supervisory Committee: Professor Gary D. Christian
Department of Chemistry

A Ag^+-exchange planar optic waveguide was fabricated with the intent of taking advantage of the significant interfacial sensitivity of the device for evanescent field chemical sensor development in the visible spectral region. However, it was discovered that selective prism and grating coupling to discrete waveguide modes was not possible due to strong crosstalk between modes in multiple mode Ag^+-exchange waveguide structures. Thus, sensor development was delayed and research was redirected towards evaluation of a multiple mode Ag^+-exchange planar waveguide device. To carry out the evaluation, the Ag^+-exchange waveguide surface was exposed to transient impulses of a series of model chemical analytes in a flowing liquid phase system. The complex multiple mode response of the waveguide was captured at relevant time intervals using a linear array detector.

Model chemical systems were chosen to characterize the Ag^+-exchange waveguide liquid phase response to bulk refractive index (glycerol), bulk absorbance (bromocresol green), and to simultaneous variations in bulk refractive index and absorbance. Cationic molecular systems were chosen to test the waveguide response to analytes which partition into or adsorb to the waveguide surface giving rise to a refractive index perturbation (Pb^{2+}) or modulations in both refractive index and absorbance (methylene blue). As temperature effects are superimposed on any measurement made with the Ag^+-exchange waveguide, the multiple mode temperature response was characterized using a thermoelectric cooler assembly to control the device temperature.

The waveguide multiple mode response is potentially multivariate to even single component analyte systems as the device response function may include concentration dependent mode coupling variations, modulations in mode crosstalk, and changes in mode outcoupling position on the array detector. Thus, chemometrics are necessarily employed to waveguide multiple mode response data to aid in interpretation and response

calibration. The application of chemometrics to the Ag^+-exchange waveguide response data provided for the deconvolution of simultaneous liquid phase refractive index and absorbance changes. The potential also exists to separate waveguide response contributions from bulk compositional changes and interfacial partitioning or binding effects.

Table of Contents

List of Figures

List of Tables

Acknowledgments

I would like to thank Lloyd Burgess and Gary Christian for their support, guidance and enthusiasm throughout my graduate years. Thanks to Rob Synovec and Martin Afromowitz for numerous helpful discussions and for providing perspective to the research. Thanks to fellow graduate students, especially those in the Burgess and Christian research groups who made contributions to the enjoyment of graduate school. Special thanks to Marina Furtado, John Koch and John Luke for their diversionary support in maintaining a proper balance. Finally, I would like to thank my family for their combined sense of humor and unwavering support from the very beginning.

Chapter 1

Introduction

1.1 General Rationale

The current emphasis on product quality and waste minimization within the chemical industry has created a growing interest in process characterization, optimization, and control. The development of measurement strategies which provide chemical process information are addressed within the field of process analytical chemistry.[1,2] The challenge posed in chemical process monitoring is to capture the process state at relevant intervals and incorporate this real-time information into automated or manual process control decisions. Realistically, measurement needs extend beyond the immediate process to encompass the surrounding process environment as industry must insure worker and public safety and document compliance with government emissions standards. The process environment can be extended even further in industries which employ a pipeline system for transporting raw materials and distributing refined chemicals.

Measurement strategies which are relevant to obtaining chemical information in a process environment are attracting considerable attention in other applications. The highly toxic radioactive waste and related products from the defense industry have created a significant problem in long-term storage and contaminated site remediation. The caretakers of such dangerous materials must maintain the structural integrity of containment vessels, monitor the chemical stability of stored materials, confirm the containment of waste plumes, and document the results of site remediation while minimizing worker exposure to hazardous materials. The study of basic environmental chemistry often requires real-time measurements in difficult to reach locations such as at the ocean floor, in ground water wells and in the atmosphere. In clinical chemistry, bedside monitoring of critical care analytes in seriously ill and surgery patients is required on a continuous or intermittent basis.

In order to address measurement problems in process chemistry, environmental monitoring, and clinical chemistry, traditional grab sampling methods are being replaced by methods allowing for real-time evaluation of complicated, often harsh chemical matrices. One approach which is particularly attractive is to develop chemical analogs to common temperature and pressure sensors which operate *in-situ* and remote from an external control device.

1.2 Chemical Sensors

1.2.1 General Description

Chemical sensors function *in situ* and provide information regarding the chemical composition of a sample at a discrete sampling point. The chemical sensor can function remote from the control device by connection via an extended electrical or optical cable. Chemical sensors measure an electrochemical, mass, optical, or thermal modulation related to the presence of a target analyte in the sample. The modulation in sensor response follows from an inherent property of the analyte or is produced by an interaction between the analyte and a selective sensor component. Attributes associated with an idealized chemical sensor include exclusive analyte selectivity, short response time, continuous measurement, small size, and simple and rugged design. Viable single use, throw-away chemical sensors are low cost and exhibit a reproducible sensor-to-sensor response function. Typical concerns in the development of chemical sensor include sensor fouling, device calibration, and sensor lifetime in severe sampling environments. In practice complete chemical specificity is difficult to obtain, so that the development of robust chemical sensors which over sample the target environment to provide some rejection towards sample interferents and a state-of-the-sensor diagnostic function have a greater chance for successful implementation.

1.2.2 Optical Sensors

The interaction of electromagnetic radiation with matter provides the basis for a significant body of spectroscopic methods (absorbance, fluorescence, Raman) for chemical analysis. Spectroscopic methods are based on the quantized interaction between electromagnetic radiation and discrete molecular energy states. Since each molecule exhibits a unique distribution of energy states, spectroscopic techniques employed for chemical analysis are inherently selective provided a relevant analysis wavelength(s) is chosen. In addition, spectroscopic methods employing broadband sources and appropriate detection schemes provide for a multivariate analysis of the sample matrix. Thus, broadband spectroscopy can be combined with multivariate data analysis techniques to optimize wavelength selection, identify and reject sample interferents and analyze multiple component samples. Interactions between radiation and matter may also produce interference effects, scattering, and polarization rotation which provide additional mechanisms for chemical sensing.

1.2.2.1 Fiber Optics

Fiber optics transmit electromagnetic radiation via successive total internal reflections from cylindrical core/clad interfaces as depicted in Figure 1.1. Total internal reflection occurs for radiation propagating in the denser core medium (n_1) when the incident angle at the interface with the rarer clad medium (n_3) exceeds the critical angle as defined by,

$$\Theta_c = \sin^{-1}(n_3/n_1). \qquad 1.1$$

The interfacial critical angle restricts the range of launch angles into the fiber which will be transmitted without reflection loss to a numerical aperture defined as,

$$NA = n_0 \sin\Theta_l = (n_1^2 - n_3^2)^{1/2} \qquad 1.2$$

where n_0 is the refractive index of the launch medium (i.e. air) and Θ_l is the launch angle. Despite the apparent propagation of radiation across a continuum of angles from the 0° to Θ_l, the fiber actually supports closely space but discrete angles of propagation termed waveguide modes. The number of allowed modes (N_m) in a waveguide structure supporting a large number of modes is approximated by,

$$N_m = 0.5(\pi\, d\, NA/\lambda)^2 \qquad 1.3$$

where d is the fiber diameter and λ is the radiation wavelength.

At each point of total internal reflection, a small portion of the total guided power penetrates across the interface to create an "evanescent" electromagnetic field in the cladding which decays exponentially with distance from the interface. In general, the total electromagnetic field amplitude associated with the evanescent field and its depth of penetration into the rarer medium, increases as the mode propagation angle approaches the critical angle and as the refractive index ratio, n_3/n_1, at the interface approaches unity.

1.2.2.2 Extrinsic Fiber Optic Sensors

The availability of low-loss optical fibers permits the extension of a wide variety of spectroscopic and optical methods to remote sampling environments. The function of optical fibers as "lossless" conduits for the transfer of electromagnetic radiation falls under the category of extrinsic fiber optic sensing. In combination with conventional instrumentation, fiber optics allow for remote spectroscopic analysis by transmitting broadband source radiation to the sample and collecting the modulated radiation for detection. This fiber optic sensing strategy relies solely on the intrinsic selectivity of the spectroscopic method. Spectrometers incorporating fiber optics for remote sensing are commercially available in the ultraviolet, visible, and near infrared spectral regions.[3] Fiber optics have also been employed for remote Raman[4-6], fluorescence[7], and phase-resolved spectroscopy.[8]

The selectivity of extrinsic fiber optic chemical sensors can be increased by the incorporation of a specific chemistry at the distal fiber end which creates a measurable optical modulation in the presence of an analyte. The chemistry can be confined to the area illuminated by the fiber optic via chemical bonding, polymer entrapment[9,10], or by incorporation within a porous bead[11-13] or membrane.[14,15] The use of a membrane potentially adds to the selectivity of the sensor by excluding interferents from the sensing region. The recent description of renewable reagent fiber optic probes provide for the use of highly specific irreversible chemistries in the extrinsic sensing format.[16-19]

1.2.2.3 Intrinsic Fiber Optic Sensors

Intrinsic fiber optic chemical sensors are based on an analyte induced perturbation in the conditions for light propagation. Commonly, the analyte perturbation results in a modulation in the evanescent electromagnetic field which penetrates a short distance ($<\lambda$) into the fiber cladding layer at each point of total internal reflection. In order to be detected, the analyte must penetrate into the cladding to produce a refractive index or absorbance interaction with the evanescent field. As evanescent field fiber optic chemical sensors monitor a small volume of sample located at the core-cladding interface, matrix effects from highly scattering or absorbing interferents are minimized. The applicability of evanescent field fiber optic sensors for chemical analysis is largely reduced to analytes which partition into polysiloxanes as they are used almost exclusively as commercial cladding materials.[20-22] The replacement of commercial cladding with a chemical reagent phase introduces limitations in achievable evanescent path lengths as cladding modification is necessarily limited to short lengths of fragile optical fiber.[23,24]

1.3 Planar Waveguides

Asymmetric thin film planar waveguides (Figure 1.2) are commonly fabricated by depositing a high refractive index waveguide layer on top of a substrate support material. A wide variety of thin film materials are available for planar waveguide fabrication including numerous polymeric and inorganic oxide films. As the sample matrix commonly serves as the planar waveguide cladding, the evanescent field samples the composition of the cover solution directly. Thin film planar waveguides maintain advantages common to fiber optic evanescent field chemical sensors while providing a large enhancement in evanescent path length per unit guide length. Thus, the sensitivity of the planar waveguide to refractive index and absorbance perturbations at the waveguide surface is significantly increased. Light transmission in thin film planar waveguides is limited to discrete, resolvable propagation angles (modes) exhibiting differential interfacial sensitivities which can be selectively monitored. Thus, the high background intensity which reduces the apparent surface sensitivity of fiber optic evanescent field chemical sensors is eliminated. The evaluation of planar waveguides as platforms for evanescent field chemical sensor development is the focus of this thesis.

1.3.1 Historical

The confinement of visible radiation within a planar waveguide structure was initially investigated as a means to study the optical properties of semiconductor p-n junctions.[25,26] The population of waveguide modes was non-selective in that mode excitation was achieved by focusing a laser source onto the edge of the junction. The development of planar optical circuits for information processing was an active area of research in the early 1960s. An important experiment along these lines was the demonstration of selective modulation of light propagating within a p-n junction by the electrooptic effect.[27] The theoretical description and experimental demonstration of discrete mode coupling using a prism coupler provided the means to excite and interrogate individual waveguide modes.[28] This important development provided selective access to each information "channel" supported by a multiple mode planar waveguide structure. The term integrated optics was introduced to describe the integration of optical components on thin film waveguide "chips" and marked the beginning of serious efforts to develop thin film technology for optical communications applications.[29] The deposition of diffraction gratings onto thin film waveguides provided an integrated method of selective waveguide mode coupling and decoupling.[30,31] Compared to prism couplers, gratings offered clear advantages including compatibility with integrated planar component designs, functional simplicity, and reproducible performance.

In parallel with the design and testing of planar optical waveguide components, considerable research effort went into the development of low loss, amorphous materials for planar waveguide fabrication. The description of ion-exchange in glass was one of the earliest reported methods for producing planar waveguides.[32]

1.3.2 Planar Waveguide Evanescent Field Chemical Sensors

A significant body of research describing the evaluation of thin film materials by measuring mode propagation constants[33-36] and observing induced optical effects[37-45] (i.e. absorption, scattering, etc.) is included in the literature. From the perspective of this discussion, waveguide evaluation is the necessary first step in identifying thin film materials for developing planar waveguide chemical sensors. However, advancements in material evaluation are not emphasized herein as the primary interest is in reviewing efforts towards the development of planar waveguide evanescent field chemical sensors.

An important distinction in discussing evanescent field chemical sensors is that between passive and active sensor devices. Passive planar waveguide evanescent field chemical sensors were initially described as an alternative to bulk optical attenuated total reflection (ATR) elements for sensitive evanescent absorbance sensing. The passive sensor device measures changes in bulk sample properties such as refractive index and absorbance. In contrast, active chemical sensors rely on a selective interaction between the waveguide surface and the analyte. For waveguides produced from inherently non-selective or chemically passive materials, surface modification is necessary for selective interfacial activation.

The application of planar optic waveguides to the analysis of chemical systems was first proposed by Midwinter.[46,47] A consideration of waveguide theory led Midwinter to conclude that thin film planar waveguides could be used as passive internal reflection elements (IREs) with sufficient path length to make ATR measurements at visible wavelengths. Subsequent experimental work by Polky and Harris confirmed that planar waveguides provided the necessary sensitivity to perform visible wavelength evanescent absorbance measurements.[48] Mitchell enumerated distinct advantages in sample volume reduction and freedom from scattering in unfiltered blood samples while evaluating the absorbance response of a planar waveguide to clinical samples.[49] The evaluation of a planar waveguide as an absorbance detector in a continuous-flow analysis system was described by Choquette.[50] The fabrication of a tantalum pentoxide (Ta_2O_5) planar waveguide with integrated grating couplers by DeGrandpre, et al. allowed for the isolation of launch and collection optics from the sensing interface.[51] A method to reduce the effects of cover refractive index on the performance of the Ta_2O_5 device as an absorbance sensor was discussed. The use of a cooled charge-coupled device (CCD) array detector allowed Saavedra and Reichert to image the faint multiple mode output from a polystyrene waveguide evaluated as a liquid phase absorbance sensor.[52] The mechanism of multiple mode excitation was described as intermodal scattering. The large scatter from polymeric waveguides was also observed to excite fluorescence emission from a liquid solution in contact with the waveguide surface.[53] The recent description of multiwavelength coupling to a planar waveguide has potential implications for future development of miniature integrated spectrometers.[54,55]

In 1983 Lukosz and Tiefenthaler described a procedure for producing thin SiO_2-TiO_2 waveguide films with an embossed surface grating.[56] Seifert, et. al have described the development of a biosensor based on the operation of the SiO_2-TiO_2 thin film waveguide structure as a differential refractometer.[57] A planar waveguide refractive index sensor configured as a Mach-Zehnder interferometer has been fabricated and tested by Hollenbach, et. al.[58]

Numerous active evanescent field chemical sensors relying on the inherent interaction between the planar waveguide and an analyte have been described. The interaction between polymeric planar waveguides and various solvent vapors have been described.[59-62] Tiefenthaler and Lukosz have demonstrated the use of a porous SiO_2-TiO_2 waveguide as a sensor for adsorbed vapors.[63,64] Spohn and Seifert have conducted a thorough experimental evaluation of the inherent stability and surface chemistry of SiO_2-TiO_2 thin film waveguides in aqueous solutions.[65] Bolton and Scherer have studied the stepwise hydration of bovine serum albumin thin film waveguides.[66] Protein adsorption to the surface of thin film polystyrene waveguides has been monitored by scatter induced protein fluorescence[67] and absorption.[68]

Typically, chemical sensor development requires surface modification to impart analyte specificity and enhance interaction capacity. Increasing the interaction capacity potentially results in greater device sensitivity and extended dynamic range. The highly selective antibody-antigen interaction has been used to advantage in the reported development of numerous immunosensors.[69-71] The fabrication of an electrochemical sensor device by deposition of a thin film of conductive SnO_2 over the waveguide layer to serve as an electrode has been described.[72] The combination of this electrochemical planar waveguide structure with an electrochromic thin film has been demonstrated as a sensor for chlorine.[73]

1.3.3 Ion-Exchange Planar Waveguides

Inorganic oxide planar optical waveguides provide a desirable platform for developing evanescent field chemical sensors for liquid phase analyses. The fabrication of ion-exchange waveguides in soda-lime silica substrates is relatively simple and the resulting silicon dioxide waveguide surface is non-porous, mechanically durable, and readily modified with numerous silane reagents. For these reasons, a number of recent publications describing chemical sensor development have employed ion-exchange waveguides.[70,72,73] These publications have focused on modifying the surface of ion-exchange waveguide elements towards specified analytes. However, in the rush to develop novel chemical sensors based on ion-exchange waveguide technology, an evaluation of the underlying ion-exchange element towards environmental perturbations has received little emphasis. Of particular concern is the observed population of all waveguide modes in multimode ion-exchange structures at distinct angles corresponding to discrete waveguide modes.[74]

1.4 Research Goals

The Ag^+-exchange planar optical waveguides which we fabricated as potential sensor elements were of sufficient thickness to support multiple modes. In evaluating the mode structure, it was confirmed that coupling a polarized laser source to Ag^+-exchange waveguides produced multiple mode output. The multiple mode coupling phenomenon in ion-exchange waveguides has neither been explicitly described nor explained in the literature. The observation of multiple mode coupling describes the existence of a pathway for intensity interchange among the various waveguide modes. Thus, the potential exists for modulations in the degree of mode intensity interchange with changes in cover solution composition. Therefore, the mechanism of multiple mode coupling in Ag^+-exchange waveguides is potentially of great importance to the performance of evanescent field chemical sensors fabricated on the Ag^+-exchange device.

The sensitivity of planar waveguide devices depends on the effective evanescent path length for interaction with the sample. For evanescent sensing of the sample phase, this statement remains approximately valid in specifying the response to traditionally nonpath length dependent phenomena such as changes in cover refractive index. In waveguide devices, the effective evanescent path length is determined by the optical properties of the materials defining the waveguide structure and the waveguide geometry. In the planar waveguide case, the liquid cover solution serves both as the sample medium and as an optical cladding. Thus, the planar waveguide effective evanescent path length and, in turn, the waveguide sensitivity is dependent on variations in optical properties with analyte concentration in the cover solution. Therefore, the relationship between the waveguide response and sample concentration is not well defined and must be determined empirically to create a relevant device calibration.[75]

As the evanescent field interaction with the cover phase is confined to a short distance from the waveguide surface, the location of analyte at the interface is necessary for detection. Thus, the association of analyte with the interface due to interaction with the glass waveguide surface will enhance the waveguide sensitivity. The Ag^+-doped soda-lime silica glass waveguide surface is expected to exhibit characteristic silica chemistry. Thus, the glass waveguide surface does not present an entirely passive interface to an aqueous cover solution. In particular, the ion-exchange behavior of the silica glass surface must be considered in characterizing the response of Ag^+-exchange planar waveguides.

The primary purpose of the research discussed in this dissertation was to evaluate the Ag^+-exchange planar optical waveguide device for potential use as a platform for liquid phase evanescent field chemical sensor development. The evaluation included a number of specific goals, including: 1) the elucidation of a feasible mechanism of multiple waveguide mode population, 2) a characterization of the multiple mode waveguide response function to a series of model chemical systems, 3) demonstrating a reproducible and calibratable waveguide response function, and 4) a determination of the inherent waveguide sensitivity to model liquid phase analytes. Photodiode array detection was used to monitor the individual mode outputs as the waveguide was exposed to liquid samples. As the measured waveguide multiple mode response was multivariate, chemometric methods were applied to aid in interpretation and calibration of waveguide response data.

The theory of light propagation in Ag^+-exchange planar waveguides is presented in Chapter 2 along with an extension of theory to describe expected waveguide response trends to various model chemical systems. The characteristics and performance of Ag^+-exchange waveguides depend on the bulk and surface chemistry of silica glass which is the topic of Chapter 3. Experimental instrumentation and procedures are discussed in detail in Chapters 4 and 5, respectively. The results of the experimental evaluation of the Ag^+-

exchange waveguide to a number of model chemical systems and temperature are presented and discussed in Chapter 6. Chapter 7 provides an opportunity to draw conclusions regarding implications of the presented thesis research to future Ag^+-exchange planar waveguide sensor development.

1.5 Notes to Chapter 1

(1) Callis, J. B.; Illman, D. L.; Kowalski, B. R. *Anal. Chem.* **1987**, 59, 624A.

(2) Riebe, M. T.; Eustace, D. J. *Anal. Chem.* **1990**, 62, 65A.

(3) Weyer, L. G.; Becker, K. J.; Leach, H. B. *Appl. Spectrosc.* **1987**, 41(5), 786.

(4) Archibald, D. D.; Lin, L. T.; Honigs, D. E. *Appl. Spectrosc.* **1988**, 42(8), 1558.

(5) Lewis, E. N.; Kalasinsky, V. F.; Levin, I. W. *Anal. Chem.* **1988**, 60(24), 2658-2661.

(6) Bello, J. M.; Vo-Dinh, T. *Appl. Spectrosc.* **1990**, 44(1), 63-69.

(7) Kenny, J. E.; Jarvis, G. B.; Chudyk, W. A.; Pohlig, K. O. *Anal. Inst.* **1987**, 16(4), 423.

(8) Bright, F. V. *Appl. Spectrosc.* **1988**, 42(8), 1531.

(9) Munkholm, C.; Walt, D. R.; Milanovich, F. P.; Klainer, S. M. *Anal. Chem.* **1986**, 58(7), 1427-1430.

(10) Zhujun, Z.; Zhang, Y.; Wangbai, M.; Russell, R.; Shakhsher, Z. M.; Grant, C. L.; Seitz, W. R.; Sundberg, D. C. *Anal. Chem.* **1989**, 61, 202-205.

(11) Berman, R. J. Ph.D. Dissertation, University of Washington, Seattle, WA, 1990

(12) Fuh, M. R. S.; Burgess, L. W.; Hirschfeld, T.; Christian, G. D.; Wang, F. *Analyst* **1987**, 112, 1159.

(13) Fuh, M. R. S.; Burgess, L. W.; Christian, G. D. *Anal. Chem.* **1988**, 60, 433-435.

(14) Peterson, J. I.; Goldstein, S. R.; Fitzgerald, R. V.; Buckhold, D. K. *Anal. Chem.* **1980**, 52(6), 864-869.

(15) Angel, S. M.; Ridley, M. N.; Langry, K.; Kulp, T. J.; Myrick, M. L. *ACS Symp. Ser.* **1989**, vol. 403, 346.

(16) Luo, S.; Walt, D. R. *Anal. Chem.* **1989**, 61(2), 174.

(17) Inman, S. M.; Stromvall, E. J.; Lieberman, S. H. *Anal. Chim. Acta.* **1989**, 217, 249.

(18) Berman, R. J.; Burgess, L. W. *SPIE Proceedings: Chemical, Biochemical and Environmental Applications of Fibers* **1990**, 1172, 206-214.

(19) Sepaniak, M. J.; Tromberg, B. J.; Alarie, J. P.; Bowyer, J. R.; Hoyt, A. M.; Vo-Dinh, T. *ACS Symp. Ser.* **1989**, vol. 403, 318.

(20) DeGrandpre, M. D.; Burgess, L. W. *Anal. Chem.* **1988**, 60, 2582-2586.

(21) DeGrandpre, M. D.; Burgess, L. W. *Appl. Spectrosc.* **1990**, 44, 273.

(22) DeGrandpre, M. D.; Ph.D. Dissertation, University of Washington, Seattle, WA, 1990.

(23) Farahi, F.; Leilabady, A. P.; Jones, J. D. C.; Jackson, D. A. *J. Phys. E: Sci. Instrum.* **1987**, 20, 435.

(24) Sutherland, R.; Dähne, C.; Place, J. F. *Anal. Lett.* **1984**, 17, 43.

(25) Yariv, A.; Leite, R. C. C. *Appl. Phys. Lett.* **1963**, 2(3), 55-59.

(26) Ashkin, A.; Gershenzon, M. *J. Appl. Phys.* **1963**, 34, 2116-2119.

(27) Nelson, D. F.; Reinhart, F. K. *Appl. Phys. Lett.* **1964**, 5, 148-150.

(28) Tien, P. K.; Ulrich, R.; Martin, R. J. *Appl. Phys. Lett.* **1969**, 14(9), 291-294.

(29) Miller, S. E. *Bell Syst. Tech. J.* **1969**, 48, 2059-2069.

(30) Dakss, M. L.; Kuhn, L.; Heidrich, P. F.; Scott, B. A. *Appl. Phys. Lett.* **1970**, 16(12), 523-525.

(31) Kogelnik, H.; Sosnowski, T. P. *Bell. Syst. Tech. J.* **1970**, 49, 1602-1608.

(32) Osterberg, H.; Smith, L. W. *J. Opt. Soc. Amer.* **1964**, 58, 1078-1084.

(33) Ulrich, R.; Torge, R. *Appl. Opt.* **1973**, 12, 2901.

(34) Kersten, R. Th. *Opt. Commun.* **1973**, 9(4), 427-431.

(35) Swalen, J. D.; Tacke, M.; Santo, R.; Fischer, J. *Opt. Commun.* **1976**, 18(3), 387-390.

(36) Swalen, J. D.; Santo, R.; Tacke, M.; Fischer, J. *IBM J. Res. Develop.* **1977**, 21, 168-175.

(37) Swalen, J. D.; Tacke, M.; Santo, R.; Rieckhoff, K. E.; Fischer, J. *Helv. Chim. Acta* **1978**, 61(3), 960-977.

(38) Rabolt, J. F.; Santo, R.; Swalen, J. D. *Appl. Spectrosc.* **1979**, 33(6), 549-551.

(39) Rabolt, J. F.; Santo, R.; Schlotter, N. E.; Swalen, J. D. *IBM J. Res. Develop.* **1982**, 26(2), 209-216.

(40) Rabolt, J. F.; Schlotter, N. E.; Swalen, J. D. *J. Phys. Chem.* **1981**, 85(26), 4141-4144.

(41) Schlotter, N. E.; Rabolt, J. F.; *J. Phys. Chem.* **1984**, 88(10), 2062-2067.

(42) Bohn, P. W. *Anal. Chem.* **1985**, 57(7), 1203-1208.

(43) Stephens, D. A.; Bohn, P. W. *Anal. Chem.* 1987, 59(21), 2563-2566.

(44) Miller, D. R.; Han, O. H.; Bohn, P. W. *Appl. Spectrosc.* **1987**, 41(2), 245-248.

(45) Miller, D. R.; Bohn, P. W. *Anal. Chem.* **1988**, 60(5), 407-411.

(46) Midwinter, J. E. *IEEE J. Quant. Elect.* **1971**, QE-7(7), 339-344.

(47) Midwinter, J. E. *IEEE J. Quant. Elect.* **1971**, QE-7(7), 345-350.

(48) Polky, J. N.; Harris, J. H. *J. Opt. Soc. Amer.* **1972**, 62(9), 1081-1087.

(49) Mitchell, G. L. *IEEE J. Quant. Elect.* **1977**, QE-13(4), 173-176.

(50) Choquette, S. J. Ph.D. Dissertation, Virginia Polytechnic Institute and State University, Blacksburg, Va., 1988.

(51) DeGrandpre, M. D.; Burgess, L. W.; White, P. L.; Goldman, D. S. *Anal. Chem.* **1990**, 62(18), 2012-2017.

(52) Saavedra, S. S.; Reichert, W. M. *Anal. Chem.* **1990**, 62(20), 2251-2256.

(53) Reichert, W. M.; Ives, J. T.; Suci, P. A.; Hlady, V. *Appl. Spectrosc.* **1987**, 41(4), 636-640.

(54) Goldman, D. S.; White, P. L.; Anheier, N. C. *Appl. Opt.* **1990**, 29(31), 4583-4589.

(55) Lytle, D. *Photonics Spectra* **1991**, 209.

(56) Lukosz, W.; Tiefenthaler, K. *Opt. Lett.* **1983**, 8(10), 537-539.

(57) Seifert, M; Tiefenthaler, K.; Heuberger, K.; Lukosz, W.; Mosbach, K. *Anal. Lett.* **1986**, 19(1), 1986.

(58) Hollenbach, U.; Efstathiou, C.; Fabricius, N.; Oeste, H.; Götz, H. *SPIE Proceedings: Micro-Optics* **1988**, 1014, 77-80.

(59) Scherer, J. R.; Bailey, G. F. *J. Membrane Sci.* **1983**, 13, 29-41.

(60) Scherer, J. R.; Bailey, G. F.; *J. Membrane Sci.* **1983**, 13, 43-52.

(61) Bowman, E. M.; Burgess, L. W. *SPIE Proceedings: Chemical, Biochemical, and Environmental Sensors II* **1990**.

(62) Bowman, E. M. Ph.D. Dissertation, University of Washington, Seattle, Wa., 1992.

(63) Tiefenthaler, K.; Lukosz, W. *Opt. Lett.* **1984**, 10(4), 137-139.

(64) Tiefenthaler, K.; Lukosz, W. *Thin Solid Films* **1985**, 126, 205-211.

(65) Spohn, P. K.; Seifert, M. *Sensors and Actuators* **1988**, 15, 309-324.

(66) Bolton, B. A.; Scherer, J. R. *J. Phys. Chem.* **1989**, 93(22), 7635-7640.

(67) Ives, J. T.; Reichert, W. M. *Appl. Spectrosc.* **1988**, 42(1), 68-72.

(68) Saavedra, S. S.; Reichert, W. M.; *Langmuir* **1991**, 7(5), 995-999.

(69) Nellen, Ph. M.; Lukosz, W. *Biosensors & Bioelectronics* **1991**, 6, 517-525.

(70) Choquette, S. J.; Locascio-Brown, L.; Durst, R. A. *Anal. Chem.* **1992**, 64(1), 55-60.

(71) Lu, B.; Lu, C.; Wei, Y. *Anal. Lett.* **1992**, 25(1), 1-10.

(72) Itoh, K.; Fujishima, A. *J. Phys. Chem.* **1988**, 92(25), 7043-7045.

(73) Piraud, C.; Mwarania, E.; Wylangowski, G.; Wilkinson, J.; O'Dwyer, K.; Schiffrin, D. J. *Anal. Chem.* **1992**, 64(6), 651-655.

(74) Choquette, S. J. private communication, National Institute of Standards and Technology, Gaithersburg, MD.

(75) Janata, J. *Principles of Chemical Sensors*; Plenum Press: New York, NY, 1989.

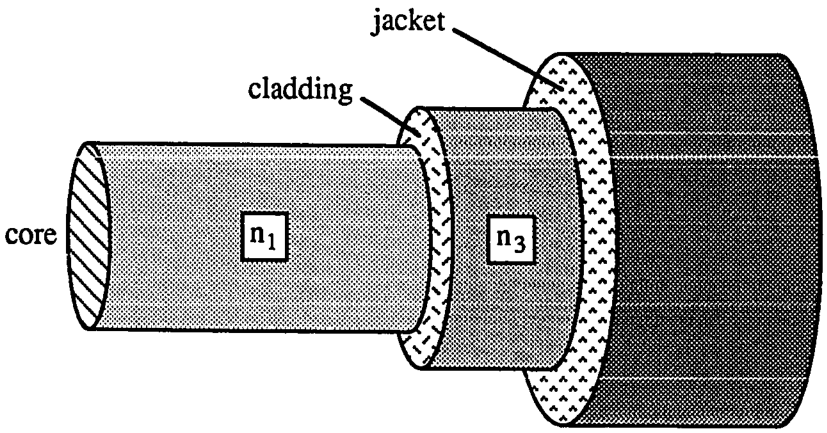

a)

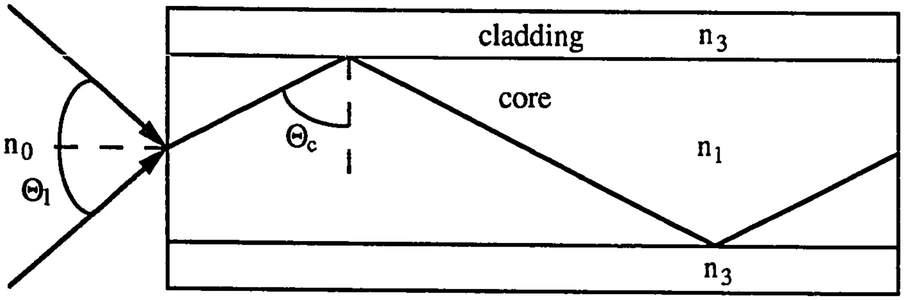

b)

Figure 1.1 Fiber optic fundamentals: a) fiber optic schematic, b) ray optic representation of light propagation in a cylindrical fiber optic.

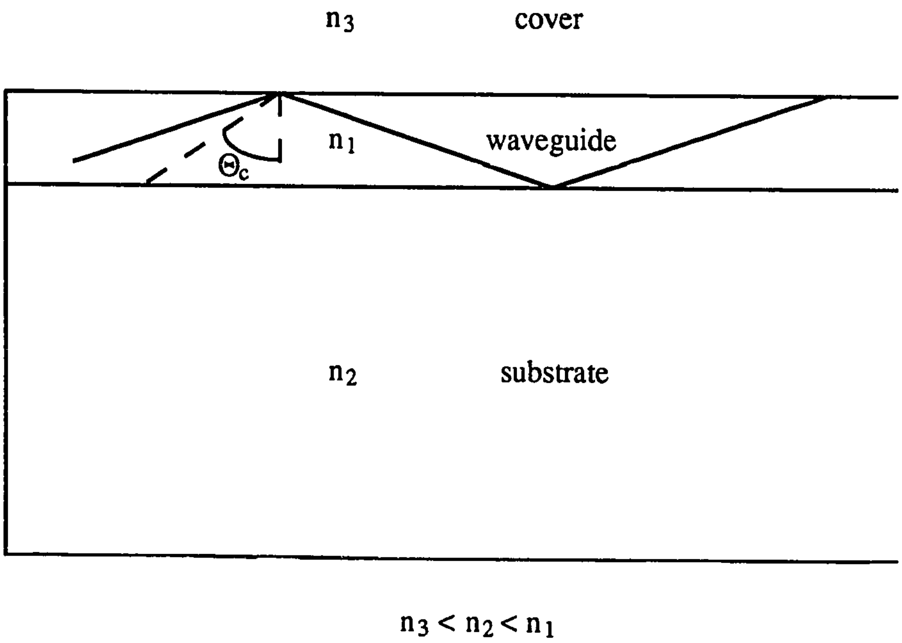

Figure 1.2 Light propagation in an asymmetric planar optic waveguide.

Chapter 2

Theory

Planar optical waveguide components have been the subject of extensive study in the semiconductor, computer, and communications industries. The design and fabrication of waveguide components for applications in these industries emphasize controlled modulation of the optical waveguide beam with isolation from potential external influences. In contrast, the design and fabrication of planar waveguide chemical sensors depend on the generation of a reproducible interaction with an analyte in an external sample matrix to produce a modulation in the optical waveguide beam. As such, the development of waveguide theory has proceeded without the necessary dialogue between scientists in these two camps to develop a rigorous description of planar waveguide device function as a chemical sensor. The current models which describe light propagation in ion-exchange waveguides do not include a consideration of environmentally induced perturbations in waveguide propagation conditions. In the following discussion, the intent is to identify waveguide parameters which control the waveguide response to external perturbations. The prediction of response trends based on a theoretical consideration of waveguide parameters will be given for later comparison with experimental results.

The physical phenomenon of an evanescent electromagnetic field associated with total internal reflection from a dielectric interface provides the basis for describing the interaction of an optical waveguide beam with its immediate environment. Thus, an understanding of total internal reflection will provide a helpful starting point in the discussion of planar optical waveguide theory. The confinement of optical power in a planar waveguide extends the concept of total internal reflection to describe multiple reflections from two parallel, planar interfaces. For a suitably small planar cavity, interference effects produce discrete angles of allowed beam propagation (modes) which require the use of waveguide couplers to selectively excite and interrogate.

2.1 Total Internal Reflection

2.1.1 Internal Reflection

An internal reflection occurs when light strikes an interface between two transparent dielectric media of differing refractive index from the denser medium side (Figure 2.1a). Reflection from a glass-air or glass-water interface for light traveling in glass are typical examples of internal reflections. At incidence angles (Θ_i) near the interfacial normal, part of the incident beam is reflected and part is transmitted. For the reflected beam, the angle of reflection (Θ_r) is equal to the angle of incidence. The reflectivity of the interface which describes the percentage of reflected power is described by Fresnel's equations.[1]

The transmitted beam is refracted away from the normal as described by Snell's Law for $n_1 > n_3$,

$$n_1 \sin\Theta_i = n_3 \sin\varphi_t. \qquad 2.1$$

As the angle of incidence increases, the angle of refraction continues to increase until a critical angle condition is reached where the predicted refraction angle becomes 90° (Figure 2.1b),

$$\Theta_c = \sin^{-1}(n_3/n_1). \qquad 2.2$$

At the critical angle, the transmitted beam disappears and the reflectivity of the interface reaches 100%. Thus, the critical angle defines the condition for total internal reflection. Total internal reflection occurs for all angles of incidence above the critical angle up to grazing incidence, $\Theta_c < \Theta_i < 90^\circ$.

2.1.1.1 Polarization

The incident beam may exhibit either perpendicular (TE or tranverse electric) or parallel (TM or transverse magnetic) polarization. The geometric designations arise in considering the alignment of radiation electric field vectors with respect to the plane of incidence (xz plane). However, for the purposes of this discussion, it will be more instructive to consider the electric field alignment with respect to the substrate-cover interface (yz plane). The electric field vector associated with the TE polarization is parallel to the reflecting yz surface. In contrast, the electric field vector for the TM polarization has components both parallel and perpendicular to the substrate-cover interface.

Below the critical angle, the reflectivity of the interface is highly dependent on the polarization of the incident beam. However, the critical angle is independent of polarization and both the TE and TM polarizations are totally reflected at incidence angles above the critical angle.

2.1.1.2 Phase Shift

The phase of the reflected beam is shifted compared to the incident beam following total reflection from a dielectric interface. The phase shift experienced by the reflected wave front can be derived from Fresnel's equations and is given as,

$$\phi_{TE} = \tan^{-1}\{(\sin^2\Theta_i - n_{31}^2)^{1/2}/(n_1 \cos\Theta_i)\} \qquad 2.3$$

and

$$\phi_{TM} = \tan^{-1}\{1/n_{31}^2\ (\sin^2\Theta_i - n_{31}^2)^{1/2}/(n_1 \cos\Theta_i)\} \qquad 2.4$$

for a TE and TM polarized incident beam, respectively. The reflection phase shift is modulated by changes in the angle of incidence and the refractive index ratio, $n_{31}=n_3/n_1$. The phase shift increases from zero at the critical angle to $\pi/2$ at grazing incidence. In contrast, the phase shift decreases as the refractive index ratio approaches unity for a given angle of incidence above the critical angle.

2.1.2 Evanescent Electric Field

At a point of total internal reflection, the superposition of incident and reflected wave fronts create a standing electromagnetic wave within the denser (substrate) medium. The standing wave is continuous across the interface giving rise to an evanescent electromagnetic wave which penetrates into the rarer (cover) medium. Both the electric and magnetic field amplitudes associated with the evanescent wave behave similarly. For example, the electric field amplitude decays exponentially with distance from the interface,

$$E(x) = E_0\, e^{-x\gamma} \qquad 2.5$$

where $E(x)$ is the evanescent electric field at some distance x normal to the interface, E_0 is the electric field amplitude at the interface, and γ is the decay constant,

$$\gamma = (n_1 k_0)(\sin^2\Theta - n_{31}^2)^{1/2}. \qquad 2.6$$

The decay constant dependence on radiation wavelength is included in the free space wave number term, $k_0=2\pi/\lambda$. As indicated in equation 2.5, the electric field amplitude in the cover medium at a given distance from the interface is related to the interfacial electric field strength and the magnitude of the decay constant. Together the interfacial electric field strength and decay constant determine the effective evanescent path length for sensing the adjacent cover solution.

2.1.2.1 E_0 - Interfacial Electric Field Amplitude

The electric field amplitude at the interface depends on 1) the polarization of incident radiation, 2) the angle of incidence, and 3) the refractive index contrast between the adjacent optical media.

1) The tangential electric field components for the TE and TM polarizations are constrained to be continuous across the interface and thus have identical amplitudes on either side. However, the normal electric field component associated with the TM polarization is not constrained to continuity across the interface and has a value larger by a factor $1/n_{31}^2$ in the cover medium than in the substrate. As result, the total interfacial electric field strength of the TM polarization is always larger than that of the TE polarization for a given incidence angle.

2) The angular dependence of the evanescent field strength differs for the two polarizations. The TE polarization exhibits a maximum in interfacial electric field amplitude at the critical angle and decreases with increasing angle of incidence to become zero for grazing incidence, $\Theta_i = 90°$. The electric field amplitude for the TM polarization tangential component is zero at the critical angle, reaches a maximum, and decreases to zero for grazing incidence. The normal TM component has maximum electric field amplitude at the critical angle and decreases with increasing incidence angle. The total electric field amplitude for the TM polarization is maximum at the critical angle and decreases to zero for grazing incidence.

3) The interfacial electric field amplitude for both polarizations increases as the refractive index ratio, n_{31}, increases. This makes intuitive sense in that as the refractive index ratio approaches unity, the interface vanishes and the electric field amplitude in the cover takes on the free wave value.

2.1.2.2 γ - Decay Constant

The decay constant describes the reduction in electric field amplitude with distance from the interface. For the purpose of probing the composition of the cover phase, it is desirable to have a small decay constant to provide for a significant effective evanescent path length. The decay constant is independent of polarization but does depend on radiation wavelength, the angle of incidence, and the refractive index ratio. In accordance with equation 2.6, the decay constant decreases with increasing wavelength, as the incidence angle approaches the critical angle, and as the refractive index ratio increases towards unity.

2.1.3 Goos-Hänchen shift

For total internal reflection, the incident and reflected rays do not share a point of intersection at the interface. Rather, there is a slight displacement of the reflected beam from the point of incidence parallel to the interface. This phenomenon is termed the Goos-Hänchen shift.[2]

2.2 Waveguide Theory

2.2.1 Ag^+-Exchange Planar Waveguide

The Ag^+-exchange waveguide structure depicted in Figure 2.2 consists of a Ag^+ doped layer bounded by a soda-lime silica substrate and a cover solution. The Ag^+-exchange fabrication process yields a gradient distribution of Ag^+ in the glass matrix which results in a graded refractive index waveguide layer. The refractive index profile exhibits a maximum at the surface, n_{max}, which monotonically decreases with depth, n(x), into the substrate.

Radiation is confined within the ion-exchanged waveguide layer via alternating total internal reflections from the waveguide-cover and waveguide-substrate interfaces. For a light ray reflected from the waveguide-cover interface at an angle, $\Theta(0)$, greater than the critical angle,

$$\Theta_c = \sin^{-1}(n_l/n_{max}) \qquad 2.7$$

the totally reflected ray encounters an optical layer of decreasing refractive index. In accordance with a slightly modified Snell's Law,

$$n_{max} \sin\Theta(0) = n(x) \sin\Theta(x) \qquad 2.8$$

the ray will be continuously refracted with depth until it is either totally reflected at the turning point, x_t, or exits through the substrate. Following total reflection, transit through the waveguide layer in the opposite direction reverses the angular refraction, $\Theta(x)$, and the light ray strikes the waveguide-cover interface at the original angle, $\Theta(0)$.

The confined light is subject to interference effects due to the similar dimensions of visible radiation wavelength and waveguide thickness (several micrometers). Constructive interference is associated with distinct angular paths of light propagation in the waveguide layer giving rise to the existence of discrete waveguide modes. The allowed angular paths of mode propagation are defined according to a resonance condition,

$$k_0\int_0^{x_t}\left(n^2(x) - N_{eff}^2\right)^{1/2} dx - \phi_{1,2} - \phi_{1,3} = m\pi \qquad 2.9$$

for

$$N_{eff} = n_{max} \sin\Theta(0) \qquad 2.10$$

where x_t is the turning point depth of the mode, N_{eff} is the effective mode refractive index, and m is the integer mode order. The resonance condition requires that the phase shifts associated with reflections from the respective interfaces ($\phi_{1,2}$ and $\phi_{1,3}$) and path length through the ion-exchange layer combine to give a total phase shift which is an integer multiple of π. Angular solutions to the resonance condition generate characteristic standing electric field patterns across the waveguide layer which have evanescent components penetrating into the substrate and cover media.

A sufficiently thick waveguide layer will support multiple modes as specified by the mode order variable, m, in equation 2.9. As waveguide mode order increases, the resonance condition predicts that the interfacial reflection angle, $\Theta(0)$, for mode coupling approaches the critical angle for the waveguide-cover interface. Thus an increase in interfacial electric field strength and a decrease in the decay constant accompany an increase in waveguide mode order. As a result, the higher order waveguide modes generate a larger evanescent electric field per reflection in the cover phase.

In addition, light coupled into higher order modes must penetrate farther into the Ag^+-exchange layer before sufficient refraction occurs for total reflection at the turning point. Therefore, there is an increase in the apparent waveguide thickness with increasing mode order. For monochromatic light propagating within the waveguide, the refraction process has a focusing effect such that all modes experience approximately the same period. The important result is that each waveguide mode in an Ag^+-exchange planar waveguide has about the same number of internal reflections per unit length of waveguide.

2.2.2 Substrate Modes

In the asymmetric ion-exchange planar waveguide structure, light confinement is controlled by the waveguide-substrate critical angle. For angles of incidence below the waveguide-substrate critical angle, light may still be confined within the structure. Substrate modes travel the entire thickness of the substrate and propagate via multiple total internal reflections from the waveguide-cover and substrate-air interfaces. Since substrate modes are totally reflected from the waveguide-cover interface, they may exhibit a response to cover solution composition. In general, substrate modes present a potential source of intensity modulation unrelated to the waveguide mode response. Fortunately, substrate modes are out coupled from the waveguide structure at angles well separated from waveguide modes. In characterizing the mode structure of ion-exchanged waveguide, scanning source input angles slightly beyond the angle where substrate modes disappear provides a convenient method for locating the highest order waveguide mode.

2.2.3 Polarization

The inherent polarization of incident radiation is preserved by the planar waveguide geometry such that mode polarization can be specified. The reflection phase shift dependence on polarization expressed in Fresnel's equations gives different solutions to the waveguide resonance equation. Thus, the resonance condition predicts a slightly different angular distribution for TE modes than for TM modes. In each case, the TM mode for a given mode order propagates at an angle closer to the critical angle than the corresponding TE mode.

2.3 Mode Coupling

As discussed, the resonance condition specifies the existence of discrete waveguide modes propagating over distinct angular paths within the ion-exchange layer. Thus, coupling source radiation to a planar waveguide requires that the source input angle matches that of a resonant waveguide mode. This procedure is not as simple as in the case of optical fiber coupling where source illumination of the fiber endface is typically sufficient for mode population. In general, the reduced thickness dimension for planar waveguides makes endface illumination an impractical method of mode excitation. Practical options for planar waveguide mode coupling are limited to the use of longitudinal couplers; either prism couplers or grating couplers. Longitudinal couplers are advantageous in that selective coupling to a specific waveguide mode in a multiple mode structure is possible.

2.3.1 Prism Couplers

Prism coupling to an ion-exchange planar waveguide is depicted in Figure 2.3. Prism coupling requires the placement of a high refractive index prism ($n_p > n_{max}$) on the planar waveguide surface. Moderate pressure is applied to the prism to maintain a thin, uniform air gap between the prism base and the waveguide surface. Light incident at the base of the prism above the critical angle for the prism-air interface undergoes total internal reflection. The internal reflection produces a standing wave within the prism and an evanescent electric field extending across the interface into the air gap. Provided the air gap is sufficiently small ($<\lambda/2$), radiation can be extracted from the decaying evanescent field and coupled into the waveguide layer. The coupling mechanism is termed frustrated total internal reflection since coupling of radiation to the waveguide "frustrates" total reflection from the prism-air interface. Efficient coupling can only occur under conditions of phase matching between the evanescent field and a resonant waveguide mode given by,

$$N_{eff} = n_p \sin\Theta_p \qquad 2.11$$

where n_p is the prism refractive index and Θ_p is the prism base angle. The reverse process of extracting radiation propagating within the waveguide by prism outcoupling occurs under identical conditions.

In general, stable prism coupling conditions are difficult to maintain in that coupled intensity is sensitive to input beam alignment and prism contact with the waveguide surface. The use of prism couplers for sensor applications requires isolation of the prisms from the sample solution and placement of source and detection components on the same side of the substrate as the sensing interface. These are critical problems preventing the realistic development of stable prism coupled waveguide sensors for liquid phase samples. For the purposes of the research discussed herein, prism couplers were used only to determine mode coupling angles in ion-exchanged waveguides.

2.3.2 Grating Couplers

An illustration of the ion-exchange planar waveguide with an etched surface grating is given in Figure 2.4. For source launch through the substrate, the overall refraction due to the intervening substrate cancels so that the actual Snell's Law refraction occurs at an imaginary air-waveguide interface. Refraction of the source beam in the waveguide layer is continuous as the beam approaches the grating at the waveguide-cover interface. The incident beam is diffracted from the surface grating from an angle near normal incidence to an axial angle above the interfacial critical angle. The combined effect of refraction and grating diffraction are described by the grating equation,

$$n_{max} \sin\Theta(0) = n_{air} \sin\Theta_l + p\lambda/\Lambda \qquad 2.12$$

where Θ_l is the launch angle, Λ is the grating period, and p is the grating order (p=±1, ±2, etc.). Grating coupling to a given waveguide mode is obtained by conversion of a source beam launched near normal incidence to match the distinct angular path corresponding to a discrete waveguide mode. A second grating can be used to diffract radiation propagating in a waveguide mode out of the waveguide layer.

Compared to prism couplers, the integration of gratings within the waveguide structure provides a more stable coupling method for use in the development of waveguide sensors. In addition to better stability, a major advantage of grating couplers is that the source and detector can be located behind the waveguide substrate thus isolating optical components from the sensing interface. This is consistent with the design of integrated planar waveguide sensor probes or detection windows into chemical processes (liquids, slurries, or solids). Waveguides with etched grating couplers were employed in the evaluation of Ag^+-exchange waveguide responses to liquid phase model systems.

The primary disadvantage of grating couplers is that coupling efficiencies are typically lower than obtained using prism couplers. The existence of reflected and transmitted components for each diffracted beam and diffraction into multiple grating orders contribute to low grating efficiencies.

2.3.3 Resonance Coupling Curve

The resonance condition predicts a distinct coupling angle for each mode in an Ag^+-exchange waveguide. However, in practice coupling occurs over a narrow angular range, albeit at reduced efficiencies, due to variations in waveguide dimensions, coupler tolerances, and imperfect source collimation. The coupling angle for a given waveguide mode is typically specified as the angle which gives maximum coupled mode intensity. The angular width of the resonance coupling curve for Ag^+-exchange planar waveguides is discussed later in the waveguide evaluation section.

2.4 Predicted Waveguide Response

In general, the experimental procedure followed in this dissertation involved exposing the waveguide to a baseline cover solution, optimizing coupling to the waveguide TM_2 mode, and monitoring the waveguide output while modulating the cover solution composition. The original source launch conditions remain fixed for the duration of each experiment.

2.4.1 Cover Refractive Index

2.4.1.1 Reflection Grating Efficiency

The surface gratings on the Ag^+-exchange waveguide diffract a near normal incidence beam to match the angular conditions for TM_2 mode coupling. The dielectric surface gratings function as reflection gratings and as such are sensitive to the reflectivity of the waveguide-cover interface. The reflectivity follows Fresnel's equations and has a complicated dependence on the refractive index ratio, n_3/n_{max}, of the interface.[3] The trend is towards a decrease in the reflectivity of the waveguide-cover interface as the refractive index ratio increases. Thus, the diffraction efficiency of each surface gratings will be modulated by variations in cover refractive index. In turn, variations in the measured TM_2 mode intensity will reflect the changes in diffraction efficiency of both grating couplers.

2.4.1.2 Resonance Coupling

The total internal reflection phase shift depends on the refractive index of the cover solution as indicated in equation 2.4 (or eqn. 2.3). An increase in the refractive index of the cover phase produces a decrease in the interfacial phase shift. In the resonance equation, the waveguide-cover reflection phase shift term must balance with the remaining terms to maintain the resonance equality. Since the waveguide-substrate reflection phase shift is a constant, the path length phase shift must be reduced to compensate. The resulting increase in mode effective index indicates that the TM_2 mode propagation angle will increase with increasing cover solution refractive index.

Resonance coupling describes the efficiency with which the source beam is converted to a propagating waveguide mode. The selection of optimum TM_2 mode coupling as the baseline condition means that resonance coupling efficiency is initially at its maximum value, I_{max} (Figure 2.5). However, the coupling efficiency is sensitive to cover refractive index as the resulting change in mode propagation angle defines a reduction in angular match between the source and the allowed mode angle. Thus a change in cover refractive index reduces the efficiency of TM_2 mode coupling and the overall TM_2 mode intensity, I_{res}. The shape of the resonance coupling curve determines the sensitivity of resonance coupling efficiency to cover refractive index changes.

2.4.1.3 TM Mode Position Shifts

A change in cover refractive index defines a condition in which the source is coupled to the waveguide with reduced efficiency due to a redefinition of the angle of maximum resonance. Imperfect source collimation, scatter, and deviations in coupler tolerances induce angular spread to the laser source beam such that significant intensity can be coupled at the redefined resonance coupling angle. The propagating TM_2 mode strikes the outcouple grating at an angle different from the baseline coupled TM_2 mode. If the relative outcoupled mode positions are recorded on an imaging detector, the adjustments in TM_2 mode propagation angle are observed as changes in mode positions.

2.4.2 Cover Absorbance

2.4.2.1 Evanescent Absorbance

The presence of an absorber in the cover medium requires the replacement of the real refractive index, n_3, in Fresnel's equations with the complex refractive index,

$$\tilde{n}_3 = n_3 (1 - i\kappa_3). \qquad 2.13$$

The attenuation coefficient, κ_3, is related to the extinction coefficient of the absorbing species. At an absorbing wavelength, the reflectivity of the substrate-cover interface above the critical angle is no longer 100% due to the coupling of a portion of the evanescent electric field to the absorber. Thus, evanescent absorbance provides a mechanism for the removal of optical energy from the TM_2 mode propagating within the planar waveguide. The strength of evanescent coupling to an absorbing analyte is expressed in terms of an effective path length, t_e. The effective path length is defined as the path length of a transmission measurement required to give an absorbance response equal to the total internal reflection response. Traditionally, the effective path length considers the net effect of contributions from the electric field amplitude, the decay constant, the refractive index ratio, and the sampling area on evanescent coupling.[1] In addition, the hundreds to thousands of internal reflections within the Ag^+-exchange waveguide amplifies the effective evanescent path length for absorbance in the cover solution. The effective evanescent path length for total internal reflection increases for longer wavelengths, for TM compared to TE waveguide modes, as the refractive index ratio increases ($>n_{31}$) and with increasing mode order. Thus, the highest order TM waveguide mode should exhibit the greatest evanescent sensitivity to bulk liquid phase absorbance.

2.4.2.2 Anomalous Dispersion

The term material dispersion describes the slight decrease in refractive index of an optical medium with increasing wavelength in the visible spectral region. The smooth material dispersion profile is interrupted in the wavelength region surrounding a strong, sharp absorbance peak due to anomalous dispersion. The normal dispersion curve is followed at wavelengths surrounding the anomalous region and at the wavelength of maximum absorbance. However, the anomalous region is identified by a decrease in refractive index on the short wavelength side and an index increase on the long wavelength side of a strong absorbance band. The magnitude of real refractive index changes associated with anomalous dispersion are expected to be small perturbations in the visible region due to the broad absorbance bands typically observed. The predicted waveguide response to refractive index changes was discussed previously and included modulations in the TM_2 mode intensity and mode outcoupling position. The magnitude of real refractive index changes around an absorbance maximum will be modulated with absorber concentration.

Since the effective evanescent path length depends on the refractive index ratio, anomalous dispersion will effect the strength of evanescent coupling to an absorbing species. This modulation in effective evanescent path length in the wavelength region of anomalous dispersion distorts the shape of evanescent absorbance response peaks.

2.4.3 Interfacial Effects

The activity of the silica glass waveguide as a cation exchange surface results in a potential ion-exchange interaction with cations in the cover matrix. The coulombic association of cations with the waveguide surface produces an interfacial refractive index perturbation which is distinctly different from the bulk cover refractive index case already considered. In the case of a bulk refractive index, the decaying evanescent electric field encounters a refractive index perturbation which extends beyond the penetration depth of the field. However, for surface adsorption, the primary evanescent interaction occurs at the interface where the cations associate with the glass waveguide. In this respect, the monolayer refractive index perturbation is essentially a modification of the waveguide layer refractive index profile, $n(x)'$. The extended evanescent field sensitivity to bulk effects is modified due to the strong interfacial interaction.

The formation of a surface adlayer changes the resonance equation boundary conditions for describing the angular distribution of allowed waveguide modes. The interfacial reflection phase shift should be very sensitive to the formation of a high index surface adlayer which will be manifest as a significant change in the TM_2 mode effective refractive index. The corresponding change in mode propagation angle will result in a change in grating efficiency, resonance coupling efficiency and in outcoupled mode position.

For a cationic absorbance dye, interaction with the waveguide surface produces both an interfacial refractive index perturbation and direct coupling to the waveguide evanescent field. The location of the absorber at the interface exposes the dye to an evanescent field strength approaching the true interfacial value, E_0, such that the effective evanescent absorbance path length is quite large. A significant enhancement in the waveguide sensitivity to cationic absorbance dyes is expected relative to a bulk absorber due to the interaction of cations with the waveguide surface.

2.4.4 Temperature

A variation in temperature produces a change in the refractive index of each layer defining mode propagation in the ion-exchange waveguide. The slight decrease in the refractive index of water with increasing temperature over the temperature range of interest is well documented.[4] The glass substrate and waveguide layer are also expected to exhibit a decrease in refractive index with increasing temperature. In general, since the waveguide layer is diffused into the substrate, the differential refractive index change at the waveguide-substrate interface should be minimal.

The effective refractive index of a waveguide mode is defined by the electric field distribution in the various optical layers composing the waveguide. Since waveguide modes sample the substrate and cover layers evanescently, the largest determinant of effective mode index is the refractive index of the waveguide layer. Changes in temperature directly perturb the refractive index of the waveguide layer such that the effective mode index is quite sensitive to temperature changes.

Allowed mode solutions to the waveguide resonance condition predict an increase in mode propagation angle as the waveguide refractive index decreases. In the case of a temperature response, the decrease in cover refractive index partially offsets the magnitude of mode angle changes. However, the greater sensitivity to perturbations in waveguide layer refractive index produces an overall increase in mode propagation angle with increasing temperature. The temperature response includes contributions from variations in TM_2 mode resonance coupling efficiency and outcoupling angle changes reflecting a perturbed mode propagation distribution.

2.5 Notes to Chapter 2

(1) Harrick, N. J. *Internal Reflection Spectroscopy*, Harrick Scientific Corporation: New York, 1979.

(2) Goos, F.; Hänchen, H. *Ann. Physik* **1943**, 43, 383.

(3) Stern, F. *Appl. Opt.* **1964**, 3, 111.

(4) Weast, R. C., Ed., *CRC Handbook of Chemistry and Physics*, 65th ed.; CRC Press Inc.: Boca Raton, FL, 1984, E-358.

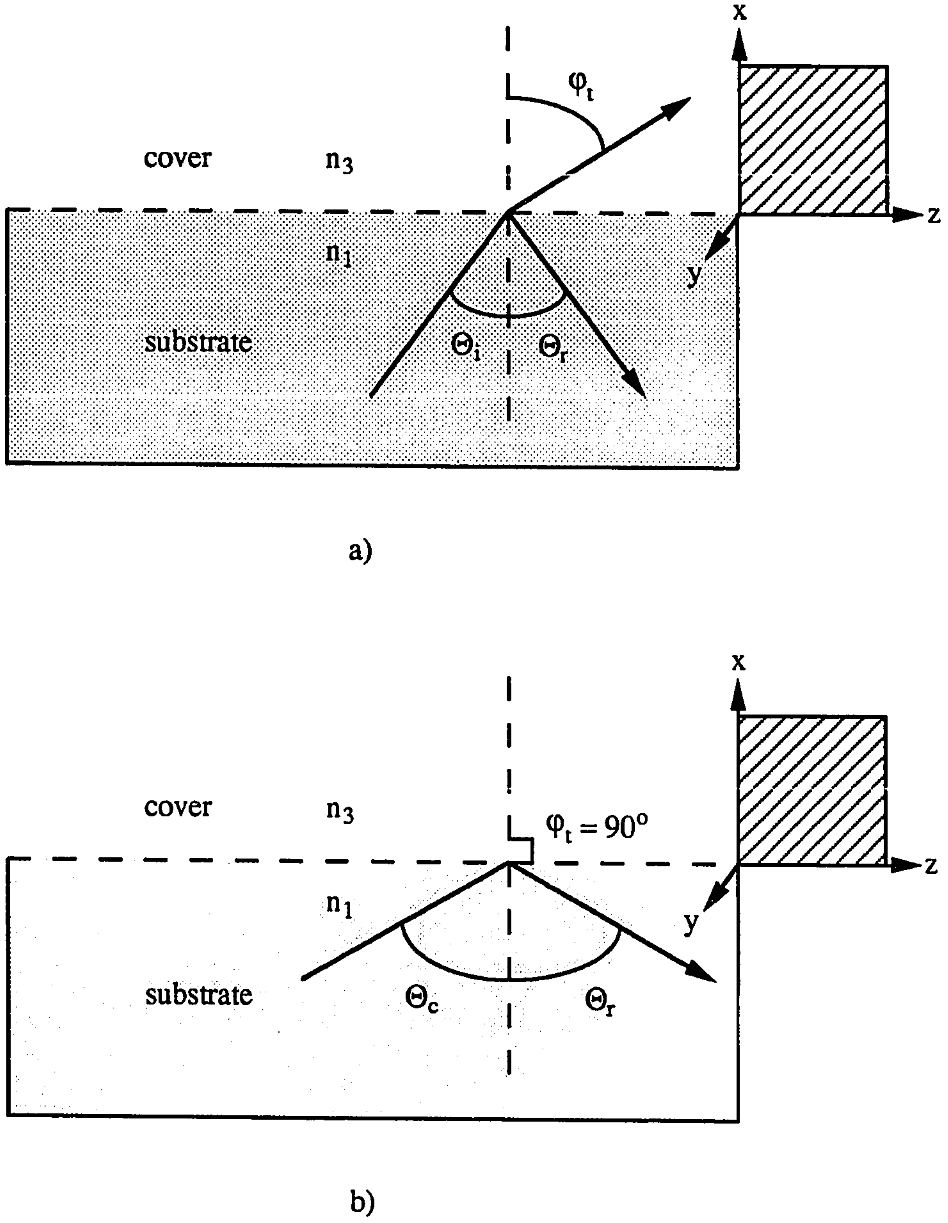

Figure 2.1 Internal reflection at an interface between two transparent media with different refractive indices. a) Partial reflection, b) total internal reflection

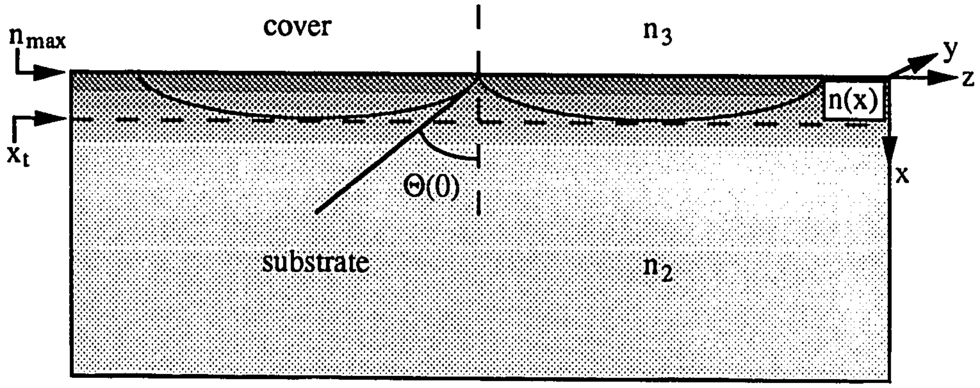

Figure 2.2 Ag^+-exchange planar optic waveguide structure with gradient index, n(x), waveguide layer.

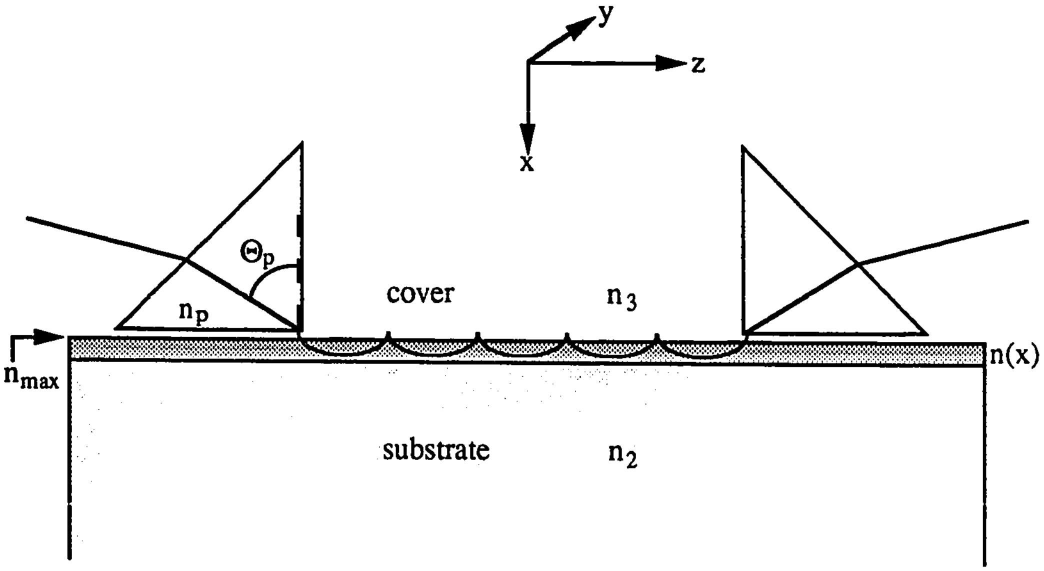

Figure 2.3 Prism coupling to a Ag^+-exchange planar optic waveguide.

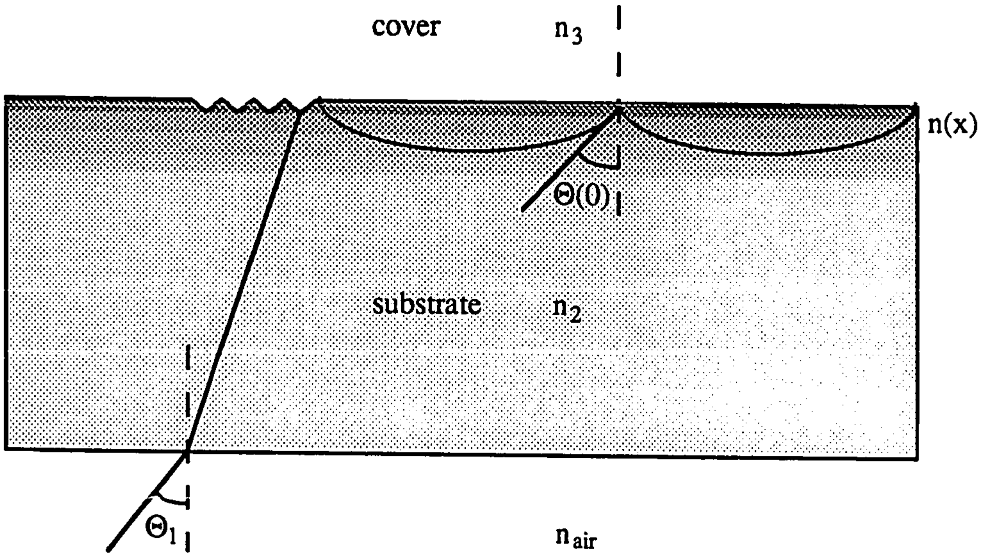

Figure 2.4 Grating coupling to a Ag^+-exchange planar optic waveguide with etched surface grating.

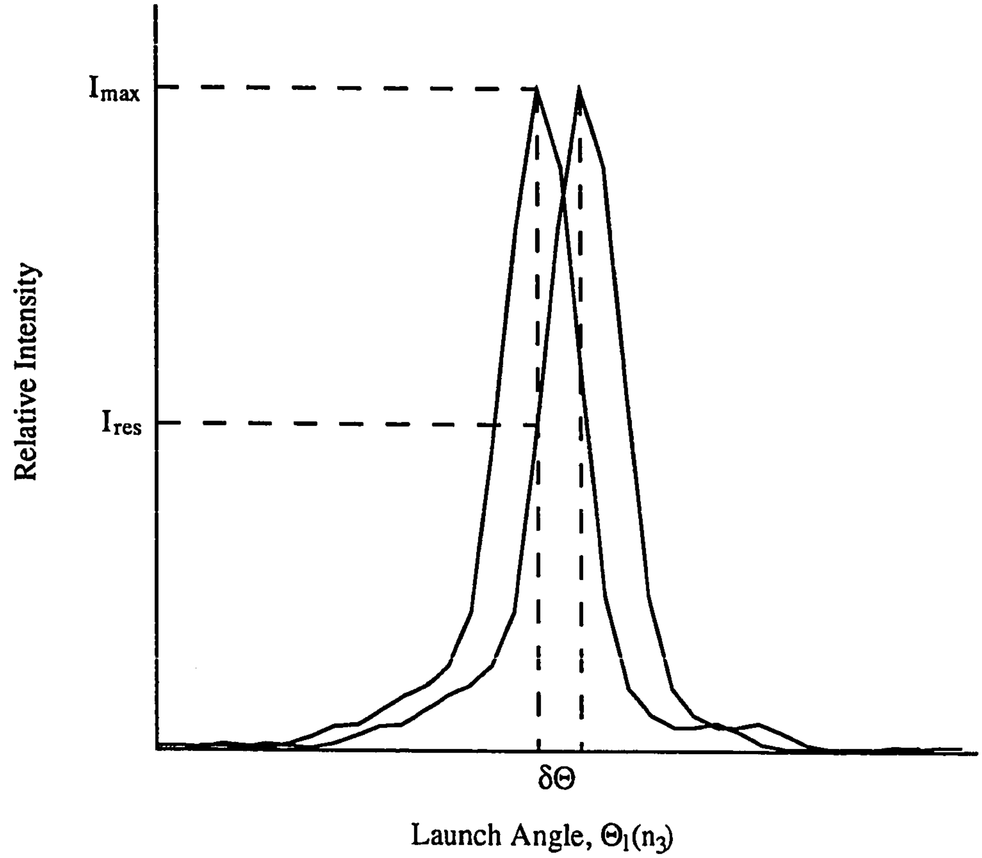

Figure 2.5 Resonance coupling curve displacement with cover refractive index.

Chapter 3

Glass

The devotion of an entire chapter to a discussion of silica glass serves to emphasize the importance of silica chemistry to the fabrication and function of Ag^+-exchange planar waveguide devices. Of particular relevance to this discussion is the chemistry of soda-lime silica glass which is a common material in the manufacture of microscope slides (microslides). The presence of mobile, monovalent cations in the bulk soda-lime glass matrix provides the basis for the production of gradient-index optical waveguides by ion-exchange. The chemical composition of silica glass determines the ion-exchange behavior and the resulting optical properties of the waveguides. While the chemical composition of soda-lime glass is not standardized, the glass formulations of microslide manufacturers tend to be similar. Typically, soda-lime silica glasses contains 15% by weight sodium oxide (Na_2O) which is the primary component controlling the ion-exchange chemistry of this glass.

The chemistry of the doped soda-lime silica glass surface controls the interaction of the ion-exchange waveguide with the immediate environment. In particular, the complicated acidity of amorphous silica provides the basis for describing the chemical activity of the silica glass waveguide interface in aqueous solutions.

3.1 Glass Structure

The glass state is commonly described as a solid phase exhibiting the disorder of a liquid. Most discussions of the structure of glass follow the guidelines set forth in the random network theory.[1] The random network theory makes a distinction between cations as being either network forming ions or network modifying ions. Network forming ions are relatively small, multiply charged cations which tend to form strong oxide bonds. Common network forming ions include silicon, boron, and phosphorus. In contrast, network modifying cations are larger, low charge cations which form weak oxide bonds.

Examples of network modifying ions include lithium, sodium, potassium, calcium, magnesium, and aluminum. In addition, a distinction is made between oxygen atoms in glass as being either bridging or non-bridging oxygens. Bridging oxygens hold the glass network together by linking network forming ions while non-bridging oxygens neutralize the charge of network modifying ions incorporated in the glass matrix.

The network forming ion in soda-lime silica glass is silicon (Si^{4+}). In order to complete its coordination, each silicon cation bonds to four oxygen atoms. The geometric distribution of oxygen atoms about the silicon cation defines a tetrahedron. This tetrahedral group serves as the basic structural unit making up the glass network. Successive tetrahedral units are linked through the interaction of bridging oxygens which form bonds with two adjacent silicon atoms. The bridging oxygen linkage is not constrained to a specific bond angle so that the relative orientation among tetrahedra in the glass network is random. It is the random orientation of this linkage which defines the amorphous structure of glass.

A number of network modifying ions including sodium (Na^+), calcium (Ca^{2+}), magnesium (Mg^{2+}) and aluminum (Al^{3+}) are incorporated into the matrix of soda-lime silica glass. In order to maintain charge neutrality in the glass matrix, non-bridging oxygen anions form weak, ionic bonds to network modifying ions. Network modifiers occupy holes in the glass network and are surrounded, on average, by six oxygen atoms. Non-bridging oxygens bond to a single silicon atom and, therefore, do not contribute to the linkage of adjacent tetrahedral units. To build a stable glass network, at least three oxygens per tetrahedral unit must participate as bridging oxygens.

Trace amounts of metal cations such as arsenic (As^{3+}), iron (Fe^{2+}) and antimony (Sb^{3+}) are found in soda-lime silica glass. In conventional applications (i.e. windows, microslides) these trace components do not affect glass performance and it is neither necessary nor cost effective for the manufacturer to refine glass of these minor constituents. The green-blue tint observed in an edge view of our microslide glass is indicative of the presence of FeO. In addition, the presence of arsenic in glass is common due to the value of arsenic in removing oxygen bubbles during the glass melting and preparation process.

3.2 Ion-Exchange in Glass

3.2.1 Ion-Exchange Process

Soda-lime silica glass contains a significant concentration of monovalent sodium (Na^+) as a network modifying ion. As described above, network modifying ions occupy holes in the glass network and are bound by the formation of weak, ionic bonds to non-bridging oxygen anions. These loosely bound cations are able to move through the glass matrix provided sufficient energy is available to overcome the activation energy for diffusion. Two distinct processes contribute to the total activation energy: 1) the coulombic energy required to separate ionic species and 2) the energy needed to squeeze the cation through a small hole in the glass network. In particular, sodium cations have considerable mobility in glass due to the weak coulombic interactions experienced by these ions and their relatively small ionic radius. The movement of sodium cations from hole-to-hole within the glass network provides a simple description of the process of sodium diffusion within the glass matrix.

The ion-exchange behavior of soda-lime silica glass is a manifestation of the existence of mobile sodium cations within the glass matrix. The ion-exchange process involves the replacement of sodium cations in glass with monovalent cations from a suitable ion source. Numerous source cations have been identified as undergoing ion-exchange in sodium containing glass including lithium, silver, potassium, rubidium, cesium, and thallium. Table 3.1 provides a list of ionic radii for these cations.

The replacement of sodium with lithium cations occurs readily but results in the shrinkage of holes in the glass network in response to the smaller network modifying cation. Depending on the extent of lithium doping, glass undergoing lithium-sodium exchange may exhibit surface cracks or deformations. The larger size of potassium, cesium, rubidium and thallium significantly increases the activation energy for diffusion in glass compared to that required for sodium diffusion. Therefore, ion-exchange between sodium and these cations require long exchange times or the assistance of electric fields to drive the process. In addition, molten salt solutions of cesium, rubidium and thallium present toxicity and/or fire hazards. The ionic radius of silver presents the best size match to sodium and the resulting ion-exchange reaction proceeds relatively fast (minutes) at reasonable temperatures (<300 °C). The following discussion will emphasize the silver for sodium ion-exchange process in planar soda-lime glass substrates.

Typically, the ion source for silver-sodium exchange in glass is a molten silver nitrate solution. Ion-exchange is performed at elevated temperatures to maintain the molten silver nitrate phase and to provide thermal energy to enhance cation mobility in the glass phase. The ion-exchange process is described according to the following chemical reaction,

$$Na^{+}_{glass} \quad + \quad Ag^{+}_{melt} \quad = \quad Na^{+}_{melt} \quad + \quad Ag^{+}_{glass} \qquad 3.1$$

where sodium ions are released into the melt to maintain charge neutrality in the glass phase. The ion-exchange process is driven by the existence of a gradient chemical potential across the glass interface. The concentration of reactants at the interface determines the magnitude of this gradient. Therefore, the boundary conditions for ion-exchange are defined by the sodium content in the glass phase and the silver melt composition. Limited control over the sodium concentration in the glass phase is possible since it is predefined by the chemical composition of commercial glasses. However, the composition of the melt phase can be manipulated by the addition of sodium and/or potassium nitrates to pure silver nitrate. Prevailing boundary conditions will influence the extent to which sodium is replaced by silver at the glass surface and has considerable effect on the eventual silver concentration profile within glass. Thus, careful choice of initial boundary conditions is key in obtaining some measure of control over the source cation concentration profile in ion-exchange glass.

The ability to maintain conditions at the interface after ion-exchange has begun is dependent on the kinetics of the process. For ion-exchange there are three distinct rates to consider:

1) mass transfer of reactants (silver) to the interface and removal of products (sodium) from the interface,
2) kinetics of the reaction at the interface,
3) and cation transport in the glass phase.

Mass transfer concerns can be largely eliminated by providing for mixing in the melt phase. However, in the absence of convective mixing, cation transport to and from the glass interface is diffusion controlled. Source depletion at the interface will occur if diffusion cannot sustain the initial gradient in chemical potential. In general, mass transfer limitations are not observed unless ion-exchange is carried-out for extended exchange times (many hours) from pure silver nitrate melts.[2]

At the interface, equilibrium conditions for the ion-exchange reaction are reached very quickly and maintained granted source depletion is avoided. In turn, this provides a constant silver ion concentration at the surface of the exchanged glass.

Cation transport in glass is entirely due to solid-state diffusion, which is a relatively slow process. For ion-exchange in the absence of an external electric field, diffusion into a planar glass phase is describe by,

$$\frac{\partial N_{src,glass}}{\partial t} = \frac{\partial}{\partial x}\left\{D^{\sim}\left(\frac{\partial N_{src,glass}}{\partial x}\right)\right\} \qquad 3.2$$

where $N_{src,glass}$ is the mole fraction of source ion in the glass, t is time, and x is depth into the glass.[3] The variable $D^{\sim}$ is the interdiffusion coefficient given by,

$$D^{\sim} = \frac{nD_{src,glass}}{\left(1-\alpha N_{src,glass}\right)} \qquad 3.3$$

where,

$$n = \frac{\partial\left(\ln a_{src,glass}\right)}{\partial\left(\ln C_{src,glass}\right)},$$

$D_{src,glass}$ - temperature dependent self-diffusion coefficient for the source ion in glass (also depends on glass composition),

$$\alpha = \left(1 - \frac{\mu_{src,glass}}{\mu_{Na^{+},glass}}\right)$$

$a_{src,glass}$ - thermodynamic activity for the source ion in glass,

$C_{src,glass}$ - absolute concentration of the source ion in glass,

$\mu_{src,glass}$ - electrochemical mobility of the source ion in glass, and

$\mu_{Na+,glass}$ - electrochemical mobility of sodium in glass.

For ion-exchange in glass, the source ion concentration profile in the glass phase is largely determined by the surface mole fraction of source ions in glass and the relative electrochemical mobilities of the exchanging cations in the glass phase. Qualitatively, these two parameters describe the cation profile resulting from ion-exchange in glass according to a number of limiting cases.

1) $\alpha \rightarrow 0$ - When the electrochemical mobilities of the exchange cations are approximately equal or the exchange is carried-out from a dilute melt solution the concentration profile can be described as an erfc (complementary error function).

2) $\alpha \rightarrow 1$ and $N_{src,glass}(surface) \rightarrow 1$ - If the chemical mobility of the indiffusing source cation is much smaller than that of the glass cation and the ion-exchange is carried out from a nearly pure melt, the concentration profile in glass tends to be step-like. The pure source cation melt phase provides for nearly complete ion-exchange at the glass surface described as $N_{src,glass}(surface) \rightarrow 1$.

3) $N_{src,glass}(surface) \rightarrow 1$ - For ion-exchange in which the ratio of cation mobilities in glass gives an intermediate value for α and the melt phase is nearly pure, the concentration profile can be described by a parabola or second-order polynomial function.

The ratio of the electrochemical mobilities for silver and sodium in soda-lime silica glass is approximately 0.5 (α=0.5) for ion-exchange from a pure silver nitrate melt.[4] The third case best approximates the exchange conditions employed herein and the silver concentration profile expected is a parabola or second-order polynomial.

Temperature limits for ion-exchange are determined by the melting point of the ionic salt source (lower limit) and the stress relaxation temperature for glass (upper limit). The choice of temperature within this range will shift equilibrium for the exchange reaction and also affect cation mobilities in the glass phase. The observation is that higher temperatures result in a greater equilibrium concentration of silver at the glass surface and deeper diffusion of silver for a given ion-exchange time.

3.2.2 Glass Refractive Index

The ion-exchange process involves the replacement of one network modifying cation with another. As a result, the basic structure of glass remains unchanged following ion-exchange. However, the doped glass phase will have modified physical properties including a different refractive index. In general, good control over ion-exchange conditions will result in a source ion distribution which exhibits a maximum in concentration at the surface and decreases with depth into the glass. Since the refractive index change is related to the presence of the source ion, the refractive index profile will be a replicate of the source ion distribution. The change in refractive index associated with ion-exchange in glass is related to the relative molar volumes (ionic radii) and electronic polarizabilities of the cations involved.

The replacement of sodium with a network modifying cation of different molar volume requires an adjustment in the glass matrix. This is due to the fact that holes in the glass network originally form to fit sodium cations. Following ion-exchange, holes in the glass network readjust to accommodate a new modifier cation. The change in glass density associated with the adjustment in hole size in the glass matrix results in a change in refractive index. In the case of lithium exchange, the glass network will collapse around the smaller ion and cause an increase in glass refractive index. In contrast, ion-exchange with a larger cation such as silver will require expansion of the glass network and a subsequent decrease in refractive index.

Electronic polarizabilities for the primary cations of interest in glass ion-exchange are included in Table 3.1. The effect of cation polarizability on the refractive index of ion-exchange glass is rather straightforward. If the source ion has a smaller electronic polarizability than the original network modifying ion, the refractive index of the ion-exchanged glass will decrease. Ion-exchange using a source ion with a larger electronic polarizability will result in an increase in glass refractive index. The latter case holds for the replacement of sodium by any cation listed in Table 3.1 except for lithium.

The net change in glass refractive index resulting from these two effects has been predicted in various theoretical treatments.[5,6] In many cases, the molar volume and electronic polarizability contributions to the net refractive index of ion-exchange glass are in opposition. Silver ion-exchange in soda-lime silica glass is an example of such a case. As noted earlier, the larger molar volume of silver compared to sodium results in an expansion in the glass network and a consequent decrease in refractive index. However, silver has a greater electronic polarizability than sodium which causes an increase in glass refractive index. Theoretical and experimental results indicate that the polarizability difference dominates and the overall effect of silver ion-exchange is an increase in glass refractive index.

As discussed, the ability to accommodate various network modifying ions is accompanied by glass expansion or contraction. Resistance to bending in thick planar substrates constrains the bulk movement of glass to a direction normal to the planar substrate surface. Therefore, ion-exchange under conditions which result in large volume changes may induce directional stress in the glass surface. In such a situation, anisotropic stress may produce optical birefringence in the exchange region. Thus, specification of the ion-exchange layer refractive index may depend on the electric field orientation of an optical probe beam. In general, birefringence is not observed for silver ion-exchange in sodium containing glasses.

3.3 Glass Cation Exchange

In contrast to soda-lime silica glass, network modifying ions are not incorporated into the structure of pure silica glass. As a result, the bulk phase physical and chemical properties of silica glass are considerably different from those of soda-lime silica glass. However, despite significant differences in the bulk phase structure, silica and soda-lime silica glass surfaces exhibit a common structural functionality (i.e. $-SiO^-$). Thus, it would be expected to observe similarities in the surface chemistry of these glasses.

Silica glass has an abundant history as a normal stationary phase material in high performance liquid chromatography (HPLC). Silica has also been examined in some detail as a cation exchange material.[7-17] Since the cation exchange properties of soda-lime glass have not been described in the literature, the following discussion focuses on silica cation exchange. Cation exchange for soda-lime silica glass is expected to proceed in an analogous manner.

3.3.1 Silica Cation Exchange

Silicon atoms exposed at the surface of a bulk silica phase maintain tetrahedral coordination via the attachment of hydroxyl groups. As a result, a fully hydroxylated silica surface has a significant population of surface silanol groups. The density of surface silanol sites has been estimated based on calculations assuming specific faces of pure crystalline silica. In particular, an estimate of 4.6 silanols/nm^2 for crystalline silica was found to be consistent with experimental measurements of site density on an amorphous silica.[18]

Silanol groups on the surface of silica glass are slightly acidic. Thus, glass exposure to an aqueous solution phase will result in the dissociation of surface silanol groups as described by,

$$(-SiOH) \quad + \quad H_2O \quad = \quad (-SiO)^- \quad + \quad H_3O^+ \qquad 3.4$$

which creates an anionic glass surface. Anionic surface sites may interact with metal cations in an aqueous electrolyte solution according to,

$$n(-Si-O)^- \quad + \quad M^{z+} \quad = \quad (-Si-O)_nM^{(z-n)+} \qquad 3.5$$

where M represents a metal. The glass/metal reaction is presented as two distinct steps which may, in actuality, occur simultaneously. The overall reaction can be described as simple cation exchange resulting from the displacement of a hydrogen ion and a coulombic association between the anionic glass site and a metal cation. The cation exchange interaction with multivalent cations may involve more than one anionic silica site as indicated by the variable n in equation 3.5. Steric considerations limit the maximum number of silica sites participating in the formation of a surface complex to two.

The above discussion is also applicable to the adsorption behavior of cationic dyes on silica surfaces. The interaction is mainly ionic and follows a cation exchange mechanism up to a surface monolayer of adsorbed dye.[19]

3.3.2 Cation Exchange Capacity

The cation exchange capacity is highly dependent on the type of silica and the solution environment. The type of silica determines the density and acidity of surface silanol exchange sites. The silanol site density for silica glass was considered above.

The acidity of the silanol group is a key factor in the cation exchange reaction since acid dissociation determines the surface charge on glass and, thus, the number of active exchange sites. To date, the nature of the acidic behavior of silica remains speculative. The estimated pK_a of acid silanol sites based on experimental infrared measurements and titration procedures is 7.1.[12,20,21] However, the pK_a of glass is strongly influenced by its environment. For example, the isoelectric point which specifies the pH at which the silica surface is neutral occurs around a pH of two. This suggests that the effective acid strength of silica surface sites in aqueous solution is greater than would be expected based on the estimated pK_a value. A number of possible explanations for the enhanced acid strength of surface silanols have been given.[14,22]

Solution phase pH is the primary environmental determinant of exchange capacity. At the isoelectric point, the neutral silica surface cannot function as a cation exchanger. However, as the solution pH increases, silanol dissociation (equation 3.4) creates an increasing population of anionic surface sites. Thus, the cation exchange capacity of silica increases with pH. The maximum solution phase pH is limited by the dissolution of silica which becomes significant at a pH of approximately 8. In general, even at a favorable solution pH only 10% to 20% of the total number of surface silanol sites are active in cation exchange.[9]

3.3.3 Complex Stability

As with conventional ion-exchangers, the stability of glass/cation surface complexes is a function of cation charge. In general, cation exchange complexes involving cations of increasing charge are more stable, i.e. trivalent > divalent > monovalent. The interaction between a silica surface and multivalent cations may involve either one or two active silica exchange sites. The relative amounts of these two potential cation exchange products varies with solution pH.[10] The cation exchange product involving a single silica exchange site is dominant at low pH. However, as the solution phase pH increases, the surface complex with two exchange sites per cation becomes more important. Multiple silica site participation in cation binding contributes to the increase in stability associated with surface complexes involving multiply charged cations.

3.3.4 Soda-Lime Silica

Soda-lime silica glass is less dense than amorphous silica due to the effect of network modifying cations on the packing of tetrahedral silicon units. Therefore, the silanol site density at a soda-lime silica surface will be slightly less than that of a pure silica surface. The estimated site density of 4.6 silanols/nm^2 for silica is valuable as an upper bound for the silanol site density on a planar soda-lime silica surface.

The acidity of surface silanol groups on soda-lime glass has not been reported. However, general observations discussed above concerning exchange capacity and the stability of surface complexes on silica are expected to hold for cation exchange on a soda-lime silica glass surface.

3.4 Notes to Chapter 3

(1) Zachariasen, W. H. *J. Am. Chem. Soc.* **1932**, 54, 3841-3851.

(2) Giallorenzi, T. G.; West, E. J.; Kirk, R.; Ginther, R.; Andrews, R. A. *Appl. Opt.* **1973**, 12(6), 1240-1245.

(3) Ramaswamy, R. V.; Srivastava, R. *J. Lightwave Technol.* **1988**, 6(6), 984-1002.

(4) Najafi, S. I. *Introduction to Glass Integrated Optics*, Artech House: Boston, 1992, p. 30.

(5) Huggins, M. L.; Sun, K. H. *J. Amer. Cer. Soc.* **1943**, 26(1), 4-11.

(6) Fantone, S. D. *Appl. Opt.* **1983**, 22(3), 432-440.

(7) Petersen, J. V.; Dessy, R. E. *SPIE Proceeding: Chemical, Biochemical, and Environmental Fiber Sensors II* **1990**, 1368, 61-72.

(8) Smith, R. L.; Pietrzyk, D. J. *Anal. Chem.* **1984**, 56(4), 610-614.

(9) Unger, K. K. *Porous Silica*, Elsevier Scientific Publishing Co.: New York, 1979, p. 133.

(10) Schindler, P. W.; Furst, B.; Dick, R.; Wolf, P. U. *J. Colloid Interface Sci.* **1979**, 55(2), 469-475.

(11) Wakatsuki, T.; Furukawa, H.; Kawaguchi, K. *Soil Sci. Plant Nutr.* **1974**, 20(4), 353-362.

(12) Strazhesko, D. N.; Strelko, V. B.; Belyakov, V. N.; Rubanik, S. C. *J. Chromatogr.* **1974**, 102, 191-195.

(13) Abendroth, R. P. *J. Colloid Interface Sci.* **1970**, 34(4), 591-596.

(14) Burwell, R. L., Jr.; Pearson, R. G.; Haller, G. L.; Tjok, P. B.; Chock, S. P. *Inorg. Chem.* **1965**, 4(8), 1123-1128.

(15) Dugger, D. L.; Stanton, J. H.; Irby, B. N.; McConnell, B. L.; Cummings, W. W.; Maatman, R. W. *J. Phys. Chem.* **1964**, 68(4), 757-760.

(16) Dushina, A. P.; Aleskovskii, V. B. *Russ. J. Inorg. Chem.* **1963**, 8(9), 1147-1149.

(17) Ahrland, S.; Grenthe, I.; Noren, B. *Acta Chem. Scand.* **1960**, 14(5), 1059-1076.

(18) deBoer, J. H.; Vleeskens, J. M. *Proc. Koninkl. Ned. Akad. Wetenschap. Ser. B* **1958**, 61, 2-11.

(19) Iler, R. K. *The Chemistry of Silica*, John Wiley & Sons: New York, 1979, p.687.

(20) Hair, M. L.; Hertl, W. *J. Phys. Chem.* **1970**, 74(1), 91-94.

(21) Schindler, P.; Kamber, H. R. *Helv. Chim. Acta.* **1968**, 51(7), 1781-1786.

(22) Vysotskii, Z. Z.; Strazhesko, D. N. in *Adsorption and Adsorbents*, vol. 1; Strazhesko, D. N., ed., Wiley Interscience: New York, 1973, p. 55.

Table 3.1 Electronic polarizability and ion radii of common cations involved in ion-exchange.

Table 3.1

Cation	Polarizability (Å)^3	Ionic Radius (Å)
Li^+	0.03	0.65
Na^+	0.41	0.95
Ag^+	2.4	1.26
K^+	1.33	1.33
Rb^+	1.98	1.49
Cs^+	3.34	1.65
Tl^+	5.2	1.49

Chapter 4

Instrumentation

4.1 Grating Fabrication

The integration of grating couplers into the planar waveguide structure provides an optically stable method of mode coupling. Etched surface gratings were fabricated using the general method described by R. Moshrezadeh, et. al.[1] The specific procedure for producing etched gratings in soda-lime silica glass substrates is described in detail by M. DeGrandpre.[2,3] A Kr^+ laser and Lloyd's mirror were used to expose an interference fringe pattern into positive photoresist spun on a glass substrate. The substrates were treated with hexamethyldisilizane prior to photoresist application to improve adhesion to glass. Following photoresist development, substrates were etched using either reactive sputtering or dilute buffered hydrofluoric acid.

A target period of 500 nm was chosen for fabricating gratings so that coupling to common waveguide materials ($1.5<n_{max}<1.7$) would occur at angles near normal incidence. Grating coupling angles near normal incidence were desirable for minimizing source reflection losses and total stray light. Scanning electron micrographs of a typical etched surface grating indicated a sinusoidal profile.

4.2 Ag^+-Exchange Waveguide Fabrication

4.2.1 Soda-Lime Silica Chemical Composition

Numerous ion-exchange waveguides were fabricated in plain microslide glass substrates purchased from Fisher Scientific (cat. no. 12550A). The chemical composition of this soda-lime silica glass as specified by the manufacturer (Erie Scientific,) is given in Table 4.1 with units specified as weight percents.

Ag^+-exchange waveguides were also fabricated in soda-lime silica substrates with etched surface gratings. The exact chemical composition of these glass substrates were unknown but are expected to be very similar to the Erie Scientific microslide glass with a sodium content of approximately 14.5%.

4.2.2 Waveguide Fabrication

A two-step cleaning procedure was followed to remove organic contaminants and particulates from glass substrates. First, soda-lime substrates were scrubbed (cotton swab) with detergent and rinsed in hot tap water. Second, the substrates were sonicated in concentrated sulfuric acid for 1/2 hour, rinsed in hot tap water and, finally, deionized water. Clean substrates were exposed to a stream of dry, filtered nitrogen gas to remove residual deionized rinse water. Dry substrates were preheated in a Precision oven at 185 °C for two hours prior to ion-exchange.

A small amount of solid silver nitrate (mp 214 °C) was added to a shallow Pyrex dish and inserted into a Thermolyne furnace (type 2000). The furnace temperature was set to maintain a temperature of 280 °C. Molten silver nitrate formed a shallow pool which covered the bottom of the Pyrex dish.

Preheated microslide substrates were removed from the oven and dropped directly into the silver nitrate melt. The depth of the silver nitrate pool was such that only one surface of a 1 mm thick microslide substrate was submerged in the melt. The melt was sufficiently viscous that air bubbles would become entrapped underneath the substrates. In order to get uniform diffusion conditions across the planar glass surface, the entire bottom surface of the substrate needs to be in contact with silver nitrate melt. To remove bubbles, one end of the substrate was pried out of the melt and then dropped back in. Following the removal of air bubbles, the oven door was shut and time zero for the exchange procedure was initiated. The temperature at time zero was less than 280 °C but since the oven was not equipped with a thermocouple the exact temperature behavior of the oven was not monitored. After a suitable exchange time (5 to 15 min), the entire $AgNO_3$ exchange bath was removed from the furnace. The glass substrate was immediately retrieved from the melt and tilted vertically to allow excess $AgNO_3$ to drain back into the Pyrex dish. The Ag^+-exchanged substrates were supported vertically on a teflon holder and air cooled to room temperature.

A layer of reduced silver and crystalline silver nitrate was removed from the Ag^+-exchange substrate surface by scrubbing with 0.1 M nitric acid. Following a rinse in hot tap water, the glass substrates were sonicated in concentrated sulfuric acid for 1/2 hour. The clean ion-exchange glass was rinsed in hot tap and deionized water and dried in a nitrogen gas stream.

4.3 Waveguide Flow Cell Assembly

A sandwich type flow cell was designed and constructed to allow for the coupling of the laser source to the waveguide and the introduction of a liquid sample phase across the waveguide surface. The waveguide flow cell consisted of the three machined pieces depicted in an assembled side view in Figure 4.1. More detailed diagrams of each flow cell piece including the dimensions which were provided to the machine shop are given in Appendix A.

The face plate provides the top piece of the flow cell sandwich which contacts the substrate side of the waveguide. The face plate has two milled windows to facilitate laser source introduction and waveguide mode collection from surface grating couplers. The face plate was milled in aluminum and designed to accommodate thermoelectric cooler components for temperature control.

A PEEK (polyetheretherketone) channel piece serves as the bottom of the flow cell sandwich. The actual flow channel was patterned in a parafilm gasket which contacts the channel piece and the waveguide surface on either side. The polymeric gasket was dimensioned lengthwise to include both waveguide surface gratings and the beam propagation region in the solution path. The thickness of parafilm is approximately 100 µm and the flow channel width was matched to the 1/16" diameter laser beam. The nonmetallic flow channel design included liquid sample contact with the PEEK channel, the parafilm gasket, and the glass waveguide surface in transit through the flow cell. Connections to the liquid inlet and outlet were made with PEEK fingertight fittings (Upchurch Scientific) through the backside of the channel.

A stainless steel L-bracket supports the entire assembly and provides a base for mounting the flow cell assembly on a rotational stage (Model 471, Newport Corp.). To simplify alignment of the three pieces in the flow cell assembly, the bracket has two guide rods extending from the front face. The channel piece slides on the guide rods and four tapped holes are provided in the bracket to secure the PEEK channel piece. The parafilm gasket and Ag^+-exchange waveguide sit on the guide rods and are pressed against the channel piece by the face plate. Nine tapped holes in the channel piece match with clearance holes in the face plate such that bolting the pieces together applies firm and uniform pressure to the glass substrate. To insure that the gasket provides an adequate seal against liquid leakage, the flow cell assembly was heated to 100 °C for 5-8 minutes prior to use. Heat softens the parafilm which then bonds more strongly to the glass and PEEK surfaces.

4.4 Optical System

The optical system for evaluating the liquid phase response of the Ag^+-exchanged planar waveguide is given in Figure 4.2. As noted earlier, all optical and detection components are isolated from the sensing interface by illuminating the grating and collecting the mode output from the substrate side. A 4.0 mW 500:1 polarized helium-neon (He-Ne) laser (Model 1104P, Uniphase Inc.) operating at 632.8 nm was used as a source. A polarizer was located directly in front of the laser to provide further rejection of the TE polarization. The external reflection from the polarizer crystal was diverted off-axis to eliminate potential laser destabilization due to re-injection of the reflected beam into the laser cavity. An aperture was included just prior to illuminating the incoupling grating to capture stray laser light due to inherent beam divergence and beam scatter.

The waveguide assembly was mounted on a rotational stage which facilitated the selection of launch angles. The He-Ne laser was aligned to grating couple directly to the TM_2 mode of the ion-exchange waveguide. The waveguide produced multiple output beams which were angularly resolved upon outcoupling from the second surface grating. In each case, the number of outcoupled beams corresponded to the total number of modes supported by the ion-exchange waveguide.

The spectral purity, polarization, and overall intensity of the outcoupled modes were controlled by including a bandpass filter (632.8 nm), a TM analyzer, and a series of neutral density filters in the optical system. There was some spreading of the beam in the horizontal plane associated with incomplete outcoupling at the leading edge of the waveguide surface grating. A lens was used to counter the spreading and obtain sharp, intense mode lines on the photodiode array detector (EG&G S-series). The array detector has 512 photodiode elements on 25 μm centers. The use of a linear array detector to image the multiple mode waveguide output gives information about the relative intensities and positions of each TM mode.

Initially, as a matter of convenience, the system was configured with the bandpass and neutral density filters on the input laser beam. However, these optics produced a significant amount of scatter in the incident beam due to imperfections in the optical materials and from collected surface dust. The induced scatter causes phase differences within the propagation path of the coherent source beam. Phase differences give rise to local interference effects which introduce variations in the spatial uniformity of the source beam. The resulting variation in spatial illumination at the incoupling grating was observed to produced considerable instability in the intensity of coupled waveguide modes. Therefore, these optical components were necessarily relocated backside between the waveguide and the array detector.

4.5 Flow System

4.5.1 Components

The flow system for evaluating the waveguide response to liquid phase analytes is shown in Figure 4.3. Flow was driven by an HPLC dual piston pump (Dionex, Model GPM-2) which provides a linearly variable flow rate over the range from 0.1 ml/min to 9.9 ml/min. The waveguide flow cell was connected to the HPLC flow system with approximately 1.3 meters of 0.5 mm id, 1.5 mm od Teflon tubing. All experiments were run at a selected flow rate of 0.2 ml/min. The associated selector valve (Dionex Microinjection Valve) was fitted with either a 100 μl or 200 μl sample loop for reproducible sample introduction. In contrast, the volume of the waveguide flow channel was only about 3 μls. Large sample volumes were chosen to minimize the effects of manual sample injection on the reproducibility of waveguide response data. The large sample volume provides for a portion of the sample zone which experiences nearly zero dispersion in transit to the waveguide flow cell. A peristaltic pump was included in the flow system to fill the sample loop while the waveguide was exposed to flowing carrier solution. The pump line was connected directly to the injection port of the selector valve.

4.5.2 Sampling Considerations

The initial step concentration profile of an injected sample plug was altered significantly in transit to the flow cell due to dispersion. The principle of controlled dispersion in flowing systems as a means for automated sample handling, dilution, and analysis is the basis for flow injection analysis.[4] Poiselle (laminar) flow is the dominant contribution to axial dispersion which is characterized by a symmetric, differential flow rate with distance from the center (axis) of a circular tube. The familiar elongation in sample zone with a maximum flow rate on axis and zero flow rate at the tube walls is obtained. Diffusion in the radial direction as driven by the resulting radial concentration gradient also contributes to dispersion. The well defined effects of axial and radial dispersion generate a transient sample zone exhibiting a reproducible concentration profile as an input into the waveguide flow cell.

The 0.20 mm^2 cross sectional area of the teflon tubing provided a good match to the 0.16 mm^2 area of the flow channel. However, the planar geometry and mismatched dimensions within the flow cell along with the 90 degree flow diversion at the flow channel entrance had an unknown effect on the input concentration profile. The dispersion characteristics of the flow cell are extremely important to the experiments since the planar waveguide sensitivity extends only a short distance from the waveguide surface. For TM modes in a Ag^+-exchange waveguide, the exponential evanescent field decay limits penetration into the cover medium to approximately 0.14 μm. Thus, the waveguide response is related to the radial analyte concentration gradient near the interface as transport of sample molecules to the waveguide surface is necessary for detection. Maximum sensitivity is obtained when sufficient analyte residence time is provided within the flow cell such that each sample molecule can diffuse to the sensing region.

A selected volumetric flow rate of 0.2 ml/min corresponds to an maximum linear flow velocity within the waveguide flow channel of 2.1 cm/sec. Thus, for an analyte located near the center of the flow cell (subjected to the maximum flow rate) the residence time is less than a second and the characteristic diffusion length is given by,

$$d^2 = 2D_m t = 2D_m L/F_l \qquad 4.1$$

where d is the diffusion length, D_m is the molecular diffusion coefficient, t is time, L is the flow channel length, and F_l is the linear flow rate. At the prevalent volumetric flow rate the characteristic diffusion length was approximately 30 μm compared to the 50 μm radius of the flow channel. Thus, in the absence of turbulent flow, diffusion to the interface allows the potential to detect sample molecules initially located within 30 μm of the planar waveguide surface. Operating at the minimum selectable volumetric flow rate of the HPLC pump (0.1 ml/min.) produces little improvement in sample residence time while adding to the analysis time.

4.6 Temperature Programming

A thermoelectric temperature control system operating over the range from 20 °C to 70 °C was manufactured by the electronics shop for the purpose of studying the temperature response of a Ag^+-exchange planar waveguide. As mentioned, the Ag^+-exchange waveguide flow cell was designed to accommodate a thermoelectric cooler and two temperature sensors. The location of the various cooler components in the Ag^+-exchange planar waveguide flow cell assembly are shown in Figure 4.4. Thermal contact between thermoelectric cooler leads and flow cell surfaces was made with stopcock grease. When integrated into the flow cell assembly, the peltier thermoelectric cooler element uses the aluminum flow cell face plate as a heat sink and the rotational stage as a heat source. The feedback temperature sensor is secured in contact with the aluminum face plate by a teflon set screw. The feedback sensor regulates the activity of the peltier cooler according to the temperature adjust set point on the external power supply. Heating of the aluminum face plate is driven by the thermoelectric device while a reduction in the temperature set point causes the device to shut down until the lower temperature is reached.

The actual substrate temperature due to heating of the face plate is measured by the substrate temperature sensor. This temperature sensor is pressed against the substrate with a teflon set screw. The substrate temperature is measured as a voltage taken from a BNC connector on the backside of the external power supply. The voltage exhibits a linear relationship to temperature in degrees Celsius as given by

$$\text{temperature}(^{o}\text{C}) = 10.204 \ \text{voltage}(\text{V}) + 0.2741. \qquad 4.2$$

4.7 Notes to Chapter 4

(1) Moshrezadeh, R.; Mai, X.; Seaton, C. T.; Stegeman, G. I. *Appl. Opt.* **1987**, 26(13), 2501.

(2) DeGrandpre, M. D. Ph.D. Dissertation, University of Washington, Seattle, Wa. 1990.

(3) DeGrandpre, M. D.; Burgess, L. W.; White, P. L.; Goldman, D. S. *Anal. Chem.* **1990**, 62(18), 2012-2017.

(4) Ruzicka, J.; Hansen, E. H. *Flow Injection Analysis*; Wiley: New York 1988.

Table 4.1 Chemical composition of Fisher Scientific soda-lime silica microslide glass, catalog number 12-550A.

Table 4.1

Glass Component		Wt.% in Glass
silicon dioxide	SiO_2	72.2 %
sodium oxide	Na_2O	14.5 %
potassium oxide	K_2O	0.3 %
calcium oxide	CaO	6.5 %
magnesium oxide	MgO	4.4 %
aluminum oxide	Al_2O_3	1.5 %
sulfer trioxide	SO_3	0.3 %
iron(III) oxide	Fe_2O_3	0.1 %
titanium oxide	TiO_2	0.05%

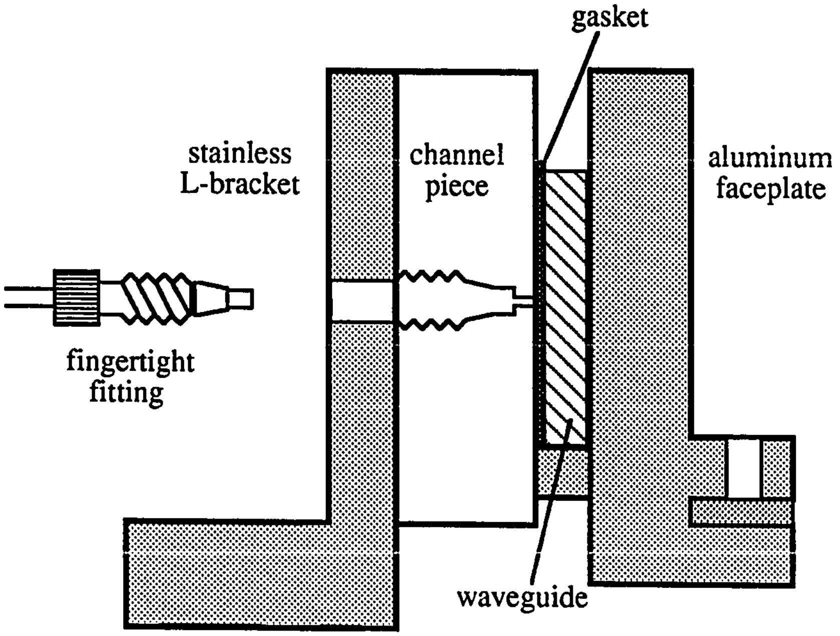

Figure 4.1 Assembled flowcell including the Ag^+-exchange planar optic waveguide and parafilm gasket.

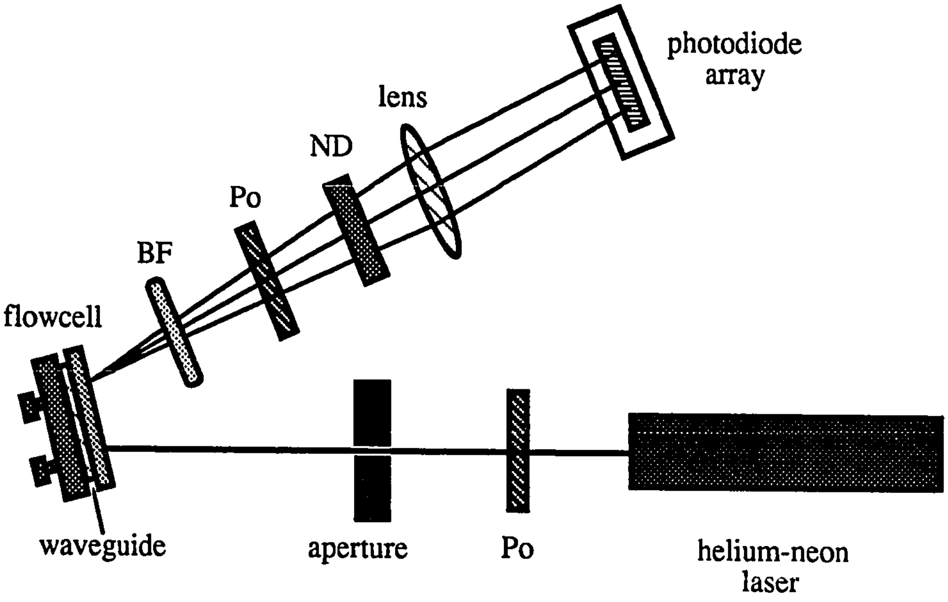

BF - bandpass filter, Po - polarizer, ND - neutral density filter

Figure 4.2 Optical system components for evaluating the liquid phase response of the Ag$^+$-exchange planar optic waveguide.

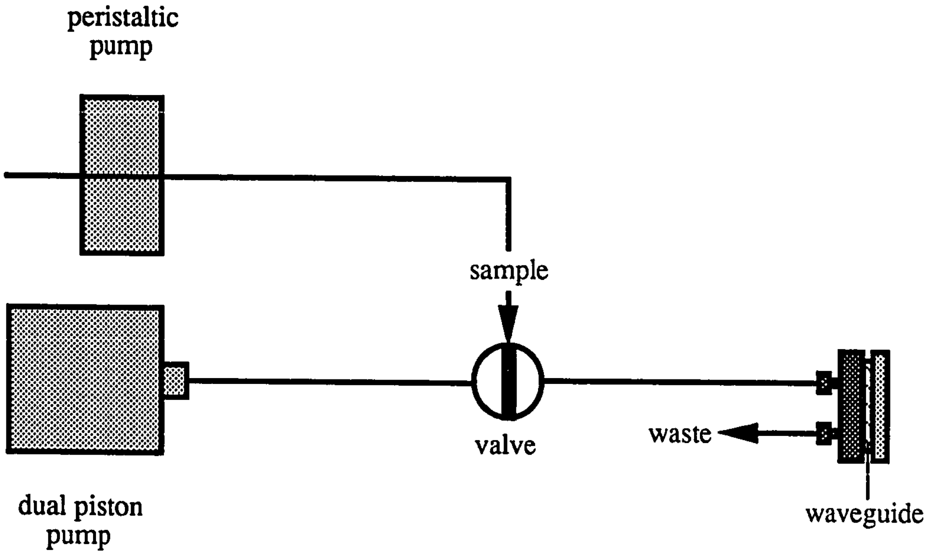

Figure 4.3 Flow system components for evaluating the liquid phase response of the Ag^+-exchange planar optic waveguide.

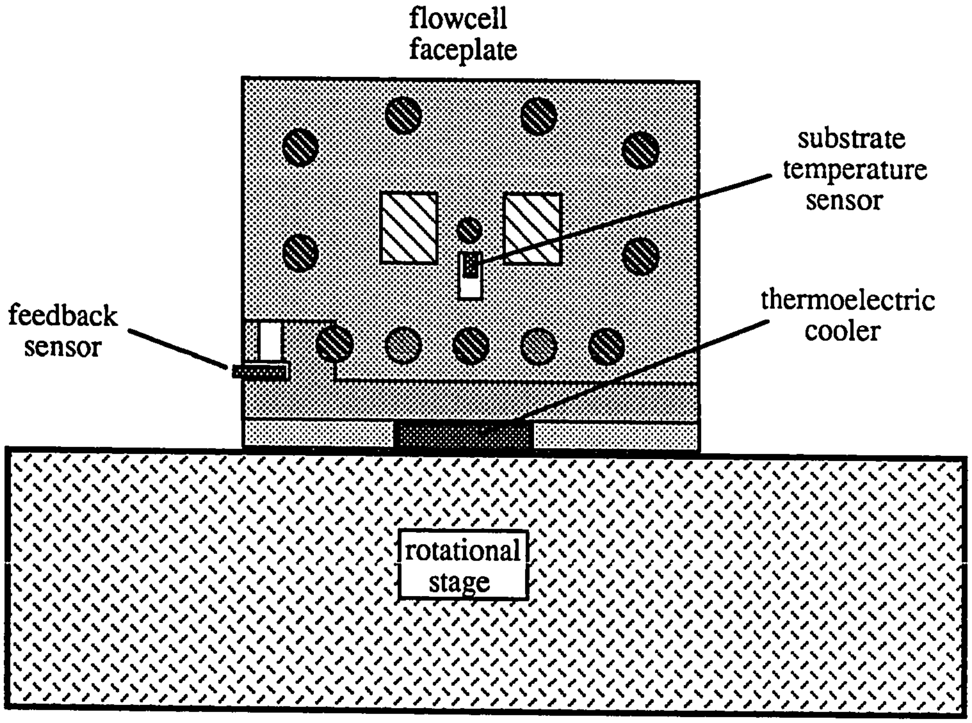

Figure 4.4 Incorporation of thermoelectric cooler components into the Ag^+-exchange planar optic waveguide flowcell.

Chapter 5

Experimental

The experimental evaluation of Ag^+-exchange waveguides necessarily begins with the characterization of the physical properties of Ag^+-exchange waveguide devices. The distinguishing feature of Ag^+-exchange waveguides is the strong crosstalk which occurs among allowed modes in a multimode waveguide structure. Modal crosstalk produces multiple response outputs from the Ag^+-exchange device which potentially provide additional information about the chemical composition of the waveguide environment. Model evaluation systems, experimental procedures, and data analysis methods for evaluating the multiple mode waveguide response are described in Chapter 5.

5.1 Waveguide Evaluation

5.1.1 Modeling Considerations

Whereas the simple fabrication of Ag^+-exchange planar waveguides is a distinct advantage, obtaining controlled and reproducible ion-exchange to produce waveguides with favorable physical properties is a major concern. To successfully pursue the production of multiple ion-exchange devices would require the ability to specify the properties of an ion-exchange waveguide from a consideration of ion-exchange parameters. The development of a model to predict waveguide properties from a well defined set of diffusion parameters involves solving the planar diffusion equation (Equation 3.2) to estimate the source ion concentration profile, relating the concentration profile to the refractive index profile, and solving the resonance equation. This procedure assumes that constant material parameters such as glass composition are readily obtainable. Of course, experimental validation of the model involves the fabrication of numerous ion-exchange devices with rigorous control over ion-exchange conditions and careful evaluation of the waveguide characteristics.

Initially, Ag^+-exchange waveguides were fabricated in our laboratory as a curiosity which, as it turns out, provides a potential device for evanescent liquid phase sensor development. In the production of Ag^+-exchange waveguides for this work the emphasis was on obtaining functioning waveguide devices using available resources. Ion-exchange boundary conditions were somewhat ill defined as substrate composition, Ag^+-exchange time, and diffusion temperature were characterized rather loosely. Thus, modeling efforts have focused on the inverse problem of estimating the refractive index profile of Ag^+-exchange structures from measured waveguide characteristics.

Ag^+-exchange waveguides were fabricated in plain microslide glass to examine the mode structure dependence on exchange time. Microslide substrates were taken from the same box to limit the possibility of variations in glass composition. Individual microslide substrates were labeled and cut in half to give substrate dimensions compatible with exchange vessels (1" x 11/2"). The labeling code gave each uncut microslide a number and a side designation, F (front) or B (back). Thus, substrates F1 and B1 are two halves but different sides of the same microslide. Conditions of ion-exchange for the various substrates are given in Table 5.1. Substrates 9C and 4E with etched and deposited chrome surface gratings respectively were also committed to the Ag^+-exchange process. Ag^+-exchange conditions for substrates 9C and 4E are include in Table 5.1.

5.1.2 Prism Coupling

The mode structure of Ag^+-exchange planar waveguides was characterized by prism coupling. Alternate polarizations of the laser were coupled to determine both the TE and TM mode structure. Two clean SF_6 prisms were fixed to the surface of Ag^+-exchange waveguides with moderate pressure and the prism coupling assembly was mounted on a rotational stage. Normal incidence was determined as the angle at which the laser reflection from the input prism face was coincident with the incoming beam. Mode coupling angles were measured relative to this normal. When evaluating normal incidence or mode coupling angles, the rotational stage was translated such that the laser beam was incident on the 90^o corner of the prism base.

Launch angles resulting in mode coupling were located by identifying waveguide mode surface scatter and maximizing outcoupled mode intensity. The mode intensity pattern output from the outcoupling prism consisted of a number of intense, striated vertical lines which were angularly separated. The number of lines in each case corresponded to the total number of modes supported by the particular Ag^+-exchange waveguide. Thus, prism coupling a collimated laser source to a Ag^+-exchange planar waveguide mode resulted in the excitation of all allowed waveguide modes. Multiple mode coupling was observed regardless of the mode directly coupled. Mode effective refractive indices for waveguide modes were calculated from measured prism coupling angles according to Equation 3.11. The manufacturer (Karl Lambrecht Corp.) specifies a refractive index, n_p, of 1.79883 at 633 nm for the SF_6 prism.

The mode structure of substrate 9C was also characterized by prism coupling. To obtain prism coupling angles free from grating effects, prisms were located between the etched surface gratings. Multiple mode coupling was observed for prism coupling to substrate 9C. Effective TM mode indices determined from prism coupling to substrate 9C are tabulated in Table 5.2.

In determining Ag^+-exchange waveguide mode coupling angles using prism couplers, the TM mode coupling angles were found to be larger than the corresponding TE mode angles. This is inconsistent with the accepted picture of mode propagation in planar waveguides. In general, the resonance condition specifies that TM modes travel closer to the critical angle than the respective TE mode for a given mode order. According to the manufacturer (Karl Lambrecht Corp.), a slight birefringence has been observed in the SF_6 prism couplers. Thus, the apparent reversal in mode coupling angles for the two polarizations is an artifact of inherent prism birefringence.

5.1.3 Waveguide Refractive Index Profiles

Refractive index profiles for Ag^+-exchange waveguides, n(x), were estimated from measured effective refractive indices by performing an inverse WKB (Wentzel-Kramer-Brillouin) analysis. A short program was written in the MATLAB environment to perform the iterative, error minimization procedure necessary to estimate mode turning points.[1] The programmed technique is applicable to ion-exchange waveguides with several modes and a smooth, monotonic decrease in refractive index. The mode turning point, x_t, and surface refractive index, n_{max}, predicted using the inverse WKB method for each waveguide mode in substrate 9C is included in Table 5.2. As discussed earlier, the effective waveguide thickness increases with mode order since these modes travel nearer the critical angle.

Refractive index profiles for Ag^+-exchange waveguides estimated from measured TM (and TE) mode effective refractive indices are presented in Figure 5.1a (and b). The refractive index profile obtained for a fifteen minute ion-exchange of either side of substrate #3 was essentially the same. Thus, the Na^+ content and distribution was observed to be similar at both substrate surfaces. Despite a five minute difference in exchange time between opposite sides of substrate #1, the refractive index profiles and diffusion depths were essentially identical. Substrates F1 and 9C were ion-exchanged for the same time but exhibit a very different refractive index profile and diffusion depth. Figures 5.1a and 5.1b emphasize the primary importance of substrate glass composition in obtaining reproducible Ag^+-exchange results.

The inverse WKB method provides an estimate for the maximum refractive index, n_{max}, at the surface of the Ag^+-exchange waveguide layer. The literature suggests that Ag^+-exchange of soda-lime silica substrates from pure $AgNO_3$ melts at 280 °C produce waveguides with a surface refractive index between 1.60 and 1.605.[2] An average calculated from individual inverse WKB predictions for each waveguide evaluated in this study gave a value for surface index of 1.604 ±0.003 refractive index units.

For waveguides exhibiting more than three modes, the refractive index profiles followed a third order polynomial function. This is inconsistent with more rigorous evaluations of the refractive index profiles of Ag^+-exchange waveguides fabricated from pure $AgNO_3$ melts which followed second order polynomial functions.[2] The estimated refractive index profiles indicate that deviations from the expected diffusion behavior are observed at the beginning of the ion-exchange process. The discrepancy most likely arises from the initial gradient in ion-exchange temperature associated with reaching the 280 °C oven set-point.

The inverse WKB method has limitations in its ability to accurately predict refractive index at the extremes, i.e. at the surface or near the substrate cut-off. Despite the consistency of our average surface refractive index with literature results, limitations in the inverse WKB predictions are typically severe in waveguides exhibiting few modes. Recent improvements in the inverse WKB method for predicting refractive index profiles of ion-exchange waveguides exhibiting two or three modes have been reported.[3,4]

5.1.4 Grating Coupling

The limited availability of soda lime silica substrates with integrated surface gratings is obvious in that only two were committed to the Ag^+-exchange procedure. The deposited chrome surface gratings on substrate 4E were destroyed by the Ag^+-exchange process and were rinsed off during the HNO_3 acid wash step. Curiously, the regions where chrome gratings previously existed still functioned quite efficiently as diffraction gratings. The surprising conclusion was that diffraction gratings could be fabricated by Ag^+-exchange through a suitable mask (chrome grating). Further evaluation indicated that the grating regions had some surface relief as pressing the grating against parafilm embossed a grating into the soft polymer. The surface relief was apparently introduced in the reactive sputtering photoresist etch step just prior to chrome deposition. The fabrication of Ag^+-exchange volume gratings through a deposited chrome diffusion mask is currently being investigated as a method to produce high efficiency gratings which eliminate the surface relief of deposited or etched gratings. Unfortunately, Ag^+-exchange waveguide 4E was broken after some preliminary coupling and liquid phase studies with the two mode waveguide device.

The current discussion pertains to waveguide 9C, which has been subjected to much, yet has miraculously survived through the completion of the described research. Ag^+-exchanged waveguide 9C has etched surface gratings separated by a 1.4 cm propagation region.

5.1.4.1 Mode Coupling Angles

The mode structure of ion-exchange waveguide 9C was determined by grating coupling. The waveguide was sandwiched into the flow cell assembly and mounted on a rotational stage. Normal incidence was defined as the angle at which the laser reflection from the substrate in front of the surface grating was coincident with the incoming beam. For determining mode coupling angles, the rotational stage was translated to maintain laser illumination of the leading edge of the incoupling grating.

Grating coupling angles were located by a sudden and drastic increase in waveguide surface scatter. The optimum launch angle for mode coupling was identified by monitoring the mode intensity on the array. Outcoupled mode intensity was collected by a lens and focused onto the photodiode array detector. As in the case of prism coupling, grating coupling to any mode of an ion-exchange planar waveguide (9C or 4E) resulted in the excitation of all allowed waveguide modes. Coupling angles for grating coupling to substrate 9C are given in Table 5.3. Note that each TE mode coupling angle is greater than that of the corresponding TM mode in accordance with the resonance condition.

5.1.4.2 Grating Period

If the grating equation (Equation 3.12) is applied to mode launch angles assuming the target grating period of 500 nm, the calculated effective refractive indices are near or below the substrate index. Thus, the true grating period deviates considerably from the target value. One method of estimating the actual grating period is to determine the launch angle at the grating which results in coincidence between the incident beam and the diffracted/reflected portion of the beam. The back-diffraction angle is measured with respect to the interfacial normal and can be related to the grating period as,

$$\Lambda = n\lambda/2\sin\alpha \qquad 5.1$$

where n is an integer and α is the back-diffraction angle. The coincidence of beams was gauged by a subjective evaluation of alignment over a short distance (<1.0 meter). The determination of back-diffraction angles from both gratings for each polarization (TE and TM) resulted in an estimated grating period of 485.4 nm ±6.9 nm.

A second method for estimating the grating period is to combine effective mode index values from prism coupling with measured grating coupling angles in the grating equation. Applying this procedure to effective refractive indexes for three waveguide modes of each polarization (six period estimates) gives an estimated grating period of 486.5 nm ±0.4 nm. The second method is preferred since coupling angle measurements were performed with greater objectivity and accuracy. Waveguide surface angles for coupled modes calculated from the grating equation using a grating period of 486.5 nm are included in Table 5.3.

5.1.4.3 Mode Polarization

Grating coupling angles for modes of a given order but different polarization are nearly coincident, separated by less than 0.05°. In addition, the TE mode is much more intense than the TM mode due to relative grating coupling efficiencies and scattering losses. Thus, it would be difficult to resolve the TE and TM polarized modes for a given mode order on an imaging detector and still maintain a compact optical system. Thus, future experiments examining the waveguide sensitivity to polarization rotation (optical activity) should be conducted by monitoring the intensity of the rotated polarization. For example, coupling directly to a TM mode and isolating the TE mode at the detector would allow for sensitive detection of TE mode intensity from a zero intensity baseline.

5.1.4.4 Resonance Coupling Curve

The shape of the resonance curve for TM_2 mode coupling was determined by scanning launch angles at 0.013° increments in the vicinity of the optimum TM_2 mode coupling angle. Care was taken to scan in a single direction to avoid backlash in the rotational stage micrometer adjustment. Outcoupled TM mode images were collected on the photodiode array for each incremented angle. The integrated TM_2 mode intensity (normalized) at each scanned angle near maximum coupling is given in Figure 5.2. The TM_2 mode resonance curve exhibited a full-width at half-maximum intensity of 0.051°.

5.1.5 Coupling Angle Sensitivity to Refractive Index

Grating coupling angles were determined with the waveguide in contact with air and deionized water. These mode coupling angles are presented in Table 5.4 along with a column indicating differences in coupling angles for the two cover media. The change in cover medium from air to water represents a step change in cover refractive index of about 0.33 refractive index units at room temperature. The tabulated data suggests a number of trends. First, mode coupling angles for a water cover are greater than the corresponding air coupling angles. Thus, as predicted by the resonance condition, mode coupling angles increase with increasing cover refractive index. Second, in general, coupling angle sensitivity to cover index increased with increasing mode order. This trend is more pronounced for the TE than the TM modes. Finally, the angular sensitivity to cover refractive index for a given TM mode was greater than that of the corresponding TE mode.

The identified trends are consistent with resonance condition predictions. In accordance with our earlier discussion of the waveguide refractive index response (Section 3.4.1), the angular sensitivity has implications for both the resonance coupling and outcoupling angle response components. As the resonant coupling angle changes in response to a cover index change, the coupling efficiency will decrease. The observed change in intensity will depend on the sharpness of the resonance curve and the angular sensitivity of the particular waveguide mode to cover index changes. For a Ag^+-exchange planar waveguide, a change in TM_2 mode coupling angle of greater than 0.051° relative to the maximum resonance angle will exceed the dynamic range and extinguish mode intensity. Assuming a linear change in mode angle with refractive index, an approximate change of 0.170 in cover refractive index would reduce TM_2 mode coupling to nearly zero efficiency.

The resonance coupling angle change can be monitored directly since the mode outcoupling angle can be associated with a position on the array detector. The significance of positional information in describing the waveguide refractive index response directly depends on the angular sensitivity of the ion-exchange waveguide to cover index.

5.2 Model Systems

5.2.1 Bulk Refractive Index

Glycerol solutions in deionized water were chosen as a model liquid phase system for testing the ion-exchange waveguide response to changes in bulk refractive index. The addition of increments of glycerol to water can be used to continuously vary the liquid phase refractive index from a value of 1.3326 (water) to 1.4735 (glycerol). The changes in refractive index associated with aqueous glycerol solutions are well characterized and follow a convenient linear relationship with glycerol concentration,

$$\Delta RI = (1.134\times10^{-4})(\text{glycerol conc. (g/L)}) \qquad (5.2)$$

where the refractive index change is relative to pure water.[5]

In addition to having a well characterized refractive index behavior, glycerol was chosen as a model molecule as it does not interact appreciably with glass[6], has no inherent absorbance at the He-Ne laser wavelength (632.8 nm) and is not optically active. While the ability to detect optical activity in a planar optical waveguide has not been established, the potential source of TM mode attenuation was avoided by using glycerol.

Twelve glycerol solutions in the concentration range from 0.704 to 34.44 g/L were prepared in deionized water as a sample set to test the waveguide bulk refractive index response. This concentration range represents a change in refractive index relative to water from 7.98×10^{-5} to 3.91×10^{-3} refractive index units. The target refractive index of sample solutions were compared with Abbe refractometer measurements. The results were consistent to within the apparent experimental precision of $\pm1.0\times10^{-4}$ refractive index units for the refractometer.

5.2.2 Bulk Absorbance

Bromocresol green solutions in phosphate buffer were chosen as the model liquid phase system for evaluating the waveguide response to changes in bulk absorbance. Bromocresol green was chosen as a model system for a number of reasons. First, bromocresol green is a large non-polar molecule which carries a negative charge in its basic form (Figure 5.3a, acid form). As such, any interaction between the anionic waveguide glass surface and the dye should be repulsive. Thus, the dye will not concentrate at the interface and the measured absorbance will be related to the bulk dye concentration.

Second, complete conversion to the anionic form of the bromocresol green molecule occurs at relatively low pH (pK 4.7) so that basic conditions which tend to degrade soda-lime silica glass are avoided. Finally, bromocresol green has a large extinction coefficient of about 38000 L mole^{-1} cm^{-1} at the 632.8 nm He-Ne laser wavelength.

Bromocresol green test solutions in the concentration range from 7.53×10^{-7} M to 1.01×10^{-4} M were prepared in pH 5.9 phosphate buffer. Visible absorbance spectra

(Hewlett Packard 8452A) were collected for each bromocresol green sample (Figure 5.4). The dye absorbance at 632 nm for a one cm path length transmission measurement is tabulated (Table 5.5) for later comparison with experimental waveguide evanescent absorbance results. The maximum absorbance wavelength for bromocresol green is at 616 nm which is blue shifted about 17 nm from the evaluation wavelength.

5.2.3 Bulk Refractive Index and Absorbance

Mixture solutions of glycerol and bromocresol green were chosen to evaluate the waveguide response to simultaneous changes in bulk refractive index and absorbance. Stock solutions of four bromocresol green dye concentrations, $5.01\text{x}10^{-6}$ M, $1.50\text{x}10^{-5}$ M, $5.00\text{x}10^{-5}$ M, and $1.00\text{x}10^{-4}$ M were prepared in pH 5.9 phosphate buffer. To make mixture solutions, known weights of glycerol were added to a volumetric flask and diluted with the appropriate bromocresol green stock solution. The bromocresol green stock dilution due to glycerol volume was considered in specifying sample composition. The prepared sample set included four pure glycerol solutions, four pure bromocresol green solutions, and twelve mixture solutions (Table 5.6). Pure glycerol samples were also prepared in pH 5.9 phosphate buffer.

5.2.4 Surface Active Refractive Index

The primary reason for choosing $Pb(NO_3)_2$ as a model system to test the ion-exchange waveguide response to surface active refractive index is the strong interaction between the divalent lead cation and silica glass.[7] Additional advantages to using Pb^{2+} as a model system include the large molar refractivity and the absence of inherent absorbance at 632.8 nm.

Three test solutions with target concentrations of $1.0\text{x}10^{-6}$ M, $1.0\text{x}10^{-5}$ M, and $1.0\text{x}10^{-4}$ M Pb^{2+} were prepared in slightly basic deionized water carrier. The carrier was prepared by adding a small volume of dilute NaOH to deionized water to obtain a solution pH of approximately 7.7. The near neutral pH was maintained to increase the cation exchange capacity of the waveguide glass surface. Fresh carrier and sample solutions were prepared and tested the same day. A pH 2.8 HNO_3 solution was prepared to rinse and regenerate the waveguide cation exchange surface.

The performance of adsorption experiments at slightly basic conditions has implications for Pb^{2+} speciation. Depending on existing solution pH and Pb^{2+} concentration, hydrolysis can convert free Pb^{2+} into a number of different complexation products.[8,9] The existence of free Pb^{2+} is favored at below a solution pH of about 5.0 and at low Pb^{2+} concentrations. At sample pH of about pH 7.7, free Pb^{2+} and $PbOH^+$ were expected to be the primary lead species over the range of sample concentrations tested. Hydrolysis to $Pb(OH)_2$ was not observed in sample solutions as evidenced by the lack of precipitate formation before or after sample evaluation.

5.2.5 Surface Active Absorbance

Methylene blue was chosen as a model system to test the waveguide response to a surface active absorber based primarily on the established interaction between the methylene blue cation and silica glass surfaces.[7,10] The dye interaction with the surface is typically associated with an enhancement in waveguide absorbance sensitivity over that predicted from simple evanescent absorbance theory. Significant tailing in the response profiles to transient dye injections are also described. In general, the formation of a stable dye adlayer is not to be expected as the large, nonpolar molecular structure of methylene blue (Figure 5.3b) reduces the effective charge interaction with the anionic waveguide glass surface. Additional reasons for using methylene blue as a model system include the relatively low pH for maintaining the blue cationic dye form and the large dye extinction coefficient (60 000 L $mole^{-1}$ cm^{-1}) at 632.8 nm.

To evaluate the waveguide response to surface active absorbance, ten methylene blue samples in the range from 2.55×10^{-7} M to 6.37×10^{-5} M were prepared. Methylene blue solutions were made in pH 5.9 phosphate buffer carrier solution. Visible absorbance spectra were collected for each methylene blue sample (Figure 5.5) and dye absorbances at 632 nm are tabulated (Table 5.7). Dye absorbances at 632 nm for a one cm path length were in the range from 0.020 to 3.158 absorbance units. Methylene blue absorbance spectra exhibited a maximum absorbance on either side of the 632.8 nm He-Ne evaluation wavelength. The absorbance maximum for the cationic methylene blue molecule occurs at 664 nm. The source of short wavelength (614 nm) absorbance in methylene blue solutions is either a tautomeric form of the dye or a product of methylene blue oxidation .[11]

5.2.6 Temperature

The temperature response of the Ag^+-exchange planar waveguide was evaluated using the thermoelectric heater assembly described earlier (section 4.6). The necessary thermal contact between the peltier device and the alignment stage presents concerns that differential thermal expansion will perturb the incoupling conditions. The evaluation was conducted over the relatively narrow temperature range from 23 °C (ambient) to 33 °C to avoid a significant disturbance to system alignment.

5.3 Experimental Procedure

5.3.1 Model Chemical Systems

In general, the surface of the Ag^+-diffused waveguide was maintained in an equilibrium hydration state by continuous exposure to deionized water between experiments. Prior to each experiment, the glass waveguide surface was exposed to the appropriate flowing carrier solution for a minimum of three hours. For each experiment described, direct TM_2 mode coupling was selected, as the highest order TM mode was expected to give the largest effective evanescent path length for measuring bulk changes in solution composition. At the beginning of each experiment, the launch angle was selected to give optimum TM_2 mode coupling in flowing carrier solution. The photodiode array image of the multiple mode waveguide output was monitored in real-time on an oscilloscope (Tektronics Model 2225, Beaverton, Oregon) to assist in optimizing alignment. This optical alignment was maintained for the duration of the experiment.

The acquisition and storage of a full 512 element photodiode array image of the mode output was computer automated at a selectable rate between 0.07 Hz and 0.2 Hz. Each stored photodiode array image was an average of five array scans. Data acquisition was initiated with the waveguide exposed to flowing carrier to establish a baseline response prior to each sample injection. After a well defined delay time, the sample loop was switched in-line with the flowing carrier solution. The data acquisition rate was chosen to oversample the waveguide response as a transient volume of sample solution was propelled through the flow cell. The software was written such that scans were collected in 48 or 60 image blocks which were assigned to a common filename. As such, each file included a temporal profile of the waveguide baseline and a single sample injection response. In general, the peak waveguide response to sample injections was observed to be nearly steady-state across a number of sampled points (images) indicating conditions of near zero dispersion (plug flow). The waveguide surface was rinsed with carrier solution for several minutes after each sample passed through the flow cell before a subsequent injection was made.

5.3.2 Temperature

Temperature experiments were conducted under conditions of stop flow following continuous, long-term exposure to deionized water. Source launch conditions were selected to optimize coupling to the waveguide TM_2 mode at the prevalent ambient temperature. After allowing sufficient source and detector warm-up times, the thermoelectric cooler was turned on and adjusted to regulate substrate temperature slightly above ambient. The data acquisition rate was set at 0.07 Hz for the collection of full photodiode array images. Temperature response data were assigned to common filenames in 60 scan blocks.

The multiple mode output was continuously recorded while the substrate temperature was changed every half hour. Thus, the steady-state temperature response was recorded as well as the transient resulting from the finite time required to heat the substrate and cover. The temperature was cycled to test for hysteresis in the waveguide response and to compare the dynamics of substrate heating and cooling.

5.4 Data Analysis

Each waveguide TM mode as imaged on the photodiode array detector was very narrow (4 diode FWHM) and all three modes were effectively described by a subset of the full 512 diode elements. Therefore, 512 element photodiode array scans were truncated to 90 or 95 diode images which retained complete TM mode information.

5.4.1 Univariate Analysis

5.4.1.1 Integrated Intensity

In order to obtain individual TM mode responses free from position shift effects, the integrated intensity of each mode peak in the truncated waveguide mode images was calculated. The integration was performed by summing the intensities recorded on each diode contributing to the image of a given waveguide mode. In this manner, the waveguide mode intensity information contained in each 90 to 95 diode image was further reduced to a single value for each mode.

To correct for long-term baseline drift, all integrated TM mode intensities in a given sample block were ratioed to the corresponding average integrated TM mode baseline intensity taken just prior to sample injection. Multiplication of the ratio corrected intensity data by 100 describes the waveguide response in terms of the percentage of mode intensity transmitted through the waveguide system with changing sample concentration.

To determine the limit of detection for each model system, the corrected baseline mode intensity data (I/I_0) was separated from the sample response data. The limit of detection (LOD) was calculated as three times the root mean square (rms) baseline noise over the course of the experiment. In general, the conversion of calculated detection limits to concentration units was complicated by the nonlinear shapes of the various response curves. Attempts at fitting nonlinear response curves with a polynomial function gave poor response prediction at low sample concentrations, often resulting in negative concentration limit of detection estimates. The average standard deviation for replicate determinations of the waveguide intensity response to each sample was used to define an estimate of experimental precision. Estimates of the experimental LOD and precision in the waveguide intensity responses to various model chemical systems were reported in percent transmission units (i.e. $I/I_0 x100$).

5.4.1.2 TM Mode Position Shift

Information regarding mode position shifts in response to sample composition was revealed in a full-width at half-maximum (FWHM) intensity analysis of each mode profile. Half-maximum intensity values were typically defined as the average intensity of two diodes on either side of each TM mode maximum. The two half-maximum values for each mode were subtracted to identify shifts in mode position. The FWHM calculation was performed such that positive difference values with respect to the baseline identified a position shift associated with an increase in mode propagation angle.

The full-width, half-maximum procedure should be free from intensity variations provided peak shapes do not change in response to changes in sample composition. However, drift in the waveguide FWHM baseline response was observed for all model systems. In order to correct for drift, the average FWHM difference prior to sample injection was subtracted from all waveguide FWHM difference responses in the corresponding sample block.

5.4.2 Multivariate Analysis

In general, model chemical systems used to evaluate the response of a Ag^+-exchange planar optical waveguide were single analyte systems. However, the single component composition of the sample does not preclude the existence of multiple waveguide response components. The application of photodiode array detection effectively captures both changes in relative mode intensities and mode positions. In a model system where the measured waveguide response exhibits multiple response components, the experiment cannot be adequately characterized by a simple univariate analysis. Thus, the multivariate approach provides a powerful method for evaluating the multiple mode waveguide response and for defining a robust calibration.

5.4.2.1 Singular Value Decomposition

The average baseline response prior to each sample injection was subtracted from each waveguide mode image in the corresponding sample block. This diode-by-diode subtraction corrected for long-term baseline drift while preserving spatial variance in the truncated waveguide mode images. Following baseline correction, replicate sample measurements were averaged together.

Rather than analyze each TM mode output separately, a singular value decomposition (SVD) was performed on mean centered data sets.[12] A multivariate analysis of the multiple mode waveguide response was pursued as a necessary step towards understanding the physical processes giving rise to the observed waveguide response. An SVD analysis attempts to describe the total variance in n-dimensional response space with a minimum number of orthogonal eigenvectors (principal components). The significance of each eigenvector in describing total experimental variance is indicated by an associated eigenvalue. The constraint to orthogonal eigenvectors may result in the inclusion of experimental variance which is unrelated. Thus, care must be taken not to assume a correlation among mode responses based entirely on their description by a common SVD eigenvector.

The variance included in each eigenvector can be further decomposed into a loading vector and a score vector. A loading vector describes the distribution of variance among the waveguide TM modes in photodiode array image (position) space. A score vector describes the temporal variance associated with changing the sample composition.

5.4.2.2 Partial Least Squares Calibration

Baseline corrected response data were calibrated against analyte concentration using the partial least squares (PLS) calibration method. The PLS and SVD methods are similar in that both attempt to reduce the dimensionality of waveguide response variance by defining a minimum number of eigenvectors. However, the eigenvectors defined in a PLS calibration may differ from those obtained in the SVD analysis because the PLS method considers concentration information when defining eigenvectors. The PLS method uses a leave-one-out prediction process for all samples in the calibration set to generate a root mean square error of cross validation (RMSECV) statistic. A minimum in the value of the RMSECV statistic identifies the number of eigenvectors to include in developing a PLS calibration model. The RMSECV value for a given calibration specifies the average error associated with predicting each sample in the calibration set. The RMSECV value is analogous to an average standard deviation describing the fit of each sample prediction with the calibration model.

Replicate sample measurements were included in the PLS analysis. Therefore, the estimation of prediction error (RMSECV) in the calibration model is dependent on the reproducibility of replicate sample measurements. Mode images from time slices defining a maximum, steady-state waveguide sample response were extracted from the full data set and averaged. The average mode responses were combined with known sample concentration information as input into the PLS calibration program.

5.5 Notes to Chapter 5

(1) White, J. M.; Heidrich, P. F. *Appl. Opt.* **1976**, 15(1), 151-155.

(2) Stewart, G.; Millar, C. A.; Laybourn, P. F. R.; Wilkinson, C. D. W.; DeLaRue, R. M. *IEEE J. Quantum Electron.* **1977**, QE-13(4), 192-200.

(3) Chiang, K. S. *J. Lightwave Technol.* **1985**, LT-3(2), 385-391.

(4) Hertel, P.; Menzler, H. P. *Appl. Phys.* **1987**, 44(B), 75-80.

(5) Weast, R. C., Ed., *CRC Handbook of Chemistry and Physics*, 65th ed.; CRC Press, Inc.: Boca Raton, FL, 1984, D-235, E-357.

(6) DeGrandpre, M. D.; Burgess, L. W.; White, P. L.; Goldman, D. S. *Anal. Chem.* **1990**, 62(18), 2012-2017.

(7) Petersen, J. V.; Dessy, R. E. *SPIE Proceedings: Chemical, Biochemical and Environmental Fiber Sensors II* **1990**, 1368, 61-72.

(8) Baes, C. F., Jr.; Mesmer, R. E. *The Hydrolysis of Cations*; John Wiley & Sons: New York, NY, 1972.

(9) Charlot, G. *Quantitative Inorganic Analysis*; Masson Et Cie: Paris, 1961.

(10) Mitchell, G. L. *IEEE J. Quantum Electron.* **1977**, QE-13(4), 173-176.

(11) Conn, H. J. *Biological Stains*, 6th ed.; Biotech Publications: Geneva, NY, 1953, p. 111.

(12) Golub, G. H.; Van Loan, C. F. *Matrix Computations*, 2nd ed.; Johns Hopkins Univ. Press: Baltimore, 1989.

Table 5.1 Conditions for Ag^+-exchange from a pure silver nitrate melt into soda lime silica microslide glass.

Table 5.1

Substrate Label	Exchange Time	Exchange Temp.
F1, B2	5 minutes	280 °C
F2, B1	10 minutes	280 °C
F3, B3	15 minutes	280 °C
9C, 4E	5 minutes	280 °C

Table 5.2 Effective refractive index and effective waveguide thickness for waveguide modes determined from prism coupling to substrate 9C.

Table 5.2

Mode	N_{eff}	Estimated x_t	Estimated n_{max}
TM_0	1.5652	1.551 µm	1.6069
TM_1	1.5348	2.820 µm	
TM_2	1.5075	4.406 µm	
TE_0	1.5640	1.536 µm	1.6066
TE_1	1.5332	2.804 µm	
TE_2	1.5075	4.491 µm	

Table 5.3 Mode coupling angles and surface propagation angles for Ag$^+$-exchange planar waveguide 9C.

Table 5.3

Mode	Θ_1	$\Theta(0)$
TM_0	15.185°	77.116°
TM_1	13.460°	73.053°
TM_2	11.868°	69.986°
TE_0	15.216°	77.201°
TE_1	13.500°	73.136°
TE_2	11.910°	70.061°

Table 5.4 A comparison of source launch angles for Ag^+-exchange planar waveguide mode coupling in an air or a deionized water cover medium.

Table 5.4

Mode	Air, Θ_l	Water, Θ_l	$\Delta\Theta_l$
TM_0	15.185°	15.290°	-0.105°
TM_1	13.460°	13.577°	-0.118°
TM_2	11.868°	11.985°	-0.117°
TE_0	15.216°	15.294°	-0.078°
TE_1	13.500°	13.598°	-0.098°
TE_2	11.910°	12.017°	-0.107°

Table 5.5 Bromocresol green absorbance at 632 nm for a one cm path length transmission measurement.

Table 5.5

Bromocresol Green Concentration	Absorbance (AU)
$7.58\text{x}10^{-7}$ M	0.0323
$1.01\text{x}10^{-6}$ M	0.0388
$2.53\text{x}10^{-6}$ M	0.0960
$5.05\text{x}10^{-6}$ M	0.1920
$7.58\text{x}10^{-6}$ M	0.2884
$1.01\text{x}10^{-5}$ M	0.3819
$2.53\text{x}10^{-5}$ M	0.9474
$5.05\text{x}10^{-5}$ M	1.8316
$7.58\text{x}10^{-5}$ M	2.4738
$1.01\text{x}10^{-4}$ M	2.8106

Table 5.6 Sample set for glycerol/bromocresol green mixture experiment.

Table 5.6

Sample No.	Glycerol conc. (g/L)	BCG Conc. (M)
1	0.852	----
2	2.820	----
3	5.780	----
4	8.628	----
5	----	5.00×10^{-6}
6	0.668	5.00×10^{-6}
7	----	1.50×10^{-5}
8	0.892	1.50×10^{-5}
9	2.888	1.50×10^{-5}
10	6.420	1.49×10^{-5}
11	10.860	1.49×10^{-5}
12	----	5.00×10^{-5}
13	0.468	5.00×10^{-5}
14	2.168	4.99×10^{-5}
15	4.368	4.97×10^{-5}
16	----	1.00×10^{-4}
17	0.864	9.99×10^{-5}
18	2.860	9.98×10^{-5}
19	5.816	9.95×10^{-5}
20	8.600	9.93×10^{-5}

Table 5.7 Methylene blue absorbance at 632 nm for a one cm path length transmission measurement.

Table 5.7

Methylene Blue Concentration	Absorbance (AU)
2.55×10^{-7} M	0.0199
5.04×10^{-7} M	0.0412
7.64×10^{-7} M	0.0602
1.02×10^{-6} M	0.0853
2.55×10^{-6} M	0.2025
5.04×10^{-6} M	0.3988
7.64×10^{-6} M	0.5978
1.02×10^{-5} M	0.7838
2.55×10^{-5} M	1.7603
6.37×10^{-5} M	3.1582

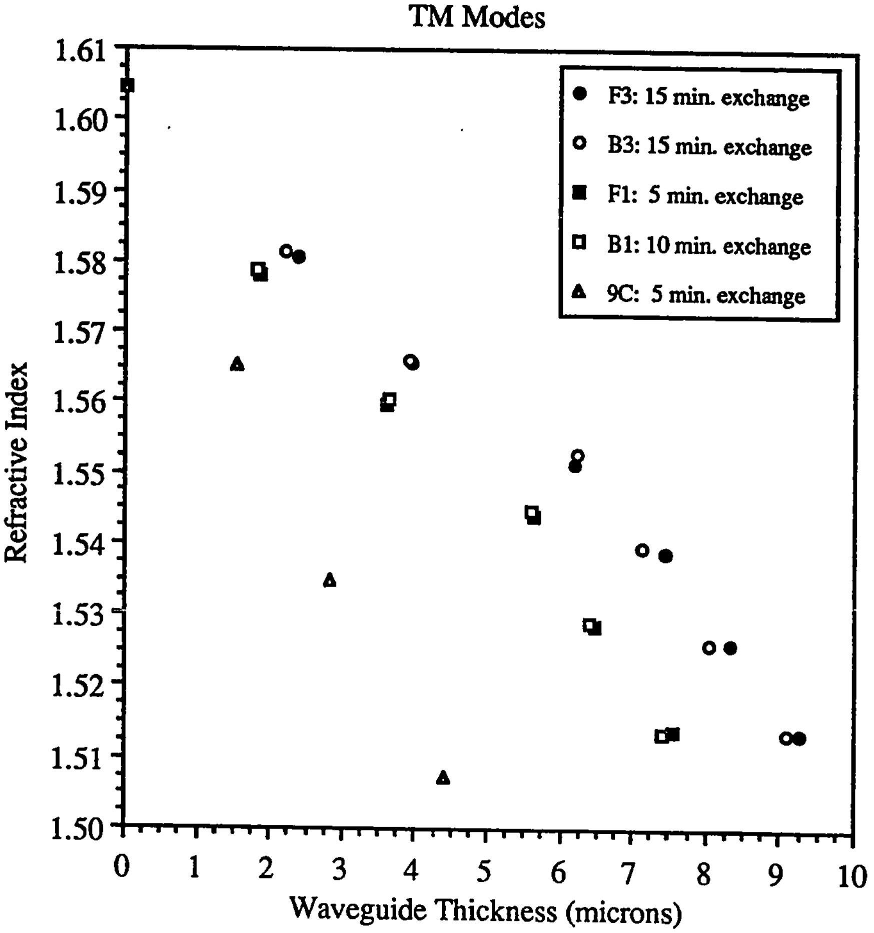

Figure 5.1a Estimated ion-exchange waveguide refractive index profiles.

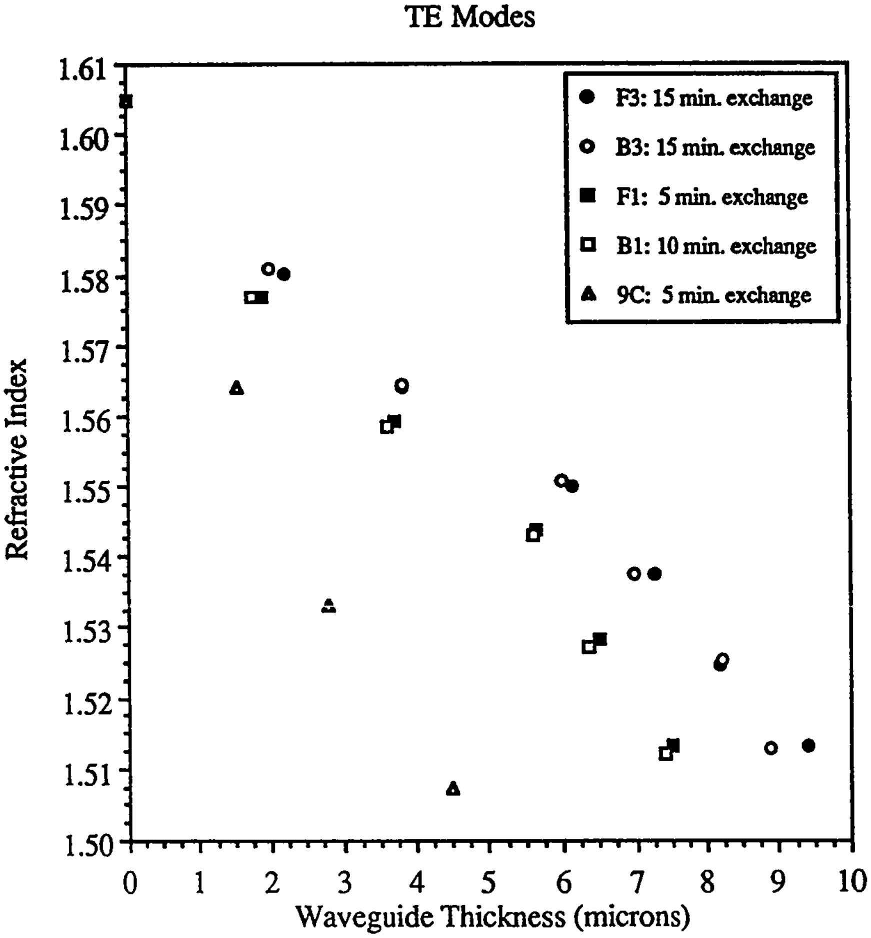

Figure 5.1b Estimated ion-exchange waveguide refractive index profiles.

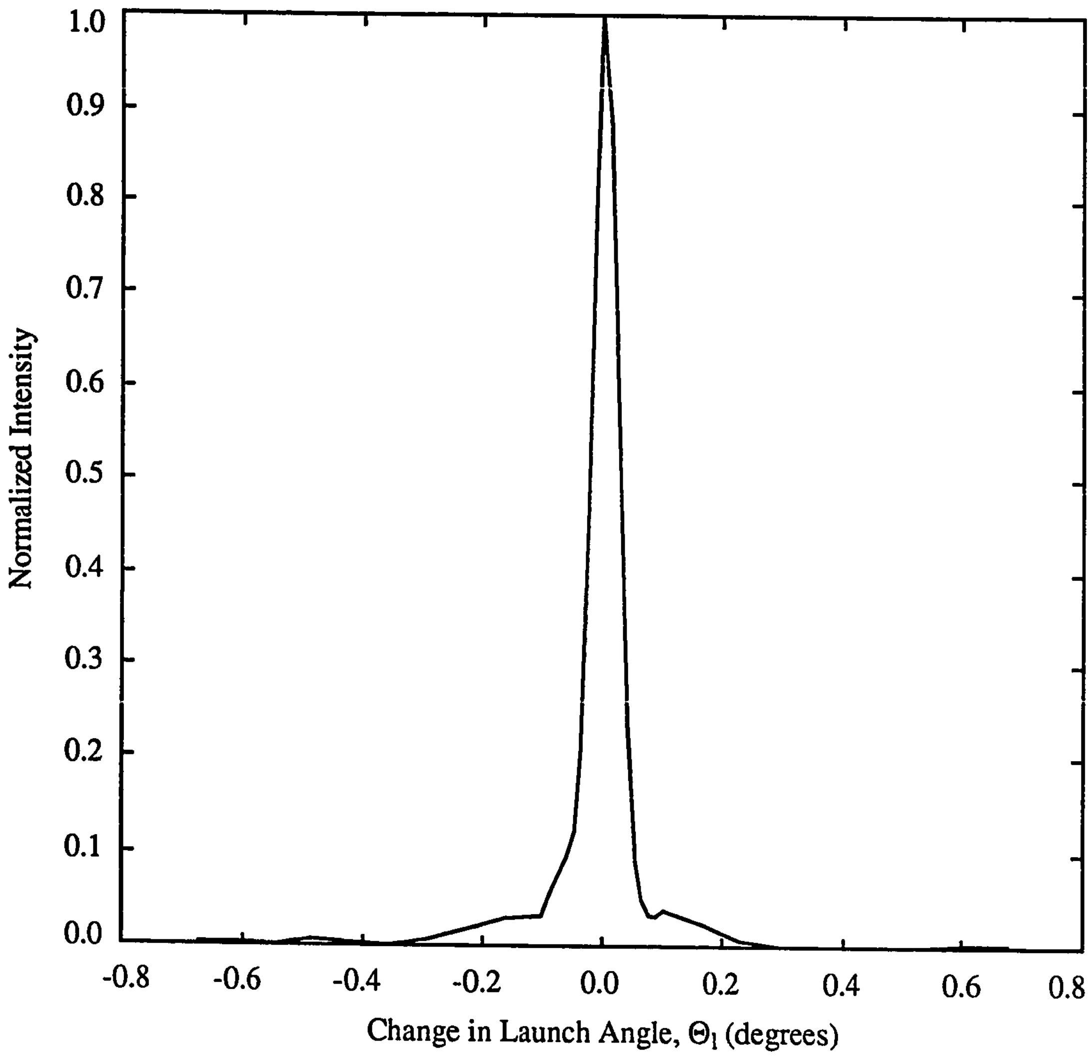

Figure 5.2 Measured TM_2 mode resonance coupling curve for Ag^+-exchange waveguide 9C.

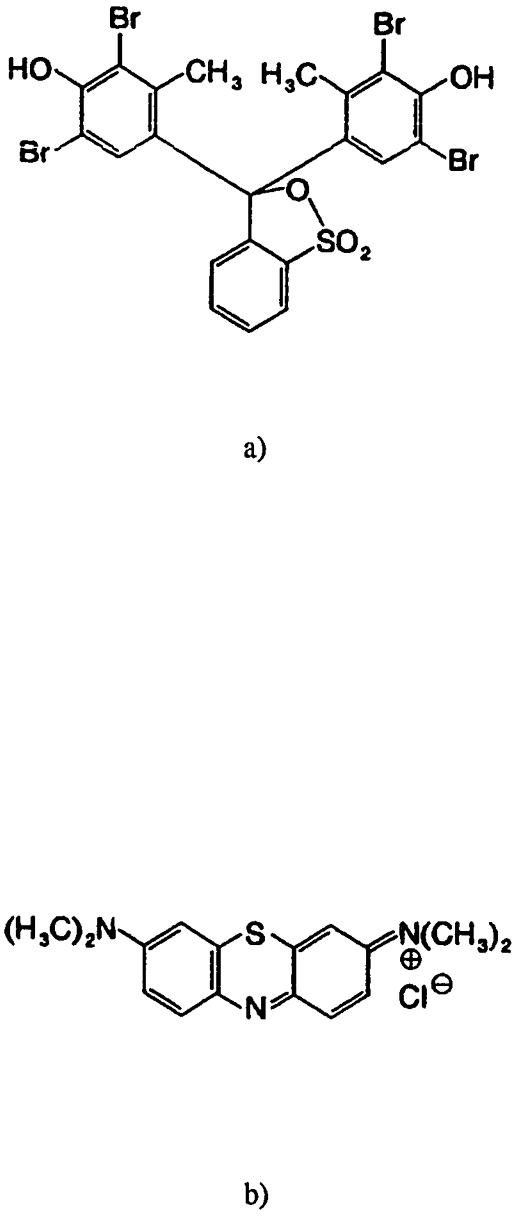

Figure 5.3 Model absorbance systems: a) bromocresol green indicator dye and b) methylene blue.

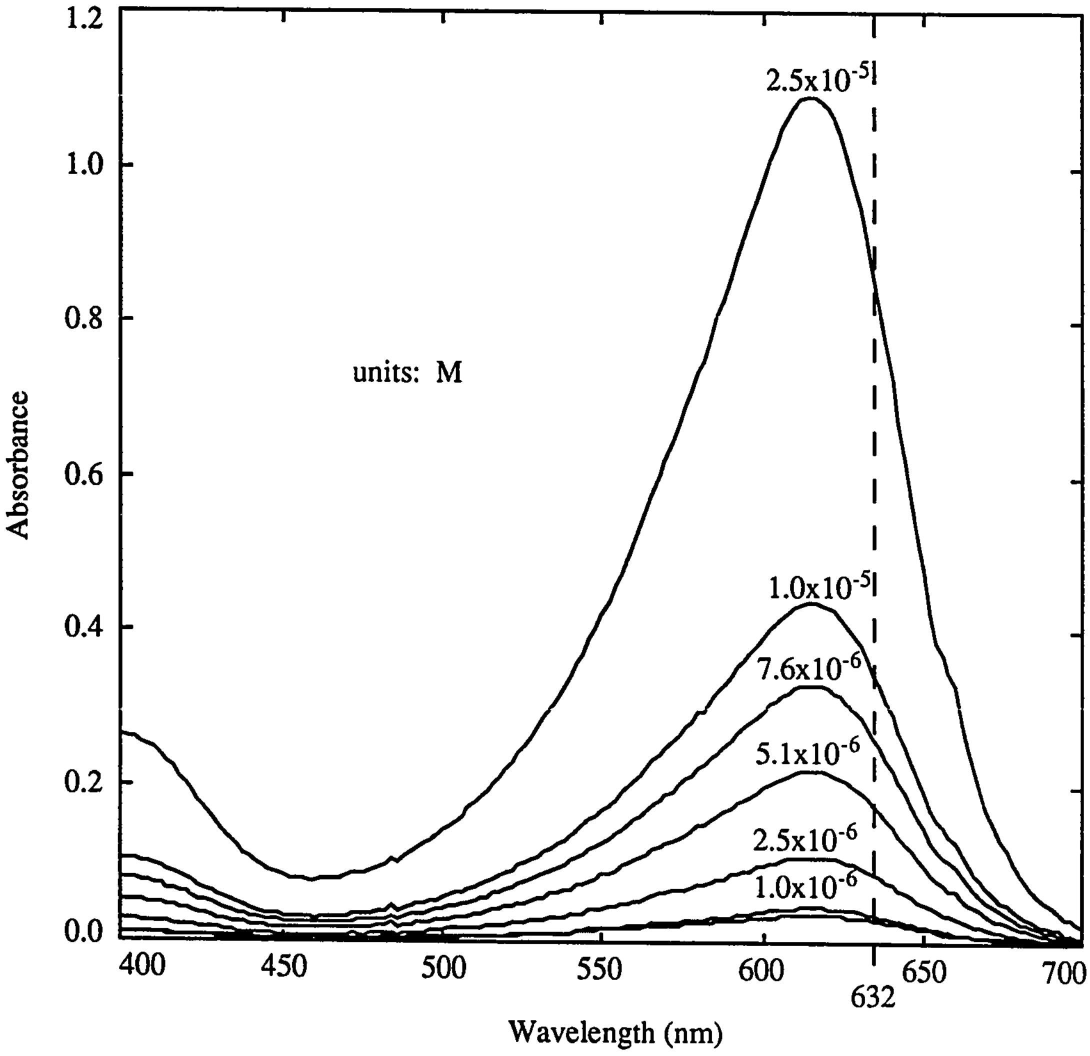

Figure 5.4 Absorbance spectra of bromocresol green calibration samples for a 1 cm transmission pathlength.

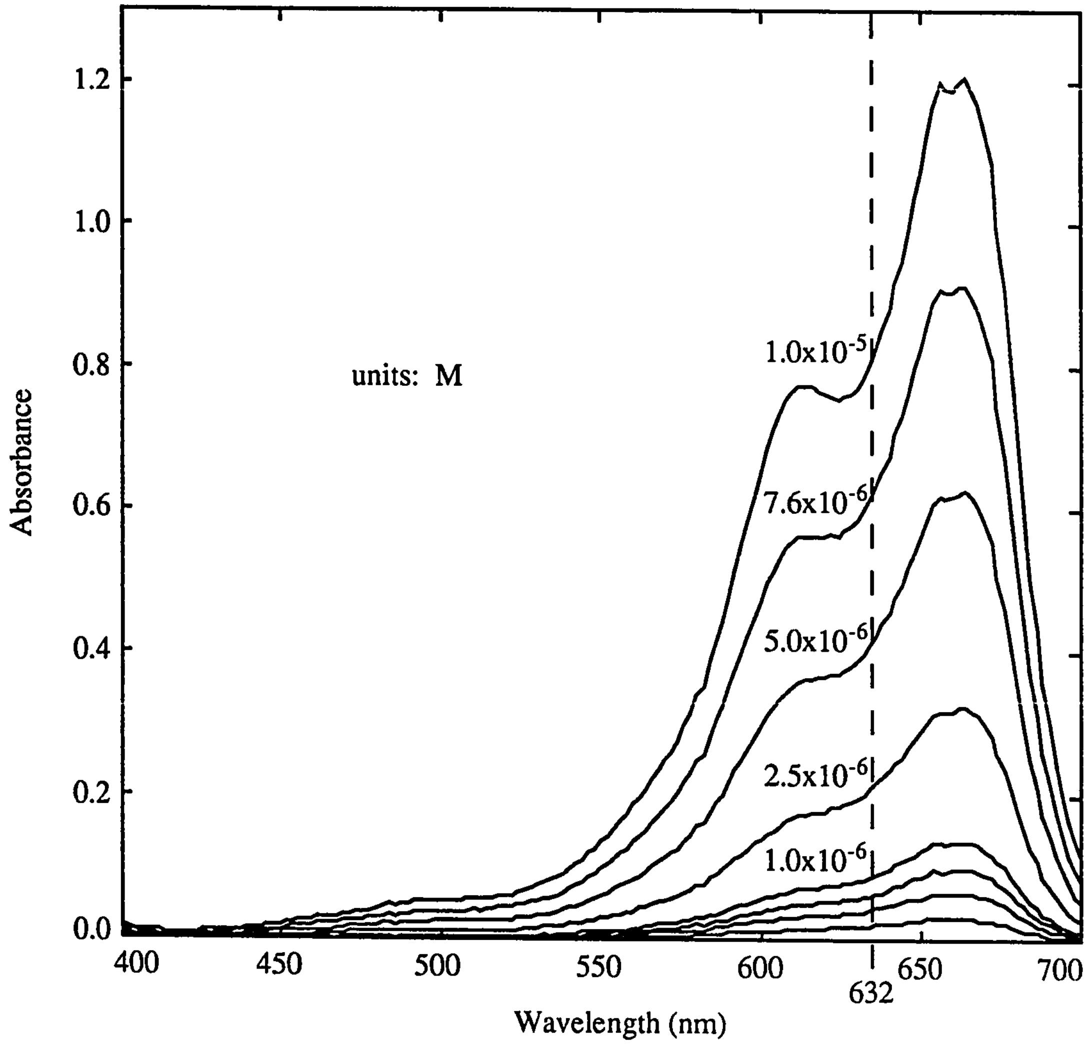

Figure 5.5 Absorbance spectra of methylene blue calibration samples for a 1 cm transmission pathlength.

Chapter 6

Results and Discussion

6.1 Multiple Mode Coupling

The combinations of diffusion time and temperature used to fabricate Ag^+-exchange waveguides produced exchange layers of sufficient thickness to support multiple modes. As previously noted, direct coupling a collimated He-Ne laser to any mode of a Ag^+-exchange waveguide results in the excitation of multiple modes. The search for a plausible mechanism describing efficient multiple mode population continues to evolve in response to ongoing empirical evaluation. This section considers proposed mechanisms which may contribute to multiple mode coupling in Ag^+-exchange waveguides.

6.1.1 Grating Effects

Multiple mode excitation behavior was initially observed in grating coupled Ag^+-exchange waveguides. Thus, the search for a potential mechanism of multiple mode coupling originally focused on surface grating effects. Inadvertent chirping of the grating period due to secondary interference effects from the photoresist patterning step is a concern. A chirped grating would diffract light from a collimated source of finite width over a range of angles. Generation of a sufficiently broad range of diffraction angles could result in direct coupling to each waveguide mode. Thus, one possible mechanism giving multiple mode output involves direct mode coupling from a chirped surface grating.

The existence of surface gratings on substrates undergoing Ag^+-exchange defines diffusion conditions in the grating region which are different from those across the remaining substrate surface. The grating structure acts as a diffusional mask which retards ion-exchange and produces a shallower exchange layer in the area under the grating region. Thus, a step offset in Ag^+-exchange layer thickness is encountered around the edges of both surface gratings. Another proposed mechanism of multiple mode population is a direct result of this step change in waveguide thickness. The coupling of mode intensity to a discrete waveguide mode in the grating region could be effectively scrambled into all allowed waveguide modes by the step change in Ag^+-exchange layer thickness. This mechanism suggests that mode scrambling should occur directly after incoupling and just prior to mode outcoupling. Further, scrambling of intensity among the modes in the propagation region between the gratings would not be expected to occur.

Due to limited availability of substrates with etched gratings, Ag^+-exchange waveguides were also made in microslide substrates without surface gratings. As such, evaluation of the waveguide mode structure was conducted with prism couplers. Prism coupling to Ag^+-exchange microslide substrates also produced multiple mode waveguide output. The observation of multiple mode output using prism couplers dismisses both of the grating effects discussed above as primary mechanisms for multiple mode coupling. The similarity in coupling behavior for both grating and prism coupled waveguides suggests that multiple mode population is an inherent property of the Ag^+-exchange structure rather than an artifact of the coupling method.

6.1.2 Scattering

Modes propagating within a waveguide are attenuated by scattering due to surface roughness and local refractive index variations in glass. In a waveguide layer supporting multiple modes, intensity scattered for one propagating mode may be captured by another waveguide mode. However, the isotropic nature of light scattering does not produce a very efficient mechanism of mode crosstalk.

In general, ion-exchange waveguides exhibited minimal visible scattering while efficiently distributing intensity among the allowed resonant modes. Thus, a scattering mechanism does not account for multiple mode excitation observed in ion-exchange waveguides.

6.1.3 Resonance Overlap

The possibility of overlap in resonance conditions for several adjacent waveguide modes in the Ag^+-exchange structure was considered as a potential mechanism for multiple mode coupling. In order for overlap to occur, the spacing between adjacent waveguide mode coupling angles would need to be similar to the angular widths of individual mode resonance coupling curves. Measured mode coupling angles (Table 5.3, Θ_l) in Ag^+-exchange waveguides have a typical separation of approximately 1.65^o. In contrast, the TM_2 mode resonance is extremely sharp with a full angular width at half-maximum intensity of 0.05°. Thus, overlap between the resonance coupling curves of adjacent waveguide modes is essentially nonexistent in an Ag^+-exchange waveguide. This potential mechanism of multiple mode coupling is not an issue in Ag^+-exchange waveguides.

6.1.4 Mode Conversion

The final potential mechanism considered here to describe multiple mode coupling in Ag^+-exchange waveguides is mode conversion.[1] Imagine that through careful selection of prevailing launch conditions, a single mode (TM_2) can be exclusively incoupled into a multiple mode Ag^+-exchange waveguide. The discrete waveguide mode initially propagates over a distinct angular path within the gradient index structure. However, the angular purity of the incoupled mode will begin to degrade immediately as changes in propagation angle are introduced due to variations in diffusion layer thickness and deviations from exact planar geometry. The angular adjustment in some portion of the overall coupled mode intensity potentially provides for sufficient angular overlap with the propagation conditions for an adjacent mode to be cross-coupled. In this manner, the overall intensity of the coupled mode is distributed among all allowed waveguide modes with some finite efficiency. The relative mode intensities resulting from mode conversion vary with propagation path length through the waveguide layer as intensity is continuously interconverted among the modes. Relative mode intensities may reach an equilibrium after a well defined, sufficiently long interaction pathlength.

In addition to providing a means for multiple mode excitation, mode conversion reduces the apparent width of mode resonance curves. The reduction in resonance widths occurs because propagation angles not exactly matching a mode resonance are more apt to incur sufficient angular adjustment for capture by an adjacent mode. For example, the resonance coupling curve half-maximum width of the TM_2 mode in Ag^+-exchange waveguide 9C is 0.05° compared with typical half-maximum widths of greater than 0.10° in step-index waveguides.

The mode conversion mechanism provides the most reasonable explanation for the observed multiple mode coupling behavior in Ag^+-exchange waveguides. Therefore, in subsequent discussion, mode conversion will be stressed as the primary mechanism of multiple mode excitation.

6.1.5 Interferometric Mode Interactions

A number of cylindrical waveguide structures have been designed in which direct intensity exchange occurs between two adjacent waveguides.[2-5] The structures respond to changes in cover solution conditions by modulating the amount of intensity exchange occurring between the waveguides. The adjacent waveguides are designed such that modes in each waveguide have the same propagation constant (angle). The exchange of intensity between degenerate modes is interferometric in nature and leads to intensity modulations which have a characteristic beat frequency.

The apparent exchange of mode intensity observed in the Ag^+n-exchange planar waveguide suggests a comparison to the interferometric waveguide structure described above. However, modes in the Ag^+-exchange waveguide have distinctly different propagation constants and, as such, are not degenerate. Therefore, direct exchange of intensity among modes in the Ag^+-exchange waveguide layer is not allowed. In order for there to be an exchange of energy, some mechanism is required to convert a portion of the intensity in one mode to match the propagation constant of a different mode.

6.2 Bulk Refractive Index

6.2.1 Univariate Analysis

6.2.1.1 Integrated Intensity

The transient Ag^+-exchange waveguide TM_2 mode intensity response to 200 μl injections of twelve glycerol samples is given in Figure 6.1a. The transient modulations in waveguide TM_2 mode intensity arise because variations in cover refractive index were dynamic as dispersed glycerol samples flowed over the waveguide surface. The general trend observed was a decrease in TM_2 mode intensity with increasing glycerol concentration. The modulation in TM_2 mode intensity primarily followed from the reduced resonance coupling efficiency associated with changes in cover refractive index. Recall that cover refractive index changes produce an angular displacement from the baseline position at the resonance coupling curve maximum. The shape of the resonance coupling curve describes TM_2 mode intensity variations as smooth, monotonic transient response profiles with increases in glycerol concentration. However, deviations are clearly observed in the experimental TM_2 response to glycerol concentrations above 21.6 g/L. In this high glycerol concentration range, the TM_2 mode resonance coupling loss approaches a limiting value of approximately 16% relative to the baseline intensity level. In addition, the temporal TM_2 intensity profiles exhibit increasingly non-symmetric peak shapes with increasing glycerol concentration.

The observed waveguide TM_2 mode intensity behavior in the high glycerol concentration range indicated the possible existence of variable system dispersion rather than a true limiting intensity response. Glycerol samples tested in this experiment had molar concentrations in the 7.6 mM to 0.37 M range. At such high concentrations, the process of radial diffusion is no longer described by a constant molecular diffusion coefficient. Rather, radial diffusion is enhanced by chemical potentials created as the convective process of axial diffusion generates a significant radial concentration gradient. As the radial diffusion process is no longer random, analyte diffuses away from regions of high concentration and is driven towards the flow channel walls which enhances axial dispersion as analyte moves to a region of slower flow. Thus, an overall increase in flow system dispersion would produce greater sample dilution and wider transient sample zones.

The existence of variable system dispersion in the glycerol experiment was confirmed by a number of observations. First, the waveguide TM_2 mode intensity reached an apparent limiting response level despite the injection of increasing concentrations of glycerol. Thus, the greater sample dilution resulting from variable system dispersion produced similar effective analyte concentrations at the waveguide surface for large injected glycerol concentrations. Second, enhanced radial diffusion towards the waveguide surface (flow cell wall) produced a TM_2 mode waveguide response at shorter times relative to the injection time with increasing sample concentration. Third, the transient TM_2 mode intensity profile widths increased with increasing sample concentration starting at 12.9 g/L glycerol. In going from 8.7 g/L to 34.4 g/L glycerol, the peak full-widths at half-maximum intensity increased from 60 to 80 seconds.

The waveguide TM_1 and TM_0 mode intensity responses to glycerol samples are given in Figure 6.1b. In general, the Ag^+-exchange waveguide TM_1 mode intensity was quite stable to changes in cover refractive index. For glycerol samples in the 6.4 g/L to 34.4 g/L range, the minimum TM_1 intensity was nearly identical and corresponded to an overall intensity loss of about 3.1%. The TM_1 mode intensity response was marked with the same variable dispersion effects as observed in the TM_2 mode response. The TM_1 mode intensity appeared to be quite sensitive to dispersion induced interfacial concentration variations. This was in marked contrast to the relative insensitivity of the mode to incremental changes in injected glycerol concentration.

The TM_0 mode intensity did not respond to glycerol samples in the range from 0.70 g/L to 2.2 g/L. However, starting at 4.3 g/L glycerol the Ag^+-exchange waveguide TM_0 intensity increased monotonically with increasing glycerol sample concentration. The temporal TM_0 mode intensity profiles were symmetric and exhibited a maximum intensity increase of approximately 7.3% for the 34.4 g/L glycerol sample. The TM_0 mode did exhibit a subtle shoulder on the trailing edge of the transient response profile which may have been an effect of the dispersion characteristics of the flow system. Alternatively, the shoulder may indicate delayed elution of some portion of the sample zone which describes partitioning of the glycerol sample into the glass stationary phase.

According to the mechanism of mode conversion, induced angle variations in the incoupled TM_2 mode result in the population of the TM_1 and TM_0 modes in Ag^+-exchange waveguides. Thus, the reduction in TM_2 mode resonance coupling efficiency accompanying cover refractive index changes should produce related losses in the measured intensities of the TM_1 and TM_0 modes. Obvious deviations from this simple model observed in the glycerol experiment indicate that the process of mode conversion is modulated by changes in the refractive index of the cover medium.

Modulations in the process of waveguide mode conversion in response to variations in cover refractive index has three apparent implications for understanding the multiple mode waveguide response. First, mode conversion is a continuous process of mode intensity interconversion over a finite interaction pathlength. The angular readjustment in mode propagation angles associated with cover refractive index produces a change in the effective interaction pathlength for mode conversion and, as such, should produce changes in relative waveguide mode intensities. Second, mode conversion involves the "capture" of intensity from the coupled mode which requires the introduction of an overlap factor to describe capture efficiency. The overlap factor must consider the angular distribution of intensity created by deviations from perfect waveguide geometry and the angular distribution of mode resonance angles at the prevalent cover refractive index. The existence of a mode conversion efficiency factor leads to the conclusion that the overall waveguide mode intensity is not necessarily conserved. Third, a theoretical model describing the process of mode conversion does not exist for the Ag^+-exchange waveguide structure. Thus, the complicated multiple mode response must be determined empirically to build a mode conversion model (calibration) applicable to a particular Ag^+-exchange waveguide structure.

In the glycerol experiment, baseline conditions optimized for TM_2 mode coupling also populate the TM_1 and TM_0 modes according to the existing interaction pathlength and efficiency for mode conversion. The introduction of glycerol samples produces an increase in cover refractive index which modulates the effective pathlength and efficiency for mode conversion. In the refractive index range tested, the TM_1 mode intensity tracked the coupled TM_2 mode intensity with little apparent effect from changes in mode conversion. In contrast, mode conversion favored greater transfer of intensity to the TM_0 mode with increasing cover index despite the decrease in coupled TM_2 mode intensity. Thus, the relative TM mode intensities varied with modulations in glycerol concentration and the total mode intensity was not conserved. Therefore, the combined response mechanisms of mode resonance coupling and mode conversion provide a reasonable description of the waveguide multiple mode intensity response to cover refractive index changes.

The analytical performance of the Ag^+-exchange waveguide in the glycerol experiment is summarized in Table 6.1. The limit of detection (LOD) was calculated as three times the root mean square (rms) baseline noise over the course of the experiment. The complicated response made conversion from to concentration units impractical such that the LOD was defined in units of percent transmission. The TM_2 mode exhibited the lowest intensity noise which makes sense as this mode was directly coupled. The average standard deviation in percent transmission for duplicate determinations of the waveguide intensity response to twelve glycerol samples was used to define an estimate of precision. The estimates of experimental precision confirmed that the waveguide multiple mode response mechanisms operated reproducibly for cover refractive index changes in the defined range.

6.2.1.2 TM Mode Position Shifts

The Ag^+-exchange TM_2 waveguide mode position shift response to injected glycerol samples is given in Figure 6.2a. A TM_2 mode position shift response was observed for all samples from 0.70 g/L to 34.4 g/L glycerol. Position shifts were defined such that positive FWHM difference values indicated an increase in mode propagation angle. The positive FWHM differences describing the TM_2 mode position shift response indicated an increase in TM_2 mode propagation angle for an increase in cover refractive index. Recall that mode propagation angles are sensitive to increases in cover refractive index since the reduced interfacial reflection phase shift contribution to the resonance equality must be offset by a pathlength phase shift term. To reduce the pathlength phase shift contribution, the effective TM_2 mode refractive index must increase which requires an increase in the TM_2 mode propagation angle.

The transient TM_2 mode FWHM difference profiles were symmetric in the low concentration range up to 6.4 g/L glycerol. Starting at 8.7 g/L, the symmetry was disrupted by the appearance of a shoulder on the trailing edge of the response profiles. The primary position shift increased with increasing glycerol concentration and exhibited a maximum shift response at a common delay time. In contrast, the profile shoulder maintained a similar response magnitude irrespective of injected glycerol concentration and the shoulder inflection occurred at later delay times with increasing glycerol concentration. An additional feature on the leading edge of TM_2 mode position shift profile indicated a sharp, negative FWHM difference spike for glycerol samples starting at 21.6 g/L. The negative displacement increased with increasing glycerol concentration.

The appearance of a shoulder on the transient position shift response profile hints at the presence of two sample components which are differentially retained. Since single component glycerol samples were injected, the position shift information describes the differential transit of a variable concentration of non-retained glycerol and a nearly constant concentration of retained glycerol. The non-retained glycerol produces a bulk refractive index variation which induces the observed concentration dependent changes in TM_2 mode propagation angles. The partitioning of some portion of the total injection volume into the silica glass stationary phase provides for delayed transport via the mobile phase. Since, in most cases, the injected glycerol concentration exceeded the capacity of the glass stationary phase, the retained concentration was limited to some fraction of the total injected concentration. The shift in delay time at which the retained glycerol was observed is related to the variable dispersion characteristics of the flow system discussed earlier. The extended return to the baseline TM_2 mode position provides additional evidence that glycerol was interacting with the glass surface. The partitioning of glycerol into the glass hydration layer may also be responsible for the sharp negative displacement in TM_2 mode position observed at high glycerol concentrations.

The TM_1 and TM_0 mode position shift responses are given in Figure 6.2b. The TM_1 mode propagation angle varies in a complicated manner with cover refractive index. At low sample concentrations, the TM_1 mode position shift response indicated a slight increase and then a decrease in propagation angle. At higher glycerol concentrations, the mode position shift response profile was characterized by multiple sharp features describing both decreases and increases in mode propagation angle. The TM_1 mode response profiles did not include a shoulder and, as such, were narrower than the TM_2 profiles.

The TM_0 mode propagation angle increases monotonically with increasing cover refractive index. Response profiles were smooth transients which returned to baseline following passage of the sample zone. As for the TM_1 mode, the symmetric TM_0 mode transient profiles were narrower than the corresponding TM_2 mode position shift profiles.

Evidence for the partitioning of glycerol into the glass stationary phase was observed exclusively in the TM_2 mode position shift profiles. Curiously, the TM_1 and TM_0 modes did not offer supporting indications of a surface interaction. Thus, propagation angles of the TM_1 and TM_0 mode were apparently unaffected by the partitioning of glycerol into the glass phase. The propagation angles of the Ag^+-exchange waveguide TM_1 and TM_0 modes were modulated only by the transient bulk cover refractive index change associated with the non-retained glycerol.

6.2.1.3 Ag^+-Exchange Waveguide Response

The injection of glycerol samples produced bulk refractive index changes across the waveguide surface. At the incoupling grating, the resonance condition defined an increase the TM_2 mode propagation angle with increasing refractive index. Thus, the TM_2 mode incoupled with reduced efficiency and outcoupled to a different position on the array detector relative to the baseline response for injections of glycerol samples. Variations in boundary conditions also modulated the process of mode conversion in the region between the gratings. Thus, the relative TM mode intensities were observed to vary with injected glycerol concentration. Due to the large glycerol concentrations injected, the transient TM mode response profile widths and magnitudes were subject to change due to the effects of variable system dispersion. An additional factor effecting the TM_2 mode response profiles was the partitioning of glycerol in the waveguide glass stationary phase. The partitioning of glycerol in the glass stationary phase extended the TM_2 mode intensity and position shift responses to delay times after the passage of the non-retained sample zone.

6.2.2 Multivariate Analysis

6.2.2.1 Singular Value Decomposition

The first principal component describes 94.03% of total experimental variance observed in the Ag^+-exchange waveguide response to glycerol samples. The primary variance contributions in the glycerol experiment comes from the TM_2 and TM_0 waveguide modes. The loading plot (Figure 6.3a) describes an inverse relationship between the waveguide TM_2 and TM_0 modes which is characteristic of the Ag^+-exchange waveguide intensity response. The corresponding score plot (Figure 6.3b) indicates a series of smooth, transient response profiles which are monotonic with injected glycerol concentration. At high glycerol concentrations, the minimum score response approaches a limiting value and the response profiles exhibit an increasingly asymmetric peak shape. The first principal component describes TM_2 and TM_0 mode intensity variations associated with cover refractive index changes.

The second principal component describes 3.35% of the remaining experimental variance observed in the multiple mode waveguide response to glycerol samples. The loading plot (Figure 6.4a) indicates relatively large variance contributions from the TM_1 and TM_0 modes. The transient response profiles in the score plot (Figure 6.4b) approach a limiting response level at about 8.68 g/L glycerol as indicated by the flat peak. However, starting at 17.2 g/L the smooth rising edge of each response profile is broken by a sharp negative going peak. For more concentrated glycerol samples, the leading edge reaches a similar score response before the peak inversion occurs. The depth of inversion increases with increasing concentration thus differentiating among samples in the high concentration range. The second principal component variance describes the intensity response of the Ag^+-exchange waveguide TM_1 mode to cover refractive index modulations.

Taken together the first two principal components describe 97.38% of the total experimental variance in the waveguide response to glycerol samples. Thus, the variance observed in the glycerol experiment was primarily due to mode intensity variations associated with TM_2 mode resonance coupling loss and changes in mode conversion.

The third principal component includes 1.15% of experimental variance observed in the Ag^+-exchange waveguide response to glycerol samples. The loading plot identifies TM_1 mode variance which is inversely related to the TM_2 and TM_0 mode variance. The score plot describes transient response profiles with sharp features exhibiting both positive and negative displacements from the baseline response level. The general trends observed in the score profiles are similar to those observed in the FWHM difference analysis of the TM_1 mode position. The third principal component describes position shift variance primarily associated with the TM_1 mode.

The fourth principal component accounts for 0.95% of experimental variance in the waveguide response to glycerol samples. The loading plot indicates a nearly exclusive variance contribution from the TM_2 mode. The variance distribution in position space describes a sharp negative and positive intensity inflection on either side of the original

TM_2 mode position. The score plot displays transient features which were discussed earlier in the TM_2 mode FWHM difference plot (Figure 6.2). Thus, the fourth principal component describes TM_2 mode position shift variance induced by cover refractive index changes.

Remaining principal components describe additional sample related variance and both random and non-random sources of experimental variance. They account for the residual 0.52% of measure experimental variance.

6.2.2.2 Partial Least Squares Calibration

The multiple mode waveguide response was nearly steady-state (zero dispersion) across six sampled points on the transient glycerol concentration profile. Therefore, the corresponding multiple mode images were averaged to define the Ag^+-exchange waveguide response to each glycerol sample. The waveguide response information and known glycerol concentrations were used to perform a PLS calibration. The RMSECV statistic for the first six calibration factors (principal components) is given in Table 6.2. A five factor calibration model results in a RMSECV value of 0.14 g/L glycerol. For a change in glycerol concentration of 0.14 g/L, the change in bulk refractive index is calculated to be 1.6×10^{-5} relative to water.

6.3 Bulk Absorbance

6.3.1 Univariate Analysis

6.3.1.1 Integrated Intensity

The transient Ag^+-exchange waveguide TM_2 mode intensity response to 200 μl injections of ten bromocresol green samples is presented in Figure 6.5a. The waveguide TM_2 mode intensity was observed to decrease with increasing dye concentration. The attenuation in TM_2 mode intensity is primarily the result of evanescent absorbance in the propagation region between the gratings. The transient profiles are symmetric throughout the concentration range tested and maintain constant widths indicating reproducible system dispersion.

The TM_1 and TM_0 waveguide mode intensity responses to bromocresol green samples are given in Figure 6.5b. The waveguide TM_1 and TM_0 mode intensities also decreased with increasing bromocresol green concentration. Again, the primary mechanism of intensity loss was evanescent coupling to bromocresol green in the cover medium.

In Ag^+-exchange planar waveguides, the total number of reflections for each TM mode is approximately the same such that differences in interfacial reflection angle determine the relative mode absorbance sensitivities. The reflection angle decreases with increasing mode order so that the effective evanescent absorbance pathlength should increase in the order, $TM_0<TM_1<TM_2$. The experimental mode intensity responses to bromocresol green sample injections indicated nearly identical mode sensitivities in the concentration range from $7.6x10^{-7}$ M to $1.0x10^{-5}$ M dye. However, above $1.0x10^{-5}$ M bromocresol green the TM_1 and TM_0 mode intensities exhibited significantly higher attenuation than the TM_2 mode.

The analytical performance of the Ag^+-exchange waveguide in the bromocresol green experiment is summarized in Table 6.3. The limits of detection and estimated experimental precision were similar for the individual TM mode intensity responses.

The absorbance of bromocresol green sample solutions was determined in a spectrophotometer using a standard 1 cm pathlength cuvette. A comparison of waveguide TM mode attenuation with the spectrophotometer absorbance at 632 nm provides an estimate of effective mode absorbance path lengths. The respective absorbance values were plotted defining the waveguide mode attenuation as y-axis variables. The relationship was nearly linear over a subset of the concentration range ($7.58x10^{-7}$ M to $2.53x10^{-5}$ M) for which the spectrophotometer absorbance was in the Beer's law range (<1.8 AU). The effective TM mode evanescent absorbance path lengths were obtained as the slopes of the corresponding lines. The slopes were normalized to a mode propagation distance (grating separation) of one cm to allow a direct comparison with the one cm pathlength transmission measurement. The effective evanescent path lengths (Table 6.4) for the Ag^+-exchange waveguide TM modes were approximately two orders of magnitude smaller than for a free wave transmission measurement.

6.3.1.2 TM Mode Position Shifts

The Ag^+-exchange waveguide TM_2 mode position shift response to bromocresol green samples indicates very slight positive FWHM difference changes at high bromocresol green concentrations. The TM_2 mode FWHM difference response suffers from poor signal-to-noise. The slight positive differences indicate a subtle increase in the TM_2 mode propagation angle with increasing bromocresol green concentration. The TM_2 mode propagation angle changes follow from an increase in cover refractive index due to anomalous dispersion in the cover medium.

The waveguide TM_1 mode also exhibits an increase in mode propagation angle with increasing bromocresol green concentration. The TM_1 mode position shift is sensitive to bromocresol green in the middle and high concentration samples. In contrast, the TM_0 mode propagation angle decreases with increasing bulk dye concentration and produces a significant response only in the high concentration range.

6.3.1.3 Ag^+-Exchange Waveguide Response

The primary mechanism of TM mode attenuation in the bromocresol green experiment is direct evanescent coupling of mode intensity to the dye molecule. Deviations from the expected order of Ag^+-exchange waveguide mode evanescent sensitivities are related to anomalous dispersion in the cover medium. Since the He-Ne laser line is offset 17 nm beyond the maximum bromocresol green absorbance wavelength, the source is operating in the anomalous region defined by an increase in cover refractive index. Thus, the TM_2 mode intensity is subject to attenuation due to reduced resonance coupling efficiency. In addition, cover refractive index changes produce variations in the process of mode conversion. Unfortunately, the changes in relative mode intensities produced by mode conversion mask the actual order of TM mode evanescent absorbance sensitivity. The different mode propagation angles resulting from the anomalous refractive index increase in the cover also produced subtle positions shifts on the array detector.

6.3.2 Multivariate Analysis

6.3.2.1 Singular Value Decomposition

The first principal component describes 98.01% of the total experimental variance observed in the waveguide response to bromocresol green samples. The loading plot (Figure 6.6a) preserves the baseline shape and position of each TM mode in describing relative variance contributions. The score plot (Figure 6.6b) reveals a series of transient profiles which indicate a monotonic waveguide response with increasing bromocresol green concentration. The entire dye concentration range down to 7.58×10^{-7} M bromocresol green appeared to be resolved from baseline noise. The observed variance in the first principal component results from evanescent absorbance of TM mode intensity by bromocresol green. In addition, correlated mode intensity variations associated with reduced TM_2 mode coupling and mode conversion are included in the first principle component.

The second principal component describes 0.17% of the remaining experimental variance observed in the waveguide response to bromocresol green samples. The loading plot identifies variance contributions from the TM_1 and TM_0 modes which are inversely related. In addition, the TM_1 and TM_0 mode variance is position shifted from their respective baseline locations. The transient score response profiles are quite noisy and the baseline is observed to drift significantly. The second principal component describes variance associated with waveguide TM mode position shifts related to anomalous material dispersion in the cover solution.

The remaining 1.82% variance in the bromocresol green data set was described by numerous principal components with little apparent correlation to bromocresol green samples. The score plots did not exhibit discernible trends and were quite noisy.

6.3.2.2 Partial Least Squares Calibration

The waveguide response was nearly steady-state across three sampled points on the transient bromocresol green profile. Therefore, the corresponding multiple mode images were averaged to define the waveguide response to bromocresol green samples. The average time response was combined with known dye sample concentrations as input into a PLS calibration. The PLS calibration results are summarized in Table 6.5. The inclusion of four principal components for sample prediction gave a RMSECV of 2.24×10^{-6} M bromocresol green.

6.4 Bulk Refractive Index and Absorbance

6.4.1 Univariate Analysis

6.4.1.1 Integrated Intensity

The Ag^+-exchange waveguide TM_2 mode intensity response to 200 µl injections of the twenty samples in the glycerol-bromocresol green mixture sample set is given in Figure 6.7a. The various sample compositions corresponding to the numbered peaks are conveniently listed in Table 5.6. The waveguide TM_2 mode responses to the four pure glycerol samples are labeled as 1 thru 4. The glycerol content increased from 0.85 g/L to 8.63 g/L which produced a change in cover refractive index of from 10^{-4} to 10^{-3} relative to the phosphate buffer carrier solution. The waveguide TM_2 mode intensity exhibited little sensitivity to cover refractive index changes in this glycerol concentration range. A change in cover refractive index of 10^{-3} was required to produce a sufficient intensity change to be resolved from baseline noise. Note that the relative changes in cover refractive index were similar to those tested in evaluating the glycerol model system using deionized water as a carrier solution. However, keep in mind that the TM_2 mode coupling angle and the shape of the resonance coupling curve depend on the absolute cover refractive index as described by the resonance condition. Thus, the refractive index sensitivity of the waveguide TM_2 mode depends on the absolute cover refractive index. The deionized water and phosphate buffer carrier solutions defined cover boundary conditions which differed in absolute index by approximately 0.0025 refractive index units from the earlier experiment. In addition, in earlier experiments glycerol was observed to partition into the waveguide glass stationary phase. The interaction of glycerol with the glass stationary phase potentially involves hydrogen bonding with glass SiOH (or SiO^-) sites. In the mixture experiment, the phosphate buffer carrier solution provides a large concentration of sodium cations (0.11 M) which may occupy hydrogen bonding sites. The elimination or reduction of interactions between the glass waveguide surface and glycerol would reduce the waveguide TM_2 mode sensitivity to injected glycerol samples.

The waveguide TM_2 mode intensity responses to four pure bromocresol green samples are labeled as 5, 7, 12, and 16 in Figure 6.7a. Bromocresol green concentration increased with sample number in the range from 5.0×10^{-6} M (#5) to 1.0×10^{-4} M (#16). The TM_2 mode intensity decreased with increasing dye content primarily due to evanescent absorbance. On average, the observed TM_2 mode attenuation was approximately 0.5% higher in the mixture experiment than in the earlier evaluation of similar bromocresol green concentrations (Section 6.3). Thus, the TM_2 mode absorbance response stability was quite good considering that nearly 3 months separated the compared experiments.

The remaining twelve samples were mixtures prepared by the addition of glycerol to bromocresol green stock solutions. In general, the addition of glycerol to bromocresol green solutions produced reductions in TM_2 mode attenuation relative to the corresponding pure dye solution response. The increased cover refractive index resulting from the addition of glycerol produces an increase in the interfacial electric field amplitude, a decrease in the decay constant, and an increase in the TM_2 mode propagation angle. The expected net result would be an increase in the effective evanescent absorbance pathlength of the Ag^+-exchange waveguide TM_2 mode. However, the cover refractive index change also produces a reduction in TM_2 mode coupling efficiency and modulations in mode conversion. As discussed earlier, the empirical nature of mode conversion tends to produce deviations from the expected Ag^+-exchange waveguide response function.

Following a replicate determination of the waveguide response to sample 17, a transient air bubble was accidentally flushed through the flow cell. Despite the averaging of triplicate sample runs, the TM_2 mode intensity reduction ($\approx$3.0%) was still apparent in

Figure 6.7a indicating moderate TM_2 mode sensitivity to the large transient cover refractive index perturbation.

The Ag^+-exchange waveguide TM_1 and TM_0 mode intensity response to mixture samples is given in Figure 6.7b. As observed for the TM_2 mode, the waveguide TM_1 mode intensity did not change appreciably in response to injected glycerol samples less concentrated than about 6.0 g/L. The evanescent absorbance of TM_1 mode intensity was observed to increase with increasing bromocresol green concentration. The Ag^+-exchange waveguide TM_1 mode attenuation was observed to decrease slightly for small additions of glycerol (≈6.5 g/L) to bromocresol green stock samples. For mixture samples with larger glycerol content, the TM_1 mode exhibited an increase in intensity loss relative to the bromocresol green stock attenuation. The movement of an air bubble over the waveguide surface produced a large modulation (>30%) in the TM_1 mode intensity.

The Ag^+-exchange waveguide TM_0 mode exhibited a significant reduction in intensity with increasing glycerol concentration. An apparent response to a 10^{-4} change in cover refractive index was obscured by the unstable TM_0 mode baseline intensity. Injections of bromocresol green samples produced large TM_0 mode intensity losses presumably due to evanescent absorbance. The TM_0 mode absorbance increased with increasing dye concentration. The TM_0 mode absorbance response was enhanced considerably over that observed in the earlier bromocresol green experiment showing an average increase in attenuation of nearly 2.0%. Also, for a given stock bromocresol green concentration, the waveguide TM_0 mode attenuation increased monotonically with increasing glycerol content.

The waveguide multiple mode response to cover refractive index changes has a significant dependence on the absolute refractive index and composition of the carrier solution. In the mixture experiment, the inverse relationship between the TM_2 and TM_0 mode intensities was not directly observed for index increases relative to a phosphate buffer carrier solution. The waveguide bromocresol green response produced similar results as observed earlier but with significant enhancements in TM mode absorbance sensitivities. In general, the waveguide multiple mode response to mixture samples appears to be a convolution of TM_2 mode resonance coupling, mode conversion and evanescent absorbance effects.

The analytical performance of the Ag^+-exchange waveguide in the glycerol-bromocresol green experiment is summarized in Table 6.6. The LOD and experimental precision indicated significantly higher system noise than observed in either the glycerol or bromocresol green experiment. Thus, the enhanced absorbance sensitivity of the TM modes in the mixture experiment comes at the expense of increased uncertainty in sample response. This was especially true for the waveguide TM_1 and TM_0 modes which were populated by mode conversion.

6.4.1.2 TM Mode Position Shifts

The Ag^+-exchange waveguide TM_2 mode position shift response to glycerol-bromocresol green mixture samples is presented in Figure 6.8a. The positive FWHM TM_2 mode response to glycerol samples indicates an increase in mode propagation angle. A TM_2 mode position shift is observed for cover refractive index changes starting at 3.0×10^{-4} (2.8 g/L glycerol). The transient TM_2 mode position shift profiles are symmetric without any indications of a shoulder as observed in the glycerol FWHM difference plot (Figure 6.2a). Thus, the partitioning of glycerol into the waveguide glass stationary phase is largely eliminated by cationic components in the phosphate buffer carrier solution.

A TM_2 position shift response to pure bromocresol green samples was not observed until a concentration of 5.0×10^{-5} M was reached. The anomalous dispersion response for the 5.0×10^{-5} M and 1.0×10^{-4} M bromocresol green samples produced small negative TM_2 mode FWHM differences. Thus, the waveguide response to high concentration bromocresol green samples produced a decrease in TM_2 mode propagation angle. The decrease in TM_2 mode propagation angle runs counter to the response expected from a consideration of the resonance condition and the earlier bromocresol green experiments.

The TM_2 mode position shift responses to mixture samples were mostly free from the effects of evanescent absorbance. For mixture solutions made from high bromocresol green concentration stock solutions, the increase in TM_2 mode propagation angle was slightly reduced compared to the pure glycerol response. The large transient decrease in cover refractive index cause by the introduction of an air bubble induced a significant decrease in the TM_2 mode propagation angle. Again, the effect is reduced due to the presentation of an average position shift response profile.

The waveguide TM_0 mode position shift response to mixture samples is given in Figure 6.8b. The TM_0 mode position shift response to pure glycerol samples gave negative FWHM differences indicating a decrease in the TM_0 mode propagation angle. The magnitude of TM_0 mode propagation angle changes were relatively insensitive to increases in glycerol concentration in the range from 2.8 g/L to 8.6 g/L. Pure bromocresol samples did not produce a discernible TM_0 mode position shift response. The TM_0 mode response to mixture samples was dependent on sample glycerol content for low dye concentration samples. The effective increase in TM_0 mode propagation angle due to the glycerol sample component was reduced for samples prepared in high bromocresol green concentration stock solutions. The position of the outcoupled TM_1 mode did not vary significantly in response to samples in the mixture data set.

6.4.1.3 Ag^+-Exchange Waveguide Response

Pure glycerol solutions produced little attenuation in apparent TM_2 mode resonance coupling efficiency despite the observed changes in TM_2 mode propagation angle. However, the transfer of intensity from the waveguide TM_2 mode to the TM_0 mode via mode conversion was very sensitive to cover refractive index changes. The increase crosstalk between the TM_2 and TM_0 modes occurred despite the observed increase in separation between respective mode propagation angles with increasing cover refractive index.

The waveguide multiple TM mode intensity response to pure bromocresol green samples produced increasing attenuation with increasing dye concentration. For high bromocresol green concentrations, a small increase in the TM_2 mode propagation angle indicated a refractive index response due to anomalous dispersion.

For mixture samples, the Ag^+-exchange waveguide TM_2 mode absorbance sensitivity for a given dye concentration did not produce an obvious trend with increasing sample glycerol concentration. In contrast, the TM_0 mode absorbance sensitivity increased with increasing glycerol concentration which is consistent with the observed decrease in TM_0 mode propagation angle. The TM_1 mode absorbance behavior was similar to that of the TM_2 mode except for large cover refractive index changes. The Ag^+-exchange waveguide multiple mode response to mixture samples produced a complicated combination of resonance coupling, mode conversion, evanescent absorbance and mode position shift effects.

6.4.2 Multivariate Analysis

6.2.2.1 Singular Value Decomposition

Prior to performing a SVD, mode images describing the waveguide air bubble response was removed from the data set. The first principal component for the remaining data describes 77.84% of the total experimental variance observed in the waveguide multiple mode response to mixture samples. The corresponding loading plot (Figure 6.9a) indicated variance contributions from each waveguide TM mode. The shape and position of the variance distributions reflect those of the TM modes in the original baseline mode image. The score plot (Figure 6.9b) reveals that the described loading variance had little predictive ability for pure glycerol samples. However, each bromocresol green sample gave a baseline resolved, transient score response which increased in amplitude with increasing dye concentration. The score response to mixture samples indicated a modulation in amplitude with respect to the corresponding pure bromocresol green sample response. The response of samples with a given dye concentration was not monotonic with the addition of an increasing amount of glycerol. The preservation of mode positions and peak shapes and the correlated decrease in mode intensities was similar behavior as was observed in the bromocresol green experiment. Thus, the first principal component describes the modulation in waveguide TM mode intensities associated with evanescent absorbance from glycerol-bromocresol green mixture samples.

The second principal component describes 14.80% of the remaining experimental variance observed in the waveguide response to mixture samples. The loading plot (Figure 6.10a) indicated an inverse variance relationship between the TM_2 and TM_0 modes. The TM_1 mode contributed little variance to the loading plot. The TM_2 mode variance was offset from its original position whereas the TM_0 mode variance distribution was positioned the same as in the baseline image. The score plot (Figure 6.10b) clearly identified a response to the four pure glycerol samples which was monotonic with increasing glycerol concentration. The score responses to pure bromocresol green samples were likewise monotonic with increasing dye concentration but were inversely related to the glycerol responses. Mixtures of the two components resulted in a score response intermediate between the pure component responses. For samples with a common dye concentration, the response increased with increasing glycerol content.

The inverse variance relationship between the Ag^+-exchange waveguide TM_2 and TM_0 modes was a signature response observed earlier in the glycerol experiment. However, in the mixture experiment, the TM_2 mode variance indicated a contribution from TM_2 mode position shifts. Thus, the second principal component describes mode intensity and positional variances associated with cover refractive index changes. Again, these variances arise from modulations in TM_2 mode resonance coupling efficiency, mode conversion, and mode propagation angles.

The third principal component describes 1.95% of experimental variance observed in the waveguide response to mixture samples. The TM_1 mode was the largest variance source described by the loading plot (Figure 6.11a). The TM_1 mode variance was inversely related to that of the TM_2 and TM_0 modes. In the score plot (Figure 6.11b), the glycerol solution response reached a limiting level for the 8.6 g/L sample which resulted in the inversion of the transient response profile. The bromocresol green samples were poorly resolved from the baseline and were inversely related to the glycerol variance. Mixture samples gave responses intermediate between the pure glycerol and bromocresol green responses.

In the previous glycerol experiment, the TM_1 mode variance and position shift information was absent from the first principal component but included in the second and third. Similarly, in the mixture experiment, the TM_1 mode variance was not described in the second principal component but appears in the third. The third principal component captures the waveguide TM_1 mode intensity variations resulting from modulations in cover refractive index. The TM_1 mode intensity changes reflect the effects of bulk refractive index modulations on the process of mode conversion.

From a discussion of the first three principal components, the value of a multivariate data analysis approach is quite obvious as it permits the extraction of variance highly correlated to each mixture component. The first principal component primarily describes variance associated with waveguide mode evanescent coupling to the bromocresol green component. The second and third components identify variance primarily related to the glycerol component. The additional anomalous cover refractive index changes produced by high bromocresol green concentrations are inversely related to the waveguide glycerol response. Thus, the prediction of glycerol and bromocresol green in mixture solutions should be possible using a multivariate technique such as PLS.

The remaining 5.41% of system variance is not concentrated in one or two additional principal components as was common in the glycerol and bromocresol green model systems. Rather, the variance contributions of additional principal components in the mixture experiment taper off very slowly. The inclusion of significant variance in a large number of principal components highlights the limitations of fitting a linear multivariate analysis to an admittedly non-linear waveguide response. The interpretation of additional variance beyond the three principal components described is neither simple nor informative.

6.4.2.2 Partial Least Squares Calibration

Four steady-state multiple mode waveguide images were extracted from each sample block and averaged. The multiple mode waveguide responses were included with known glycerol and bromocresol green concentrations to perform a PLS calibration. The

RMSECV statistic for the first six calibration factors is provided in Table 6.7. For a five factor calibration model, a RMSECV value of 0.26 g/L glycerol is obtained which corresponds to a refractive index change of $2.9\text{x}10^{-5}$ relative to the phosphate buffer carrier. The five factor PLS calibration also gives a RMSECV value of $4.02\text{x}10^{-6}$ M for bromocresol green.

The glycerol experiment and bromocresol green experiments gave RMSECV values of 0.14 g/L and $2.24\text{x}10^{-6}$ M respectively. The results obtained in the mixture experiment are very similar. Thus, the PLS calibration results from the mixture experiment confirm that the multivariate analysis can be used to predict simultaneous changes in refractive index and absorbance. The approach is effective because the waveguide multiple mode intensities and positions are modulated differentially by the two sample components. This multiple component prediction should be possible for any multimode Ag^{+}-exchange planar waveguide device. The effectiveness of a single mode Ag^{+}-exchange waveguide in predicting multiple sample components is questionable at best.

6.5 Surface Active Refractive Index

6.5.1 Univariate Analysis

6.5.1.1 Integrated Intensity

The Ag^{+}-exchange waveguide TM_2 mode intensity response to five consecutive 100 μl injections of three $Pb(NO_3)_2$ samples are presented in Figure 6.12a. The waveguide TM_2 mode intensity decreased in a series of distinguishable steps for consecutive injections of the 10^{-4} M Pb^{2+} sample. The first three injections were marked with a transient increase in TM_2 mode intensity prior to the decrease in intensity. Following each Pb^{2+} injection the TM_2 mode intensity level remained depressed which indicated a non-transient Pb^{2+} response. The non-transient waveguide TM_2 mode response is indicative of an ion-exchange interaction between the anionic waveguide glass phase and Pb^{2+}. Thus, Pb^{2+} remained bound at the glass interface after the solution phase Pb^{2+} was removed from the flow cell. The TM_2 mode intensity response step size varied markedly with each injection. The overall attenuation in TM_2 mode intensity following multiple 10^{-4} M Pb^{2+} sample injections was approximately 30%. There was no evidence indicating that saturation of anionic glass ion-exchange sites had been reached from the accumulative effects of the five sample injections. The baseline TM_2 mode response level was recovered following a single injection of 1.6×10^{-3} M HNO_3. Individual steps were difficult to distinguish for the TM_2 mode response to multiple 10^{-5} M and 10^{-6} M Pb^{2+} sample injections. The overall effect of five injections of these samples was a slight increase in the TM_2 mode intensity relative to baseline.

The literature suggests an estimated silanol site density on an amorphous silica substrate of approximately 4.6 silanols/nm^2.[6] In the Pb^{2+} experiment, the total waveguide surface area interrogated by the propagating modes included about 2.5×10^{13} nm^2. Thus, the detector surface has an estimated 1.2×10^{14} silanol sites which provide potential sites for cation-exchange. However, even at a favorable solution pH (i.e. 7.7), the number of active cation-exchange sites was expected to be 10% to 20% of the total.[7] Therefore, the saturation waveguide response was limited to 20% of a cation monolayer as a best case which would provide for the binding of a total weight of 66.0 ng Pb^{2+}.

For 10^{-4} M Pb^{2+}, each sample injection corresponded to the introduction of 3.31 μg of Pb^{2+} into the flow cell. Thus, the total per injection weight was 50 times the theoretical capacity of the glass ion-exchange surface. As a waveguide TM_2 mode response was observed for each injection, saturation of the waveguide cation-exchange capacity was not reached despite the large relative injection weights. There are a number of potential explanations for the low capture of total injected Pb^{2+}. First, only a fraction of the total injected Pb^{2+} weight was able to diffuse to the waveguide interface at the existing analyte residence time. The Pb^{2+} residence time was limited to about one second by the relatively fast linear flow rate. Second, conditions which were required to enhance the cation-exchange capacity of the glass phase increased the number of potential Pb^{2+} hydrolysis species. Thus, the concentration of free Pb^{2+} was reduced by hydrolysis at the prevalent slightly basic solution pH and large Pb^{2+} sample concentration. Third, the effective surface silanol binding capacity was modified by the binding of Pb^{2+} at the interface. The displacement of H^+ from surface silanol sites by Pb^{2+} reduces the acidity of the waveguide surface. The increasingly basic surface induces further dissociation of protons from silanol sites which produces additional active cation-exchange sites. From this perspective, each Pb^{2+} injection may result in saturation of the existing cation-exchange capacity of the waveguide surface. However, as a result of interfacial Pb^{2+} binding, additional surface cation-exchange sites are activated. In agreement with the literature, the "true" cation-exchange saturation level is reached somewhere between 10% and 20% of a Pb^{2+} monolayer. The variations in TM_2 mode response step-size provides strong evidence that the adsorption of Pb^{2+} at the interface modulates the glass capacity for cation-exchange.

The cation-exchange interaction between the Ag^{+}-exchange waveguide and Pb^{2+} produces a modulation in the TM_2 mode due to the formation of a bound Pb^{2+} surface layer. The result is essentially a modified waveguide layer with a perturbed refractive index profile, n(x)'. The observed attenuation in TM_2 mode intensity for 10^{-4} M Pb^{2+} injections results from the reduced resonance coupling efficiency accompanying changes in the waveguide surface refractive index. Note that the waveguide TM_2 mode sensitivity to adsorbed Pb^{2+} translates to much less than a surface monolayer (<20%).

The increase in TM_2 mode intensity accompanying the first few 10^{-4} M Pb^{2+} injections is also observed as the waveguide response to the 1.0×10^{-5} M and 1.0×10^{-6} M Pb^{2+} samples. The reduced TM_2 mode resonance coupling efficiency expected from a cation-exchange interaction may be obscured by a modulation of mode conversion. The 2×10^{-4} change in cover refractive index associated with the 10^{-4} and 10^{-5} M Pb^{2+} samples may also be a factor in the waveguide TM_2 mode response.

The Ag^{+}-exchange waveguide TM_1 and TM_0 mode intensity response to Pb^{2+} sample injections is given in Figure 6.12b. The TM_1 and TM_0 mode intensity attenuation for multiple injections of 10^{-4} M and 10^{-5} M Pb^{2+} produced step offset from baseline mode intensities. The TM_1 and TM_0 mode were more sensitive than the TM_2 mode for injections of 10^{-4} M Pb^{2+}, exhibiting overall intensity losses of 40% and 35%, respectively. The adsorption responses to injections of 10^{-5} M Pb^{2+} drifted slightly, indicating the release of some exchanged cations. These mode also produced an accumulated decrease in the TM_1 and TM_0 mode intensity for injections of the 10^{-6} M Pb^{2+} sample.

6.5.1.2 TM Mode Position Shifts

The Ag^{+}-exchange waveguide TM_2 mode position shift response to Pb^{2+} samples is given in Figure 6.13a. The TM_2 mode position shift indicated a positive step offset in the FWHM difference baseline with a superimposed transient shift modulation for injections of 10^{-4} M and 10^{-5} M Pb^{2+}. The 10^{-6} M Pb^{2+} produced a positive offset without the transient position shift component. The positive values of FWHM difference indicated an increase in TM_2 mode propagation angles. The expected response based on an modification of the waveguide layer refractive index profile, n(x)', would lead to a decrease in TM_2 mode propagation angle.

The waveguide TM_1 and TM_0 mode position shift response to Pb^{2+} injections is given in Figure 6.13b. The TM_1 mode position shift response described step decreases in

FWHM difference for injections of 10^{-4} M and 10^{-5} M Pb^{2+} samples. The initial response to multiple injections of these samples was a slight increase in FWHM difference. The consecutive 10^{-6} M Pb^{2+} sample injections produced a slight overall decrease in FWHM difference. The overall TM_1 mode position shift response indicated a decrease in mode propagation angle with increasing Pb^{2+} adsorption to the waveguide surface.

The TM_0 mode exhibited a decrease in mode propagation angle for multiple injections of 10^{-4} M Pb^{2+} samples as indicated by the decreasing FWHM difference. The TM_0 mode did not give a significant mode propagation angle change for injections of the more dilute Pb^{2+} samples. Considerable hysteresis was observed in the TM_1 and TM_0 mode position shift responses upon recovery of a baseline response following the first injection of HNO_3.

6.5.1.3 Ag^+-Exchange Waveguide Response

The waveguide TM_2 mode cation-exchange response produced a decrease in resonance coupling efficiency with incremental additions of adsorbed Pb^{2+}. The apparent superimposed effects of mode conversion on the TM_2 mode intensity response to 10^{-4} M Pb^{2+} injections are, in fact, real resonance coupling effects as confirmed by the correlated TM_2 mode propagation angle changes. The transient increase in TM_2 mode intensity and propagation angle may be the result of bulk refractive index effects due to the concentration of non-adsorbed Pb^{2+} near the interface. Another possible explanation is a competitive cation-exchange effect with a less strongly bound cation such $PbOH^+$. Competitive interaction with the waveguide surface would also provide an additional reason for the low capture of injected Pb^{2+} cation by the waveguide cation-exchange surface.

The intensity and position shift responses of the Ag^+-exchange waveguide TM_1 and TM_0 modes follow the expected response trends for the adsorption of Pb^{2+} at the waveguide surface. The reduction in mode intensities was primarily the result of a reduction in TM_2 mode resonance coupling efficiency. The decrease in TM_1 and TM_0 mode propagation angles is consistent with the modified waveguide refractive index profile. Thus, in the Pb^{2+} experiment, the waveguide multiple mode response was adequately described without the need to invoke modulations in mode conversion to explain response deviations.

6.5.2 Multivariate Analysis

The first principal component accounts for 96.12% of the total experimental variance observed in the waveguide response to multiple injections of Pb^{2+} samples. The loading plot (Figure 6.14a) describes different relative variance contributions from the three waveguide TM modes. The TM mode variance exhibits the peak shapes and positions observed in baseline mode images. The score plot (Figure 6.14b) reveals a series of non-transient step-offset responses for consecutive injections of 10^{-4} M and 10^{-5} M Pb^{2+} samples. The magnitude of response steps varies with injection number. Multiple injections of 10^{-6} M Pb^{2+} produced very little change in the score baseline response. A single HNO_3 injection displaced bound Pb^{2+} quickly and without significant hysteresis. The first principal component describes the attenuation of waveguide multiple mode intensities resulting from the adsorption of Pb^{2+} at the waveguide surface.

The next two principal components describe 3.54% and 0.19% of remaining experimental variance respectively. The second principal component describes an inverse relationship between the intensity of the TM_2 mode and the TM_1 and TM_0 modes. The third principal component includes mode variance associated with position shifts.

Over 99% of the experimental variance observed in the Ag^+-exchange waveguide multiple mode response to Pb^{2+} was interpreted as due to mode intensity changes. Not coincidentally, the effects of mode conversion were essentially absent from the waveguide cation-exchange response.

6.6 Surface Active Absorbance

6.6.1 Univariate Analysis

6.6.1.1 Integrated Intensity

The waveguide TM_2 mode intensity responses to 200 μl injections of ten methylene blue samples is presented in Figure 6.15a. Also included for the purpose of comparison is the waveguide TM_2 mode response to 200 μl injections of two bromocresol green samples. The TM_2 mode attenuation was observed to increase with increasing methylene blue concentration due primarily to evanescent absorbance. The minimum TM_2 mode intensity was attained at different delay times depending on methylene blue concentration. For example, the 7.6×10^{-7} M dye sample was retained for 135 seconds compared to 110 seconds for the 1.0×10^{-5} M methylene blue sample. In addition, the transient TM_2 intensity profiles exhibited varying half-minimum widths and considerable tailing. Tailing was most apparent at high methylene blue concentrations ($>10^{-6}$ M) where the response did not reach baseline before the data acquisition block was terminated at 280 seconds after injection. The observed variations in methylene blue retention time, transient profile widths, and profile tailing indicate that the cationic methylene blue molecule was interacting with the waveguide cation-exchange surface. The charge interaction produces partitioning of the methylene blue cation into the glass waveguide stationary phase. The decrease in retention time with increasing concentration reveals that sites on the waveguide cation-exchange surface became saturated which led to a large population of unretained cations at high sample concentrations. Thus, the observed TM_2 mode evanescent attenuation response was the combined effect of absorbance from bound stationary phase and bulk cover phase methylene blue.

Additional evidence for a partitioning interaction can be obtained from a comparison of the waveguide TM_2 mode response to methylene blue and bromocresol green. For bromocresol green injections, Ag^+-exchange waveguide mode attenuation is the result of evanescent absorbance from the bulk cover solution. A direct comparison of the TM_2 mode attenuation indicates that the absorbance resulting from an injection of 2.5×10^{-6} M methylene blue was nearly equivalent to that of 10^{-4} M bromocresol green. Similarly, the 5.0×10^{-6} M methylene blue TM_2 mode absorbance response was similar to the 5.0×10^{-4} M bromocresol green waveguide absorbance. Thus, nearly a two order of magnitude increase in TM_2 mode attenuation was observed for direct comparison of methylene blue to the bromocresol green response. This despite only a factor of two difference in the measured molar extinction coefficients of the two dye molecules.

The Ag^+-exchange waveguide TM_1 and TM_0 mode intensity response to methylene blue is given in Figure 6.15b. The TM_1 and TM_0 mode intensities also decreased monotonically with increasing methylene blue concentration. The transient profile features described for the TM_2 mode are reproduced by the Ag^+-exchange waveguide TM_1 and TM_0 mode intensity responses to methylene blue. The interaction of methylene blue with the waveguide surface did not effect the relative order of mode sensitivities as they were the same as for the bromocresol green response. However, in the bromocresol green experiment, the TM_2 and TM_1 mode evanescent path lengths were nearly identical whereas the methylene blue results indicated a greater difference in absorbance path lengths between the two modes.

The analytical performance of the Ag^+-exchange planar waveguide intensity response to methylene blue samples is summarized in Table 6.8. The increased LOD and reduced experimental precision for the evaluation of analytes which interact strongly with the anionic waveguide surface are general trends observed in the Pb^{2+} and methylene blue experiment.

The absorbance of methylene blue samples was determined in a 1 cm pathlength transmission measurement for comparison with the waveguide TM mode absorbance responses. The waveguide TM mode attenuation responses were plotted vs spectrophotometer absorbance. The relationship was linear over the narrow concentration range from 2.5×10^{-6} M to 1.0×10^{-5} M methylene blue. The effective evanescent path lengths of each waveguide TM mode were obtained as the slopes of the corresponding lines. The slopes were normalized to a mode propagation distance of 1 cm and are given in Table 6.9. The TM mode effective evanescent absorbance path lengths attainable for the evaluation of molecules which interact with the waveguide surface are significant and approach free wave transmission path lengths.

6.6.1.2 TM Mode Position Shifts

The waveguide TM_2 mode position shift response to methylene blue samples is given in Figure 6.16a. The positive TM_2 mode FWHM difference for concentrations above 2.5×10^{-6} M methylene blue indicates an increase in mode propagation angle. The TM_2 mode position shift profiles exhibit differences in maximum response times and profile widths at half-maximum with varying methylene blue sample concentration. The partitioning of methylene blue into the waveguide glass stationary phase is the primary mechanism responsible for the waveguide TM_2 mode position shift response. At 2.5×10^{-5} M methylene blue, the peak shift response reaches a steady-state indicating that saturation of the waveguide surface capacity for adsorbed methylene blue is maintained. The adlayer formed is transient in that the removal of bulk phase methylene blue from the flow cell is accompanied by desorption of dye from the surface. The overall FWHM difference is depressed somewhat from the lower concentrations perhaps indicating an effect due to anomalous dispersion at the high dye concentrations. The FWHM difference increase resulting from the transient modification in the waveguide layer, $n(x)'$, would be partially offset by an anomalous decrease in cover refractive index at 632.8 nm.

A reproducible, sharp peak shift feature marks the leading edge of the 2.5×10^{-5} M and 6.4×10^{-5} M methylene blue response profiles. Unfortunately, the waveguide adlayer response was collected with insufficient time resolution to better characterize this sharp feature. The sharp transient increases with increasing methylene blue concentration and may be related to the kinetics of adlayer formation. The feature was not observed until after the waveguide was pretreated with an saturation dye layer from exposure to the first 2.5×10^{-5} M methylene blue injection.

The 5.0×10^{-4} M bromocresol green sample also gave a TM_2 mode peak shift response. However, the bromocresol green peak shift response was unrelated to the interaction of the dye molecule with the surface. For bromocresol green, the TM_2 mode position shift response resulted from an increase in cover refractive index due to anomalous dispersion at 632.8 nm.

The Ag^+-exchange waveguide TM_1 and TM_0 position shift responses to methylene blue samples are given in Figure 6.16b. Waveguide exposure to methylene blue samples produces a relatively insignificant TM_1 mode position shift response. The transient response profiles are very different depending on methylene blue sample concentration.

The negative waveguide TM_0 mode FWHM difference response indicates a decrease in mode propagation angle. Despite the inverse relationship between TM_2 and TM_0 mode propagation angles, the TM_2 and TM_0 mode response profiles exhibit similar features. Variations in TM_0 position shift maximum response times, half-maximum widths, and profiles shapes are observed. Thus, the decrease in TM_0 mode propagation angle is the result of a modification in the waveguide layer refractive index profile associated with partitioning of methylene blue at the waveguide interface. Again, the TM_0 mode response to high methylene blue concentrations indicated the formation of a surface saturation dye adlayer. The maximum TM_0 mode position shift responses are delayed even further than the maximum TM_2 mode responses. Presumably the TM_0 mode evanescent field is confined closer to the interface and, therefore, observes a slower average transit of material across the waveguide surface than the TM_2 mode. The TM_0 mode position shift response for the injection of 5.0×10^{-4} M bromocresol green was due to anomalous dispersion.

6.6.1.3 Ag^+-Exchange Waveguide Response

The partitioning of methylene blue at the Ag^+-exchange waveguides significantly enhances the evanescent absorbance path lengths of the TM modes. The three TM modes exhibited the same transient features due to evanescent attenuation of mode intensity. The dye interaction with the waveguide surface also generated a transient adlayer which produced a modified waveguide layer refractive index profile. The perturbation in interfacial refractive index produced changes in the TM_2 and TM_0 mode propagation angles. As in the Pb^{2+} adlayer response, the methylene blue partitioning response (position shift) of the TM_2 and TM_0 modes were inversely related.

6.6.2 Multivariate Analysis

6.6.2.1 Singular Value Decomposition

The first principal component accounts for 99.66% of the total experimental variance observed in the Ag^+-exchange waveguide multiple mode response to methylene blue samples. The loading plot (Figure 6.17a) indicates variance contributions from each waveguide TM mode. In general, the mode peak shapes and positions in the baseline multiple mode images are maintained in the loading plot. The transient response profiles in the corresponding score plot (Figure 6.17b) indicate considerable tailing and exhibit maximum score responses at different delay times. Clearly, the first principal component describes evanescent attenuation of intensity from all three waveguide TM modes due to coupling to the methylene blue molecule.

The next two principal components describe 0.28% of the remaining experimental variance in the methylene blue experiment. The second and third principal component loading plots include variance which describes both TM mode intensity and position shifts. The corresponding score plots exhibit complicated temporal response profiles and lend little insight into the source of waveguide response variance.

6.6.2.2 Partial Least Squares Calibration

Shifting maximum response times complicated the definition of steady-state response times. Thus, six waveguide multiple mode responses were extracted from the data block for each sample and averaged. The average responses were combined with known sample concentrations as input into a PLS calibration. The RMSECV statistic for the first six calibration factors is given in Table 6.10. For a five factor calibration model, the PLS calibration gives a RMSECV of $2.88\text{x}10^{-6}$ M methylene blue. Note that the minimum RMSECV values are similar for the bromocresol green and methylene blue data set. This occurred because the enhancement in methylene blue absorbance due to glass partitioning was not a significant effect at low dye concentrations.

6.7 Temperature

6.7.1 Univariate Analysis

6.7.1.1 Integrated Intensity

The Ag^+-exchange waveguide TM_2 mode intensity response to controlled heating and cooling of the substrate is presented in Figure 6.18a. The TM_2 mode coupling conditions were optimized under ambient conditions, corresponding to a temperature of 22.8 °C. However, the actual temperature range tested was from 25.5 °C to 33.0 °C.

Thus, the experiment was conducted in a temperature range displaced 2.7 °C to 10.2 °C from the temperature of optimum TM_2 mode coupling.

From an initial steady-state 26.6 °C waveguide response, the time trace described the variation in TM_2 mode intensity as step changes in temperature were induced. In producing a step increase in temperature, the transient heating curve was a convolution of the peltier heater performance and the thermal characteristics of the waveguide structure. Substrate heating resulted in a sharp decrease in the TM_2 mode intensity towards a minimum which was reached 45 seconds after the peltier heater was reset to the higher temperature. The TM_2 mode intensity then increased slowly towards to a steady-state intensity level which was reached between 4 to 8 minutes after the step temperature change was induced.

A step reduction in temperature produced the opposite TM_2 mode intensity response behavior. The transient cooling curve reflects the kinetics of waveguide cooling as the peltier device automatically shut down until the feedback sensor indicated the set temperature. The sharp, transient increase in TM_2 mode intensity accompanying the decrease in temperature reached a maximum after 45 seconds. The TM_2 intensity then decreased towards a steady-state reached between 4 and 8 minutes after the step change in temperature was triggered. In general, the time to reach a steady-state was larger when the peltier device was heating the substrate rather than when the waveguide was cooling. The sharp transient TM_2 intensity response had an apparent dependence on the magnitude of the induced temperature changes. Thus, larger temperature steps produced transient TM_2 mode responses with qualitatively larger amplitudes.

The sharp transient in waveguide TM_2 mode intensity to step temperature changes resulted from the kinetics of heating and cooling the substrate, waveguide, and cover layers. The transient was not an artifact of peltier performance as the direct measurement of substrate temperature confirmed smooth, monotonic heating and cooling to set temperatures. It should be kept in mind that the waveguide was being heated by contact with the substrate while the TM_2 waveguide mode was confined to the waveguide layer on the opposite face of the microslide. The sharp leading edge temperature response described the time necessary to heat or cool the planar waveguide to a uniform temperature which was approximately 45 seconds. A change in the temperature of the waveguide layer produced a variation in the refractive index of the substrate and waveguide layer. The TM_2 mode intensity response reflects the modulation in mode resonance coupling efficiency associated with temperature induced waveguide refractive index changes. In general, the resonance coupling efficiency should increase as the temperature approaches the 22.8 °C temperature at which optimum coupling was defined.

The slow intensity variation from the sharp minimum or maximum to a steady-state level described the transfer of heat between the waveguide surface and cover solution. The change in temperature of the cover modified the refractive index, thereby modulating the refractive index contrast at the waveguide-cover interface. As a result, the TM_2 mode coupling angle changes and a further variation in mode resonance coupling efficiency was observed. The TM_2 mode resonance coupling modulation caused by cover refractive index partially offsets the coupling efficiency change associated with heating or cooling of the waveguide structure.

The steady-state TM_2 mode intensity level described the equilibrium Ag^+-exchange waveguide response at the indicated substrate temperature. The first scan across the defined temperature range did not produce steady-state TM_2 mode intensity levels which were consistent with subsequent temperature scans. However, following the original temperature scan, the TM_2 mode intensity to a given substrate temperature was highly reproducible. There was no evidence that the effect was the result of waveguide performance. Rather the heating effect was thought to be the result of inconsistent contact between the heater leads and the waveguide device. Stopcock grease was applied to thermoelectric heater and thermocouple contacts with the waveguide assembly to eliminate air gaps and facilitate the transfer of heat between surfaces. Reproducible contact apparently required an initial scan across the temperature range of interest. The well-resolved waveguide TM_2 mode intensity step for a 0.5 °C change in substrate temperature gave an indication of the temperature sensitivity of the Ag^+-exchange device.

The intensity response of the TM_1 and TM_0 waveguide modes to the same step changes in substrate temperature are given in Figure 6.18b. The temporal traces reveal similar features and trends as discussed in connection with the TM_2 mode temperature response. However, the intensity responses of the TM_1 and TM_0 modes were of reduced magnitude and were poorly reproduced even after the initial temperature cycle across the tested range. As the TM_1 and TM_0 modes were not directly coupled at the input grating yet exhibit the same features as observed in the waveguide TM_2 mode temperature response, it would appear that modulations in mode conversion do not appreciably contribute to the temperature response. Thus, the overall intensity propagating within the TM_1 and TM_0 modes were primarily related to variations in TM_2 mode resonance efficiency accompanying changes in device temperature.

The analytical performance of the Ag^+-exchange waveguide response to step changes in temperature is summarized in Table 6.11. The poor estimated experimental precision was heavily influenced by results from the initial temperature scan. As described, the waveguide temperature response reproducibility improved markedly after the initial scan through the tested temperature range.

6.7.1.2 TM Mode Position Shifts

The Ag^+-exchange waveguide TM_2 mode position shift response to induced temperature changes is given in Figure 6.19a. The position shift response had similar features as were described in the waveguide TM_2 mode intensity response. Again, sharp transients marked the beginning of each waveguide position shift response to a step change in temperature. The transient described the variation in TM_2 mode propagation angle as the waveguide and cover solution were heated or cooled to a uniform temperature. In the TM_2 mode position shift profiles, the transient cover solution heating response occurred significantly faster than the cooling response. This was not surprising since cooling relies on loss of heat to the ambient environment whereas heating was driven by the peltier device.

In general, the steady-state TM_2 mode FWHM difference response increased with increasing substrate temperature. The exception was the temperature step from 25.5 °C to 26.0 °C which resulted in a decrease in FWHM difference. The positive waveguide TM_2 mode FWHM difference response indicated an increase in TM_2 mode propagation angle with increasing temperature. Although the steady-state TM_2 mode position shift response exhibited considerable noise, the steady-state response levels for replicate scans of a common temperature were reproducible following the initial scan of the temperature range.

The waveguide TM_1 and TM_0 mode position shift responses to step changes in substrate temperature are presented in Figure 6.19b. The mode position shift profiles exhibit the same features observed in the TM_2 mode intensity and position shift profiles. The TM_1 and TM_0 mode FWHM difference traces follow the transient changes in temperature induced in the waveguide layer and the water cover solution. A step change in temperature produced a displacement from one steady-state response level to another. The general trend observed was an increase in TM_1 and TM_0 mode propagation angles with increasing substrate temperature. The peak shift reproducibility and the overall noise level was reduce for both the TM_1 and TM_0 modes relative to the TM_2 mode position shift response. The reproducibility in temperature response improved markedly after the initial temperature scan across the tested range.

6.7.1.3 Ag^+-Exchange Waveguide Response

The application of a step change in substrate temperature produced a modulation in the refractive index of the waveguide structure and the cover solution. The prevalent temperature gradient across the structure defined transient boundary conditions for mode propagation. Transient boundary conditions produced variations in the TM_2 mode propagation angle which were observed as position shifts on the array detector. In turn, the variations in the TM_2 mode propagation angle produced modulations in the TM_2 mode resonance coupling efficiency at the incoupling grating. The attainment of a uniform temperature produced a steady-state TM_2 mode intensity and position shift response level. The TM_2 mode intensity and position shift response trends to step temperature changes were reproduced by the TM_1 and TM_0 modes. Curiously, the effects of modulated mode conversion were not observed in the univariate temperature response data even though cover index changes were induced.

6.7.2 Multivariate Analysis

6.7.2.1 Singular Value Decomposition

The first principal component describes 96.47% of the total experimental variance observed in the waveguide response to step changes in substrate temperature. The loading plot (Figure 6.20a) describes variance contributions from all three TM modes. The waveguide TM_2 mode temperature response variance is primarily encoded as a modulation in mode intensity. The variance contributions from the TM_1 and TM_0 modes indicate shifts in position relative to baseline. The score plot (Figure 6.20b) reproduces trends discussed earlier with regards to the waveguide intensity and position shift responses. Step changes in substrate temperature cause transient heating and cooling responses which eventually reach stable, steady-state response levels. After scanning the tested temperature range, the score response levels to a common temperature were very reproducible.

The first principal component describes variance associated with the coupled TM_2 mode intensity and the propagation angles of all three waveguide TM modes. The TM_2 mode intensity is modulated by changes in resonance coupling efficiency at the incoupling grating. The shift in allowed mode propagation angles responsible for the reduction in TM_2 coupling efficiency are transduced as mode position shifts in the plane of the array detector. These effects are manifestations of the same resonance phenomenon and thus exhibit highly correlated responses to temperature induced refractive index changes.

The next three principal components describe 2.92% of the remaining experimental variance observed in the waveguide response to changes in substrate temperature. The second principal component describes additional variance associated with the redistribution of mode intensity to increased mode propagation angles. The third principal component includes variance indicating an inverse relationship between the TM_1 and TM_0 mode which is commonly observed as an effect of mode conversion. The fourth principal component primarily describes a position shift in the coupled TM_2 mode.

6.7.2.2 Partial Least Squares Calibration

The steady-state waveguide multiple mode response to each temperature tested was defined as an average of 90 or 100 image scans. The replicate determinations of the waveguide response to 25.5 °C, 28.0 °C, 30.5 °C, and 33.0 °C were included as separate measurements. The average multiple mode images were combined with measured substrate temperatures to perform a PLS calibration. The RMSECV statistic for the first six calibration factors is given in Table 6.12. For a four factor model, the PLS calibration gives a RMSECV of 0.12 °C. This was for calibration of the Ag^+-exchange waveguide multiple TM mode response over the temperature range from 25.5 °C to 33.0 °C.

6.8 Notes to Chapter 6

(1) Personick, S. D. *Bell Syst. Tech. J.* **1971**, 50(3), 843-859.

(2) Attridge, J. W.; Leaver, K. D.; Cozens, J. R. *J. Phys. E: Sci. Instrum.* **1987**, 20(5), 548-553.

(3) Attridge, J. W.; Cozens, J. R.; Leaver, K. D.; Webster, N. L. *J. Lightwave Tech.* **1985**, LT-3(5), 1084-1091.

(4) Meltz, G.; Dunphy, J. R.; Morey, W. W.; Snitzer, E. *Appl. Opt.* **1983**, 22(3), 464-476.

(5) Cozens, J. R.; Boucouvalas, A. C. *Electron. Lett.* **1982**, 18(3), 138-140.

(6) deBoer, J. H.; Vleeskens, J. M. *Proc. Koninkl. Ned. Akad. Wetenschap. Ser. B* **1958**, 61, 2-11.

(7) Smith, R. L.; Pietrzyk, D. J. *Anal. Chem.* **1984**, 56(4), 610-614.

Table 6.1 Analytical performance of the Ag^+-exchange waveguide multiple mode intensity response to glycerol samples.

Table 6.1

Mode	LOD	Est. Precision
TM_2	0.22%	0.17%
TM_1	0.39%	0.12%
TM_0	0.48%	0.14%

Table 6.2 Results of a partial least squares calibration on the Ag^+-exchange waveguide multiple mode response to glycerol samples.

Table 6.2

Principal Component	RMSECV
1	3.43 g/L
2	0.55 g/L
3	0.41 g/L
4	0.26 g/L
5	0.14 g/L
6	0.10 g/L

Table 6.3 Analytical performance of the Ag^+-exchange waveguide multiple mode intensity response to bromocresol green samples.

Table 6.3

Mode	LOD	Est. Precision
TM_2	0.30%	0.14%
TM_1	0.30%	0.12%
TM_0	0.44%	0.18%

Table 6.4 Ag^+-exchange waveguide TM mode effective evanescent absorbance path lengths for the bromocresol green model system normalized to a grating separation of 1 cm.

Table 6.4

Mode	corr. coef.	y-int	slope (cm)
TM_2	0.982	8.34×10^{-4}	0.0077
TM_1	0.986	1.14×10^{-3}	0.0088
TM_0	0.993	7.22×10^{-4}	0.0089

Table 6.5 Results of a partial least squares calibration on the Ag^+-exchange waveguide multiple mode response to bromocresol green samples.

Table 6.5

Principal Component	RMSECV
1	3.64×10^{-6} M
2	2.48×10^{-6} M
3	2.32×10^{-6} M
4	2.24×10^{-6} M
5	2.24×10^{-6} M
6	2.23×10^{-6} M

Table 6.6 Analytical performance of the Ag^+-exchange waveguide multiple mode intensity response to glycerol-bromocresol green mixture samples.

Table 6.6

Mode	LOD	Est. Precision
TM_2	0.52%	0.21%
TM_1	0.60%	0.30%
TM_0	1.87%	0.60%

Table 6.7 Results of a partial least squares calibration on the Ag^+-exchange waveguide multiple mode response to glycerol-bromocresol green mixture samples.

Table 6.7

Principal Component	Glycerol RMSECV	Bromocresol Green RMSECV
1	0.638 g/L	6.25×10^{-6} M
2	0.469 g/L	5.65×10^{-6} M
3	0.300 g/L	4.10×10^{-6} M
4	0.250 g/L	4.26×10^{-6} M
5	0.260 g/L	4.02×10^{-6} M
6	0.304 g/L	3.95×10^{-6} M

Table 6.8 Analytical performance of the Ag^+-exchange waveguide multiple mode intensity response to methylene blue samples.

Table 6.8

Mode	LOD	Est. Precision
TM_2	0.44%	0.53%
TM_1	0.69%	0.71%
TM_0	1.33%	1.21%

Table 6.9 Ag^+-exchange waveguide TM mode effective evanescent absorbance path lengths for the methylene blue model system normalized to a grating separation of 1 cm.

Table 6.9

Mode	corr. coef.	y-int	slope (cm)
TM_2	0.988	-0.139	0.52
TM_1	0.987	-0.094	0.36
TM_0	0.992	-0.144	0.58

Table 6.10 Results of a partial least squares calibration on the Ag^+-exchange waveguide multiple mode response to methylene blue samples.

Table 6.10

Principal Component	RMSECV
1	1.30×10^{-5} M
2	9.42×10^{-6} M
3	3.81×10^{-6} M
4	3.03×10^{-6} M
5	2.88×10^{-6} M
6	3.17×10^{-6} M

Table 6.11 Analytical performance of the Ag^+-exchange waveguide multiple mode response to temperature modulations.

Table 6.11

Mode	LOD	Est. Precision
TM_2	0.65%	1.84%
TM_1	0.83%	2.04%
TM_0	0.77%	1.14%

Table 6.12 Results of a partial least squares calibration on the Ag^+-exchange waveguide multiple mode response to step temperature changes.

Table 6.12

Principal Component	RMSECV
1	0.484 °C
2	0.201 °C
3	0.155 °C
4	0.121 °C
5	0.124 °C
6	0.151 °C

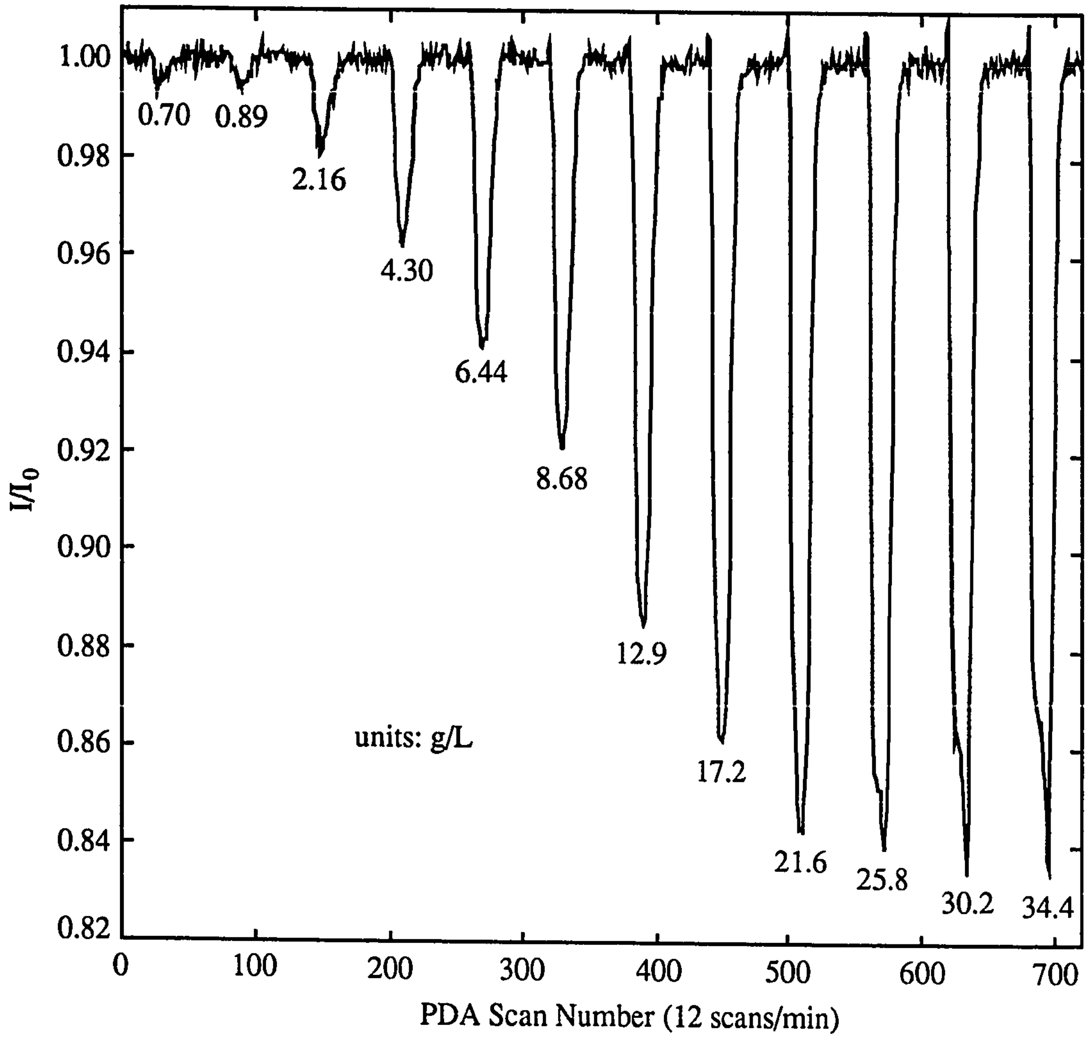

Figure 6.1a Ag^+-exchange waveguide 9C TM_2 mode integrated intensity response to glycerol samples.

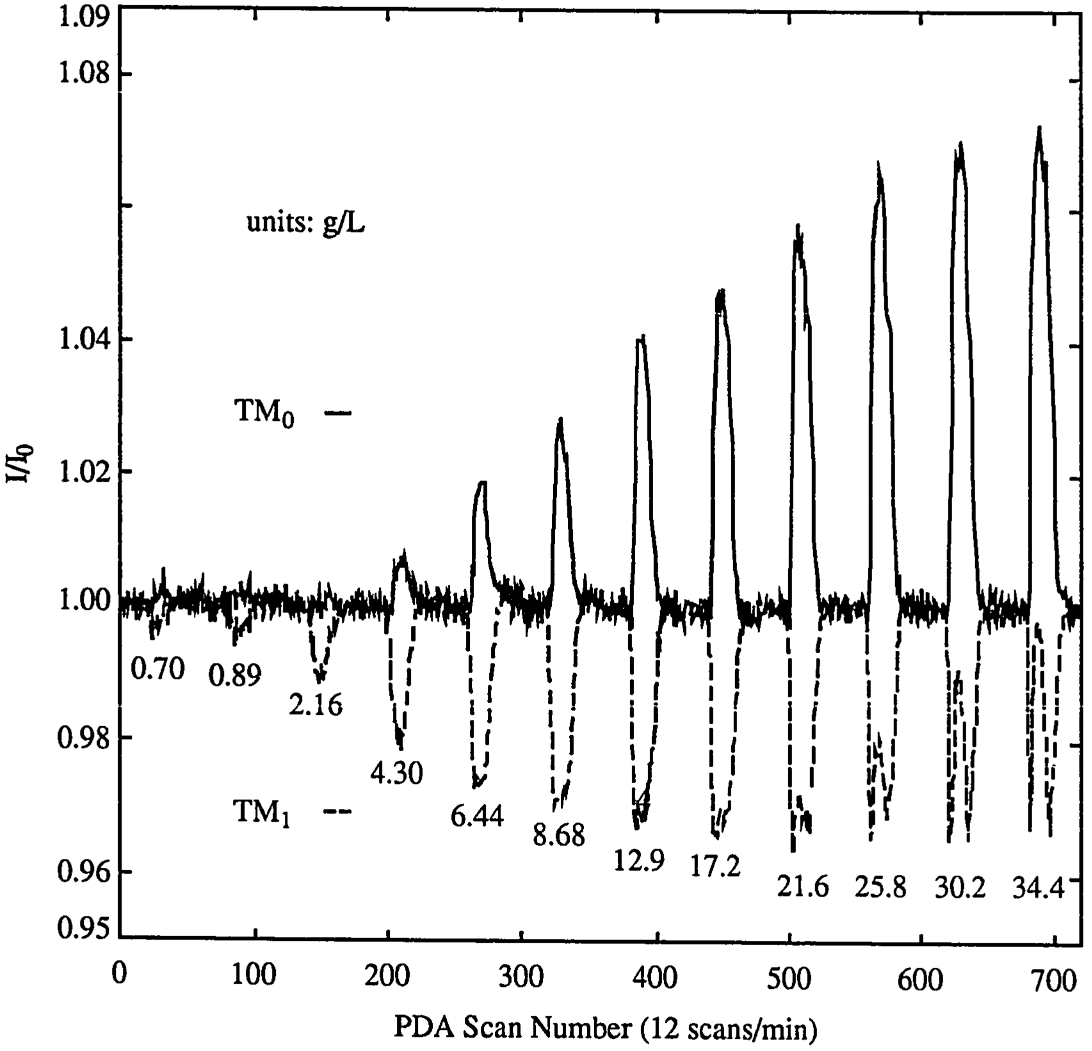

Figure 6.1b Ag$^+$-exchange waveguide 9C TM$_1$ and TM$_0$ mode integrated intensity response to glycerol samples.

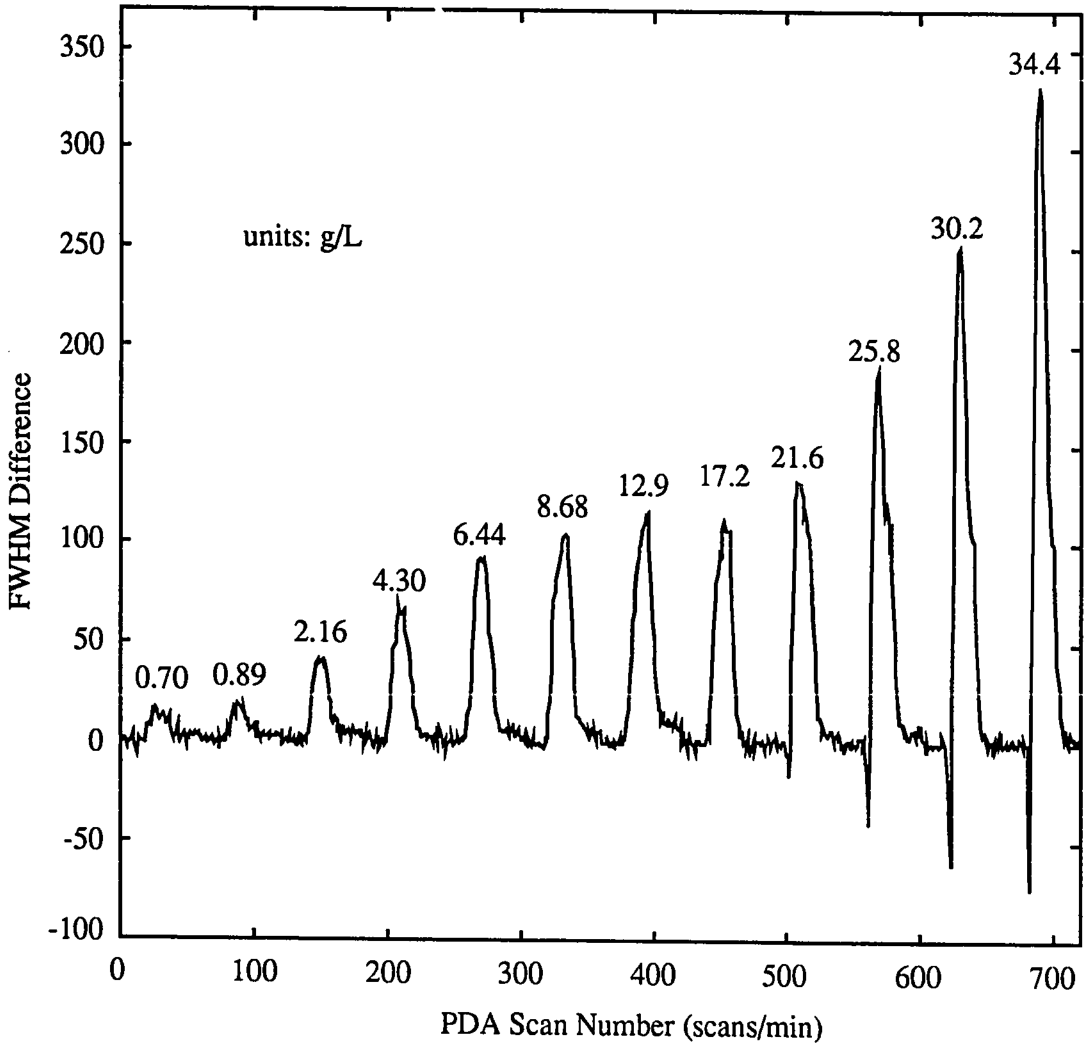

Figure 6.2a Ag$^+$-exchange waveguide 9C TM$_2$ mode position shift response to glycerol samples.

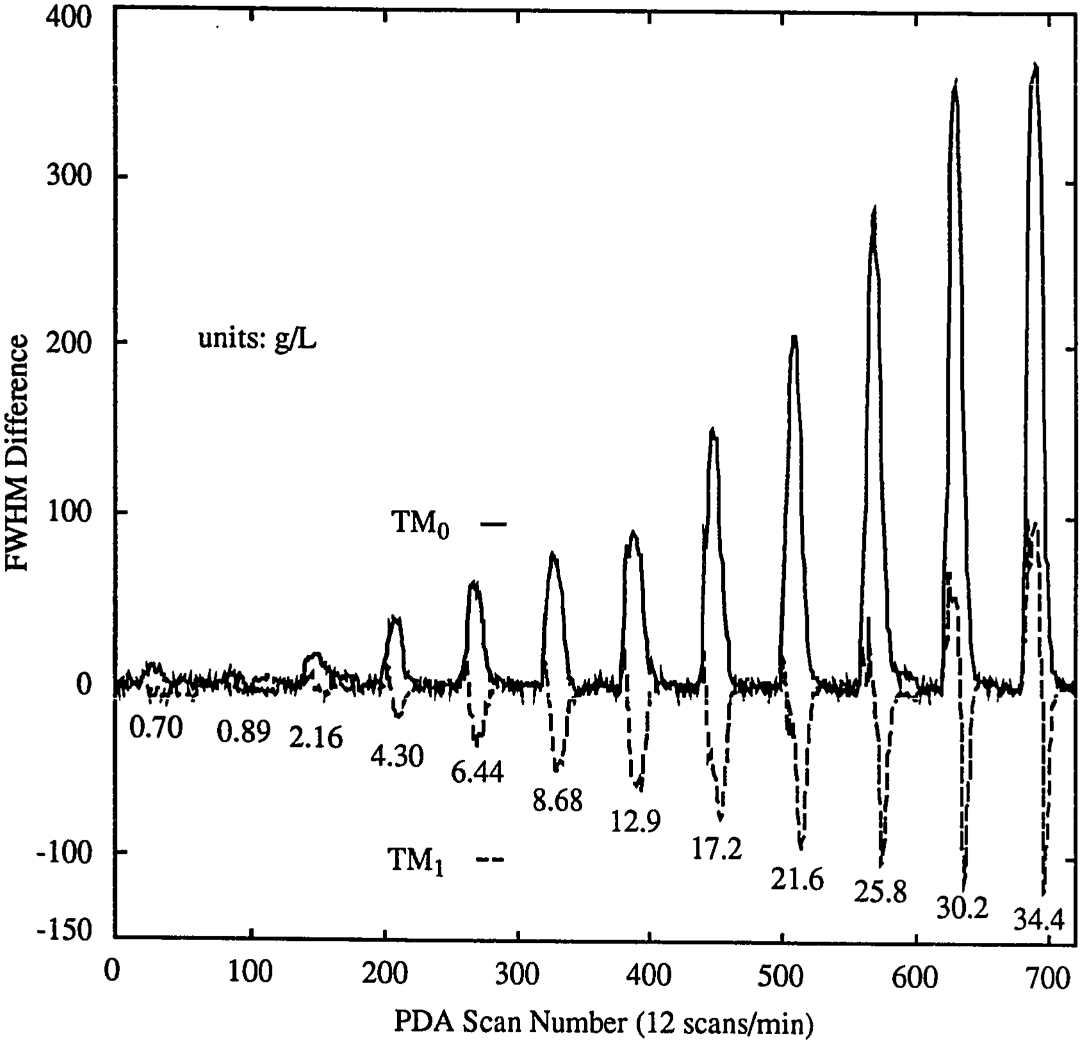

Figure 6.2b Ag$^+$-exchange waveguide 9C TM$_1$ and TM$_0$ mode position shift response to glycerol samples.

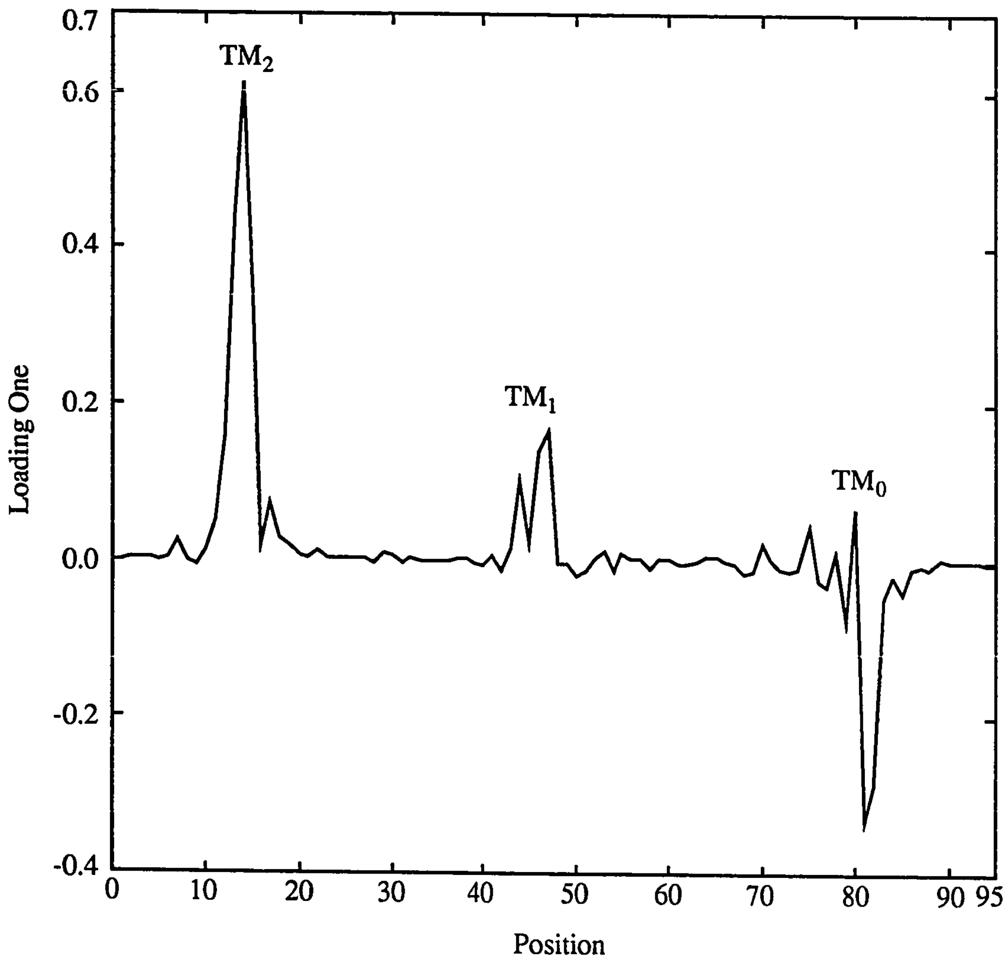

Figure 6.3a Ag$^+$-exchange waveguide 9C loading one response to glycerol samples.

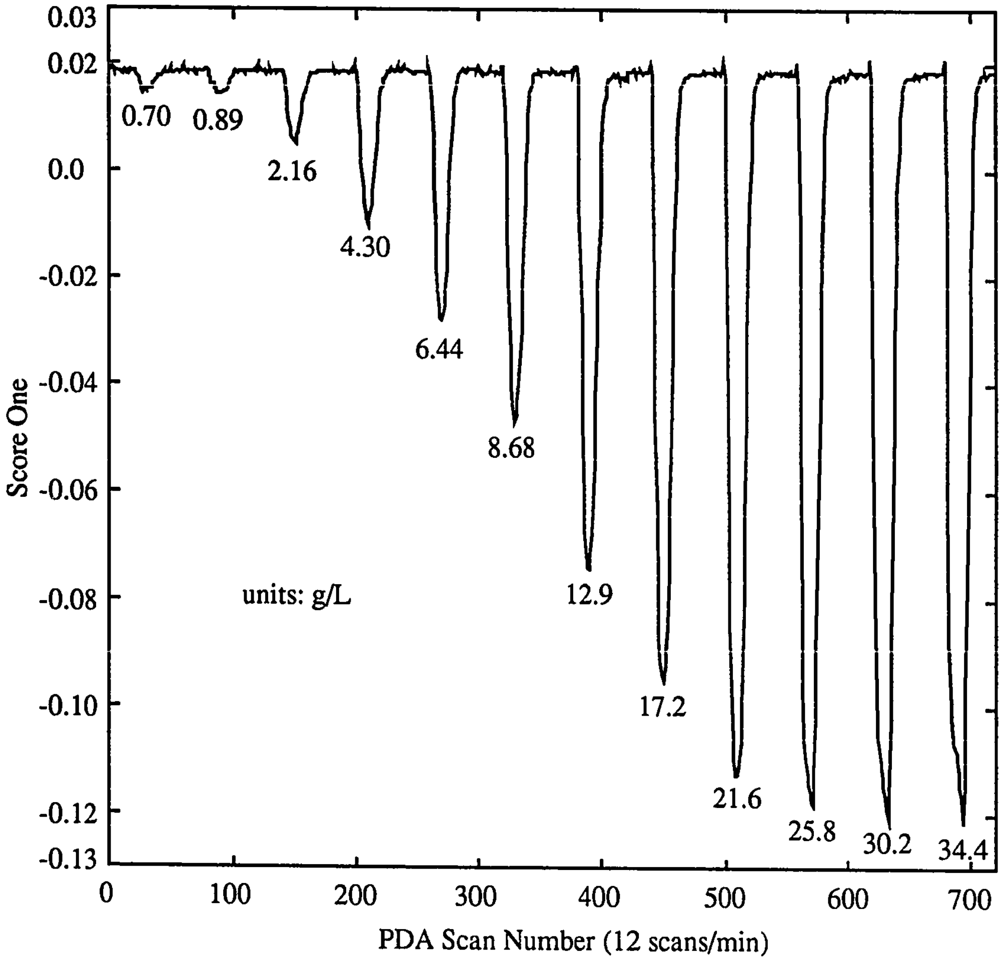

Figure 6.3b Ag^+-exchange waveguide 9C score one response to glycerol samples.

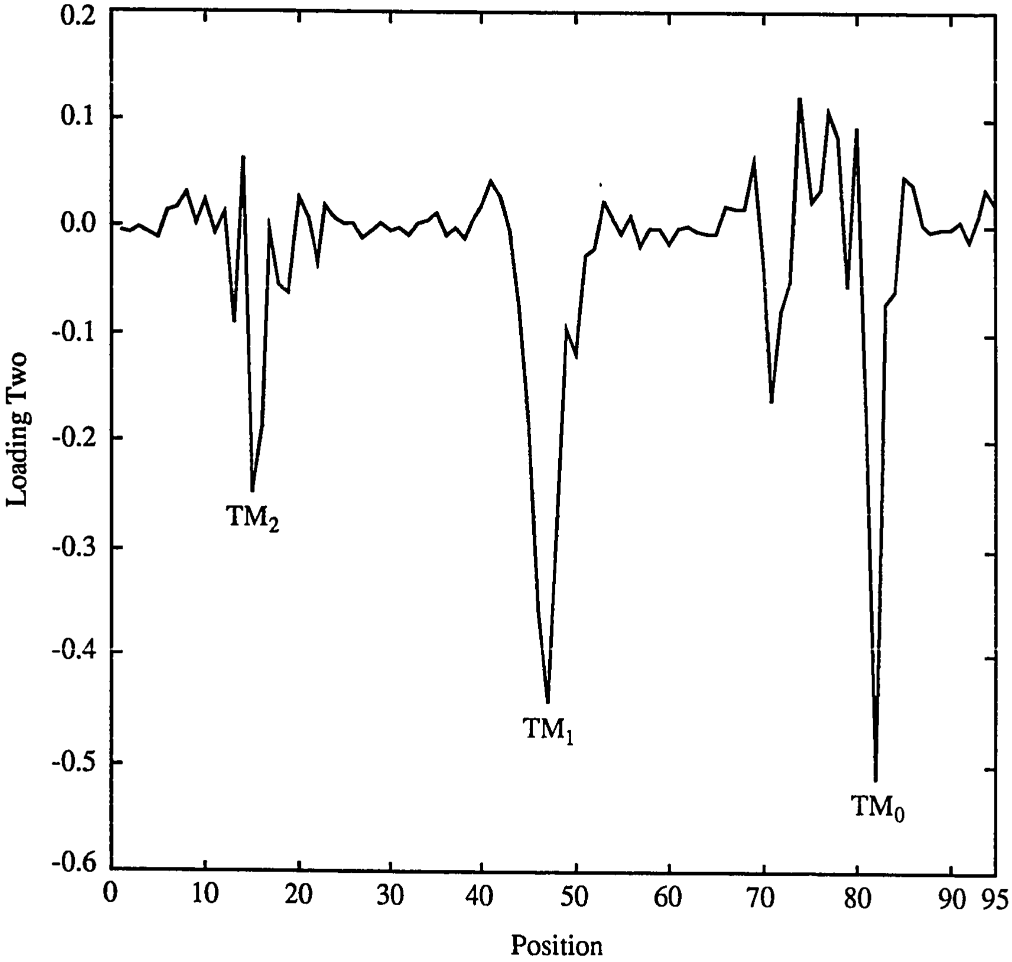

Figure 6.4a Ag$^+$-exchange waveguide 9C loading two response to glycerol samples.

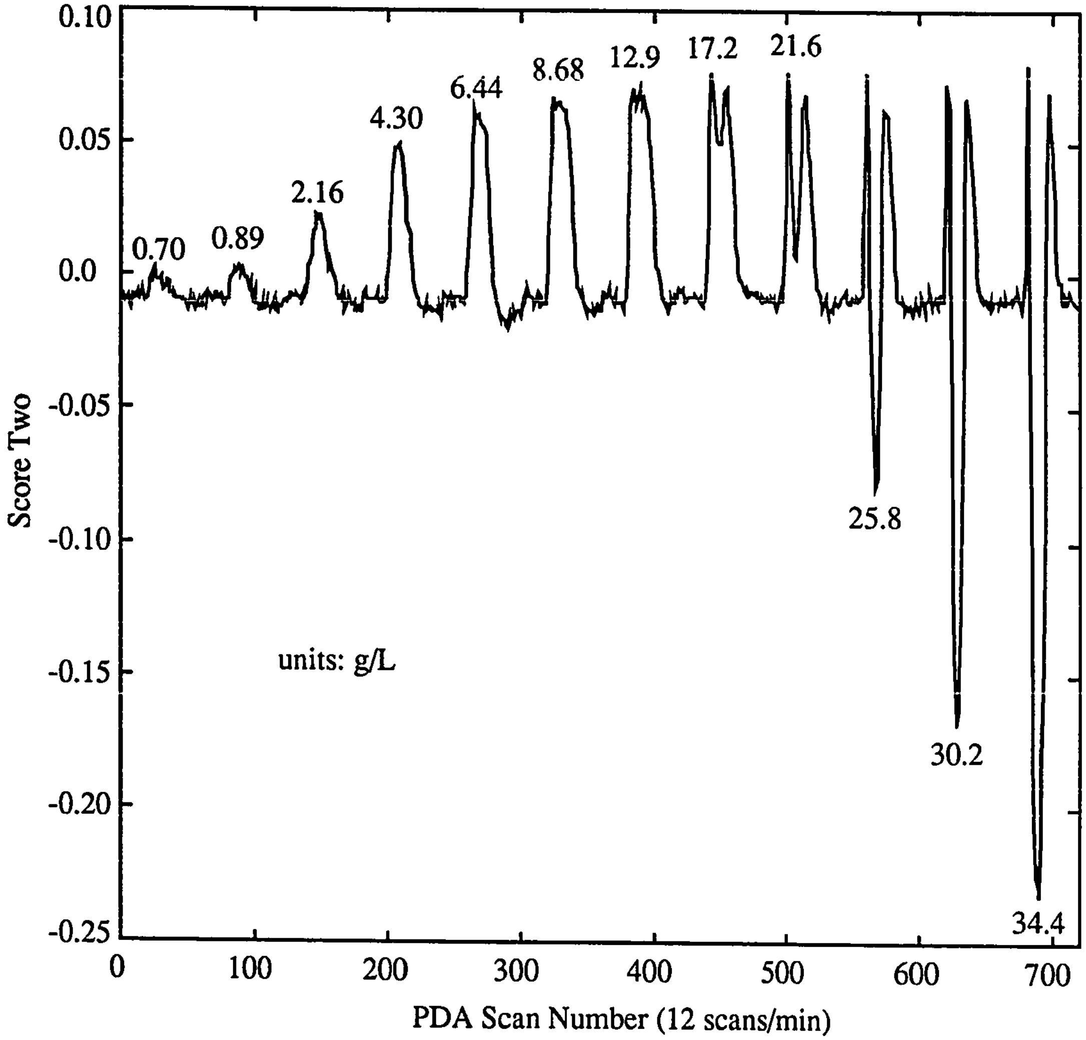

Figure 6.4b Ag^+-exchange waveguide 9C score two response to glycerol samples.

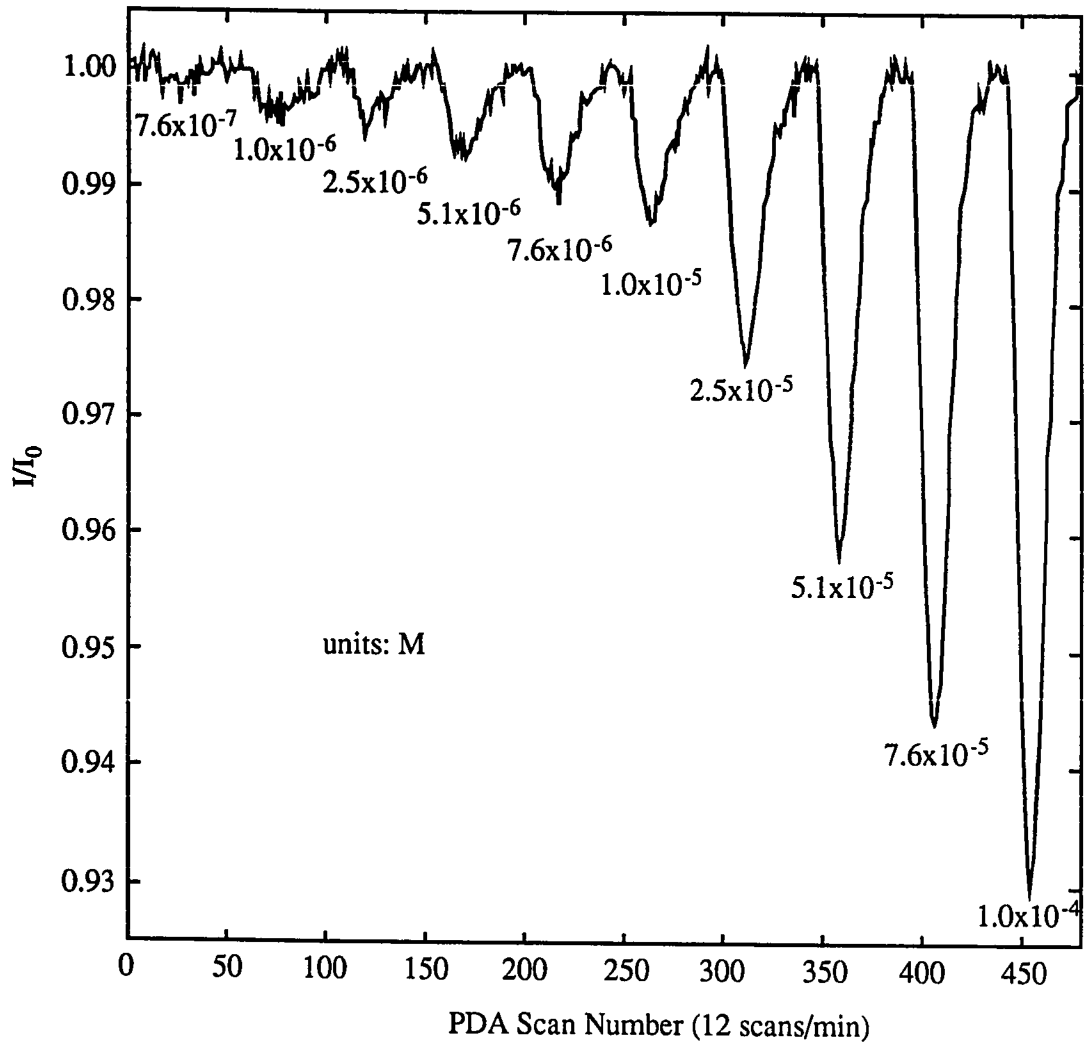

Figure 6.5a Ag^+-exchange waveguide 9C TM_2 mode integrated intensity response to bromocresol green samples.

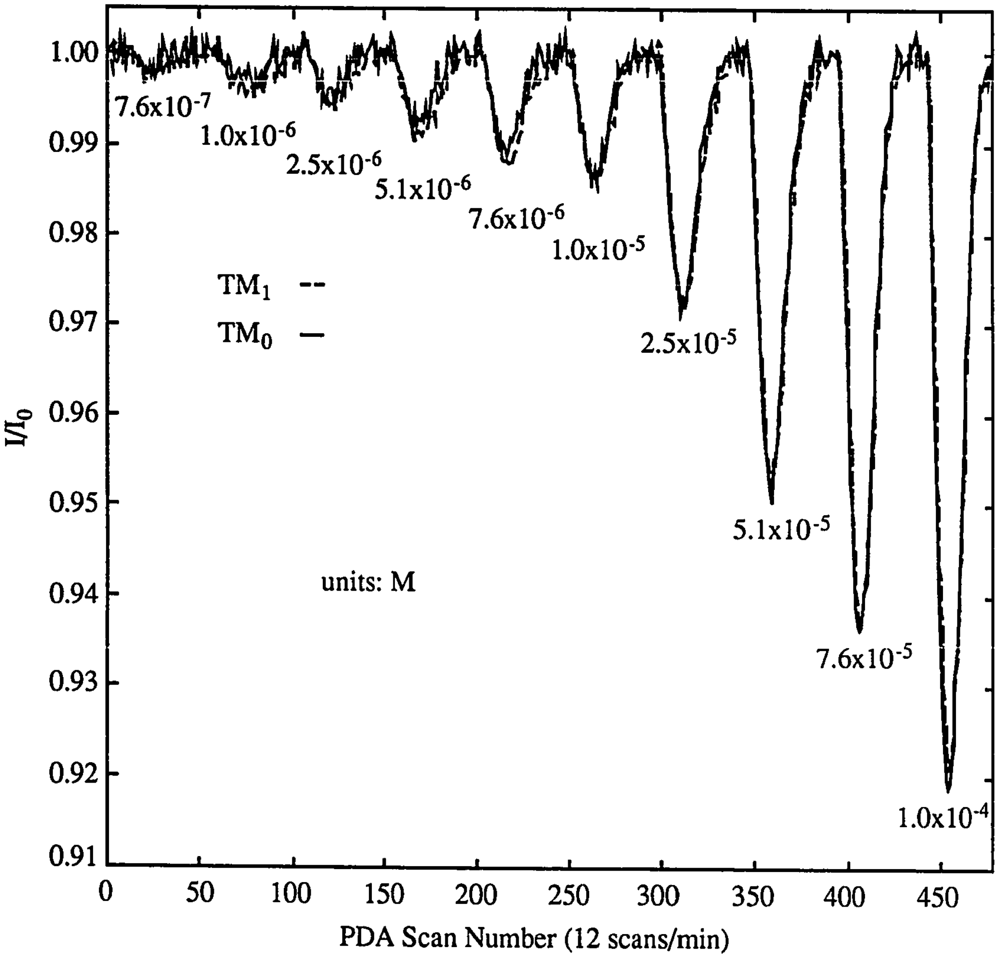

Figure 6.5b Ag^+-exchange waveguide 9C TM_1 and TM_0 mode integrated intensity response to bromocresol green samples.

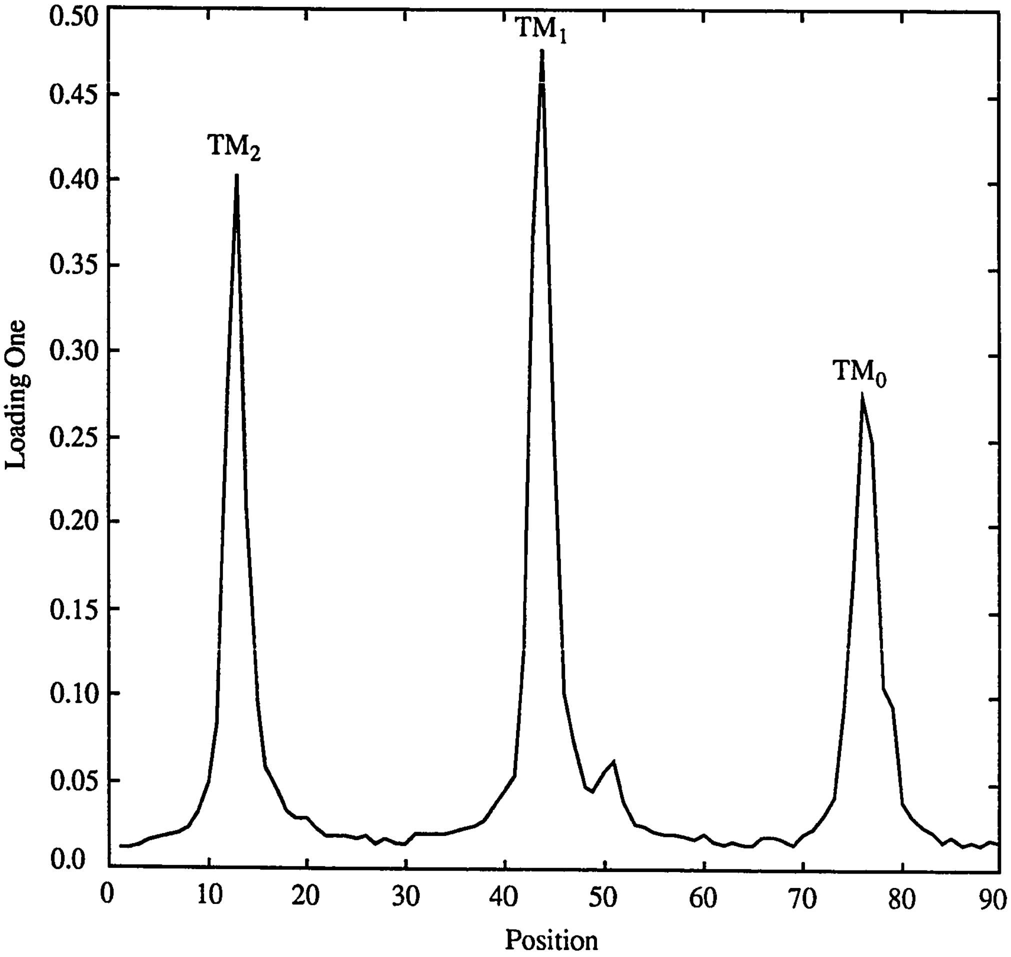

Figure 6.6a Ag$^+$-exchange waveguide 9C loading one response to bromocresol green samples.

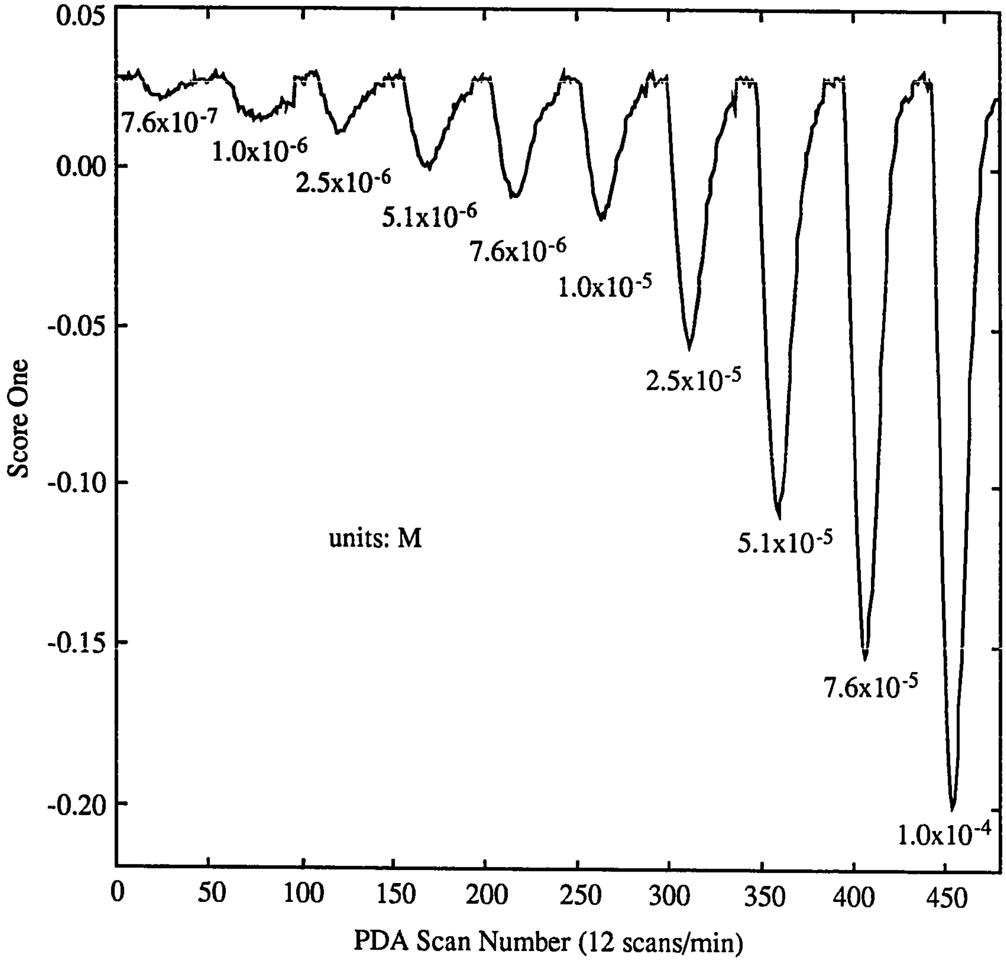

Figure 6.6b Ag^+-exchange waveguide 9C score one response to bromocresol green samples.

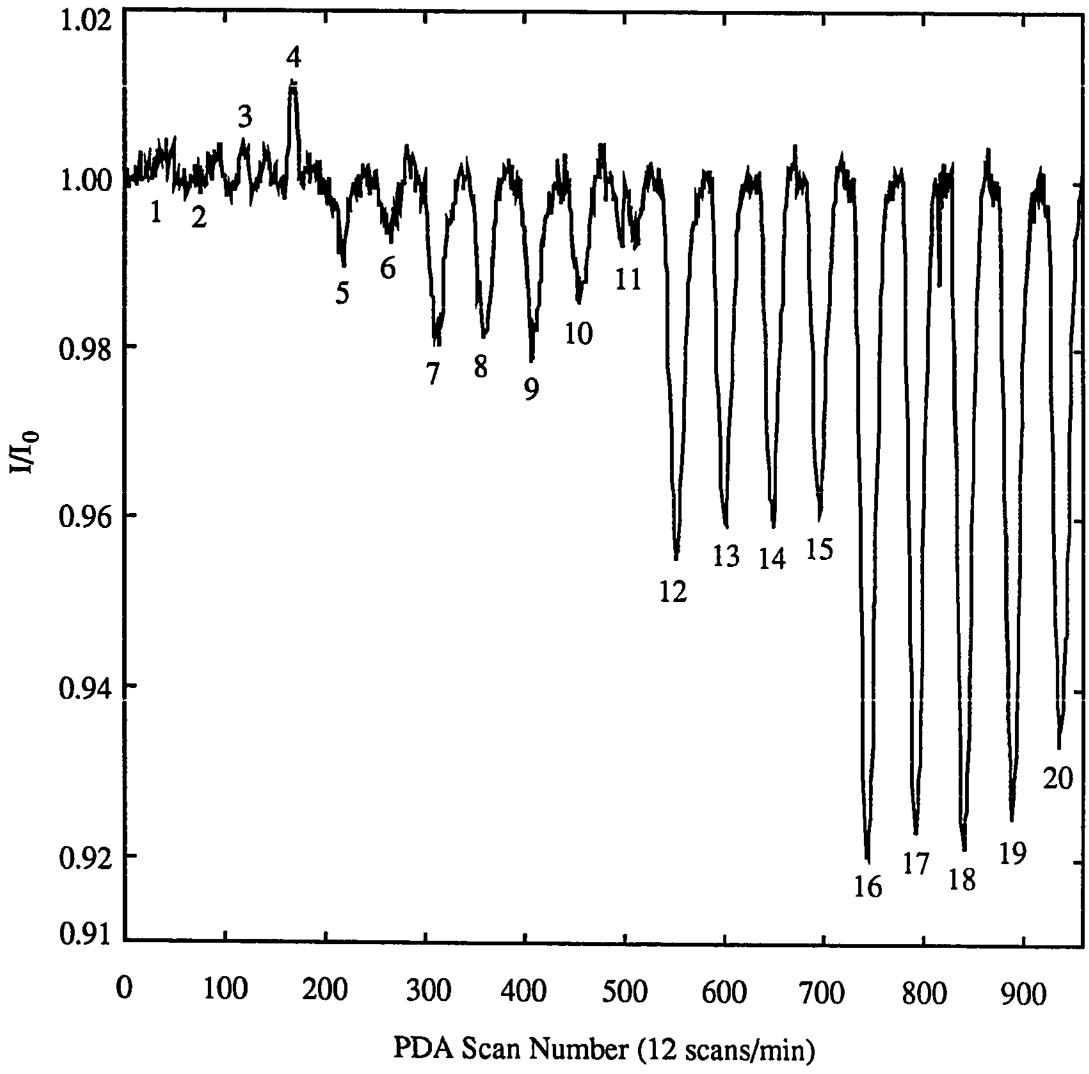

Figure 6.7a Ag$^+$-exchange waveguide 9C TM$_2$ mode integrated intensity response to glycerol-bromocresol green mixture samples.

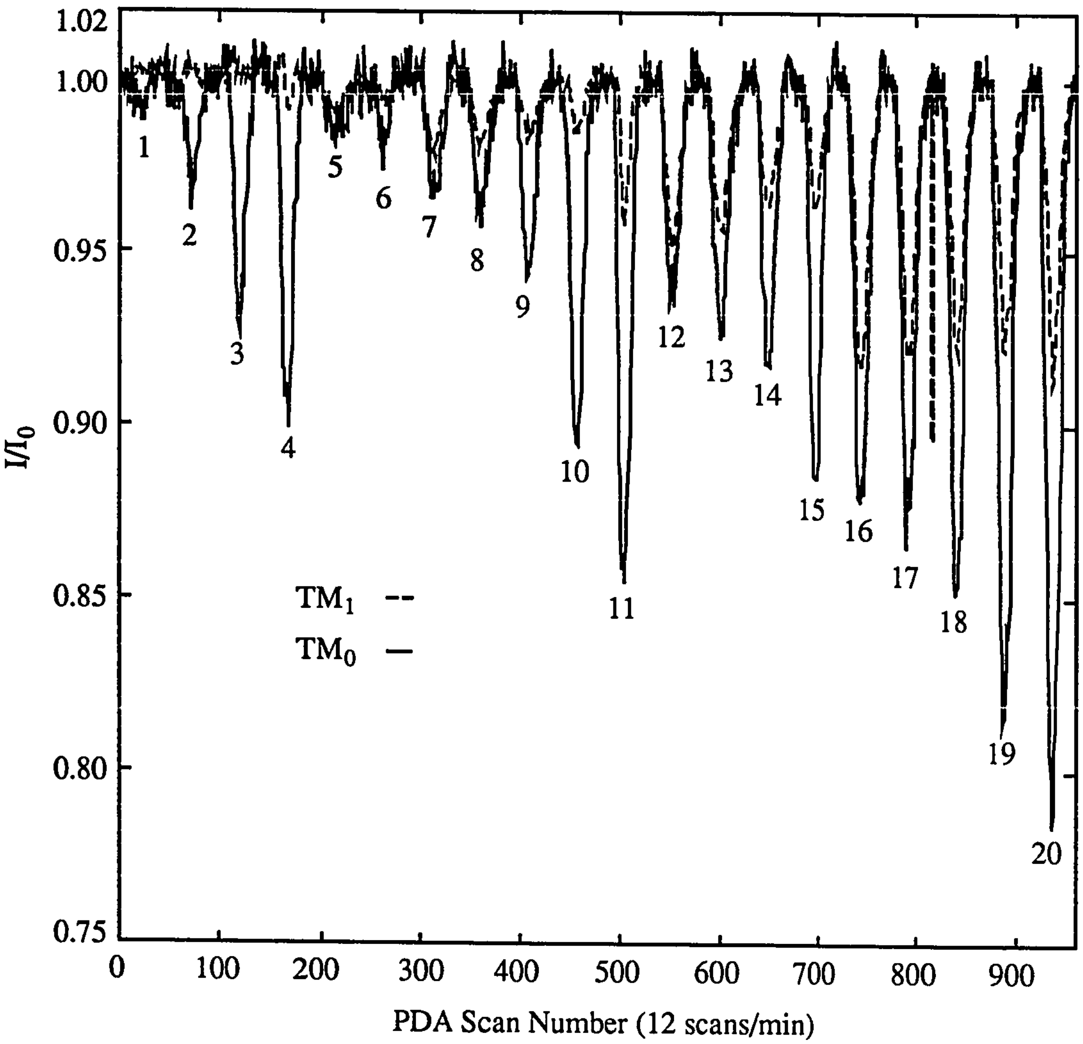

Figure 6.7b Ag^+-exchange waveguide 9C TM_1 and TM_0 mode integrated intensity response to glycerol-bromocresol green mixture samples.

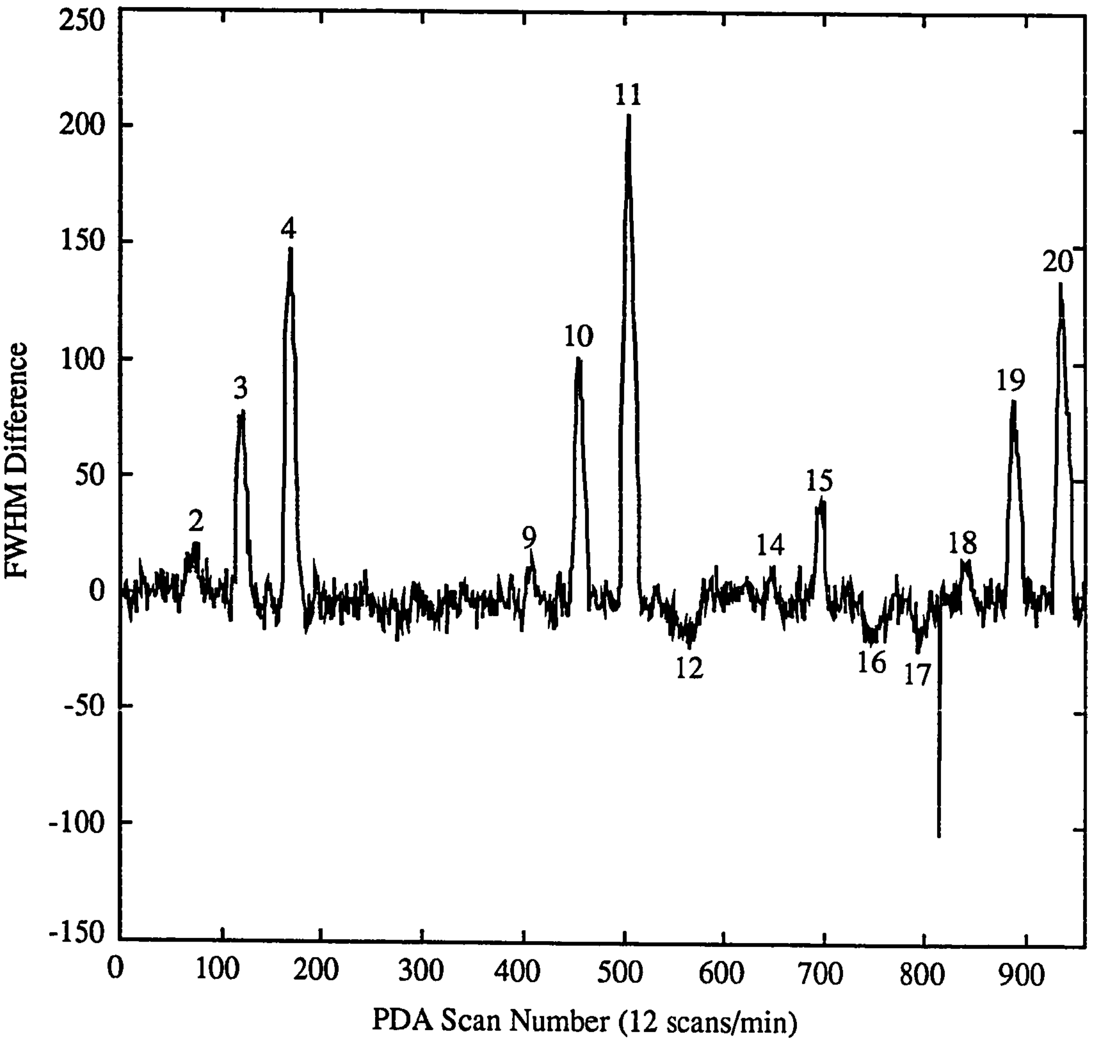

Figure 6.8a Ag^+-exchange waveguide TM_2 mode position shift response to glycerol-bromocresol green mixture samples.

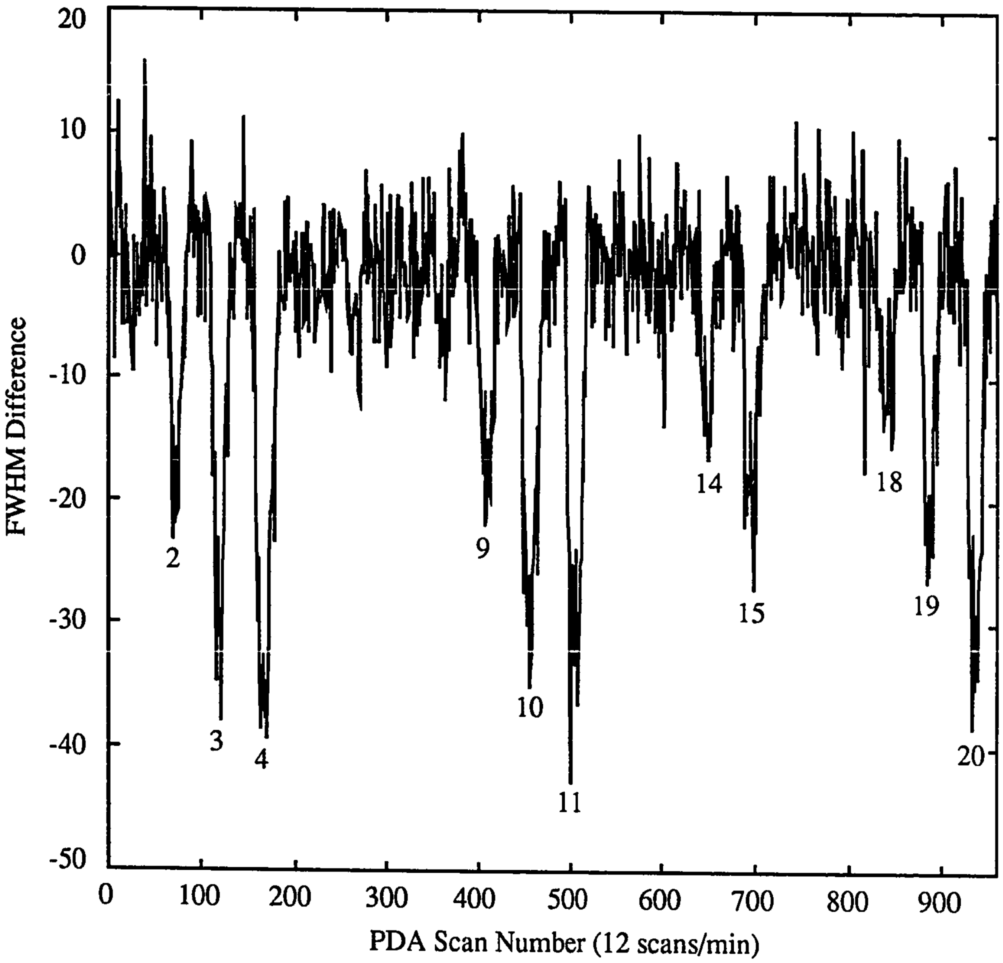

Figure 6.8b Ag$^+$-exchange waveguide 9C TM$_0$ mode position shift response to glycerol-bromocresol green mixture samples.

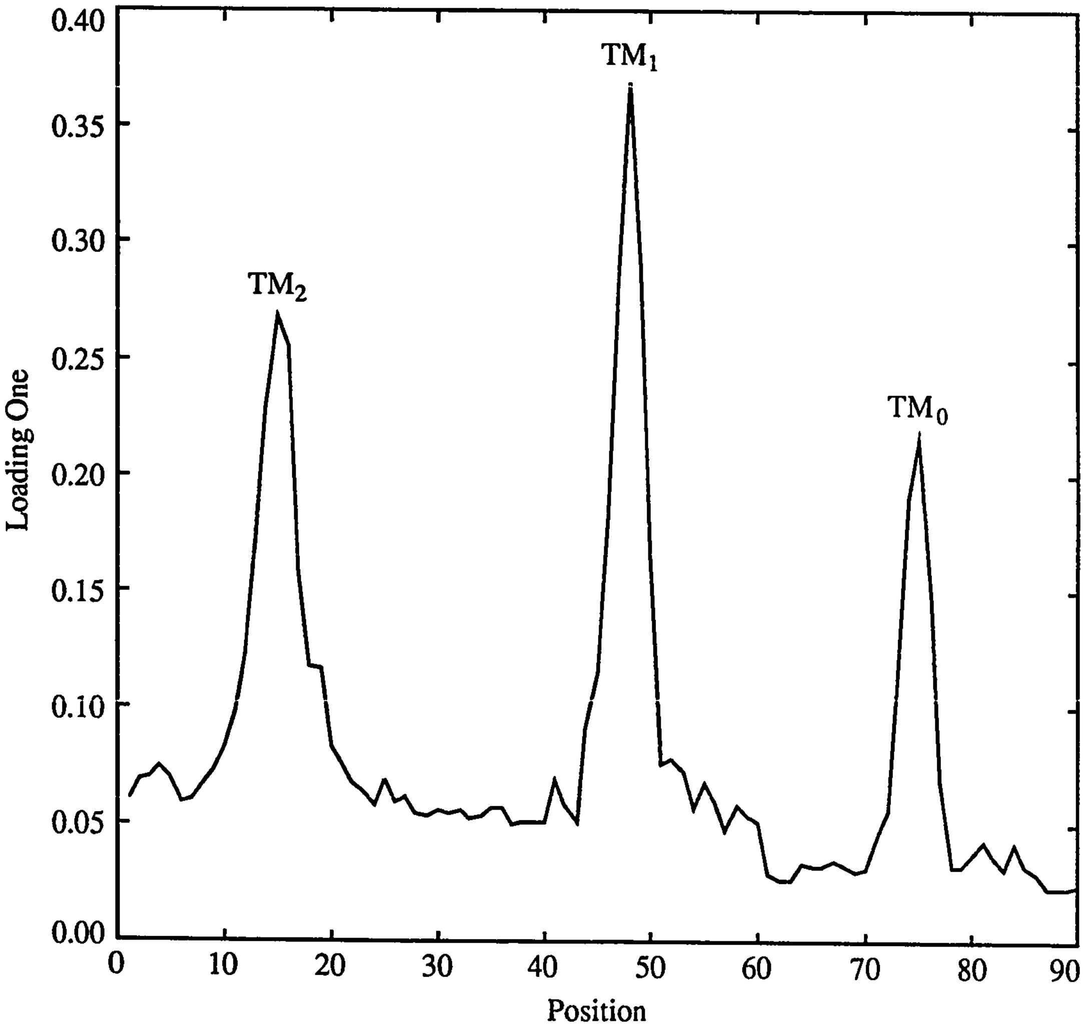

Figure 6.9a Ag$^+$-exchange waveguide 9C loading one response to glycerol-bromocresol green mixture samples.

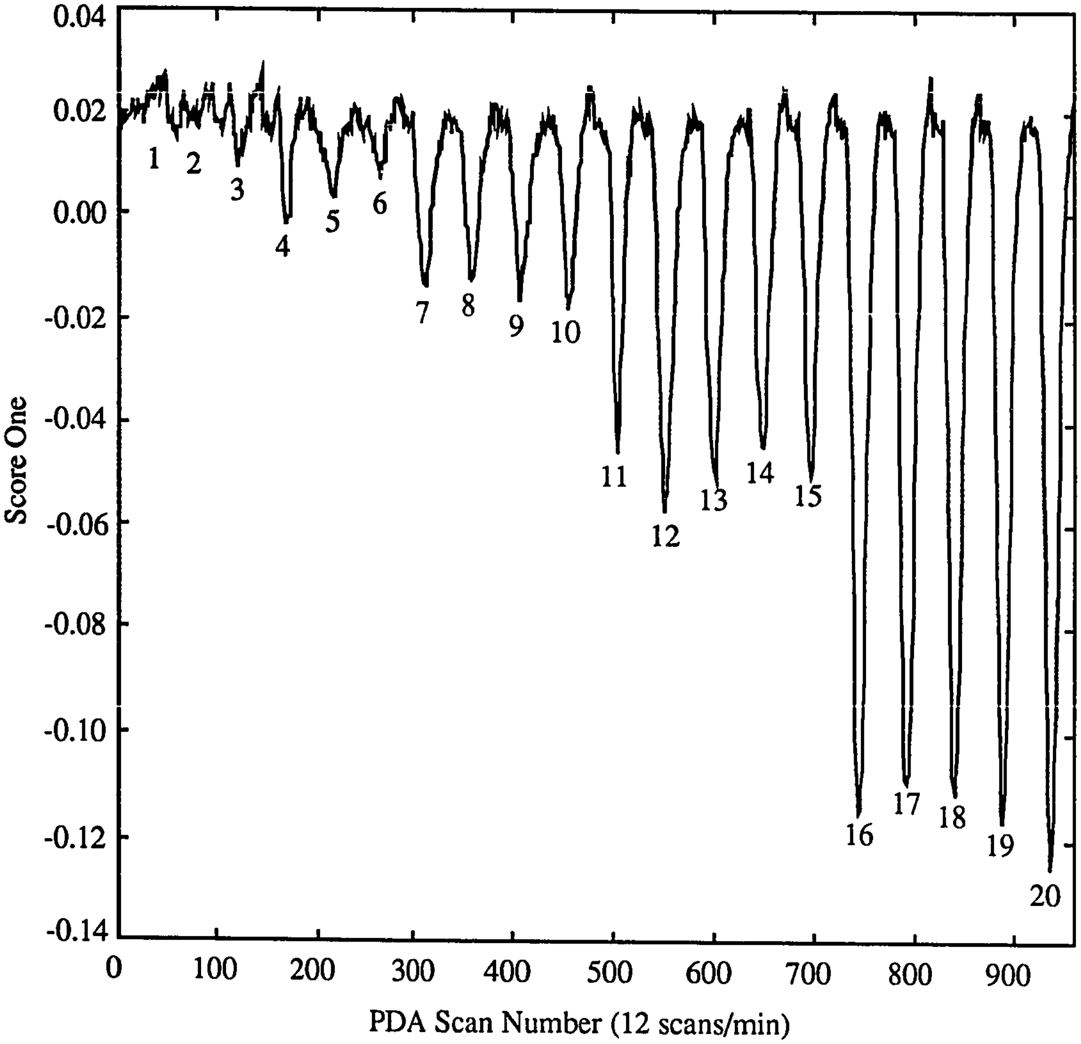

Figure 6.9b Ag^+-exchange waveguide 9C score one response to glycerol-bromocresol green mixture samples.

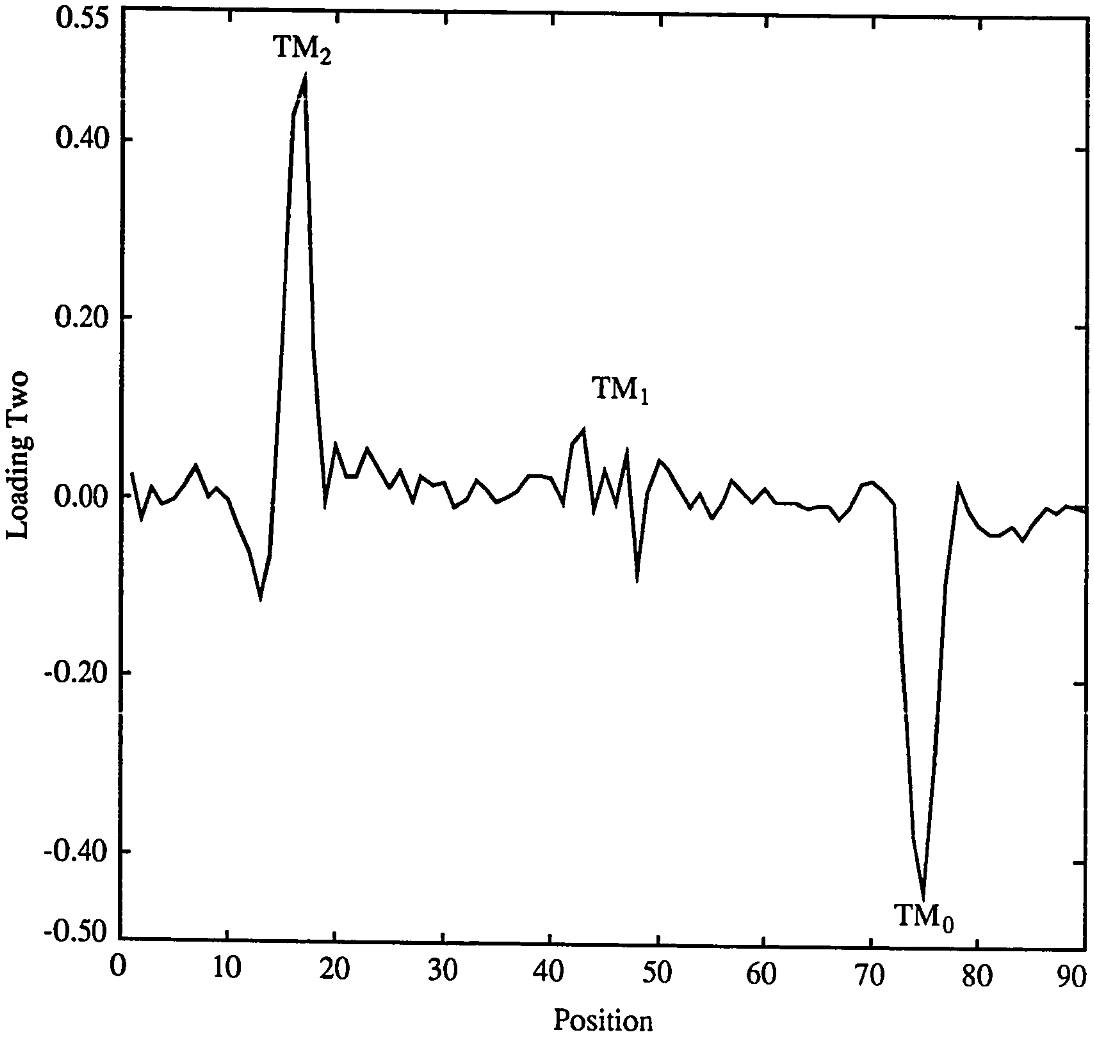

Figure 6.10a Ag$^+$-exchange waveguide 9C loading two response to glycerol-bromocresol green mixture samples.

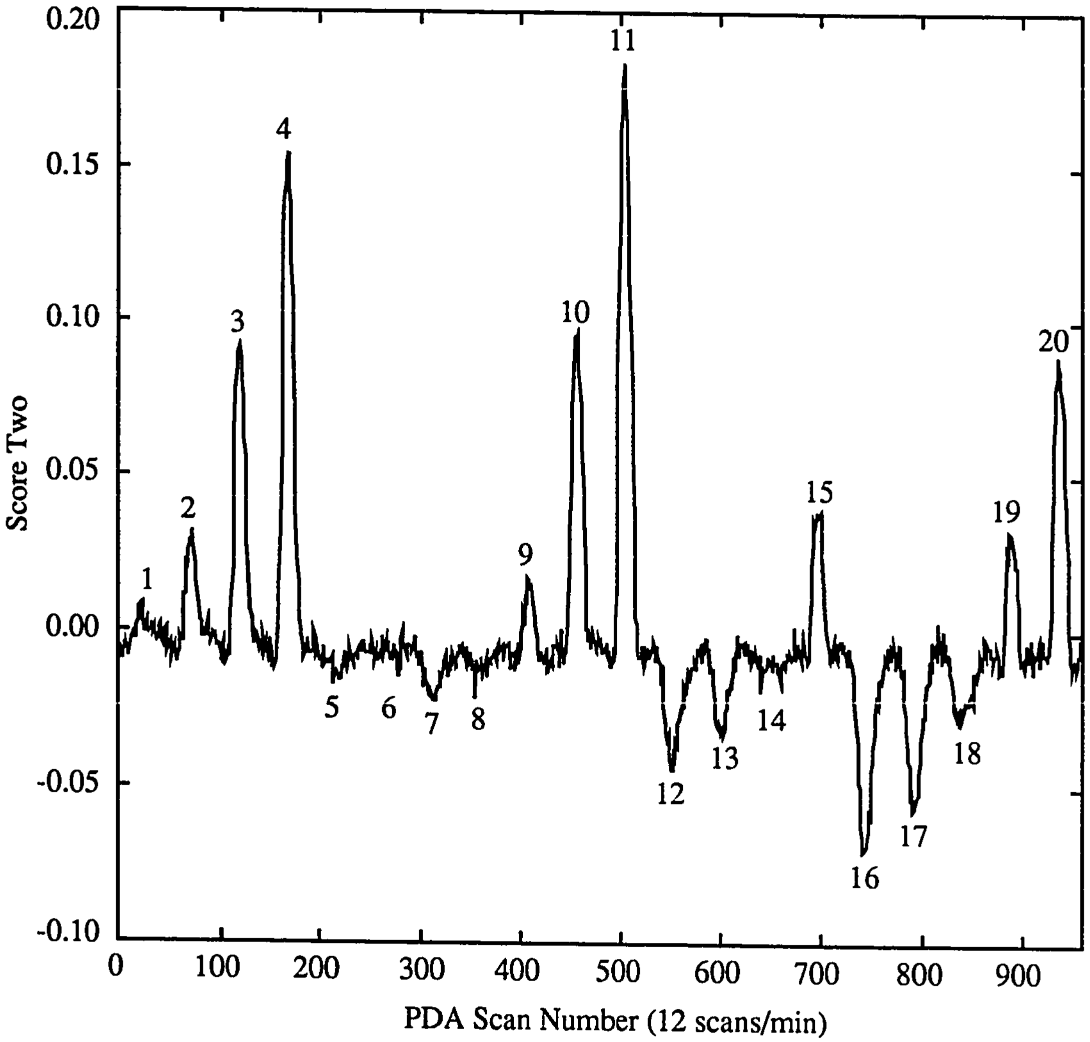

Figure 6.10b Ag^+-exchange waveguide 9C score two response to glycerol-bromocresol green mixture samples.

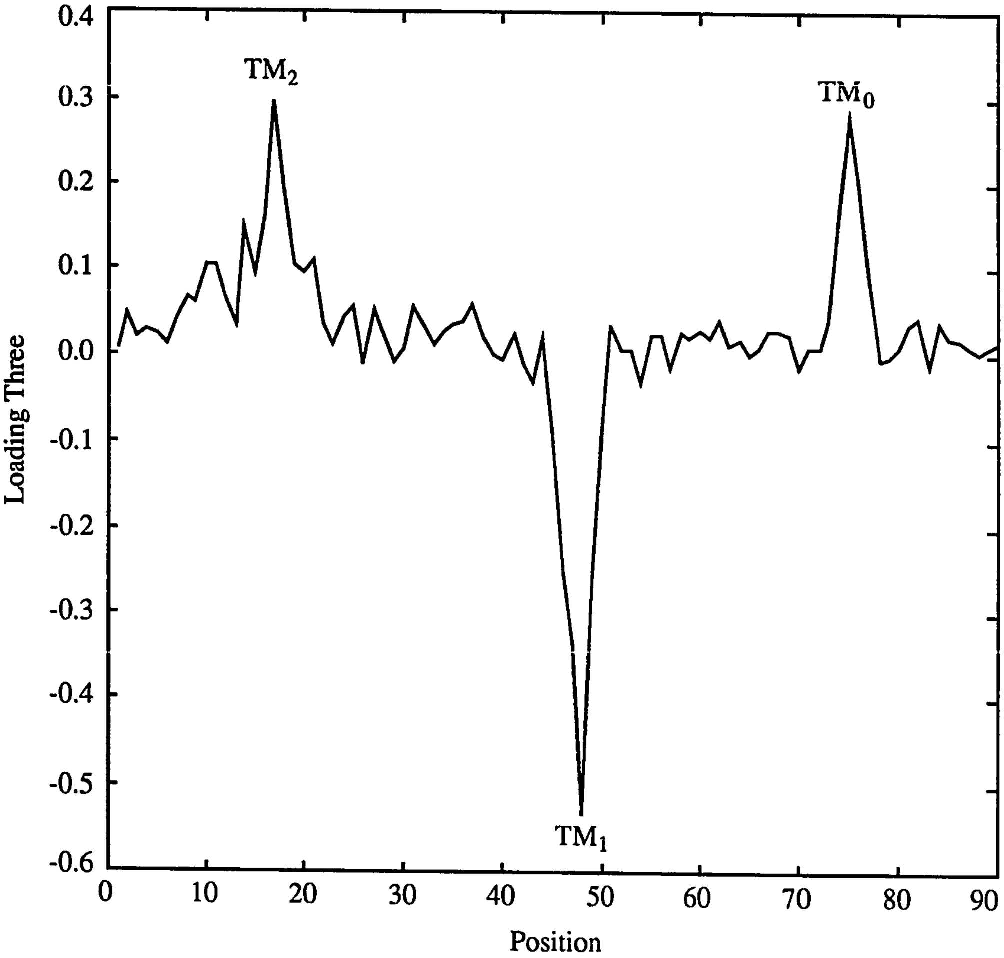

Figure 6.11a Ag^+-exchange waveguide 9C loading three response to glycerol-bromocresol green mixture samples.

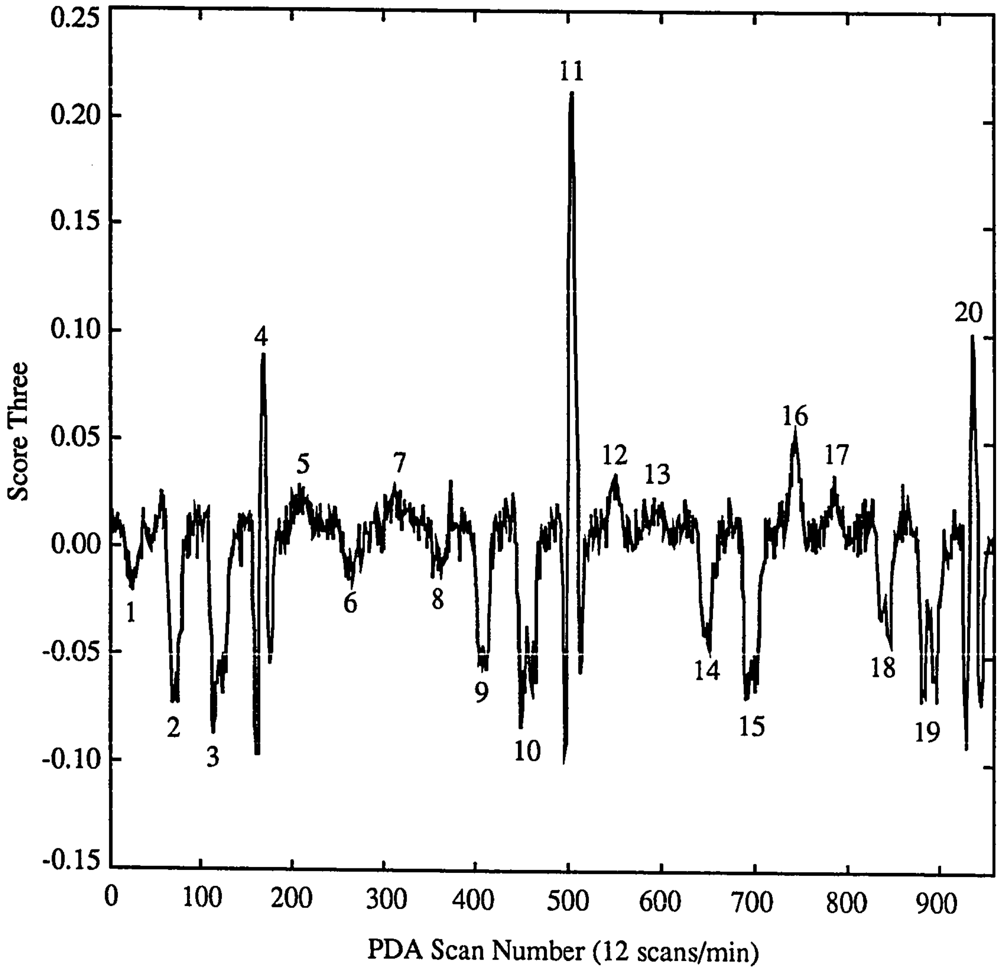

Figure 6.11b Ag$^+$-exchange waveguide 9C score three response to glycerol-bromocresol green mixture samples.

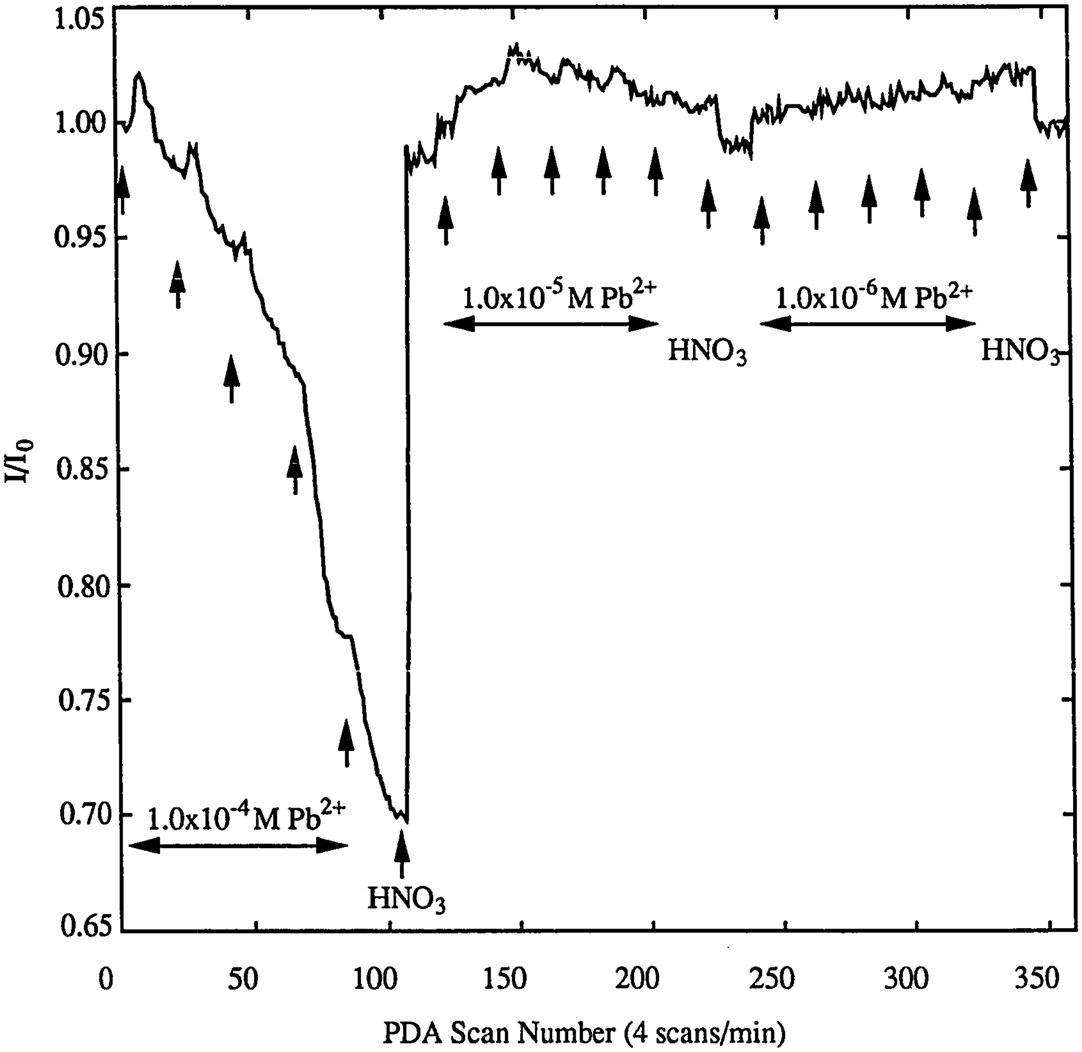

Figure 6.12a Ag$^+$-exchange waveguide 9C TM$_2$ mode integrated intensity response to Pb^{2+}samples.

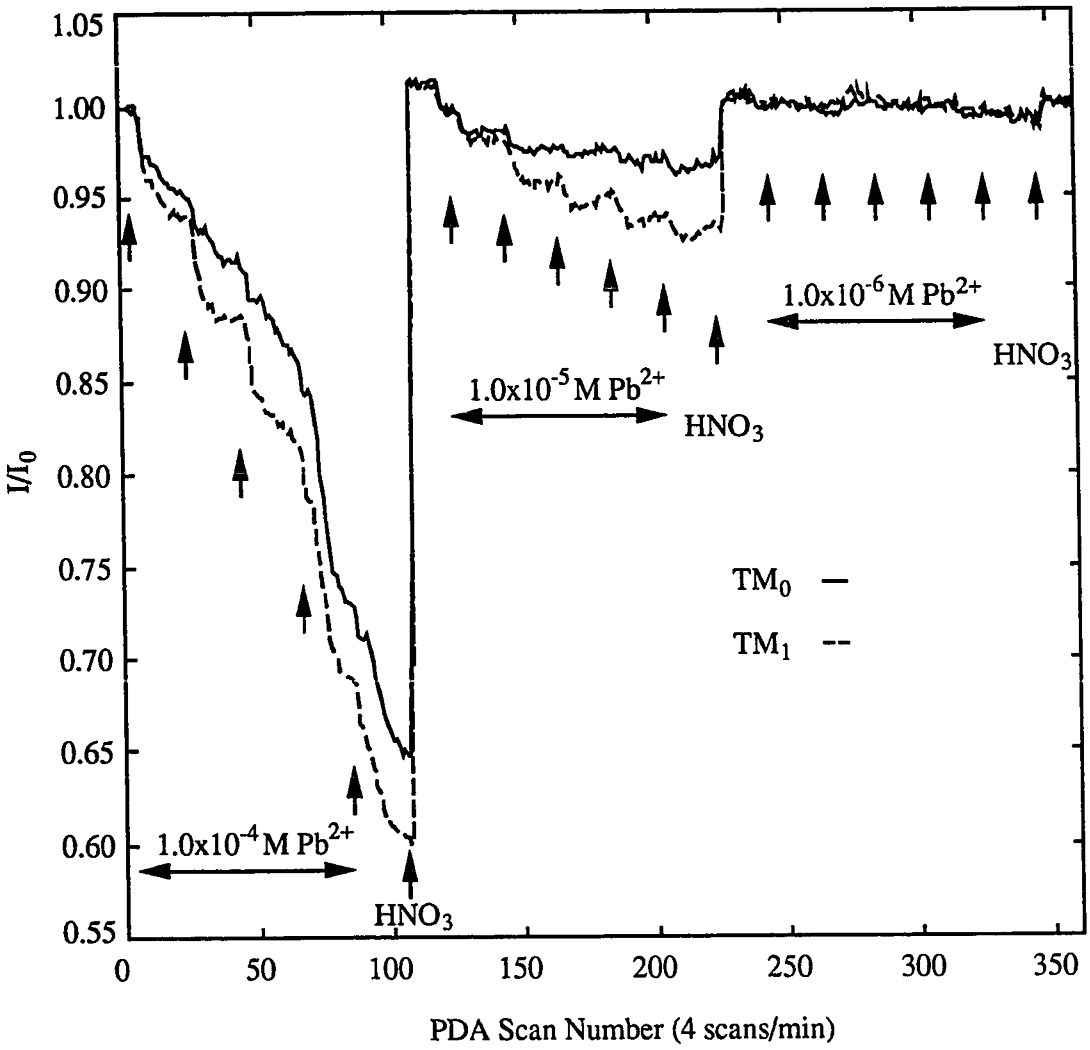

Figure 6.12b Ag^+-exchange waveguide 9C TM_1 and TM_0 mode integrated intensity response to Pb^{2+}samples.

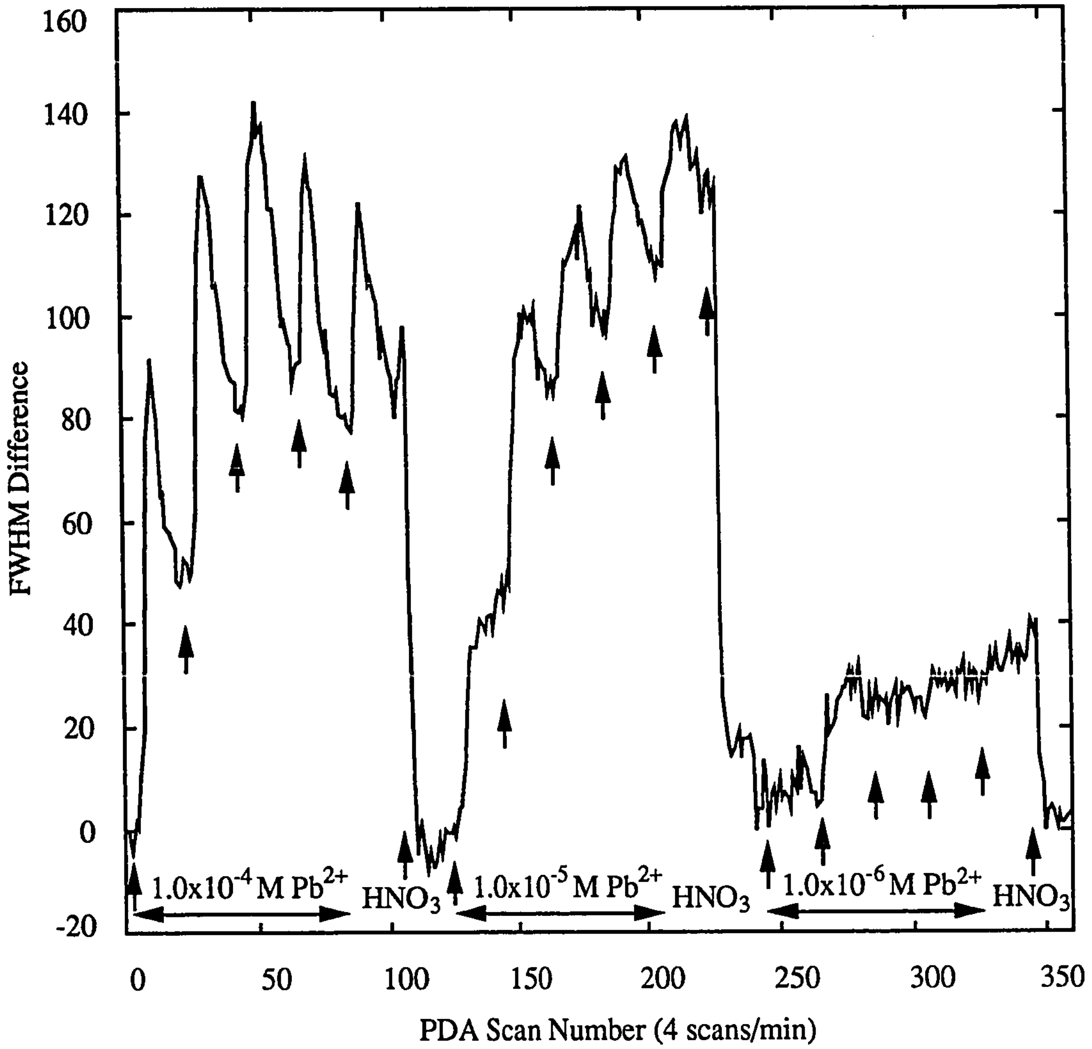

Figure 6.13a Ag$^+$-exchange waveguide 9C TM$_2$ mode position shift response to Pb^{2+}samples.

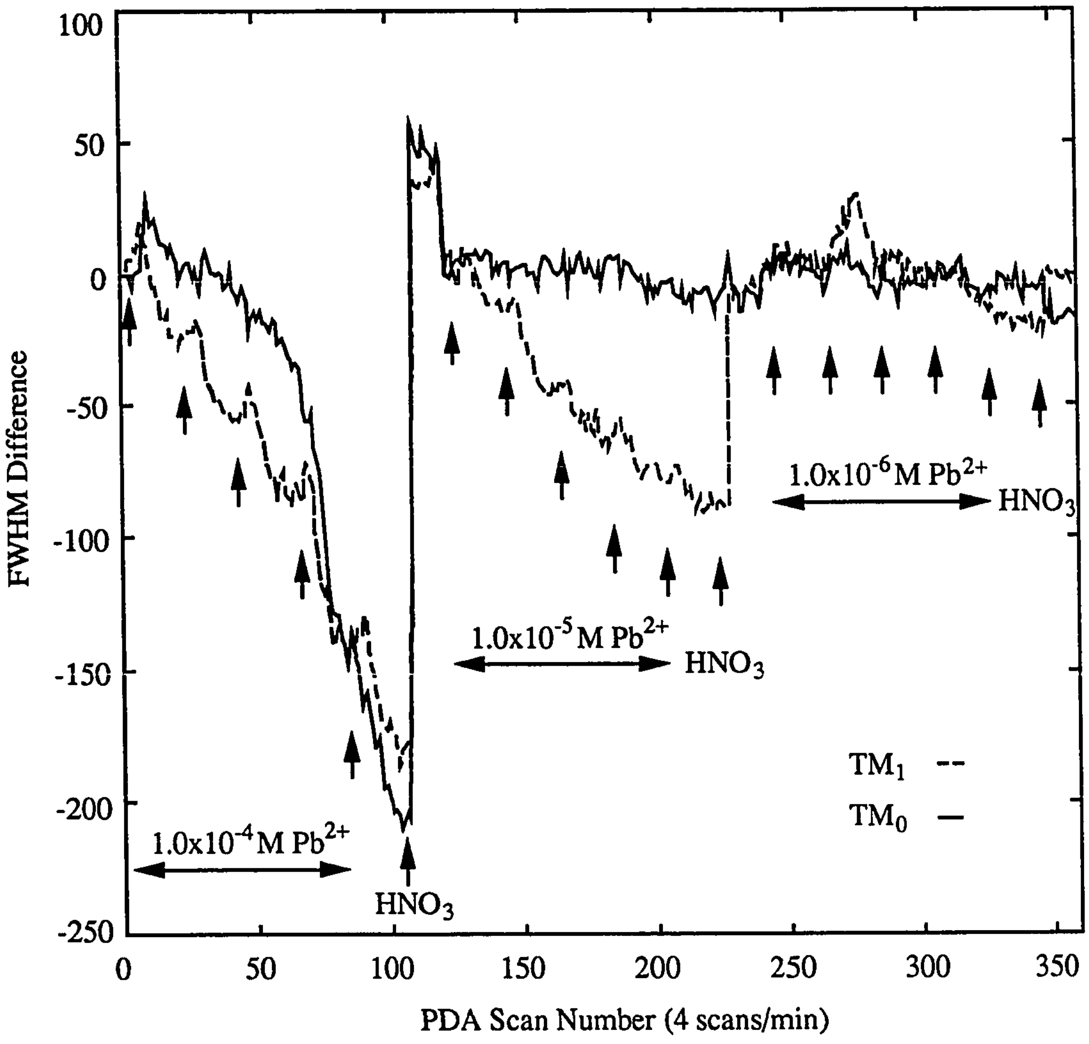

Figure 6.13b Ag$^+$-exchange waveguide 9C TM$_1$ and TM$_0$ mode position shift response to Pb^{2+}samples.

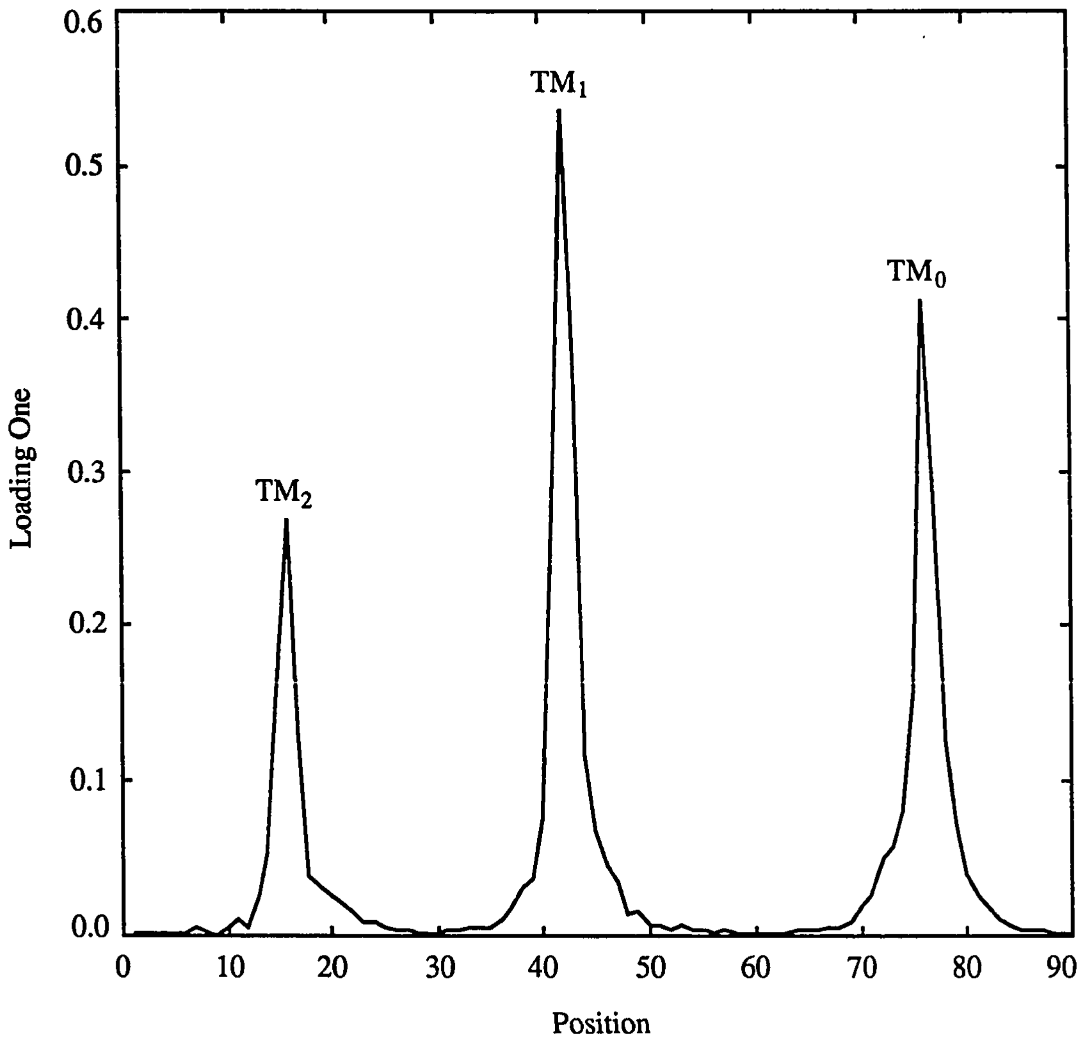

Figure 6.14a Ag$^+$-exchange waveguide 9C loading one response to Pb^{2+}samples.

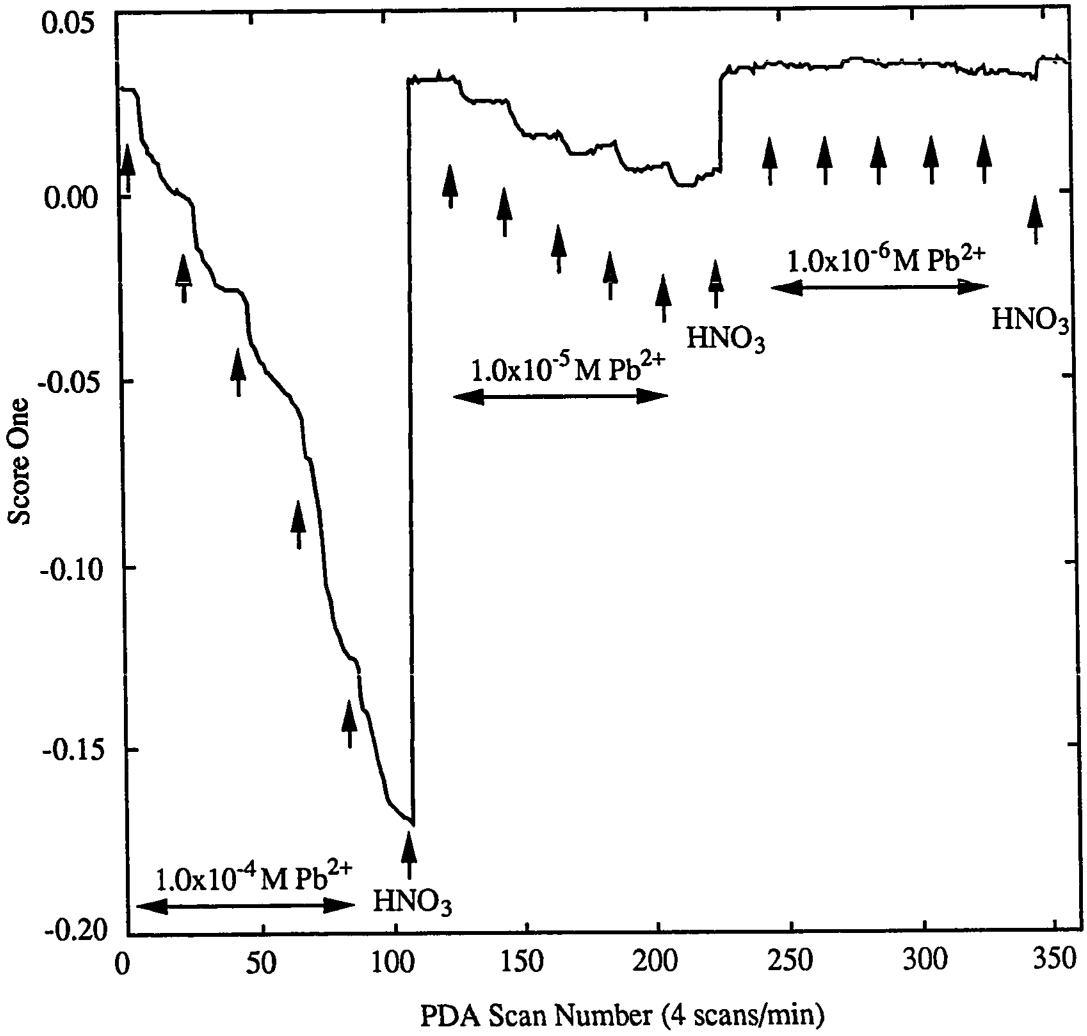

Figure 6.14b Ag$^+$-exchange waveguide 9C score one response to Pb^{2+}samples.

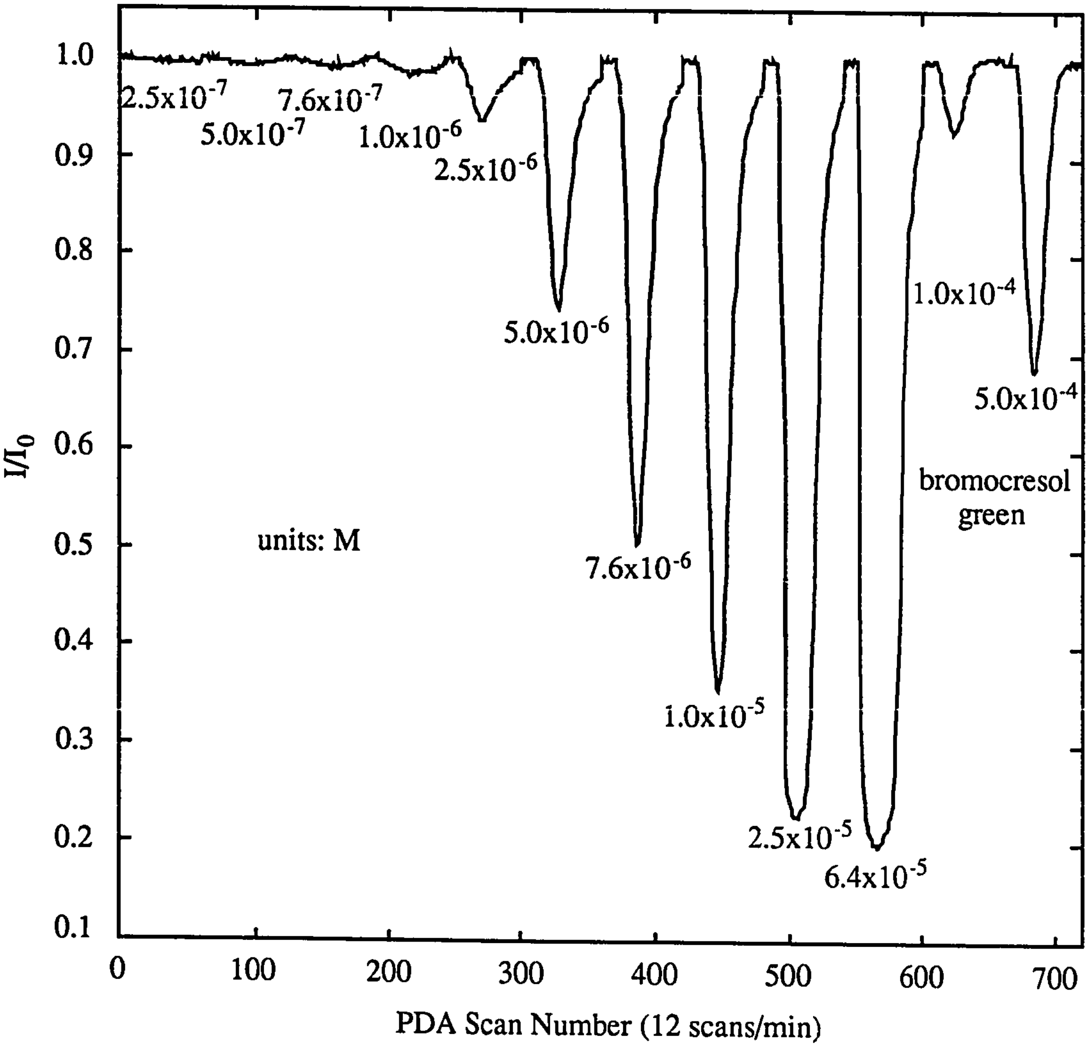

Figure 6.15a Ag^+-exchange waveguide 9C TM_2 mode integrated intensity response to methylene blue samples.

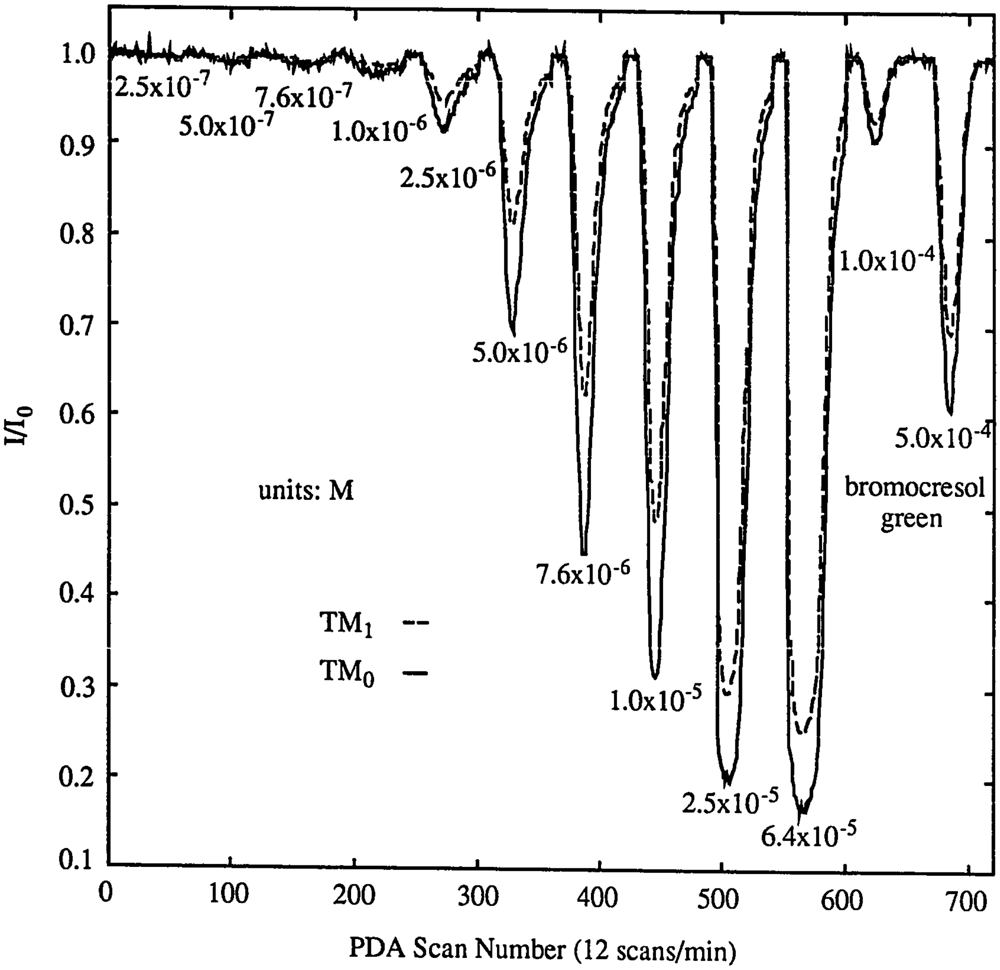

Figure 6.15b Ag^+-exchange waveguide 9C TM_1 and TM_0 mode integrated intensity response to methylene blue samples.

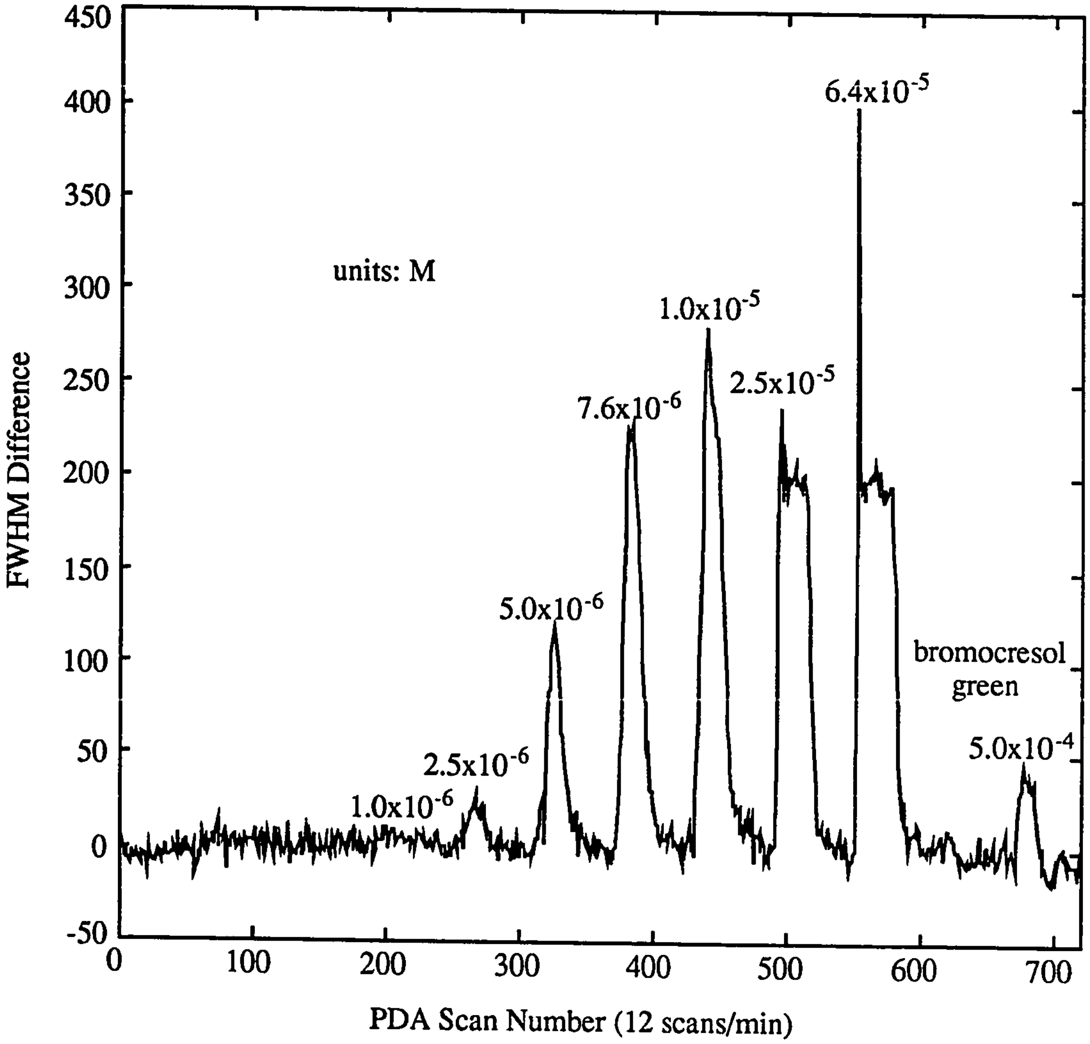

Figure 6.16a Ag^+-exchange waveguide 9C TM_2 mode position shift response to methylene blue samples.

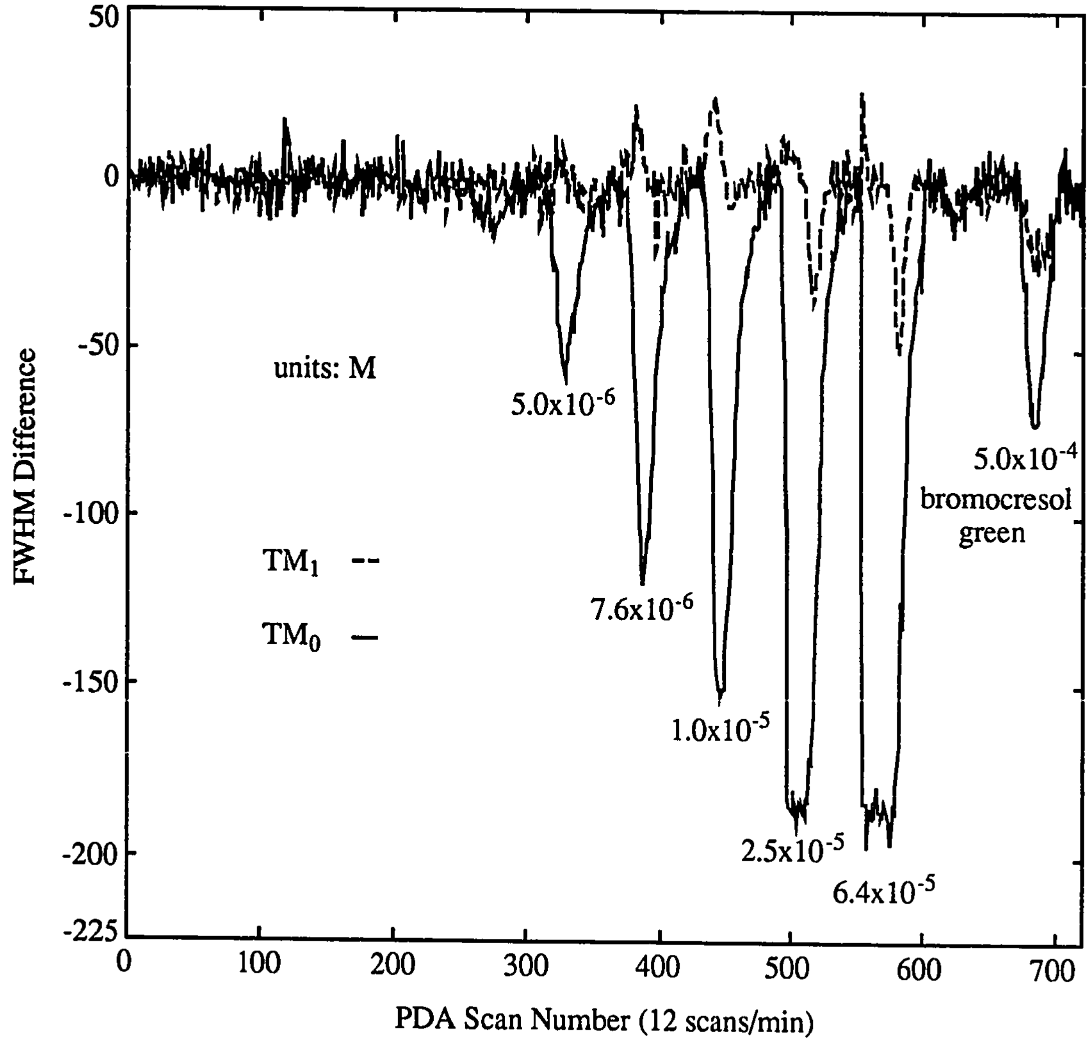

Figure 6.16b Ag^+-exchange waveguide 9C TM_1 and TM_0 mode position shift to methylene blue samples.

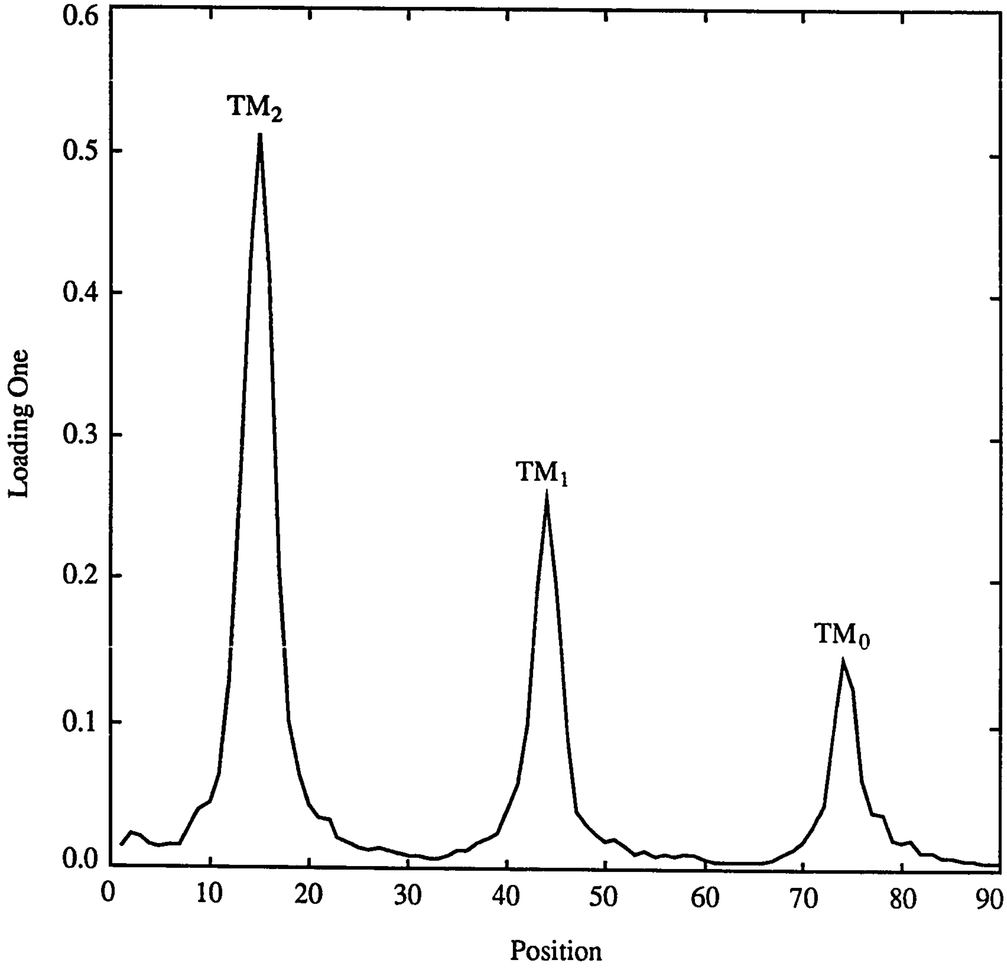

Figure 6.17a Ag$^+$-exchange waveguide 9C loading one response to methylene blue samples.

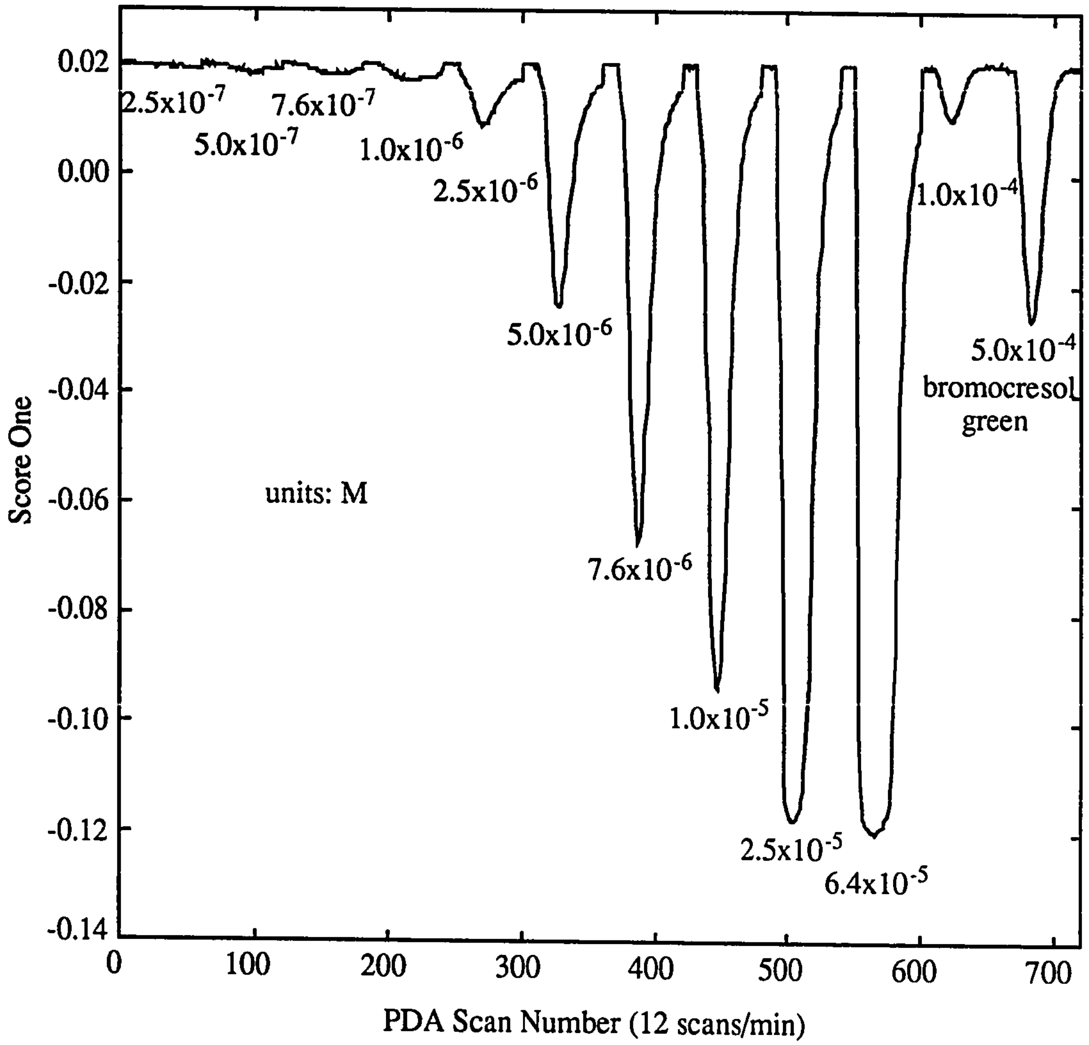

Figure 6.17b Ag^+-exchange waveguide 9C score one response to methylene blue samples.

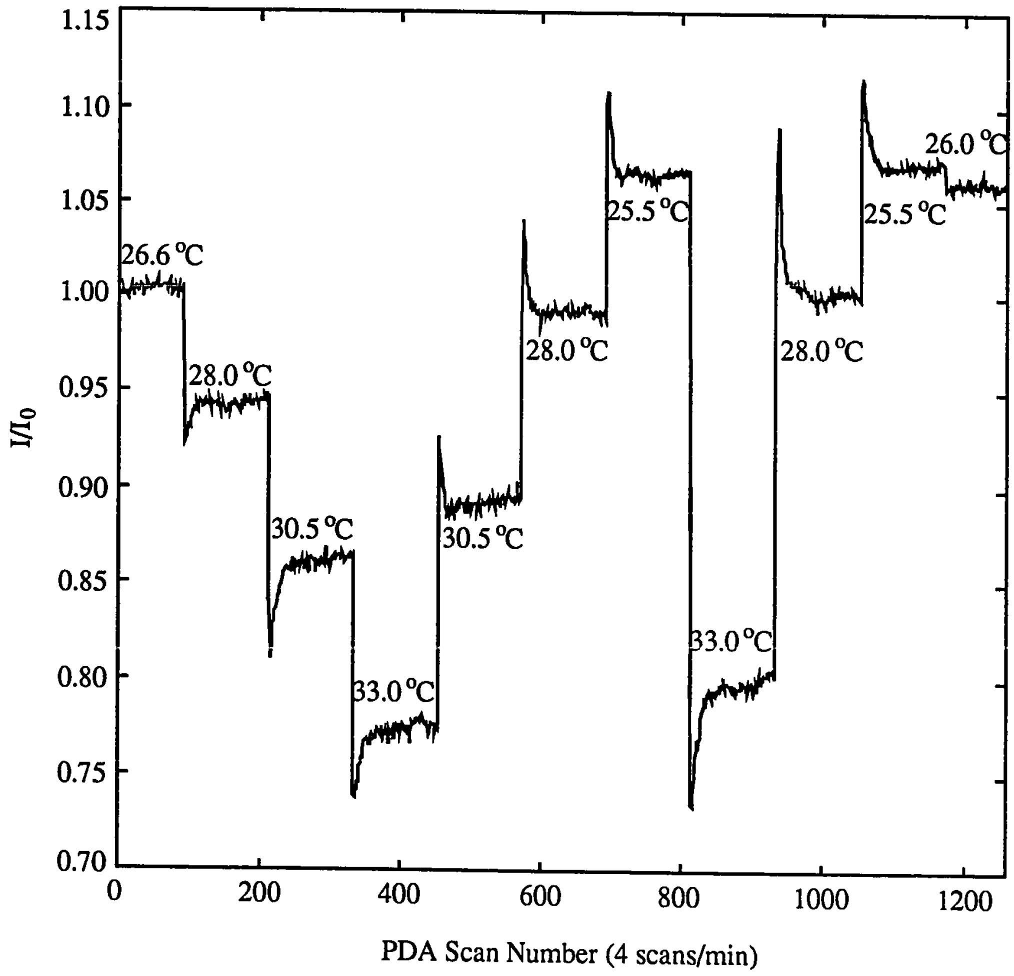

Figure 6.18a Ag$^+$-exchange waveguide 9C TM$_2$ mode integrated intensity response to step temperature changes.

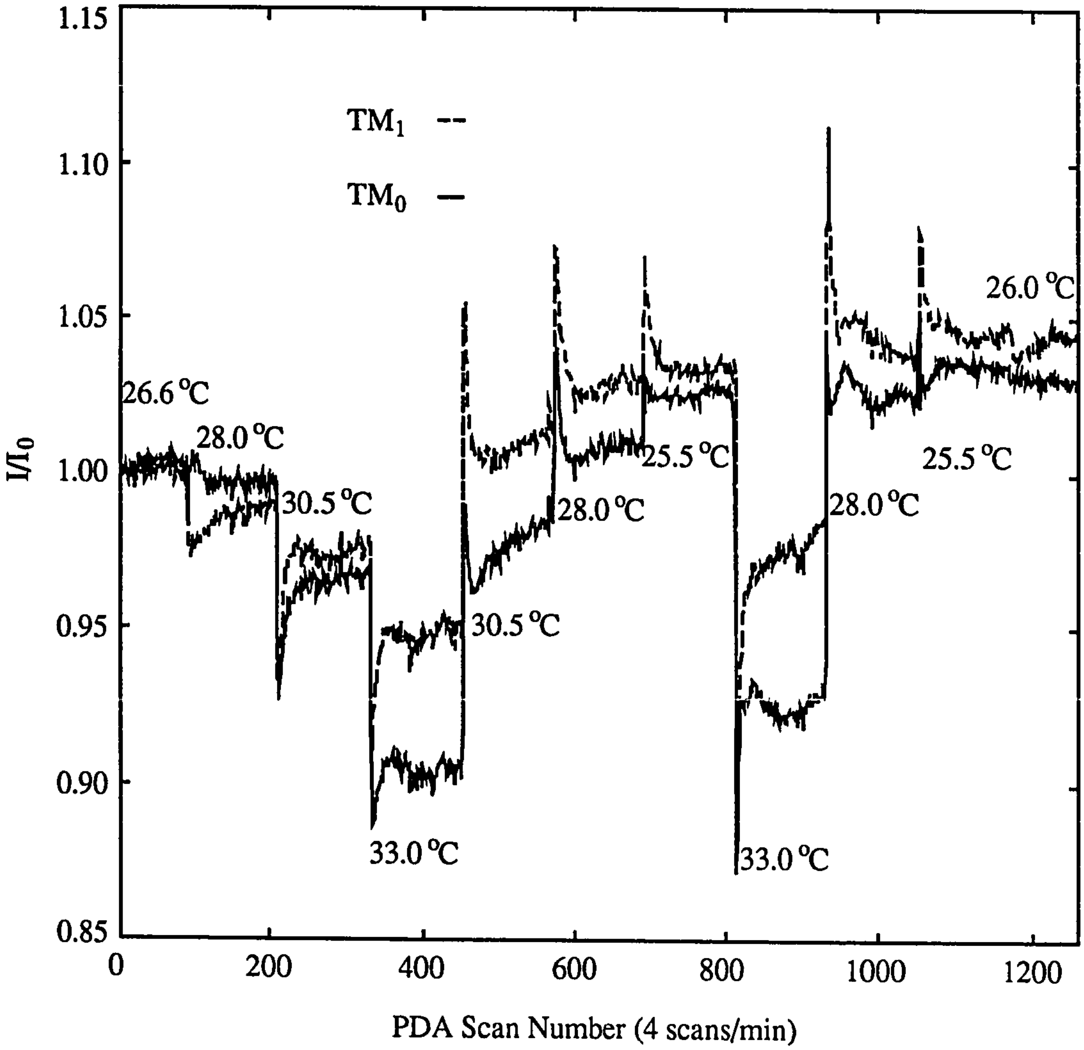

Figure 6.18b Ag$^+$-exchange waveguide 9C TM$_1$ and TM$_0$ mode integrated intensity response to step temperature changes.

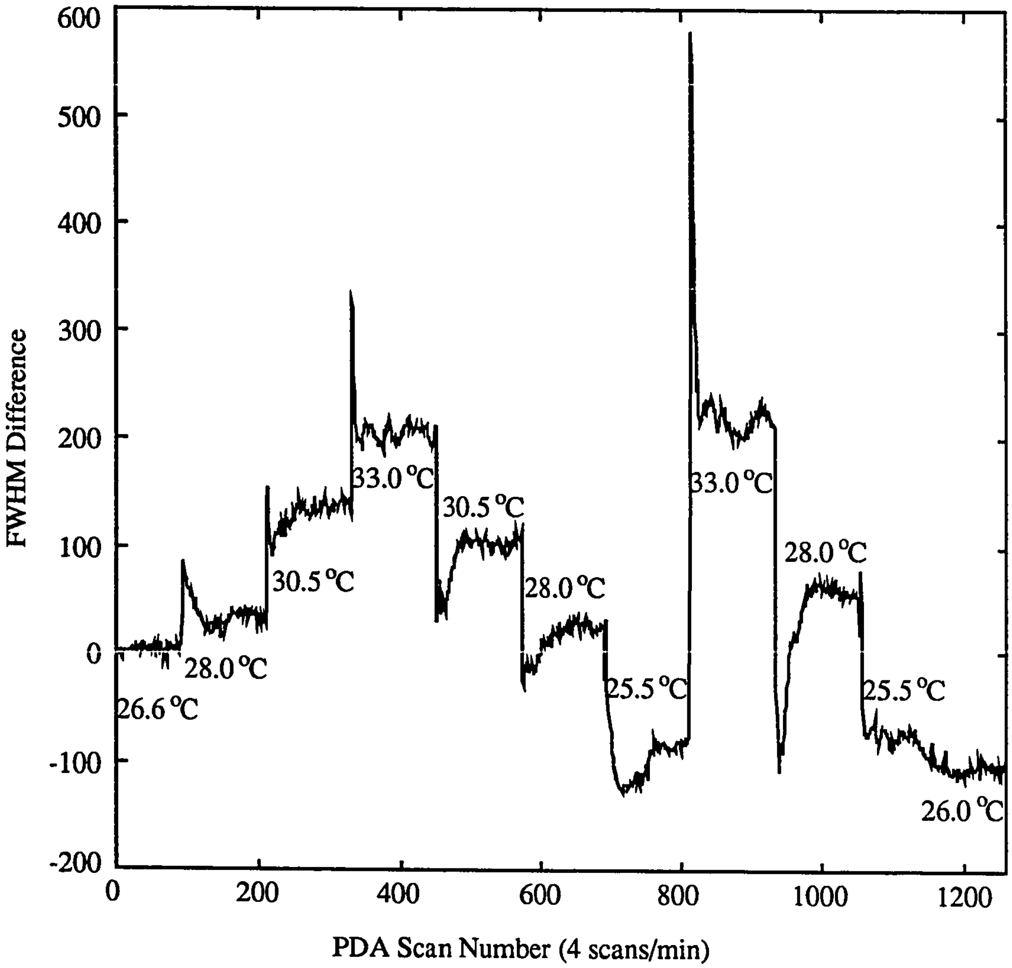

Figure 6.19a Ag$^+$-exchange waveguide 9C TM$_2$ mode position shift response to step temperature changes.

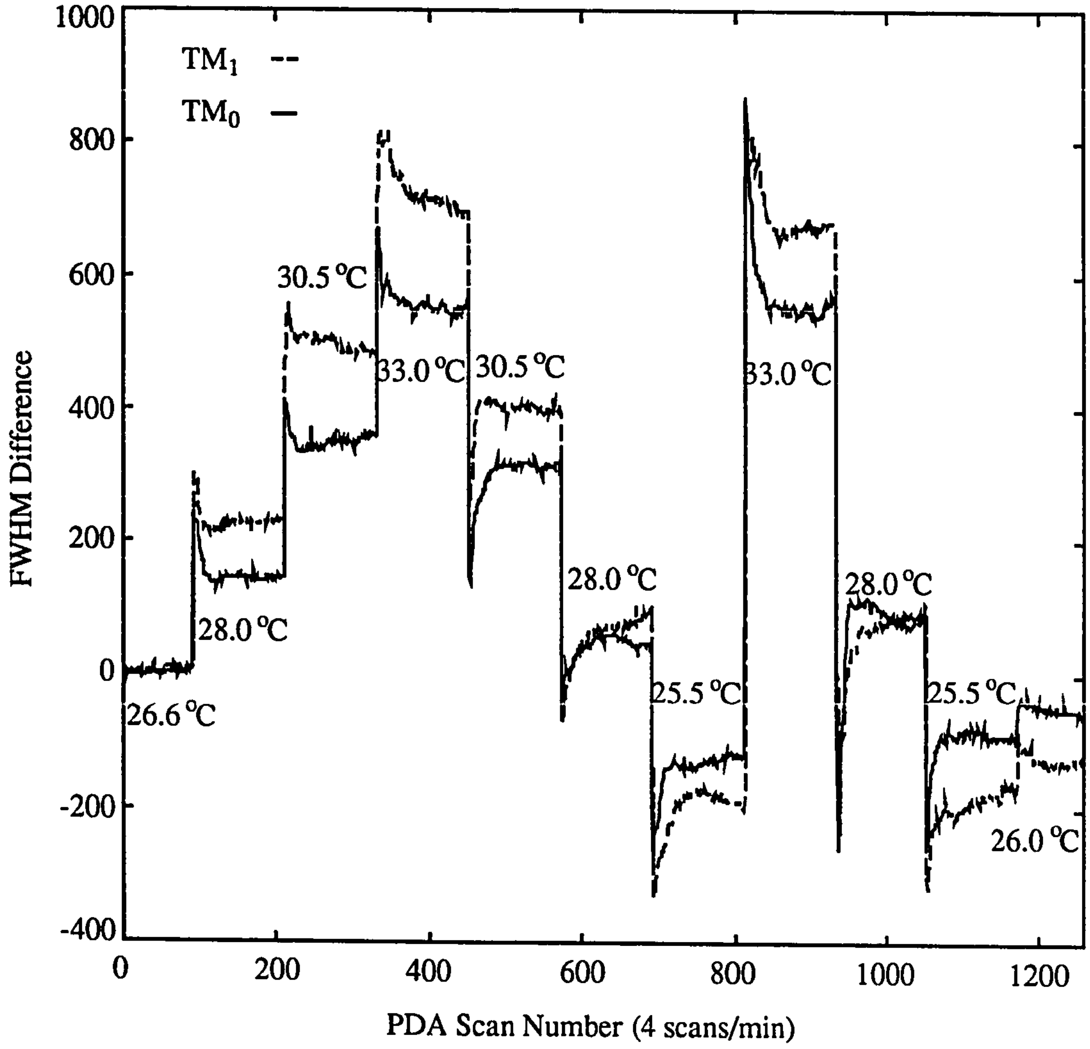

Figure 6.19b Ag^+-exchange waveguide 9C TM$_1$ and TM$_0$ mode position shift response to step temperature changes.

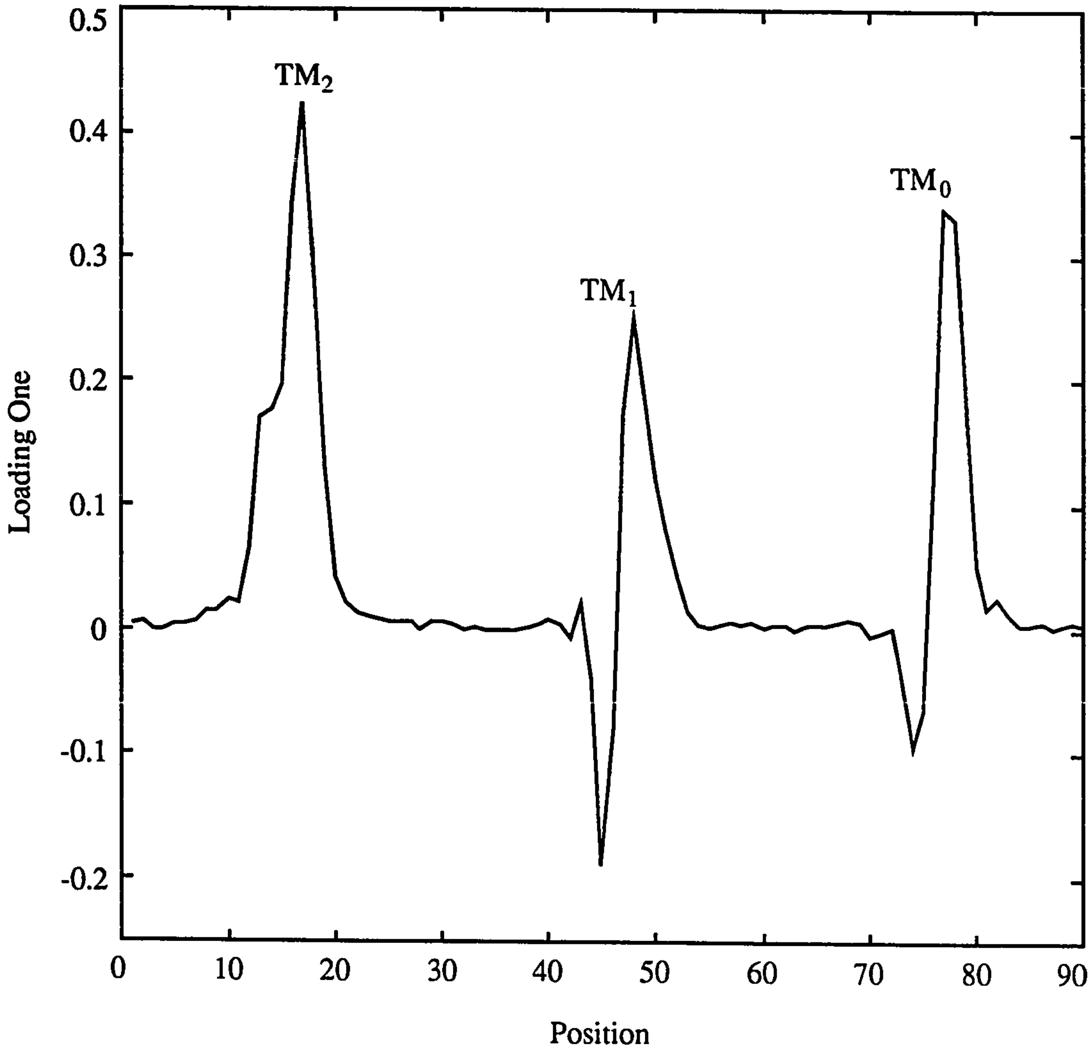

Figure 6.20a Ag$^+$-exchange waveguide 9C loading one response to step temperature changes.

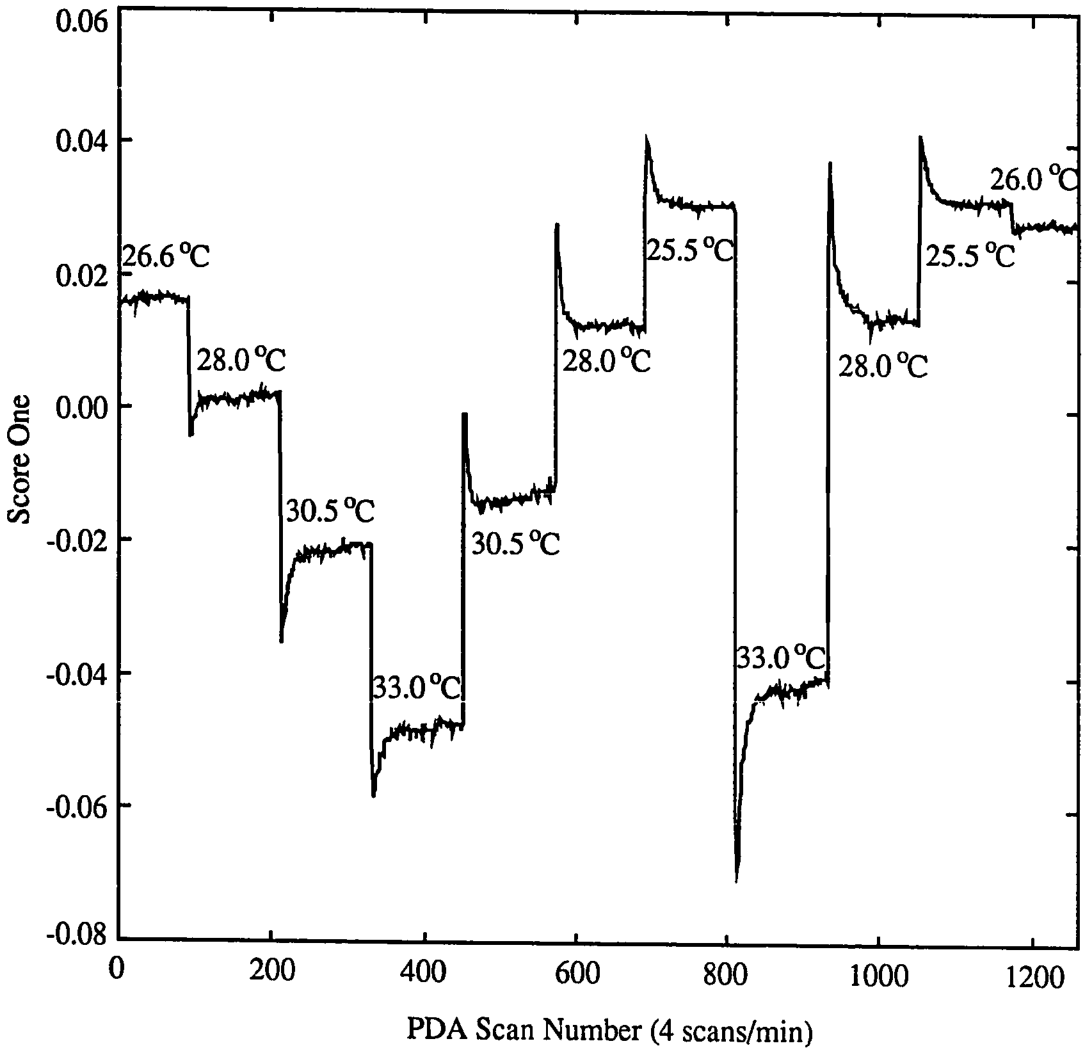

Figure 6.20b Ag$^+$-exchange waveguide 9C score one response to step temperature changes.

Chapter 7

Conclusion

7.1 Summary

7.1.1 Mode Conversion

The mechanism of mode conversion provides a reasonable explanation of multiple mode excitation in Ag^+-exchange waveguides. Modulations in mode conversion were most evident in model systems involving changes in the bulk refractive index of the cover solution. Unfortunately, a model describing the effects of mode conversion on the relative mode intensities for well-defined cover composition changes does not exist. The difficulty in deconvoluting grating coupling and decoupling effects from mode conversion effects may prevent the development of a relevant statistical model for predicting mode conversion effects. Reducing grating effects by masking these regions of the waveguide may provide an approach to deconvolution of the true mode conversion response. In the meantime, the mechanism of mode conversion stands as an empirical factor to describe trends not consistent with standard waveguide theory. From an applications point of view, the ability to obtain consistent device-to-device response function is a primary concern for successful implementation of the technology. Thus, an individual understanding of each response component may be sacrificed provided the overall response among numerous waveguide devices is reproducible.

7.1.2 Ag^+-Exchange Waveguide Response Function

In order to discuss the Ag^+-exchange waveguide response function, it is convenient to divide the waveguide structure into three distinct regions, the incoupling grating region, the mode propagation region, and the outcoupling grating region. At the incoupling grating, information about the composition of the cover solution is encoded as a variation in the coupled intensity of the selected mode. The incoupling grating response is related exclusively to the refractive index in the cover solution above the grating area.

In the mode propagation region, the interaction between the evanescent field and the cover solution can produce attenuations in mode intensity due to evanescent absorbance or variations in relative mode intensities due to modulations in mode conversion. At the outcoupling grating, the angle at which the various modes outcouple describes the angle at which each mode propagates in the mode propagation region. Thus, cover refractive index changes in the mode propagation region which extend into the outcoupling grating region are encoded as position changes on a linear array detector.

7.1.3 Ag^+-Exchange Waveguide Calibration

The Ag^+-exchange waveguide response to model systems was a complicated, nonlinear combination of multiple TM mode intensity variations and position shifts. Despite the obviously nonlinear waveguide response function, a linear partial least square (PLS) calibration gave reasonably good prediction errors for calibration samples. The calibrations set included replicate waveguide response determinations to each sample taken over the course of a typical experiment which lasted from three to nine hours. Temperature control of the waveguide system over the course of an experiment to determine cover composition could be incorporated to produce a more stable optical waveguide response.

7.1.4 Ag^+-Exchange Waveguide Sensitivity

The univariate and multivariate statistics presented earlier provide valid estimates of the waveguide sensitivity to modulations in the composition of the cover solution. The significant sensitivity of the waveguide to analytes which partitioned into or adsorbed to the anionic glass surface produced an enhanced response sensitivity relative to the corresponding bulk model system. In particular, the effective evanescent path length for cationic methylene blue which partitioned into the glass phase was nearly 30 times that of anionic bromocresol green. The implications for the development of evanescent field chemical sensors is clear as the waveguide sensitivity to interfacial partitioning is extremely high.

7.1.5 Ag^+-Exchange Waveguide Mixture Response

As discussed in the introduction chapter of this dissertation, modulations in planar waveguide boundary conditions produce variations in the effective evanescent path length of a waveguide device. This is particularly a problem in the evanescent measurement of sample absorbance when simultaneous refractive index modulations are occurring. However, the Ag^+-exchange waveguide response function to cover refractive index and absorbance changes were observed to be significantly different. Thus, the inclusion of multiple mode response data combined with multivariate statistics provided the necessary leverage to deconvolute and predict both components in a mixture system. The significance of this multivariate analysis has implications beyond the development of evanescent absorbance sensors. The potential exists to deconvolute bulk and surface active analytes on the basis of characteristic multiple mode response patterns. As such, the multiple mode response may also provide a diagnostic for surface fouling.

7.2 Future Work

The basic Ag^+-exchange waveguide research described in this dissertation has laid the foundation for the development of planar waveguide evanescent field chemical sensors. To take advantage of the surface sensitivity of the evanescent detection method, the next step involves modification of the waveguide surface to produce a selective or semi-selective chemical interface. In the present grating format characterized by superimposed solution and optical propagation paths, the modified waveguide surface can be evaluated as an planar adsorbent phase. An example of an application would be as a surface for accumulating and detecting metals at low concentrations in the liquid phase.

For a waveguide device with surface gratings defining mode propagation 90° to the direction of flow, modification of the waveguide surface with a common chromatographic stationary phase would allow for the separation and time resolved, on-column detection of partitioning analytes. Again, the application of a multiple mode Ag^+-exchange waveguide as the platform for a planar chromatographic system adds the potential to differentiate mobile phase disturbances from partitioning interactions. Such an ability would be particularly valuable in gradient mobile phase separations.

7.3 Outlook

The Ag^+-exchange planar optical waveguide response data presented in this thesis were characteristic of a single waveguide device. A major concern in the development of evanescent field chemical sensor based on the Ag^+-exchange waveguide platform is the ability to fabricate multiple devices exhibiting similar multiple mode response behavior. In particular, can suitable soda-lime glass materials with reproducible chemical composition and sodium distribution produce waveguides with the same mode structure and similar mode conversion characteristics. The fabrication of Ag^+-exchange waveguides from better quality soda-lime glass with well-defined surface grating structures is currently being investigated as continuing planar waveguide research.

An additional concern is the day-to-day performance reproducibility of the waveguide device. The Ag^+-exchange waveguide response calibrations indicated stable and reproducible device function over the course of many hours. However, for practical implementation, the device must operate over the long term (weeks to months) within tolerances set during a calibration step.

The multivariate response function associated with the multiple mode Ag^+-exchange waveguide produces an integrated, rugged, and robust device for developing chemicals sensors. Another parameter which certainly will contribute to the successful use of planar waveguide technology is the incorporation of multiple wavelength mode excitation. The successful coupling of broadband sources operating in the near-IR[1] and visible[2] to planar waveguides represent significant steps towards the development of miniature, integrated spectrometers and multi-wavelength chemical sensors. The development of integrated spectrometers or chemical sensors for remote, *in-situ* applications is very realistic due to the compatibility of fiber optic and planar waveguide technology.

7.4 Notes to Chapter 7

(1) Goldman, D. *CPAC Monitor* 1992, 24, 1-4.

(2) Tracy, D. private communication, Perkin Elmer Corporation, Newtown, CT.

List of References

(1) Abendroth, R. P. *J. Colloid Interface Sci.* **1970**, 34(4), 591-596. "Behavior of a pyrogenic silica in simple electrolytes"

(2) Ahrland, S.; Grenthe, I.; Noren, B. *Acta Chem. Scand.* **1960**, 14(5), 1059-1076. "The ion exchange properties of silica gel"

(3) Angel, S. M.; Ridley, M. N.; Langry, K.; Kulp, T. J.; Myrick, M. L. *ACS Symp. Ser.* **1989**, vol. 403, 346. "New developments and applications of fiber-optic sensors"

(4) Archibald, D. D.; Lin, L. T.; Honigs, D. E. *Appl. Spectrosc.* **1988**, 42(8), 1558. "Raman spectroscopy over optical fibers with the use of a near-IR FT spectrometer"

(5) Ashkin, A.; Gershenzon, M. *J. Appl. Phys.* **1963**, 34, 2116-2119. "Reflection and guiding of light at p-n junctions"

(6) Attridge, J. W.; Leaver, K. D.; Cozens, J. R. *J. Phys. E: Sci. Instrum.* **1987**, 20(5), 548-553. "Design of a fibre-optic pH sensor with rapid response"

(7) Attridge, J. W.; Cozens, J. R.; Leaver, K. D.; Webster, N. L. *J. Lightwave Tech.* **1985**, LT-3(5), 1084-1091. "Coaxial fiber sensors"

(8) Baes, C. F., Jr.; Mesmer, R. E. *The Hydrolysis of Cations*; John Wiley & Sons: New York, NY, 1972.

(9) Bello, J. M.; Vo-Dinh, T. *Appl. Spectrosc.* **1990**, 44(1), 63-69. "Surface enhanced Raman scattering fiber-optic sensor"

(10) Berman, R. J. Ph.D. Dissertation, University of Washington, Seattle, WA, 1990. "Renewable reagent based fiber optic chemical sensors"

(11) Berman, R. J.; Burgess, L. W. *SPIE Proceedings: Chemical, Biochemical and Environmental Applications of Fibers* **1990**, 1172, 206-214. "Renewable reagent fiber optic based ammonia sensor"

(12) Bohn, P. W. *Anal. Chem.* **1985**, 57(7), 1203-1208. "Theory of spectroscopic sampling in thin amorphous films"

(13) Bolton, B. A.; Scherer, J. R. *J. Phys. Chem.* **1989**, 93(22), 7635-7640. "Raman spectra and water absorption of bovine serum albumin"

(14) Bowman, E. M. Ph.D. Dissertation, University of Washington, Seattle, Wa, 1992. "Development of a polymeric thin film optical waveguide chemical vapor sensor"

(15) Bowman, E. M.; Burgess, L. W. *SPIE Proceedings: Chemical, Biochemical, and Environmental Sensors II* **1990**. "Evaluation of polymeric thin film waveguides as chemical sensors"

(16) Bright, F. V. *Appl. Spectrosc.* **1988**, 42(8), 1531. "A new fiber-optic-based multifrequency phase-modulation fluorometer"

(17) Burwell, R. L., Jr.; Pearson, R. G.; Haller, G. L.; Tjok, P. B.; Chock, S. P. *Inorg. Chem.* **1965**, 4(8), 1123-1128. "The adsorption and reaction of coordination complexes on silica gel"

(18) Callis, J. B.; Illman, D. L.; Kowalski, B. R. *Anal. Chem.* **1987**, 59(9), 624A-637A. "Process analytical chemistry"

(19) Charlot, G. *Quantitative Inorganic Analysis*; Masson Et C^{ie}: Paris, 1961.

(20) Chiang, K. S. *J. Lightwave Technol.* **1985**, LT-3(2), 385-391. "Construction of refractive-index profiles of planar dielectric waveguides from the distribution of effective indices"

(21) Choquette, S. J.; Locascio-Brown, L.; Durst, R. A. *Anal. Chem.* **1992**, 64(1), 55-60. "Planar waveguide immunosensor with fluorescent liposome amplification"

(22) Choquette, S. J. Ph.D. Dissertation, Virginia Polytechnic Institute and State University, Blacksburg, Va., 1988. "The application of planar optical waveguides to absorption spectrometry in flow injection analysis"

(23) Conn, H. J. *Biological Stains*, 6th ed.; Biotech Publications: Geneva, NY, 1953, p. 111.

(24) Cozens, J. R.; Boucouvalas, A. C. *Electron. Lett.* **1982**, 18(3), 138-140. "Coaxial optical coupler"

(25) Dakss, M. L.; Kuhn, L.; Heidrich, P. F.; Scott, B. A. *Appl. Phys. Lett.* **1970**, 16(12), 523-525. "Grating coupler for efficient excitation of optical guided waves in thin films"

(26) deBoer, J. H.; Vleeskens, J. M. *Proc. Koninkl. Ned. Akad. Wetenschap. Ser. B* **1958**, 61, 2-11. "Chemisorption and physical adsorption of water on silica. IV. nature of the surface"

(27) DeGrandpre, M. D. Ph.D. Dissertation, University of Washington, Seattle, Wa., 1990. "Fiber optic and thin film planar waveguide evanescent field chemical sensors"

(28) DeGrandpre, M. D.; Burgess, L. W.; White, P. L.; Goldman, D. S. *Anal. Chem.* **1990**, 62(18), 2012-2017. "Thin film planar waveguide sensor for liquid phase absorbance measurements"

(29) DeGrandpre, M. D.; Burgess, L. W. *Appl. Spectrosc.* **1990**, 44(2), 273. "A fiber-optic FT-NIR evanescent field absorbance sensor"

(30) DeGrandpre, M. D.; Burgess, L. W. *Anal. Chem.* **1988**, 60(23), 2582-2586. "Long path fiber optic sensor for evanescent field absorbance measurements"

(31) Dugger, D. L.; Stanton, J. H.; Irby, B. N.; McConnell, B. L.; Cummings, W. W.; Maatman, R. W. *J. Phys. Chem.* **1964**, 68(4), 757-760. "The exchange of twenty metal ions with the weakly acidic silanol group of silica gel"

(32) Dushina, A. P.; Aleskovskii, V. B. *Russ. J. Inorg. Chem.* **1963**, 8(9), 1147-1149. "Chromatography of heavy metals on silica gel"

(33) Fantone, S. D. *Appl. Opt.* **1983**, 22(3), 432-440. "Refractive index and spectral models for gradient-index materials"

(34) Farahi, F.; Leilabady, A. P.; Jones, J. D. C.; Jackson, D. A. *J. Phys. E: Sci. Instrum.* **1987**, 20, 435-436. "Optical-fibre flammable gas sensor"

(35) Fuh, M. R. S.; Burgess, L. W.; Christian, G. D. *Anal. Chem.* **1988**, 60, 433-435. "Wavelength division multiplexer for fiber optic sensor readout"

(36) Fuh, M. R. S.; Burgess, L. W.; Hirschfeld, T.; Christian, G. D.; Wang, F. *Analyst* **1987**, 112, 1159. "Single fibre optic fluorescence pH probe"

(37) Giallorenzi, T. G.; West, E. J.; Kirk, R.; Ginther, R.; Andrews, R. A. *Appl. Opt.* **1973**, 12(6), 1240-1245. "Optical waveguides formed by thermal migration of ions in glass"

(38) Goldman, D. S. *CPAC Monitor* **1992**, 24, 1-4. "Internal reflection spectroscopy in the NIR"

(39) Goldman, D. S.; White, P. L.; Anheier, N. C. *Appl. Opt.* **1990**, 29(31), 4583-4589. "Miniaturized spectrometer employing planar waveguides and grating couplers for chemical analysis"

(40) Golub, G. H.; Van Loan, C. F. *Matrix Computations*, 2nd ed.; Johns Hopkins Univ. Press: Baltimore, 1989.

(41) Goos, F.; Hänchen, H. *Ann. Physik* **1943**, 43, 383. "Über das eindringen des totalreflektierten lichtes in das dünnere medium"

(42) Hair, M. L.; Hertl, W. *J. Phys. Chem.* **1970**, 74(1), 91-94. "Acidity of surface hydroxyl groups"

(43) Harrick, N. J. *Internal Reflection Spectroscopy*, Harrick Scientific Corporation: New York, 1979.

(44) Hertel, P.; Menzler, H. P. *Appl. Phys.* **1987**, 44(B), 75-80. "Improved inverse WKB procedure to reconstruct refractive index profiles of dielectric planar waveguides"

(45) Hollenbach, U.; Efstathiou, C.; Fabricius, N.; Oeste, H.; Götz, H. *SPIE Proceedings: Micro-Optics* **1988**, 1014, 77-80. "Integrated optical refractive index sensor by ion-exchange in glass"

(46) Huggins, M. L.; Sun, K. H. *J. Amer. Cer. Soc.* **1943**, 26(1), 4-11. "Calculation of density and optical constants of a glass from its composition in weight percentage"

(47) Iler, R. K. *The Chemistry of Silica*, John Wiley & Sons: New York, 1979, p.687.

(48) Inman, S. M.; Stromvall, E. J.; Lieberman, S. H. *Anal. Chim. Acta.* **1989**, 217, 249. "Pressurized membrane indicator system for fluorogenic-based fiber-optic chemical sensors"

(49) Itoh, K.; Fujishima, A. *J. Phys. Chem.* **1988**, 92(25), 7043-7045. "An application of optical waveguides to electrochemistry: construction of optical waveguide electrodes"

(50) Ives, J. T.; Reichert, W. M. *Appl. Spectrosc.* **1988**, 42(1), 68-72. "Protein adsorption on the surface of a thin-film polymer integrated optical waveguide"

(51) Janata, J. *Principles of Chemical Sensors*; Plenum Press: New York, NY, 1989.

(52) Kenny, J. E.; Jarvis, G. B.; Chudyk, W. A.; Pohlig, K. O. *Anal. Inst.* **1987**, 16(4), 423. "Remote laser-induced fluorescence monitoring of groundwater contaminants: prototype field instrument"

(53) Kersten, R. Th. *Opt. Commun.* **1973**, 9(4), 427-431. "Numerical solution of the mode-equation of planar dielectric waveguides to determine their refractive index and thickness by means of a prism-film coupler"

(54) Kogelnik, H.; Sosnowski, T. P. *Bell. Syst. Tech. J.* **1970**, 49, 1602-1608. "Holographic thin film couplers"

(55) Lewis, E. N.; Kalasinsky, V. F.; Levin, I. W. *Anal. Chem.* **1988**, 60(24), 2658-2661. "Near-infrared fourier transform Raman spectroscopy using fiber-optic assemblies"

(56) Lukosz, W.; Tiefenthaler, K. *Opt. Lett.* **1983**, 8(10), 537-539. "Embossing technique for fabricating integrated optical components in hard inorganic waveguiding materials"

(57) Lu, B.; Lu, C.; Wei, Y. *Anal. Lett.* **1992**, 25(1), 1-10. "A planar quartz waveguide immunosensor based on TIRF principle"

(58) Luo, S.; Walt, D. R. *Anal. Chem.* **1989**, 61(2), 174. "Fiber-optic sensors based on reagent delivery with controlled-release polymers"

(59) Lytle, D. *Photonics Spectra* **1991**, 209. "A very small spectrometer with very big potential"

(60) Meltz, G.; Dunphy, J. R.; Morey, W. W.; Snitzer, E. *Appl. Opt.* **1983**, 22(3), 464-476. "Cross-talk fiber-optic temperature sensor"

(61) Midwinter, J. E. *IEEE J. Quant. Elect.* **1971**, QE-7(7), 339-344. "On the use of optical waveguide techniques for internal reflection spectroscopy"

(62) Midwinter, J. E. *IEEE J. Quant. Elect.* **1971**, QE-7(7), 345-350. "Theory of an ultra-broad-band optical dielectric waveguide coupler system"

(63) Miller, D. R.; Bohn, P. W. *Anal. Chem.* **1988**, 60(5), 407-411. "Depth profiling with standing waves. recovery of thin-film functional group distributions"

(64) Miller, D. R.; Han, O. H.; Bohn, P. W. *Appl. Spectrosc.* **1987**, 41(2), 245-248. "Quantitative raman spectroscopy of homogeneous molecular profiles in optical waveguides via direct measurement"

(65) Miller, S. E. *Bell Syst. Tech. J.* **1969**, 48, 2059-2069. "Integrated optics: an introduction"

(66) Mitchell, G. L. *IEEE J. Quant. Elect.* **1977**, QE-13(4), 173-176. "Absorption spectroscopy in scattering samples using integrated optics"

(67) Moshrezadeh, R.; Mai, X.; Seaton, C. T.; Stegeman, G. I. *Appl. Opt.* **1987**, 26(13), 2501. "Efficient grating couplers for polymer waveguides"

(68) Munkholm, C.; Walt, D. R.; Milanovich, F. P.; Klainer, S. M. *Anal. Chem.* **1986**, 58(7), 1427-1430. "Polymer modification of fiber optic chemical sensors as a method of enhancing fluorescence signal for pH measurements"

(69) Najafi, S. I. *Introduction to Glass Integrated Optics*, Artech House: Boston, 1992, p. 30.

(70) Nellen, Ph. M.; Lukosz, W. *Biosensors & Bioelectronics* **1991**, 6, 517-525. "Model experiments with integrated optical input grating couplers as direct immunosensors"

(71) Nelson, D. F.; Reinhart, F. K. *Appl. Phys. Lett.* **1964**, 5, 148-150. "Light modulation by the electrooptic effect in reversed-biased GaP p-n junctions"

(72) Osterberg, H.; Smith, L. W. *J. Opt. Soc. Amer.* **1964**, 58, 1078-1084. "Transmission of optical energy along surfaces: part II: inhomogeneous media"

(73) Personick, S. D. *Bell Syst. Tech. J.* **1971**, 50(3), 843-859. "Time dispersion in dielectric waveguides"

(74) Petersen, J. V.; Dessy, R. E. *SPIE Proceedings: Chemical, Biochemical, and Environmental Fiber Sensors II* **1990**, 1368, 61-72. "Direct exchange of metal ions onto silica waveguides"

(75) Peterson, J. I.; Goldstein, S. R.; Fitzgerald, R. V.; Buckhold, D. K. *Anal. Chem.* **1980**, 52(6), 864-869. "Fiber optic pH probe for physiological use"

(76) Piraud, C.; Mwarania, E.; Wylangowski, G.; Wilkinson, J.; O'Dwyer, K.; Schiffrin, D. J. *Anal. Chem.* **1992**, 64(6), 651-655. "Optoelectrochemical thin-film chlorine sensor employing evanescent fields on planar optical waveguides"

(77) Polky, J. N.; Harris, J. H. *J. Opt. Soc. Amer.* **1972**, 62(9), 1081-1087. "Absorption from thin-film waveguides"

(78) Rabolt, J. F.; Santo, R.; Schlotter, N. E.; Swalen, J. D. *IBM J. Res. Develop.* **1982**, 26(2), 209-216. "Integrated optics and raman scattering: molecular orientation in thin polymer films and langmuir-blodgett monolayers"

(79) Rabolt, J. F.; Schlotter, N. E.; Swalen, J. D. *J. Phys. Chem.* **1981**, 85(26), 4141-4144. "Spectroscopic studies of thin film polymer laminates using raman spectroscopy and integrated optics"

(80) Rabolt, J. F.; Santo, R.; Swalen, J. D. *Appl. Spectrosc.* **1979**, 33(6), 549-551. "Raman spectroscopy of thin polymer films using integrated optical techniques"

(81) Ramaswamy, R. V.; Srivastava, R. *J. Lightwave Technol.* **1988**, 6(6), 984-1002. "Ion-exchanged glass waveguides: a review"

(82) Reichert, W. M.; Ives, J. T.; Suci, P. A.; Hlady, V. *Appl. Spectrosc.* **1987**, 41(4), 636-640. "Excitation of fluorescent emission from solutions at the surface of polymer thin-film waveguides: an integrated optics technique for the sensing of fluorescence at the polymer/solution interface"

(83) Riebe, M. T.; Eustace, D. J. *Anal. Chem.* **1990**, 62(2), 65A-71A. "Process analytical chemistry: an industrial perspective"

(84) Saavedra, S. S.; Reichert, W. M. *Langmuir* **1991**, 7(5), 995-999. "In situ quantitation of protein adsorption density by integrated optical waveguide attenated total reflection spectrometry"

(85) Saavedra, S. S.; Reichert, W. M. *Anal. Chem.* **1990**, 62(20), 2251-2256. "Integrated optical attenuated total reflection spectrometry of aqueous superstrates using prism-coupled polymer waveguides"

(86) Scherer, J. R.; Bailey, G. F. *J. Membrane Sci.* **1983**, 13, 29-41. "Water in polymer membranes. part I water sorption and refractive index of cellulose acetate"

(87) Scherer, J. R.; Bailey, G. F. *J. Membrane Sci.* **1983**, 13, 43-52. "Water in polymer membranes. Part II raman scattering from guided laser beams"

(88) Schindler, P. W.; Furst, B.; Dick, R.; Wolf, P. U. *J. Colloid Interface Sci.* **1979**, 55(2), 469-475. "Ligand properties of surface silanol groups"

(89) Schindler, P.; Kamber, H. R. *Helv. Chim. Acta.* **1968**, 51(7), 1781-1786. "Acidity of silanol groups"

(90) Schlotter, N. E.; Rabolt, J. F. *J. Phys. Chem.* **1984**, 88(10), 2062-2067. "Raman spectroscopy in polymeric thin film optical waveguides. 1. polarized measurements and orientational effects in two-dimensional films"

(91) Seifert, M; Tiefenthaler, K.; Heuberger, K.; Lukosz, W.; Mosbach, K. *Anal. Lett.* **1986**, 19(1), 1986. "An integrated optical biosensor (IOBS)"

(92) Sepaniak, M. J.; Tromberg, B. J.; Alarie, J. P.; Bowyer, J. R.; Hoyt, A. M.; Vo-Dinh, T. *ACS Symp. Ser.* **1989**, vol. 403, 318. "Design considerations for antibody-based fiber-optic chemical sensors"

(93) Smith, R. L.; Pietrzyk, D. J. *Anal. Chem.* **1984**, 56(4), 610-614. "Liquid chromatographic separation of metal ions on a silica column"

(94) Spohn, P. K.; Seifert, M. *Sensors and Actuators* **1988**, 15, 309-324. "Interaction of aqueous solutions with grating couplers used as integrated optical sensors and their pH behaviour"

(95) Stephens, D. A.; Bohn, P. W. *Anal. Chem.* 1987, 59(21), 2563-2566. "Long path length absorption measurements in thin dielectric films"

(96) Stern, F. *Appl. Opt.* **1964**, 3, 111. "Transmission of isotropic radiation across an interface between two dielectrics"

(97) Stewart, G.; Millar, C. A.; Laybourn, P. F. R.; Wilkinson, C. D. W.; DeLaRue, R. M. *IEEE J. Quantum Electron.* **1977**, QE-13(4), 192-200. "Planar optical waveguides formed by silver-ion migration in glass"

(98) Strazhesko, D. N.; Strelko, V. B.; Belyakov, V. N.; Rubanik, S. C. *J. Chromatogr.* **1974**, 102, 191-195. "Mechanism of cation exchange on silica gels"

(99) Sutherland, R.; Dähne, C.; Place, J. F. *Anal. Lett.* **1984**, 17(B1), 43-53. "Preliminary results obtained with a no-label, homogeneous, optical immunoassay for human immunoglobulin G"

(100) Swalen, J. D.; Tacke, M.; Santo, R.; Rieckhoff, K. E.; Fischer, J. *Helv. Chim. Acta* **1978**, 61(3), 960-977. "Spectra of organic molecules in thin films"

(101) Swalen, J. D.; Santo, R.; Tacke, M.; Fischer, J. *IBM J. Res. Develop.* **1977**, 21, 168-175. "Properties of polymeric thin films by integrated optical techniques"

(102) Swalen, J. D.; Tacke, M.; Santo, R.; Fischer, J. *Opt. Commun.* **1976**, 18(3), 387-390. "Determination of optical constants of polymeric thin films by integrated optical techniques"

(103) Tiefenthaler, K.; Lukosz, W. *Thin Solid Films* **1985**, 126, 205-211. "Grating couplers as integrated optical humidity and gas sensors"

(104) Tiefenthaler, K.; Lukosz, W. *Opt. Lett.* **1984**, 10(4), 137-139. "Integrated optical switches and gas sensors"

(105) Tien, P. K.; Ulrich, R.; Martin, R. J. *Appl. Phys. Lett.* **1969**, 14(9), 291-294. "Modes of propagating light waves in thin deposited semiconductor films"

(106) Ulrich, R.; Torge, R. *Appl. Opt.* **1973**, 12, 2901. "Measurement of thin film parameters with a prism coupler"

(107) Unger, K. K. *Porous Silica*, Elsevier Scientific Publishing Co.: New York, 1979, p. 133.

(108) Vysotskii, Z. Z.; Strazhesko, D. N. in *Adsorption and Adsorbents*, vol. 1; Strazhesko, D. N., ed., Wiley Interscience: New York, 1973, p. 55.

(109) Wakatsuki, T.; Furukawa, H.; Kawaguchi, K. *Soil Sci. Plant Nutr.* **1974**, 20(4), 353-362. "Specific and non-specific adsorption of inorganic ions"

(110) Weast, R. C., Ed., *CRC Handbook of Chemistry and Physics*, 65th ed.; CRC Press Inc.: Boca Raton, FL, 1984, E-358.

(111) Weyer, L. G.; Becker, K. J.; Leach, H. B. *Appl. Spectrosc.* **1987**, 41(5), 786. "Remote sensing fiber optic probe NIR spectroscopy with chemometric data treatment"

(112) White, J. M.; Heidrich, P. F. *Appl. Opt.* **1976**, 15(1), 151-155. "Optical waveguide refractive index profiles determined from measurement of mode indices: a simple analysis"

(113) Yariv, A.; Leite, R. C. C. *Appl. Phys. Lett.* **1963**, 2(3), 55-59. "Dielectric-waveguide mode of light propagation in p-n junctions"

(114) Zachariasen, W. H. *J. Am. Chem. Soc.* **1932**, 54, 3841-3851. "The atomic arrangement in glass"

(115) Zhujun, Z.; Zhang, Y.; Wangbai, M.; Russell, R.; Shakhsher, Z. M.; Grant, C. L.; Seitz, W. R.; Sundberg, D. C. *Anal. Chem.* **1989**, 61(3), 202-205. "Poly(vinyl alcohol) as a substrate for indicator immobilization for fiber-optic chemical sensors"

Appendix A

Flow Cell Design

Step One: Front View

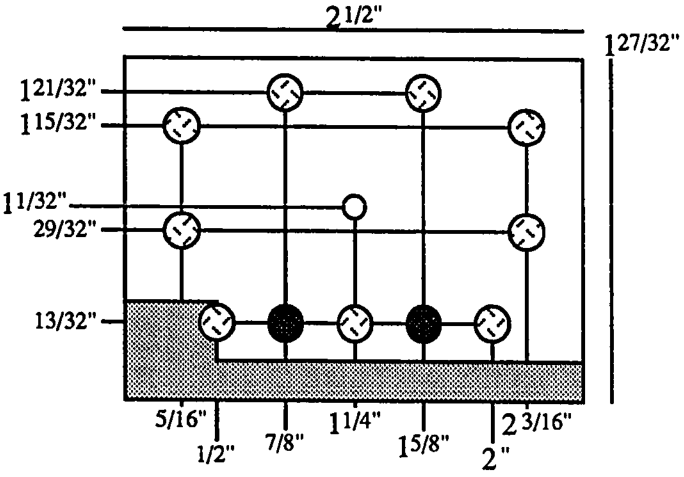

<u>Step One: Front View</u>

● - clearance for 3/16" diameter
stainless steel guides

◌ - clearance for 6-32 threads,
countersink front side

○ - tap thru 6-32 threads
(teflon set screw)

Figure a.1 Aluminum flow cell face plate: step one.

Step Two: Front View

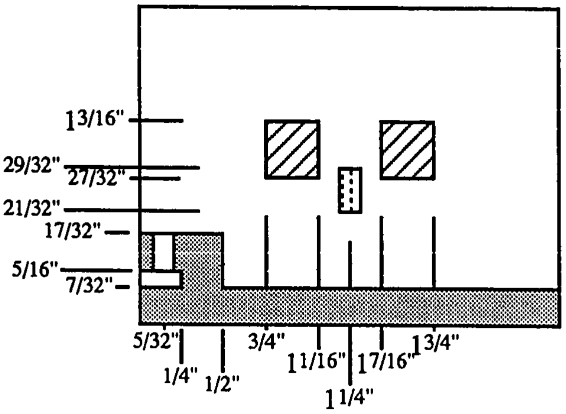

Side View

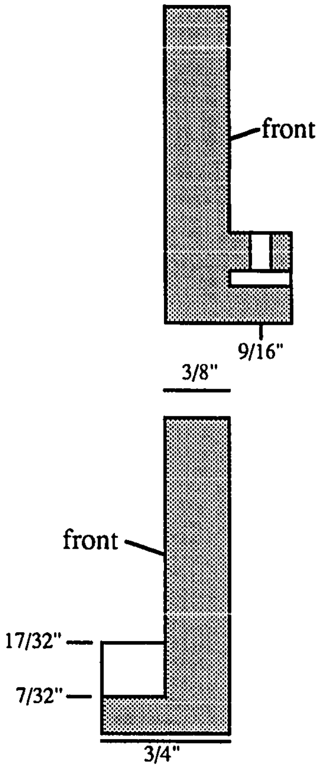

Step Two: Front View

▯ - tap thru 6-32 threads (teflon set screw)

⁞ - mill 1/8" window thru, center below teflon set screw

▨ - mill window thru, 30 degree bevel front outside edges

Figure a.2 Aluminum flow cell face plate: step two.

Step Three: Back View

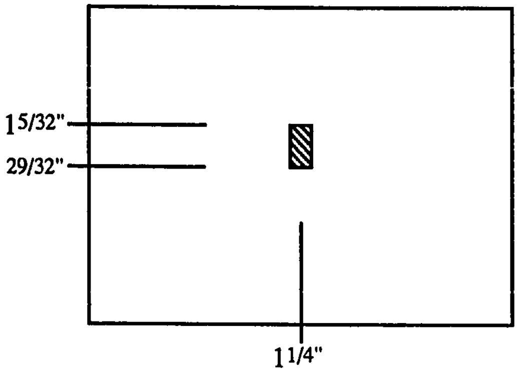

Step Two: Back View

- require a very flat, smooth back surface

▨ - mill 1/8" width, 3/32" depth

Finished Faceplate

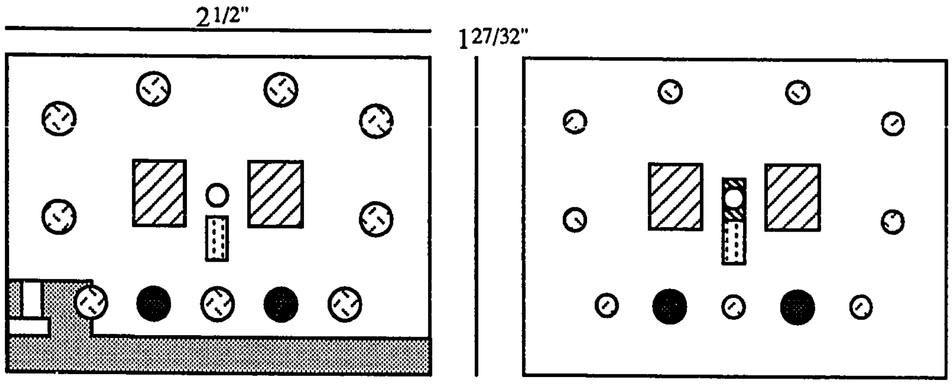

Front View **Back View**

Figure a.3 Aluminum flow cell face plate: step three and finished views.

Step One: Front View

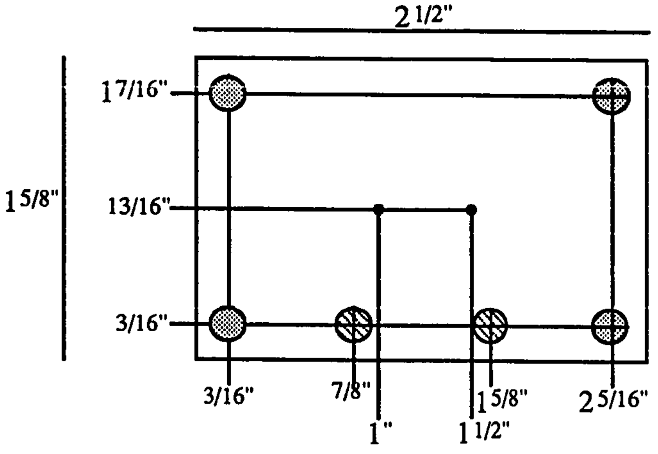

Side View

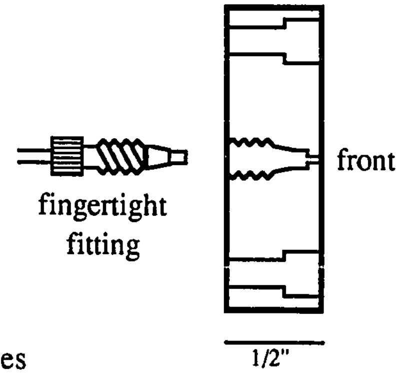

Step One: Front View

▨ - clearance for 3/16" diameter stainless steel guides

◍ - clearance for 6-32 threads, countersink frontside

• - drill 0.5 mm thru entire width, tap with 10-32 threads 3/16" thru backside, fit to ferrule on fingertight fitting

Figure a.4 PEEK channel piece: step one.

Step Two: Front View

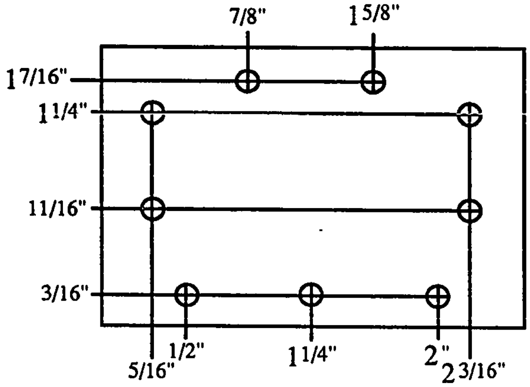

Step Two: Front View

○ - tap thru with 6-32 threads

Finished Channel Piece

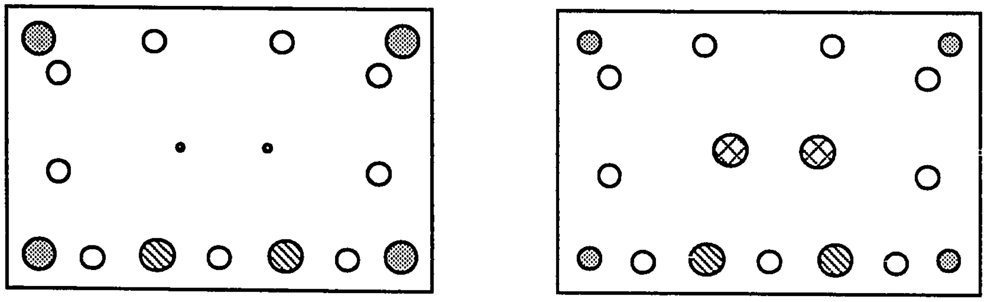

Front View **Back View**

Figure a.5 PEEK channel piece: step two and finished views.

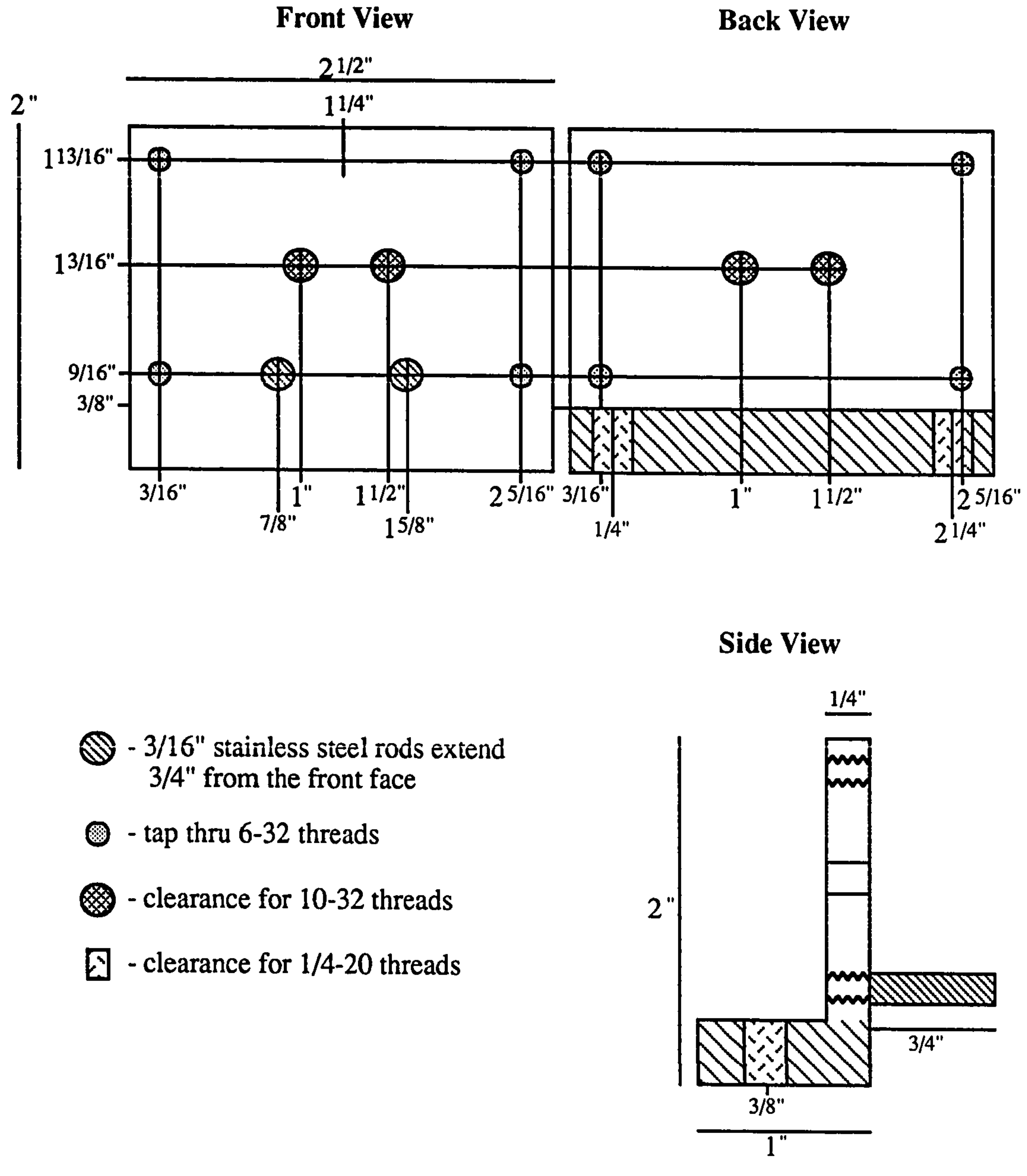

▨ - 3/16" stainless steel rods extend 3/4" from the front face

● - tap thru 6-32 threads

⊕ - clearance for 10-32 threads

☐ - clearance for 1/4-20 threads

Figure a.6 Stainless steel L-bracket: front, back, and side views.

Vita

Kevin J. Kuhn

Education

Bachelor of Arts, Chemistry with Physics and Business Economics minors, University of Minnesota, Morris, 1987.

Doctor of Philosophy, Analytical Chemistry, University of Washington, 1993.

Dissertation Title

Evaluation of a Planar Optic Waveguide as a Platform for Evanescent Field Chemical Sensor Development

Publications

Kuhn, K. J.; Burgess, L. W. "Chemometric Evaluation of the Multiple Mode Response of an Ion-Diffused Planar Optical Waveguide to Liquid Phase Analytes," *Anal. Chem.* **1993**, 65(10), 1390.

Kuhn, K. J.; Burgess, L. W. "Evaluation of an Ion-Exchanged Integrated Optic Waveguide for Solution Phase Chemical Sensing," *SPIE Proceedings: Chemical, Biochemical, and Environmental Fiber Sensors IV* **1992**.

Kuhn, K. J.; Hahn, B.; Percec, V.; Urban, M. W. "Structural and Quantitative Analysis of Surface Modified Poly(vinylidene fluoride) Films Using ATR FT-IR Spectroscopy," *Appl. Spectrosc.* **1987**, 41(5), 843.